ERNEST ORLANDO LAWRENCE BERKELEY NATIONAL LABORATORY

Molecular Beam Studies of Unimolecular and Bimolecular Chemical Reaction Dynamics Using VUV Synchrotron Radiation as a Product Probe

RECEIVED
FEB 1 / 1998
OSTI

David A. Blank

Chemical Sciences Division

August 1997

Ph.D. Thesis

DISCLAIMER

DISCLAIMER

Portions of this document may be illegible electronic image products. Images are produced from the best available original document.

Molecular Beam Studies of Unimolecular and Bimolecular Chemical Reaction Dynamics Using VUV Synchrotron Radiation as a Product Probe

David Andrew Blank
Ph.D. Thesis

Department of Chemistry
University of California, Berkeley

and

Chemical Sciences Division
Ernest Orlando Lawrence Berkeley National Laboratory
University of California
Berkeley, CA 94720

August 1997

Molecular Beam Studies of Unimolecular and Bimolecular Chemical Reaction Dynamics Using VUV Synchrotron Radiation as a Product Probe

by

David Andrew Blank

B. S. (University of California at Los Angeles) 1992

A dissertation submitted in partial satisfaction of the requirements for the degree of

Doctor of Philosophy

in

Chemistry

in the

GRADUATE DIVISION

of the

UNIVERSITY of CALIFORNIA at BERKELEY

Committee in charge:

Professor Yuan T. Lee, Chair
Professor Daniel M. Neumark
Professor Y. Ron Shen

Fall 1997

Abstract

Molecular Beam Studies of Unimolecular and Bimolecular Chemical Reaction Dynamics Using VUV Synchrotron Radiation as a Product Probe

by

David Andrew Blank

Doctor of Philosophy in Chemistry

University of California at Berkeley

Professor Yuan T. Lee, Chair

This dissertation describes the use of a new molecular beam apparatus designed to use tunable VUV synchrotron radiation for photoionization of the products from scattering experiments. The apparatus was built at the recently constructed Advanced Light Source at Lawrence Berkeley National Laboratory, a third generation 1-2 GeV synchrotron radiation source. The new apparatus is applied to investigations of the dynamics of unimolecular reactions, photodissociation experiments, and bimolecular reactions, crossed molecular beam experiments.

The first chapter describes the new apparatus and the VUV radiation used for photoionization. This is followed by a number of examples of the many advantages provided by using VUV photoionization in comparison with the traditional technique of electron bombardment ionization. At the end of the chapter there is a discussion of the data analysis employed in these scattering experiments.

The remaining four chapters are complete investigations of the dynamics of four chemical systems using the new apparatus and provide numerous additional examples of the advantages provided by VUV photoionizaiton of the products. Chapters 2-4 are photofragment translational spectroscopy studies of the photodissociation dynamics of dimethyl sulfoxide, acrylonitrile, and vinyl chloride following absorption at 193 nm. All of these systems have multiple dissociation channels and provide good examples of the ability of the new apparatus to unravel the complex UV photodissociation dynamics that can arise in small polyatomic molecules.

Chapter 5 is a crossed molecular beam investigation of the hydrogen atom abstraction reaction from propane by atomic chlorine at collision energies of 8.0, 11.5, and 31.6 kcal/mol. This study is made possible by the ability to probe the propyl radical product with near zero background from scattered propane reactant molecules as a result of the selective ionization provided by VUV photoionization. The reaction exhibits two different reaction mechanisms. Collisions with large impact parameters involve a previously unreported spectator/stripping mechanism and collisions with smaller impact parameters react via a direct mechanism with impulsive recoil of the products.

To my Mother, Father

and

Colene

Table of Contents

Table of figures

Acknowledgements

First and foremost I owe thanks to Prof. Yuan T. Lee for giving me the opportunity to be a part of so many extraordinary experiments. His love of science provided the best possible atmosphere for learning and his legendary scientific intuition and teaching skills made every discussion a wonderful and memorable learning experience.

I owe much of what I learned during my 5 years in the Lee Group to the tutelage of Simon North. It was his overly energetic and enthusiastic approach to the experiments that led to my initial decision to join the group. He introduced me to the instruments, to the wonders of PTS, and to a better class of music. Our collaboration on the B-machine will stand as one of my greatest experiences in experimental science. Our scientific collaboration extended beyond his graduation with him visiting from Brookhaven to participate in experiments on End Station One. These collaborations became chapters 2-4 of this thesis. And, most importantly, we became good friends. (I should also thank his wife Diana who had to put up with me by association.)

Arthur Suits arrived at the end of my second year and was charged with the dubious task of managing the group as Yuan spent more of his time in Taiwan. I enjoyed working with Arthur both during my time on campus and at the Chemical Dynamics Beamline after I moved to the hill.

Allan Bracker became a good friend with whom I enjoyed many scientific as well social discussions as we watched the group at Berkeley come to an end.

After moving to the hill I put together End Station One with Xueming Yang who did an excellent job designing the machine. I had a good time working with him on the initial experiments at ES1.

During my last year I worked with Naoki Hemmi on ES1 whose quiet demeanor made him very easy to get along with. I wish him continued success on ES1. I should also thank the members of the End Station Two team, Matt Evans and Chia-Wei Hsu, who made it easy to share the precious ALS time on Beamline 9. Phil Heimann was essential to the success of the Chemical Dynamics Beamline and John Bozek made the sharing of Beamline 9 with the numerous visitors on the Atomic and Molecular Physics Beamline easier than anyone suspected it could be.

There is also everyone else in the group during my stay to thank. Everyone helped out at one time or another. Those who I had the greatest interaction with include Domenico Stranges, Jim Myers, Hongtao Hou, and an enjoyable stint with Marc Vrakking doing H-atom Rydberg tagging from the dissociation of methyl radicals. Toward the end I enjoyed interacting with Weizhong Sun, David Blunt, Eloy Wouters, Darcy Perterka, and many interesting discussions with Musa Ahmed. And while we didn't become the best of friends, Ralf Kaiser did provide a wealth of entertainment.

None of the experiments I participated in would have been possible without the assistance of the extraordinary support staff both on campus and at the ALS. On campus Eric and Hans in the machine shop were invaluable and without Phil the helium compressor on the C-level would have been a lost cause. At the ALS, Charlie and Wayne-O were able to provide anything needed to get the experiments running (and

legal). The magic of Andrew Mei in machining all kinds of exotic materials was central to the success of all of the radical sources.

I don't have thanks enough for Ann Lawhead and Marian Grebanier, the administrative assistants. They kept everything together in a group that tried so hard to screw up most everything involved with the university bureaucracy.

Finally I would like to thank my parents whose uncompromising love and support is the reason for my success. And Colene, who has put up with the kind of neglect only graduate school can produce, supported me through the endless night shifts at the ALS, and who still wants to become my wife.

Chapter 1

An Introduction to End Station One at the Chemical Dynamics Beamline

1. Introduction

The use of electron impact ionization (EI) coupled with mass selection for detection of scattered reaction products in crossed molecular beam investigations of bimolecular chemical reactions[1,2] and investigations of unimolecular photochemical reactions[3,4] has proven to be one of the most powerful and general techniques for unraveling the detailed underlying dynamics in an enormous number of chemical systems. The experiments measure laboratory angular and velocity distributions for scattered reaction products under single collision, crossed molecular beams, or collisionless, photodissociation in a single molecular beam, conditions. These observed asymptotic properties of the products can then be used to obtain flux maps of the center of mass, cm, angular and velocity distributions revealing a wealth of details about the interactions involved in the chemical reactions.[5]

EI followed by mass selection has a number of important advantages. Optical detection methods (*ex.* multiphoton ionization, direct absorption) often require specific spectroscopic information about the product being detected thus greatly limiting the

products that can be effectively probed. In addition, state specific detection greatly reduces the number of products being probed from the already very small product density inherent to these types of experiments since the products can be spread over a very large number of quantum states. A typical experiment produces only $\sim 10^6$ product molecules / second with an average velocity of ~ 1000 m/s at an ionization region which is only ~ 0.5 cm^3. EI coupled with mass selection provides sufficient sensitivity to detect most products under these conditions and offers the ability to detect those products without any requirement concerning detailed information about the molecule, for example knowledge about the spectroscopy of the molecule.[5] The resulting state independent product detection can detect most chemical species and provides a complete overall picture of the dynamics for a wide range of chemical systems. For this reason the technique is often referred to as "universal" detection. However, even with the proven success of EI it has a number of limitations.

One of the most severe limitations results from background generated by dissociative ionization when using EI. When attempting to detect products at a mass-to-charge ratio (m/e) below that of the reactant(s), note that this is always the case for photodissociation experiments, dissociative ionization of reactant molecules can generate a substantial background at the m/e of interest. This is particularly evident in investigations involving hydrocarbons where dissociative ionization often leads to large backgrounds over a wide range of masses. The background generated by dissociative ionization of reactant molecules can lead to extremely long signal averaging ending with a poor signal to noise ratio (s/n) in the time of flight spectrum (TOF). Often the result is

even worse with the detection sensitivity being lowered to the point where the experiment is no longer feasible. Dissociative ionization of other reaction products, either the momentum matched partner fragments or products from a competing reaction channel, can also produce interfering signals in TOF spectra.

While being one of its greatest advantages, the near total lack of selectivity provided by EI, and hence the universal detection capability, is also one of its greatest shortcomings. With mass selection being the only form of product discrimination, background can come from molecules with different chemical identities but the same mass. One of the most severe examples of this problem is the notoriously large background at m/e 28 that comes from ionization of CO, a permanent resident of the stainless steel ultra high vacuum (UHV) detector chamber with a partial pressure of $\sim 10^{-11}$ torr. This very large background not only prevents detection of CO reaction products, but also prevents detection of other molecules at the same mass, _ex._ ethene. In addition, adjacent masses are also affected. The enormous background requires an extremely high mass resolution to reduce leakage at m/e 27 and m/e 29. Increasing the mass resolution of the quadrupole mass filter results in a reduction in ion transmission leaving a no win situation, the background and signal are reduced simultaneously. A similar problem, further complicated by dissociative ionization, also exist for all of the residual gasses that have reasonable partial pressures in the detection chamber. In addition to CO these include H_2, CH_4, H_2O, and CO_2. A more direct result of the lack of selectivity is the inability to assign the chemical identity of reaction products in cases where multiple

products can have same mass. One of the most challenging examples is in cases of multiple isomers of a given reaction product.

Finally, EI limits the ultimate velocity resolution that can be achieved. In most experiments the velocity resolution is limited by the ratio of the uncertainty in the location of product ionization, determined by the effective length of the ionizer, and the nominal neutral flight length of the reaction products. While increasing the neutral flight length (d) provides increased resolution it also rapidly becomes a liability as product number density drops with d^2. EI is spatially limited by space charge effects and under the best of conditions has an effective length of ~0.5 cm.[6] With a typical neutral flight length of 30 cm the flight length resolution is 1/60 or an uncertainty of ~2%.

All of the problems associated with EI mentioned above can be solved or greatly improved upon using tunable vacuum ultraviolet (VUV) photoionization (PI), while at the same time maintaining the universal detection capability that is the greatest asset of EI. The difficulty lies in generating a continuous source of tunable VUV radiation with sufficient flux to allow detection of the extremely low product number densities. While laser technology has continued to develop at a rapid pace, the generation of continuous VUV light by nonlinear mixing techniques is currently unable to generate a sufficient flux of photons to make the experiments viable. Pulsed lasers are able to achieve much higher peak powers, however both continuous and pulsed lasers are restricted to limited tunability, and pulsed ionization adds additional complexity to velocity analysis of the products. The answer comes from the recently construct Advance Light Source (ALS) at

Lawrence Berkeley National Laboratory. The ALS is a third generation synchrotron light source and offers tunable VUV radiation with very high photon flux.

To take advantage of the ALS a new crossed molecular beam instrument has been constructed which uses the tunable VUV radiation for product PI.[7] The machine is referred to as End Station One (ES1) and it is part of the Chemical Dynamics Beamline at the ALS. The rest of this chapter provides a description of ES1, a description of the VUV radiation used for PI at ES1, and gives a number of initial examples of the advantages provided by VUV PI. Later in the chapter there is a section describing the data analysis employed for crossed molecular beam reactive scattering and photofragment translational spectroscopy (PTS) experiments. The rest of this dissertation provides examples of complete investigations using ES1, highlighting many of the advantages offered by this next generation crossed molecular beam apparatus. Chapters 2-4 are investigation of the UV photodissociation of three small molecules, dimethyl sulfoxide, acrylonitrile, and vinyl chloride, and chapter 5 is a crossed molecular beam investigation of the Cl + propane reaction.

2. End Station One

The design of End Station One was bases on a previously constructed apparatus that is described in detail elsewhere[4,8] with a number of significant improvements.[7] A drawing of ES1 is shown in figure 1. ES1 has two mutually perpendicular differentially pumped molecular beam source chambers that are rotatable about their crossing point

(also known as the interaction region). Two source chambers make the apparatus capable of performing crossed molecular beam scattering experiments in addition to PTS experiments, which were the exclusive purpose of the previous instrument. PTS experiments are accomplished by using only one molecular beam source and sending a photodissociation laser perpendicular to the drawing in figure 1 along the axis of rotation for the source chambers.   •

The molecular beam sources are pumped by high throughput 2000 l/s magnetically suspended (mag-lift) turbo molecular pumps (Seiko Seiki STPH2000C) backed by 500 cfm roots blowers. These pumps are capable of pumping 2000 l/s up to a pressure of 1 torr providing sufficient pumping for typical continuous molecular beam source operation. The sources are rotatable about $130°$ ($20°$ beyond horizontal for each of the two sources.) A single 2000 l/s mag-lift turbo pump (Seiko Seiki STP2000C) pumps the main scattering chamber. The floor of the main chamber is equipped with a nickel-plated copper liquid nitrogen (LN_2) cooled panel (~3'x3'). A helium expansion cold head cools a copper panel just behind the interaction region (known as the "gobbler") to ~20 K. The gobbler places a 20 K surface along the viewing axis of the detector providing a substantial reduction in background from molecules that are deflected into the detector. There are two retractable mechanical chopper wheels for velocity analysis of the molecular beams and scattered reaction products. The wheels come in from the top and bottom of the apparatus allowing access for one of the wheels at any source rotation angle.

The detector is also based on a previous design[1] with three regions of differential pumping leading to an ionization region followed by a quadrupole mass filter and a Daly ion counter. The most significant difference is that the design accommodates the use of VUV synchrotron radiation from the ALS as a PI source. A detailed drawing of the detector is shown in figure 2. The third region of differential pumping is cooled to 77 K with LN_2 and the PI region is cooled to ~15 K using a helium expansion cold head. The VUV PI radiation is focused to 150x250 µm at the center of the ionization region, and after passing through the ionization region impinges on a UHV/VUV calorimeter to provide continuous monitoring of the VUV flux. The nominal neutral flight length from the axis of rotation of the source chambers (the interaction region) to the VUV PI radiation is currently 15.1 cm. The nominal neutral flight length from the mechanical chopper wheels is 11.9 cm, however it should be noted that the chopper wheels are not keyed into position leaving this distance subject to change in the future.

The detector is exclusively pumped by mag-lift turbo pumps (Seiko Seike STP300, STP600). The pumps are backed into an addition mag-lift turbo pump (Osaka TG250M) that is then backed by an oil-free mechanical pump (Edwards ESDP-30) providing the detector with a completely hydrocarbon free pumping system. Under typical experimental conditions the ionization region is maintained at $(2\text{-}3)\text{x}10^{-11}$ torr. Following PI, the ions are extracted and guided to the quadrupole with a series of ion lenses. The instrument is also equipped with EI, shown in figures 1 and 2, for use when the VUV undulator radiation is not available. The cage of the Brink ionizer[6] serves as an ion lens when using VUV PI. The nominal neutral flight length from the interaction

region to the effective center of the EI ionizer is currently 31.3 cm and the distance from the chopper wheels to the EI ionizer is currently 28.1 cm.

Theoretical resolution as determined by the detector. When using PI the ionization region is 250 µm long and the nominal neutral flight length is 15.1 cm from the interaction region. The resulting uncertainty in the flight length ($\Delta d/d$) is 0.0017. For a typical product traveling with a laboratory velocity of 1000.00 m/s this represents an uncertainty in the measured laboratory velocity of ±0.83 m/s or $< \pm 0.1\%$. The theoretical in-plane angular resolution is determined by the height of the PI region at 150 µm (the plane is defined by the detector axis and the propagation of the two molecular beam sources). For a nominal neutral flight length of 15.1 cm, the in-plane angular resolution is 0.06°. The out-of-plane angular resolution, along the propagation of the undulator PI radiation, is determined by the defining aperture at the entrance to the PI region. The aperture is currently 3 mm giving an out-of-plane angular resolution of 1.1°. Of course, the extremely high velocity and angular resolution offered by having such a well defined PI region means that the resolution will almost always be limited by other experimental factors. These factors include the uncertainty in the reactant velocity(ies) (speed ratio), angular width of the molecular beam(s), and the physical size of the interaction region.

3. The VUV PI Radiation

The ALS, a third generation 1-2 GeV synchrotron radiation source, provides the tunable VUV radiation used for product PI.[9] ES1 is part of the Chemical Dynamics

Beamline (known as beamline 9.0.2 at the ALS) and uses the radiation from the sector 9 insertion device, a 10 cm period 4.5 m undulator (U10). A schematic diagram of the portion of beamline 9.0.2 involving ES1 is shown in figure 3. With the storage ring filled to 400 mA at 1.5 GeV the undulator provides ~10^{16} photons/sec with a bandwidth of ~2.5% and the fundamental frequency is tunable from 7-50 eV. The output of the undulator mirrors the electron bunches in the storage ring. When the storage ring is operated in the multi-bunch mode the resulting VUV radiation is pulsed at ~500 MHz. The time profile of the pulses is roughly gaussian with a FWHM of 35 ps and spaced 2 ns apart. On the time scale of the experiments carried out at ES1 (µsec time scale), the 500 MHz light can be considered as a continuous PI source.

In addition to the fundamental frequency, the undulator also produces substantial flux in the higher harmonics. It is necessary to filter out these higher harmonics in order to exploit the advantage of PI. The higher energy harmonics will lead to extensive dissociative ionization and will defeat any selectivity afforded by the use of VUV PI. The first two mirrors used to direct the photon beam from the U10, M1 and M2, absorb a substantial fraction of the higher harmonics above 50 eV and remove almost all of the radiation above 100 eV. A windowless rare gas filter is employed to remove the remaining harmonics.[10,11] A schematic diagram of the gas filter is shown in figure 3. The filter consists of a gas cell filled with ~30 torr of a rare gas (He, Ne, Ar) surrounded by 3 regions of differential pumping bringing the pressure down to 10^{-9}-10^{-10} torr at the entrance and exit of the filter. Figure 4 shows spectra of the undulator radiation taken with a transmission grating spectrometer placed where ES1 appears in figure 3.[11] The top

spectrum was taken with the gas filter evacuated. Contributions from the first and higher order harmonics are indicated in the figure. The additional signals result from higher orders of the transmission grating. The bottom spectrum was taken under the same conditions as the top with 30.2 torr of Ne in the gas filter. The result was a complete ($>10^4$) suppression of the higher order harmonics without any significant reduction in flux at the fundamental frequency.

The energy profile of the resulting fundamental frequency of the undulator radiation was measured using the 6.7 m monochromator at End Station 2.[12] The scans were taken at an undulator gap of 31 mm with the storage ring running at 1.9 GeV and with different settings of the horizontal and vertical defining apertures. The cone of radiation emitted by the undulator is red shifted from the center out. Therefore, as the defining apertures are opened the energy profile of the radiation shows a broadening to the red. The resulting energy widths, $\Delta E/E$, for the 3 settings of the apertures (horizontal x vertical) shown in figure 5 are 0.045 at 10x8 mm, 0.025 at 5x4 mm, and 0.020 at 2.5x2.0 mm.

The total photon flux at ES1 using different rare gases in the gas filter was measured using a VUV calorimeter and is shown in figure 6. The measurements were normalized to 400 mA in the storage ring at 1.5 GeV and were measured with the apertures set at 10x8 mm. Under typical operating conditions there are $(1.0-1.5) \times 10^{16}$ photons/sec available at ES1. Decreasing the apertures to 5x4 mm in order to improve the energy resolution results in a decrease in total photon flux of ~75%. It is important to note in figure 5 that to the blue side of the peaks the intensity does not return to the

background level recorded with the apertures closed. There is a constant 3-5% background to the high energy side of the fundamental peak which appears to extend indefinitely. This high energy tail accounts for the increase seen in the total flux measurements in figure 6 at the same energy, *ex.* 13 eV, for different gasses used in the gas filter. The transmission cutoff of the gas filter is determined by the IP of the rare gas being used in the filter, IP(Ar)=15.76 eV, IP(Ne)=21.56 eV, IP(He)=24.59 eV. A higher cutoff leaves more of the high energy tail being transmitted, thus increasing the measured total flux at a given energy. To provide further filtering of the high energy tail for lower energy settings of the undulator we installed a removable MgF_2 window between M3 and ES1, see figure 3. The MgF_2 window has a transmission cutoff around 11.2 eV[13] and used in conjunction with Ar in the gas filter typically leads to ~50% reduction in photon flux over the Ar alone.

To illustrate the significant effect that the high energy tail is capable of producing, figure 7 shows mass spectra of an on-axis molecular beam containing 16% propane in He from m/e 40-48. The IP for propane is 10.9 eV.[14] The top spectrum was taken with the undulator radiation set to 9.5 eV, Ar in the gas filter, and the apertures set to 10x8 mm. The bottom spectrum was taken under identical conditions with the addition of the MgF_2 filter. The top spectrum demonstrates that even with the undulator radiation set below the IP for propane there is still significant ionization of propane, parent m/e 44, as well as significant dissociative ionization to m/e 41-43. The bottom spectrum shows that the addition of the MgF_2 filter results in a 10^4 reduction in the signal by removing the

high energy tail of the undulator radiation between the Ar cutoff of 15.76 eV and the MgF$_2$ cutoff of 11.2 eV.

4. The Advantages of VUV PI: A few examples.

As discussed in the introduction, the goal in constructing ES1 was to overcome many of the limitations of EI. Presented here are a few initial examples of results obtained using tunable VUV PI on ES1. A number of additional examples demonstrating the many advantages provided by ES1 can be found throughout the rest of this dissertation.

Reduction/elimination of dissociative ionization. Figure 8 shows TOF spectra from the photodissociation of ozone at 248 nm at m/e 16 (O$^+$) and m/e 32 (O$_2^+$). The spectra were taken with the undulator fundamental at 18 eV and the gas filter was evacuated. The spectra were averaged over 200,000 laser shots each at a laser fluence of 2000 mJ/cm^2. The spectra are dominated by reaction 1 and the peaks can be assigned to the vibrational progression of the O$_2$(a$^1\Delta$) product.

$$O_3 \rightarrow O_2(a^1\Delta, v{=}0\text{-}4) + O(^1D_2) \hspace{2cm} (\text{rxn } 1)$$

Notice that there is no evidence for dissociative ionization of the O$_2$ products appearing in the m/e 16 (O$^+$) TOF spectrum even without use of the gas filter. In a previous study of the photodissociation of ozone at 193 nm using EI the authors found substantial

dissociative ionization of the O_2 products at m/e 16.[15] At 193 nm the dissociation involves additional reaction channels and the overlapping of signals from the O and O_2 products made the analysis of the m/e 16 TOF extremely challenging.

Figure 9 shows TOF spectra from the photodissociation of benzene at 193 nm. The dissociation laser fluence was ~300 mJ/cm^2 and the spectra were averaged over 200,000 laser shots each. There are three major dissociation channels for benzene at 193 nm, reactions 2-4.

$$C_6H_6 \rightarrow H + C_6H_5 \qquad \text{(rxn 2)}$$

$$C_6H_6 \rightarrow H_2 + C_6H_4 \qquad \text{(rxn 3)}$$

$$C_6H_6 \rightarrow CH_3 + C_5H_3 \qquad \text{(rxn 4)}$$

In a previous investigation of the photodissociation of benzene at 193 nm using EI, the m/e 76 ($C_6H_4^+$) TOF spectra was dominated by dissociative ionization of the C_6H_5 product in reaction 2.[16] The substantial interference at m/e 76 from reaction 2 made it extremely difficult to assign the portion of the TOF spectra resulting from reaction 3. The top of figure 9 shows TOF spectra for m/e 77 and m/e 76 at photoionization energies of 11.9 eV and 10.0 eV respectively. The two peaks are clearly resolved with almost no contribution to the m/e 76 spectra from dissociative ionization of C_6H_5 products from reaction 2. This allows a unique measurement to be made for reaction 3 without interference from reaction 2. The bottom of figure 9 shows a TOF spectrum for m/e 63 ($C_5H_3^+$) products from reaction 4. In the previous investigation the authors were not able

to obtain a TOF spectrum for m/e 63 using EI. There were two factors that prevented the measurement of a m/e 63 TOF spectrum. First, when using EI there is tremendous background at m/e 63 from dissociative ionization of reactant benzene molecules. This background is removed by using PI. Second, the C_5H_3 product is not very stable and the harsh ionization provided by EI leads to preferential dissociative ionization. PI provides a "soft" ionization allowing the C_5H_3 products to be observed at their parent mass.

Selectivity. In addition to background reduction, PI offers selective ionization based on the photoionization curves of the products. One obvious advantage is to discriminate between two chemical different products that have the same parent mass. An example of this type of selectivity is shown in figure 8 in Chapter 3 of this dissertation. The figure shows the ability to discriminate between TOF for C_2H_3 and HCN photoproducts from the dissociation of acrylonitrile at 193 nm at the parent mass for *both* molecules, m/e 27.

Another example of selectivity is the ability to discriminate between products with the same chemical identity based on their electronic state. Figure 10 shows TOF spectra for O_2 (m/e 32) products from the photodissociation of ozone at 193 nm at three different photoionization energies. At 193 nm there are multiple thermodynamically available dissociation channels which can produce O_2 in any of its first three electronic states. The contributions from four of the dissociation channels are assigned in the top TOF spectra in figure 10. In the previous investigation using EI the authors had to assign the different peaks based on kinematic arguments.[15] By measuring the dependence of

each peak on the photoionization energy we are able to make direct assignments of the O_2 electronic states providing confirmation of the previous assignments.

It is also interesting to note in figure 10 the very different dependence of the signal on the PI energy for vibrationally cold O_2 products, $O_2(X)$, and vibrationally exited O_2 products, $O_2(X,v)$, both in their ground electronic state. While both peaks have comparable intensities at a PI energy of 17.0 eV, at a PI energy of 10.5 eV the peak for vibrationally cold O_2 has disappeared while the peak for vibrationally excited O_2 has become the largest feature in the TOF spectrum. This is an example of the large effect internal excitation can have on the photoionization curve of a product. The large change in the photoionization curve with internal excitation, and in particular the red shift in the photoionization onset, suggests the possibility of selectivity for products based on internal excitation. Figure 11 shows TOF spectra for SO (m/e 48) photoproducts from the photodissociation of SO_2 at 193 nm. The spectra are vibrationally resolved with the peaks marked indicating SO(v=0-2). At a PI energy of 12.0 eV the ratio of the contributions from each of the SO vibrational levels is in good agreement with previous investigations using EI.[17] However, at a PI energy of 10.0 eV, below the IP for SO of 10.32 eV[14], the TOF spectrum shows clear discrimination against the SO products with lower internal excitation. The SO(v=0) peak is gone at a PI energy of 10.0 eV and the SO(v=1) peak has been reduced by ~½ with respect to the SO(v=2) peak. It should also be noted that the although the two spectra in figure 11 have been scaled to the same size, the spectra at PI = 10.0 eV had a signal intensity 20 times lower than the signal at 12.0 eV due to the difference in the photoionization cross-section.

Photoionization spectra of scattered products. Another advantage of ES1 is the ability to measure the photoionization spectrum for scattered reaction products. Spectra are typically recorded by sitting at a given scattering angle and integrating the TOF signal while stepping over the PI energy. In order to increase the energy resolution it is usually preferable to close the VUV defining apertures to 5x4 mm, see figure 5. An example of photoionization spectra for reaction products is shown in figure 12. Figure 12 shows the photoionization spectra for both of the products from reaction 5 in the photodissociation of 1,3-butadiene at 193 nm.

$$C_4H_6 \rightarrow CH_3 + C_3H_3 \qquad\qquad (rxn\ 5)$$

The photoionization spectra contain a wealth of information from chemical identity to information about internal excitation. Of course, much of this information depends on the availability of quantitative data concerning the photoionization of the product in question. Unfortunately, in most cases this type of data is currently not available. For the C_3H_3 product (m/e 39) figure 12 represents the first direct photoionization measurement on this molecule. For most unstable compounds, the difficulty in producing them under conditions where they can be readily studied has prevented any previous investigation. Photodissociation and reactive scattering provide a means to generate many of these unstable molecules allowing investigation of their photoionization properties. With a prudent choice of reaction system one could conceivably prepare molecules with a large range of different, well defined, internal energies. It would then be possible on ES1 to

quantitatively investigate the effects of internal energy on the photoionization spectrum. The current lack of this type of quantitative information has relegated interpretations of red shifts in the photoionization spectra of reaction products to qualitative discussions.

Detection of CO. The final example of the advantages of ES1 is the detection of CO. Carbon monoxide is prevalent in combustion related reactions and the difficulty in detecting it using traditional EI has prevented investigations of a number of important combustion reactions. Using EI, CO is almost impossible to detect above the overwhelming background from CO in the detector. A high partial pressure of CO is unavoidable in a stainless steel UHV chamber, and the 2000 °C carbonized tungsten filament and large ionization volume associated with traditional EI greatly exacerbates matters, resulting in a typical background count rate at m/e 28 of 1 MHz. Using PI, and with cooling of the ionization region to ~20 K, the CO background count rate at m/e 28 is reduced to ~4000 Hz at a PI energy of 14.8 eV and using Ar in the gas filter. Figure 13 shows a TOF spectrum for the CO products from the photodissociation of oxalyl chloride at 193 nm[18], reaction 6.

$$Cl\text{-}CO\text{-}CO\text{-}Cl \rightarrow Cl + COCl + CO \rightarrow 2Cl + 2CO \qquad \text{(rxn 6)}$$
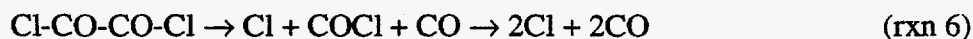
The spectrum was averaged for only 100,000 laser shots at a photodissociation laser fluence of ~500 mJ/cm^2. The photoionization energy was set at 14.5 eV and argon was used in the gas filter. For comparison, the reader is referred to the dissertation of S. W.

North where heroic efforts were required to acquire TOF spectra at m/e 28 for both N_2 and CO photoproducts using traditional EI techniques.[19]

5. Data Analysis: The forward convolution method.

While the experiments on ES1 (as well as all other experiments using the TOF technique) measure velocity and angular distributions in the laboratory frame, the desired quantity that reveals the underlying dynamics is the velocity and angular flux distribution in the center of mass frame, $I_{cm}(\Theta_{cm}, E_T)$. Θ_{cm} is the cm scattering angle and E_T is the *total* cm translational energy release. We obtain $I_{cm}(\Theta_{cm}, E_T)$ from the measured laboratory velocity and angular distributions using the method referred to as forward convolution. Presented here is only a brief description of the forward convolution method. For more complete discussions the reader is referred to references 20 and 21.

The first step is the conversion from cm flux per unit solid angle to laboratory flux per unit solid angle, equation 1.

$$I_{lab}(v, \theta_{lab}) = \frac{v^2}{u^2} \cdot I_{cm}(u, \Theta_{cm}) \qquad \text{(eqn. 1)}$$

In equation 1, v is the laboratory velocity and u is the cm velocity. The transformation Jacobian is v^2/u^2 and accounts for the fact that the solid angle subtended by the detector is proportional to $1/u^2$ in the cm frame and $1/v^2$ in the laboratory frame. Due to the time dependent, and thus velocity dependent, ionization probability, our experiments measure

number density in the ionizer, not flux. Accounting for this factor of laboratory velocity the resulting expression for laboratory number density is shown in equation 2.

$$N_{lab}(v, \theta_{lab}) \propto \frac{v}{u^2} \cdot I_{cm}(u, \Theta_{cm})$$

(eqn. 2)

In a laboratory TOF spectrum we are measuring the number density as a function of time. Relating the flight time, t, to the velocity _via_ the flight length, l, the result is equation 3.

$$N_{lab}(t, \theta_{lab}) \propto \frac{l^2}{u^2 \cdot t^3} \cdot I_{cm}(u, \Theta_{cm})$$

(eqn. 3)

The final result is equation 4 following conversion of the I_{cm} dependence on u to E_T using $u \propto E^{1/2}$.

$$N_{lab}(t, \theta_{lab}) \propto \frac{l^2}{u \cdot t^3} \cdot I_{cm}(E_T, \Theta_{cm})$$

(eqn. 4)

Equation 4 is then convoluted over the instrument response function, including the angular acceptance of the detector, the angular and velocity spread(s) in the reactant beam(s), and the physical size of the interaction and ionization regions.

Using equation 4 and a trial $I_{cm}(E_T, \Theta_{cm})$ the laboratory TOF spectra and angular distributions can be simulated. The simulation can then be compared to the data and the trial $I_{cm}(E_T, \Theta_{cm})$ iteratively adjusted until a best fit to the data is obtained. In practice it is necessary to simplify the simulation by assuming that the cm angular and translation energy distributions are _completely separable_:

$$I_{cm}(E_T, \Theta_{cm}) = P(E_T) \cdot T(\Theta_{cm})$$ (eqn. 5)

This rather severe assumption is often acceptable due to weak coupling of the two distributions. Crossed molecular beam investigations of reaction that proceed *via* a long-lived intermediate complex are common examples of weak coupling between $P(E_T)$ and $T(\Theta_{cm})$. However, this assumption is not always acceptable. In crossed molecular beam investigations of reactions that exhibit direct mechanisms there is often strong coupling between $P(E_T)$ and $T(\Theta_{cm})$. Examples of strong coupling are the reactions of atomic chlorine and bromine with ozone.[22] Strong coupling between $P(E_T)$ and $T(\Theta_{cm})$ is also found in the reaction of atomic chlorine with propane which is the topic of Chapter 5 of this thesis. In the analysis of crossed molecular beam experiments we account for coupling between $P(E_T)$ and $T(\Theta_{cm})$ by simulating the cm product flux with n sets of uncoupled $P(E_T)$ and $T(\Theta_{cm})$, each weighted by w_i.

$$I_{cm}(E_T, \Theta_{cm}) = \sum_{i=1}^{n} w_i \cdot P(E_T) \cdot T(\Theta_{cm})$$ (eqn. 6)

The result provides a reasonable representation of a coupled distribution with larger n required as the degree of coupling and complexity increases. A set of four uncoupled $P(E_T)$ and $T(\Theta_{cm})$ were required to obtain satisfactory fits to the data from Cl + propane in Chapter 5 of this thesis.

Two different computer programs were employed for fitting either the crossed molecular beam or PTS experiments. The Cl + propane crossed molecular beam experiments in Chapter 5 were fit using the program GMTHRASH, an updated version of the code originally written by Buss *et al.*[20] In addition to allowing point-form $P(E_T)$'s and $T(\Theta_{cm})$'s the program also provides general functional forms that were used in fitting the Cl + propane data. When reasonable fits to the data can be achieved, using the functional forms for $P(E_T)$ and $T(\Theta_{cm})$ is desirable since it serves to greatly reduce the number of adjustable parameters compared with point-form versions of $P(E_T)$ and $T(\Theta_{cm})$. The $P(E_T)$ used was based on an RRK form and is shown in equation 7.

$$P(E_T) = (E_T\text{-}B)^P \cdot (E_{avail}\text{-}E_T)^Q \qquad \text{(eqn. 7)}$$

In equation 7 E_{avail} is the total available energy and B, P, and Q serve as adjustable parameters. The $T(\Theta_{cm})$ was generated by a sum of Legendre polynomials with the relative weighting of each of the polynomials serving as adjustable parameters.

The PTS experiments in Chapters 2-4 were fit with the program CMLAB2. CMLAB2 is and updated version of the original CMLAB program for forward convolution analysis of photodissociation experiments written by X. Zhao.[21] J. D. Myers rewrote the program with many improvements including an interactive graphical user interface that greatly accelerates the analysis.[23] The $P(E_T)$'s are currently restricted to point-form. The photofragment angular distribution for a single photon excitation is given by the well known expression derived by Zare[24], equation 8.

$$P(\theta) \;=\; \frac{1}{4\pi}\cdot\left(1 + \beta\cdot P_2(\cos\theta)\right) \qquad\qquad \text{(eqn. 8)}$$

$P_2(\cos\theta)$ is the second Legendre polynomial, θ is the angle between the product recoil vector and the electronic transition dipole, and β is commonly referred to as the anisotropy parameter. CMLAB2 is capable of simultaneously simulating multiple primary dissociation channels as well as secondary decomposition of primary photodissociation products. Derivation of the expression for forward convolution simulation of secondary photofragments follows in a similar fashion to the brief derivation for equation 4 presented above and requires a few additional assumptions. For the details the reader is again referred to reference 21 for the definitive derivation and to the first chapter of reference 19 for a wonderful, in depth discussion of the topic. Secondary decomposition of primary photodissociation products is found in the photodissociation of dimethy sulfoxide, Chapter 2 of this thesis, and vinyl chloride, Chapter 4 of this thesis.

References

[1] Y. T. Lee, J. D. McDonald, P. R. LeBreton, and D. R. Hershback, *Rev. Sci. Instrum.* **40**, 1402 (1969).

[2] Y. T. Lee, Science **236**, 793 (1987).

[3] F. E. Busch, R. T. Mahoney, R. T. Morse, and K. R. Wilson, *J. Chem. Phys.* **51**, 449 (1969); R. W. Diesen, J. C. Wahr, and S. E. Adler, *J. Chem. Phys.* **50**, 3635 (1969).

[4] A. M. Wodtke and Y. T. Lee in *Molecular Photodissociation Dynamics*, eds. M. N. R. Ashfold and J. E. Baggott (Royal Society of Chemistry, London, 1987)

[5] Y. T. Lee in *Atomic and Molecular Beam Methods*, ed. G. Scoles (Oxford University Press, New York, 1988).

[6] G. O. Brink, *Rev. Sci. Instrum.* **37**, 857 (1966).

[7] X. Yang, D. A. Blank, J. Lin, A. G. Suits, Y. T. Lee, A. M. Wodtke, *Rev. Sci. Instrum. Submitted*, April 1997.

[8] A. M . Wodtke, Ph.D. thesis, University of California, Berkeley, (1986).

[9] 1-2 GeV Synchrotron Radiation Source, Lawrence Berkeley Laboratory and University of California, PUB-5172 Rev., July 1986.

[10] A. G. Suits, P. Heimann, X. Yang, M. Evans, M. Evans, C. W. Hsu, K. Lu, A. H. Kung, and Y. T. Lee, *Rev. Sci. Instrum.* **66**, 5405 (1995).

[11] P. A. Heimann, M. Koike, C. W. Hsu, M. Evans, C. Y. Ng, D. A. Blank, A. G. Suits, and Y. T. Lee, SPIE, (1996), vol. **2856**, 90.

[12] P. A. Heimann, M. Koike, C. W. Hsu, M. Evans, K. T. Lu, C. Y. Ng, A. G. Suits, and Y. T. Lee, _Rev. Sci. Instrum, accepted_ May 1997.

[13] J. A. R. Samson, _Techniques of Vacuum Ultraviolet Spectroscopy_, Wiley, New York, 1967.

[14] Handbook of Chemistry and Physics, D. R. Lide (CRC, Boca Raton, 1995).

[15] D. Stranges, X. Yang, J. D. Chesko, and A. G. Suits, _J. Chem. Phys._ **102**, 6067 (1995).

[16] A. Yokoyama, X. Zhao, E. J. Hintsa, R. E. Continetti, and Y. T. Lee, _J. Chem. Phys._ **92**, 4222 (1989).

[17] P. Felder, C. S. Effenhauser, B. M. Haas, and J. R. Huber _Chem. Phys. Lett._ **148**, 417 (1988).

[18] N. Hemmi and A. G. Suits, _submitted to_ J. Chem. Phys., February 1997.

[19] S. W. North, Ph.D. Thesis, University of California, Berkeley, (1995).

[20] R. J. Buss, Ph.D. Thesis, University of California, Berkeley (1979).

[21] X. Zhao, Ph.D. Thesis, University of California, Berkeley (1988).

[22] J. Zhang, Ph.D Thesis, University of California, Berkeley (1993).

[23] J. D. Myers, Ph.D. Thesis, University of California. Berkeley (1993).

[24] R. N. Zare, _Mol. Photochem._ **4**, 1 (1972).

Figure Captions

Figure 1:   Schematic drawing of End Station One, the rotatable crossed molecular

beam apparatus at the Chemical Dynamics Beamline.

Figure 2:   Detailed drawing of the detector for End Station One.

Figure 3:   Schematic diagram of the portion of the Chemical Dynamics Beamline

relating to End Station One. The dashed line shows the path taken by the

VUV radiation from the undulator to End Station One. The gas filter and

MgF_2 filter are discussed in the text.

Figure 4:   Spectra of the undulator radiation taken by a transmission grating

spectrometer parked just behind End Station One demonstrating suppression

of higher harmonics from the undulator. The top panel shows the spectrum

with the gas filter evacuated and the bottom panel shows the spectrum with

30.2 torr of neon in the gas filter. The harmonics from the undulator are

marked, other features are the result of higher orders of the grating.

Figure 5:   Energy profile of the undulator radiation taken with the 6.7 m

monochromator at End Station Two. The undulator gap is 31 mm and the

storage ring was running at 1.9 GeV. The plots are for different settings of the horizontal and vertical defining apertures (horz x vert). The resulting energy resolution, $\Delta E/E$, is 0.045 at 10x8 mm, 0.025 at 5x4 mm, and 0.020 at 2.5x2.0 mm.

Figure 6:   Total photon flux at End Station One as a function of energy for different rare gases in the gas filter. Measurements from a storage ring running at 1.5 GeV and are normalized to a storage ring current of 400 mA.

Figure 7:   On axis mass spectra of a molecular beam containing 16% propane (IP=10.9 eV) in helium. Top spectrum was taken with the undulator fundamental at 9.5 eV and argon in the gas filter. Bottom spectrum was taken under identical conditions with the addition of the MgF_2 filter.

Figure 8:   TOF spectra for m/e 16 (O^+) and m/e 32 (O_2^+) from the photodissociation of ozone at 248 nm, $O_3 \rightarrow O_2(a^1\Delta, v=0\text{-}4) + O(^1D_2)$. The $O_2(a^1\Delta)$ vibrational progression is labeled. Note the lack of dissociative ionization of the O_2 products at m/e 16.

Figure 9:   TOF spectra from the photodissociation of benzene at 193 nm. The spectra show products from reactions 2-4 in the text. Note the lack of dissociative ionization from the m/e 77 signal at m/e 76.

Figure 10:   TOF spectra for m/e 32 (O_2^+) from the photodissociation of ozone at 193 nm for 3 different photoionization energies, top 17.0 eV, middle 13.5 eV, and bottom 10.5 eV. The assignments of the various dissociation channels are marked in the top TOF spectrum.

Figure 11:   TOF spectra for m/e 48 (SO^+) from the dissociation of SO_2 at 193 nm. The spectra were taken at photoionization energies of 12.0 eV (solid line) and 10.0 eV (dashed line). The IP for SO is 10.32 eV. The spectrum at 10.0 eV has been scaled x20 with respect to the spectrum at 12.0 eV. The SO vibrational progression, v=0-2, is labeled.

Figure 12:   Photoionization spectra for the products of reaction 5 in the text from the photodissociation of 1,3 butadiene at 193 nm. The top is m/e 39 ($C_3H_3^+$) and the bottom is m/e 15 (CH_3^+).

Figure 13:   TOF spectrum for m/e 28 (CO^+) products from the dissociation of oxalyl chloride at 193 nm. The spectrum was only averaged for 100,000 laser shots at a dissociation laser fluence of ~500 mJ/cm^2.
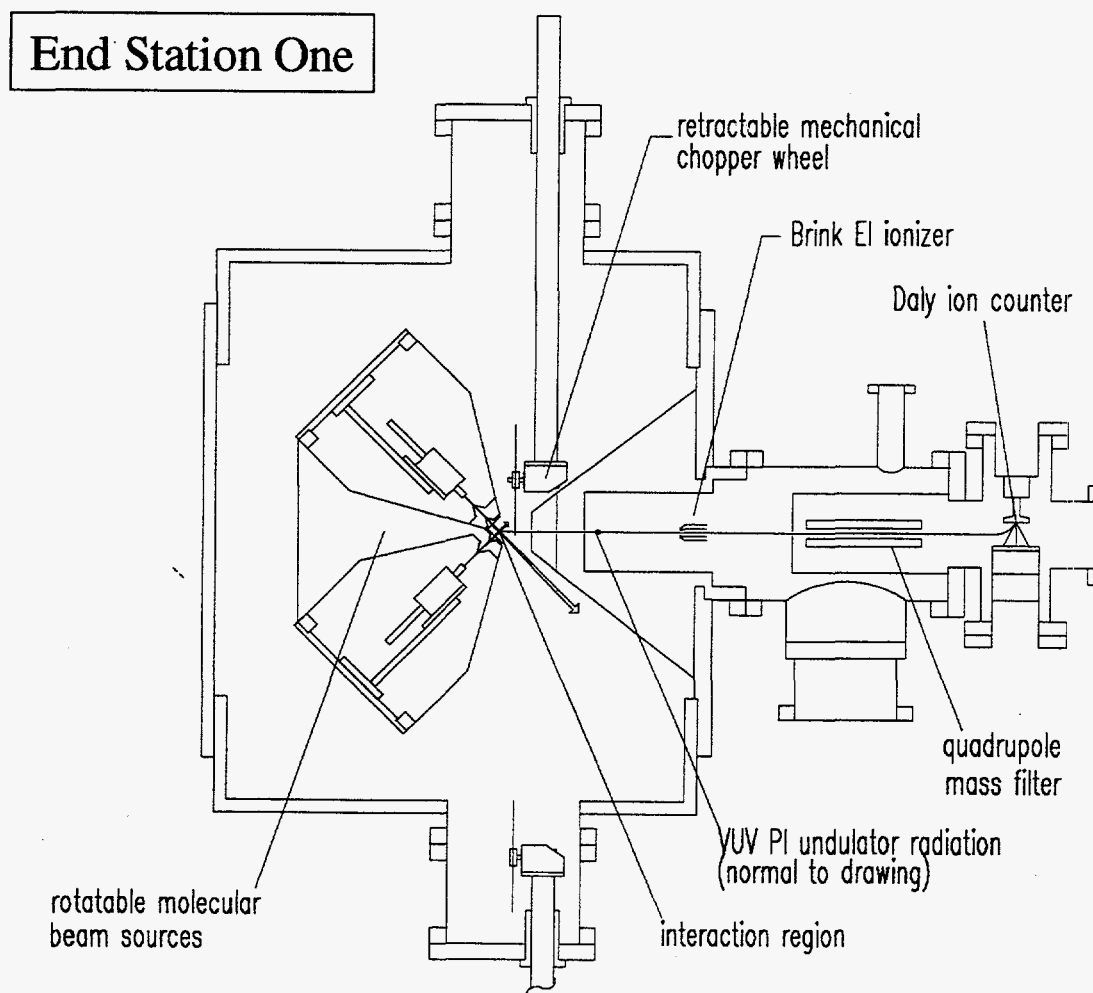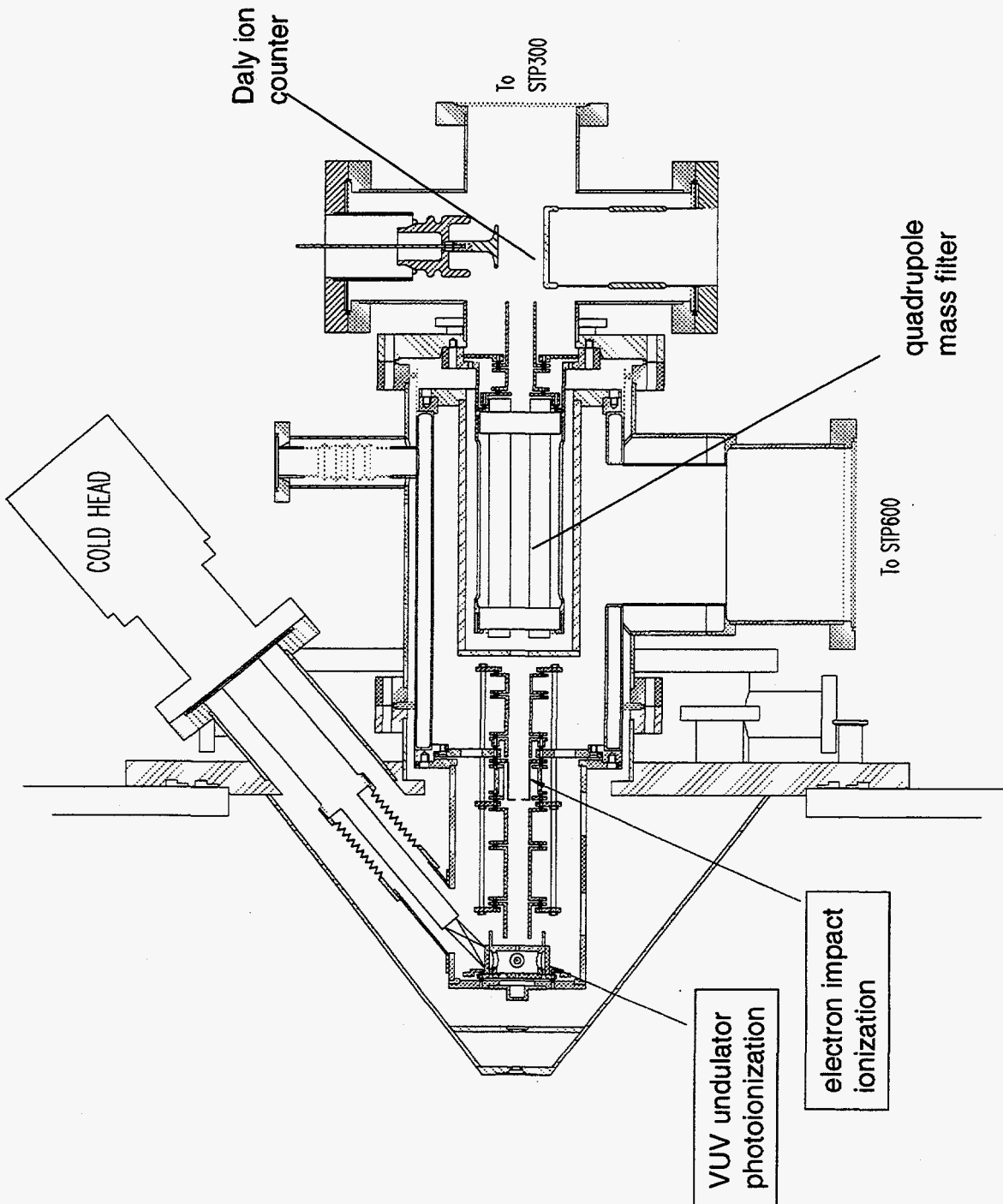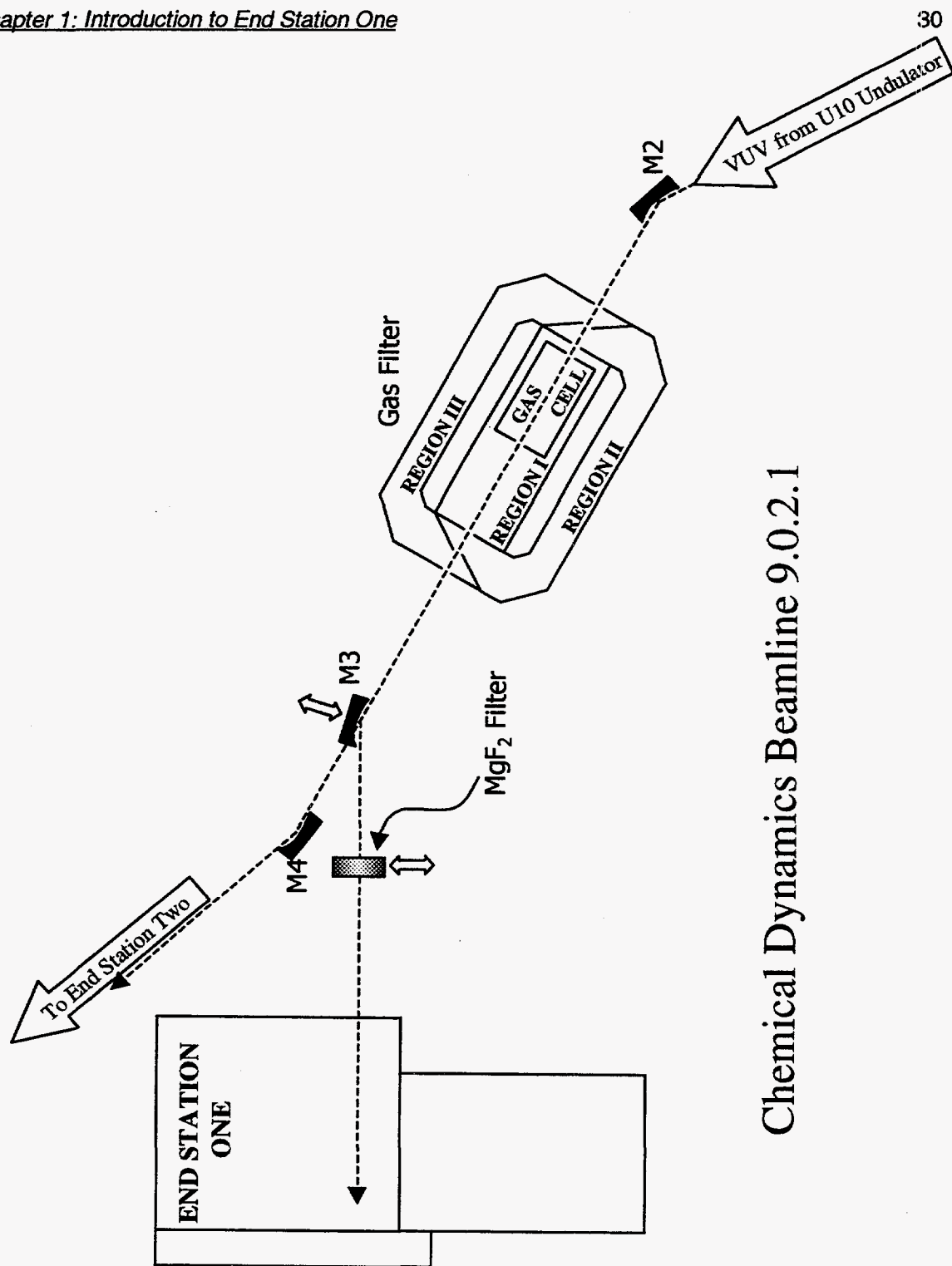
End Station One

retractable mechanical
chopper wheel

Brink EI ionizer

Daly ion counter

quadrupole
mass filter

VUV PI undulator radiation
(normal to drawing)

rotatable molecular
beam sources

interaction region

figure 1

figure 2

Chemical Dynamics Beamline 9.0.2.1
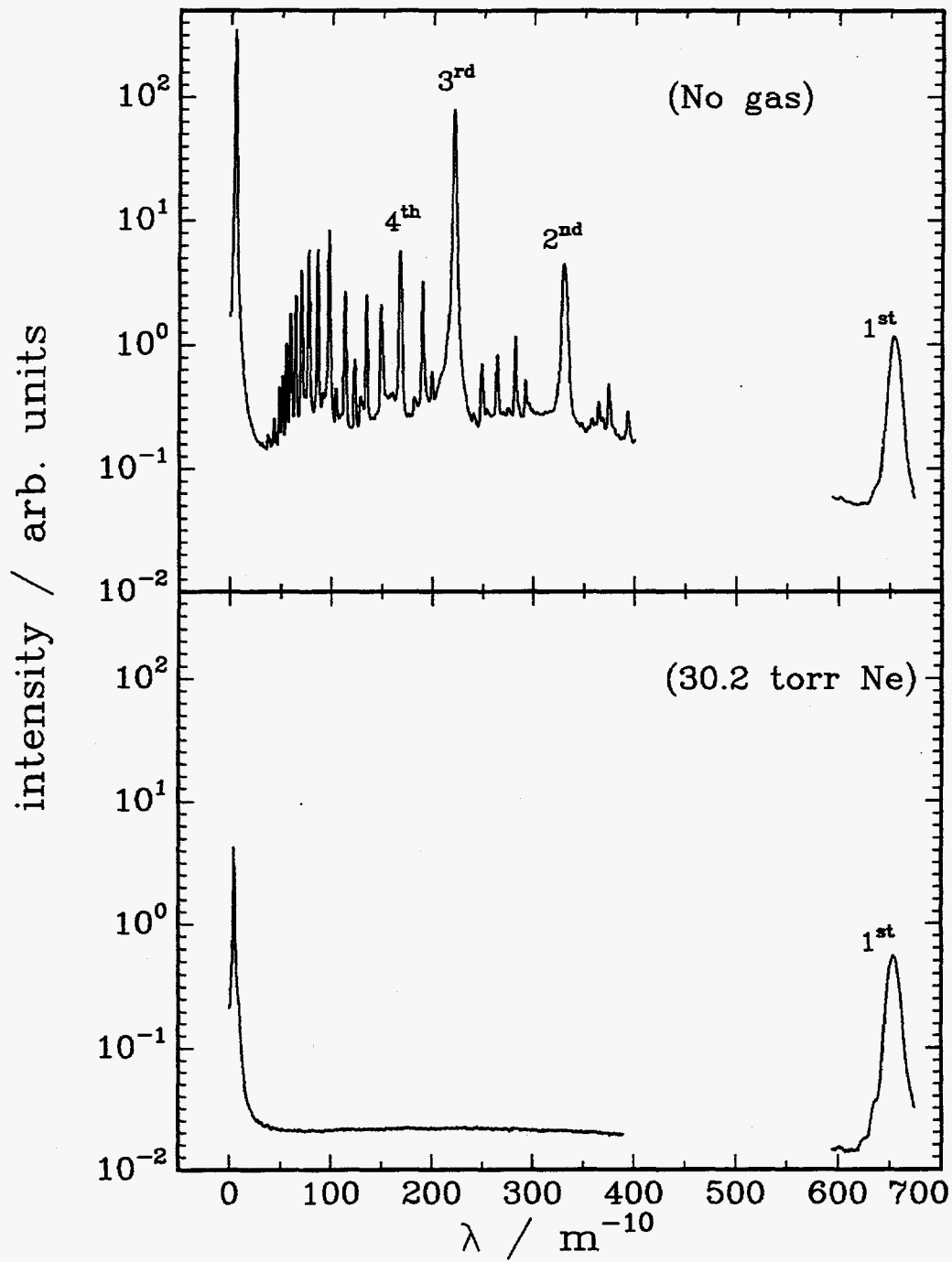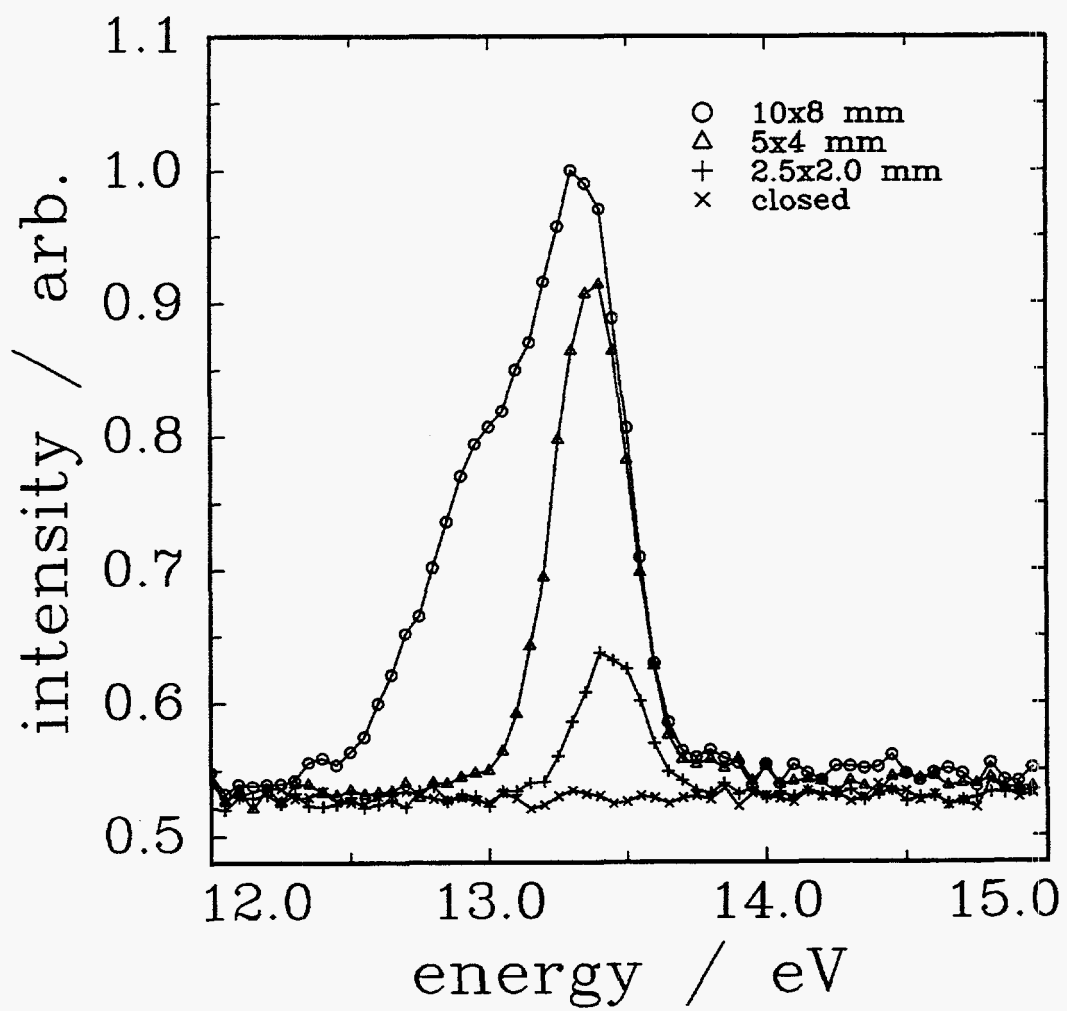
Figure 3
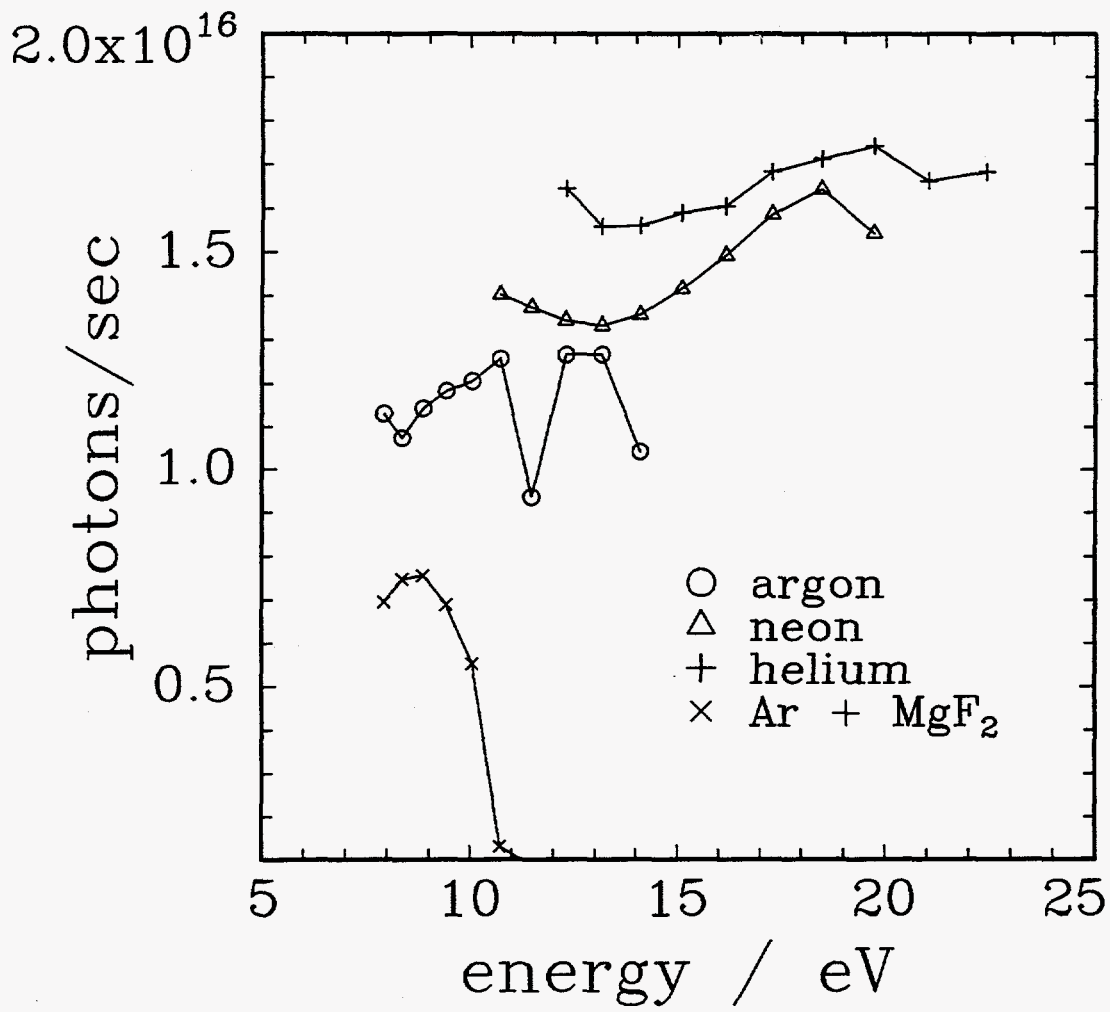
figure 4
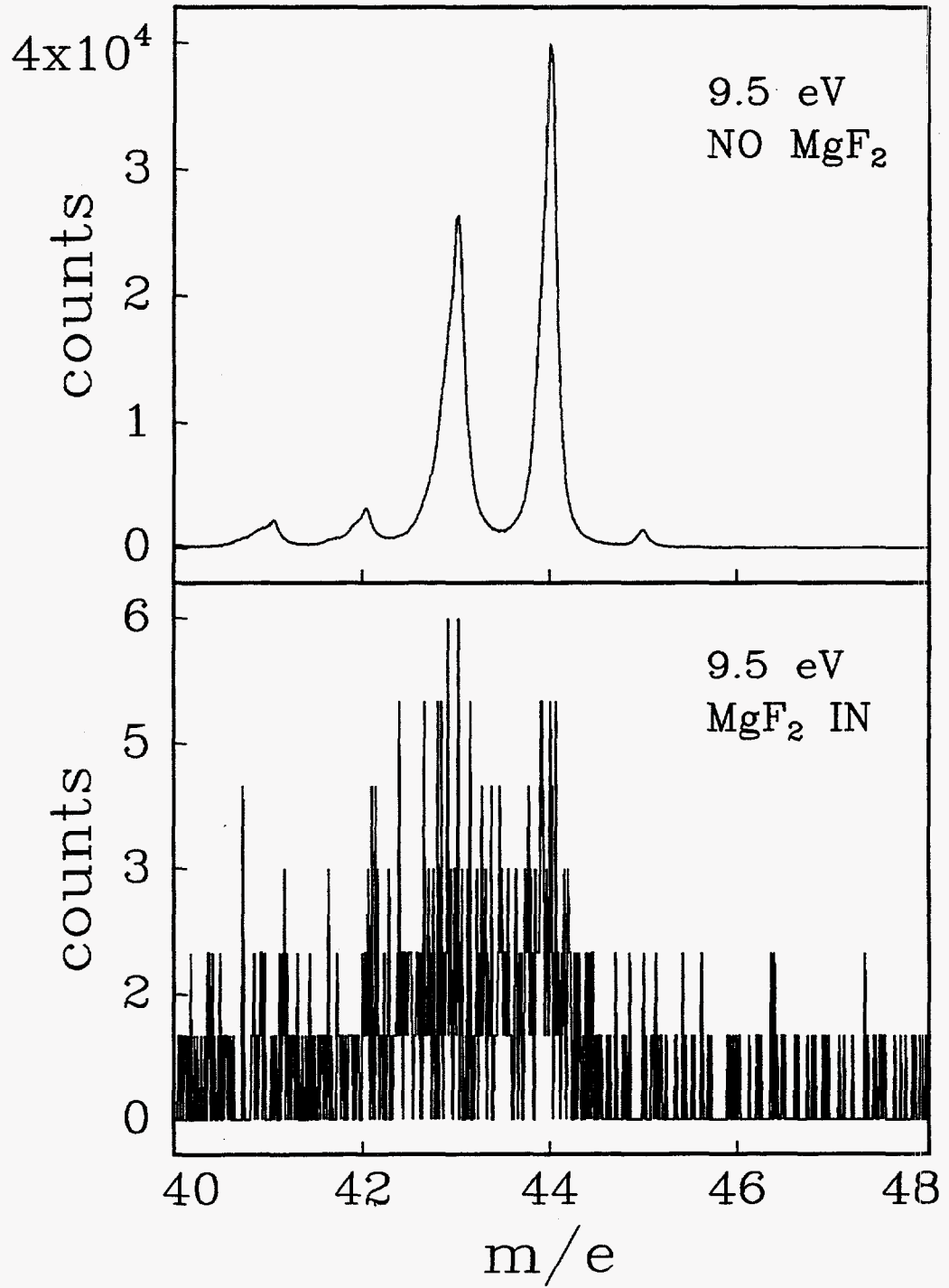
figure 5
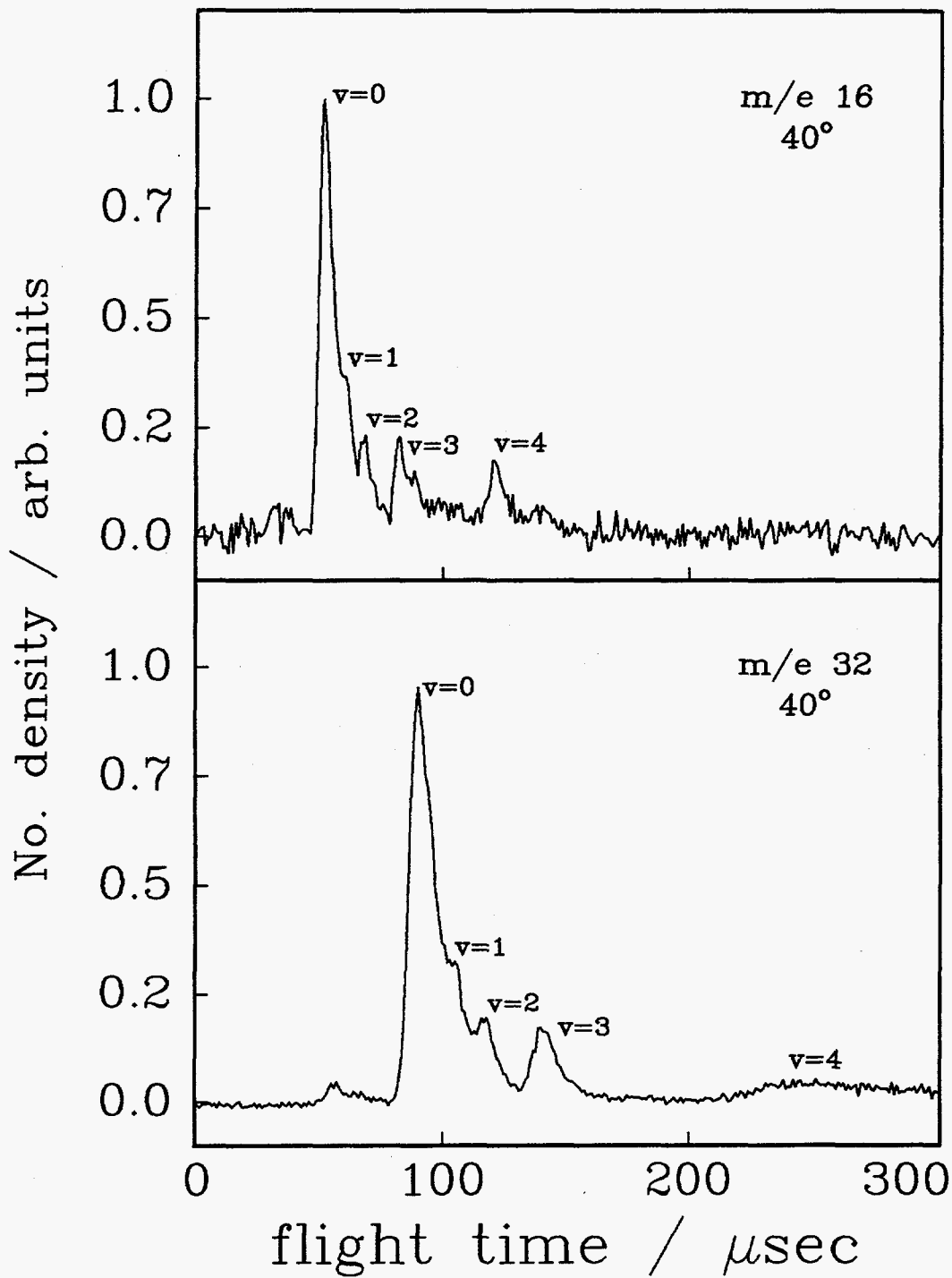
figure 6
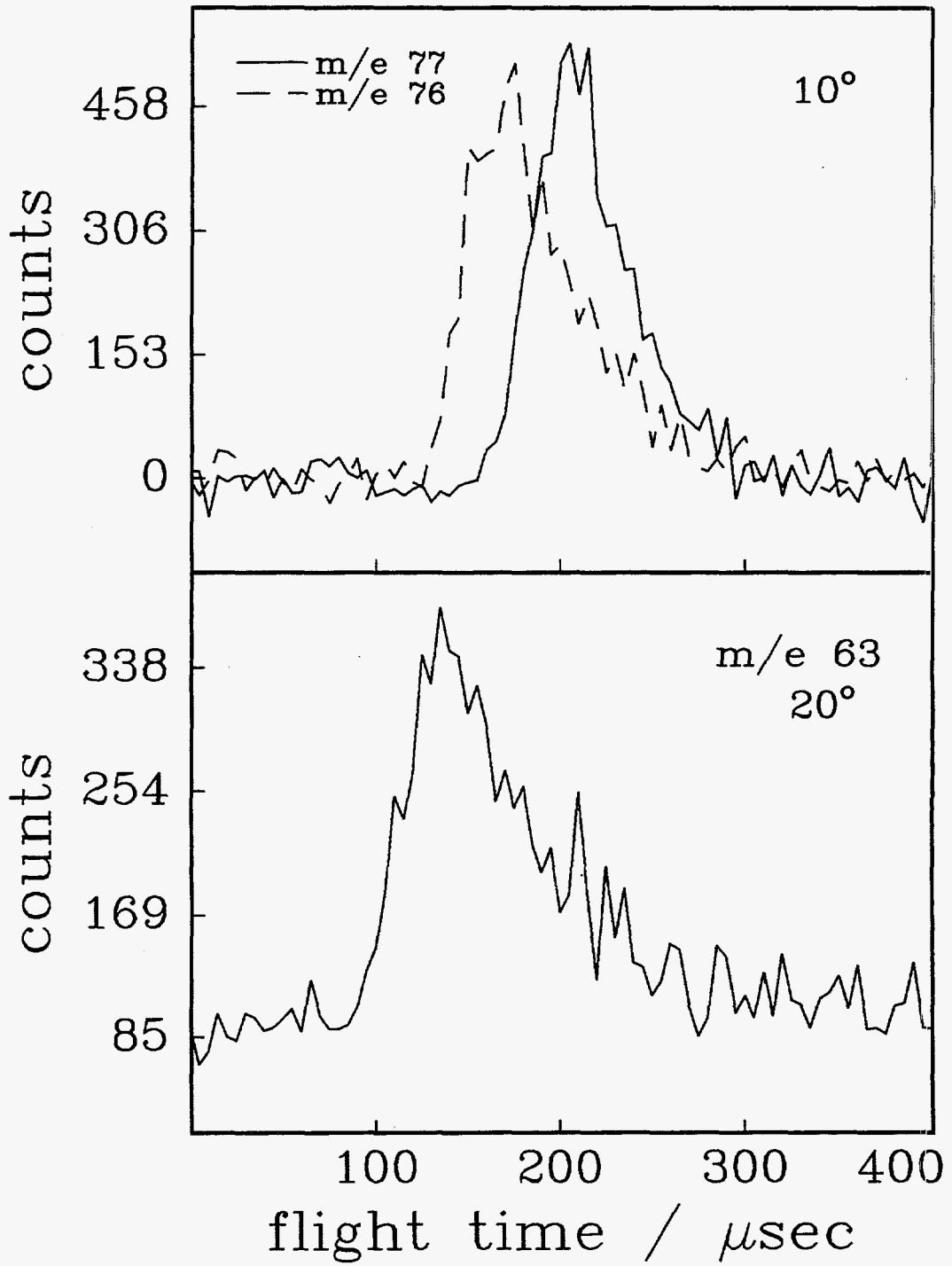
figure 7
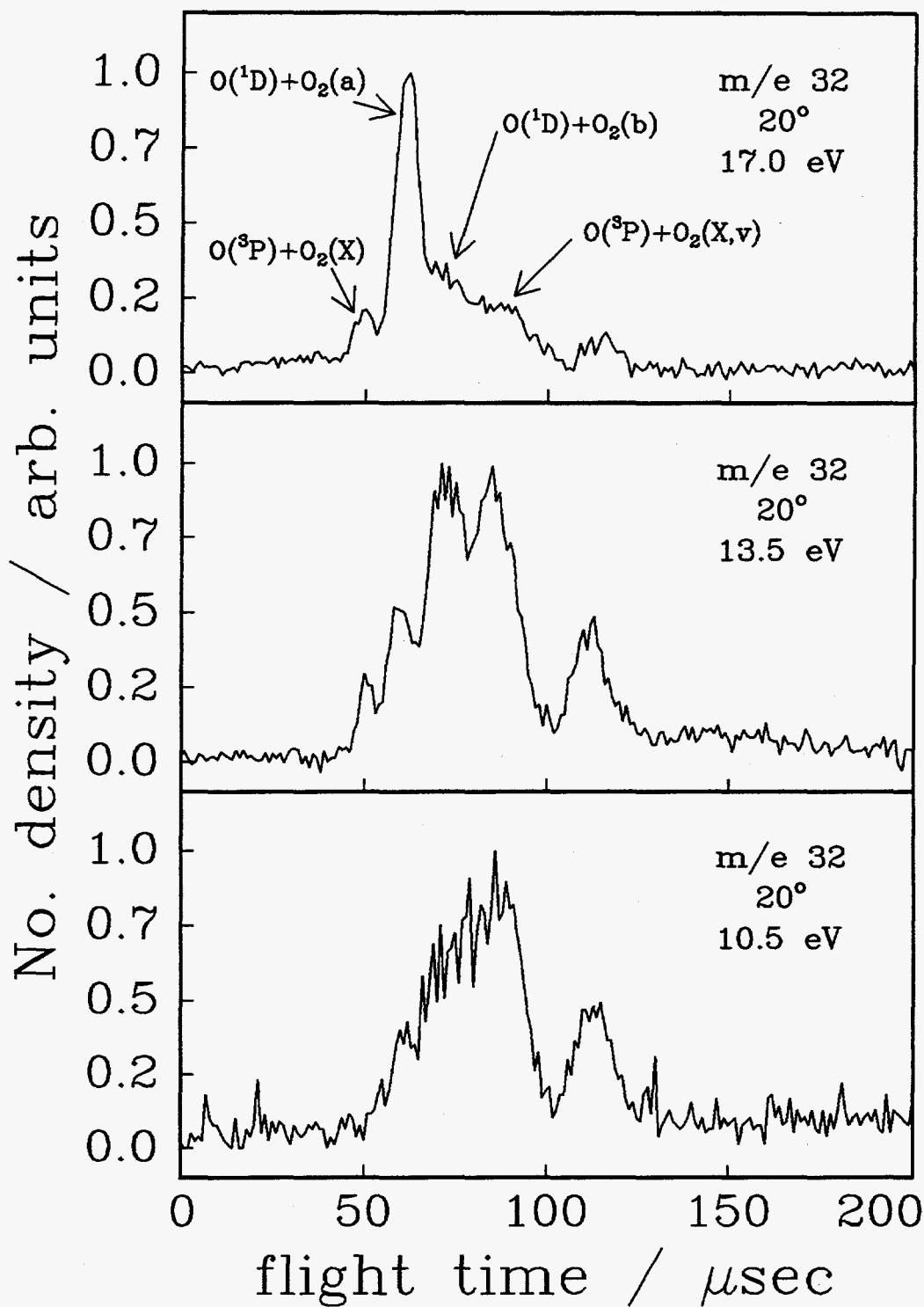
figure 8
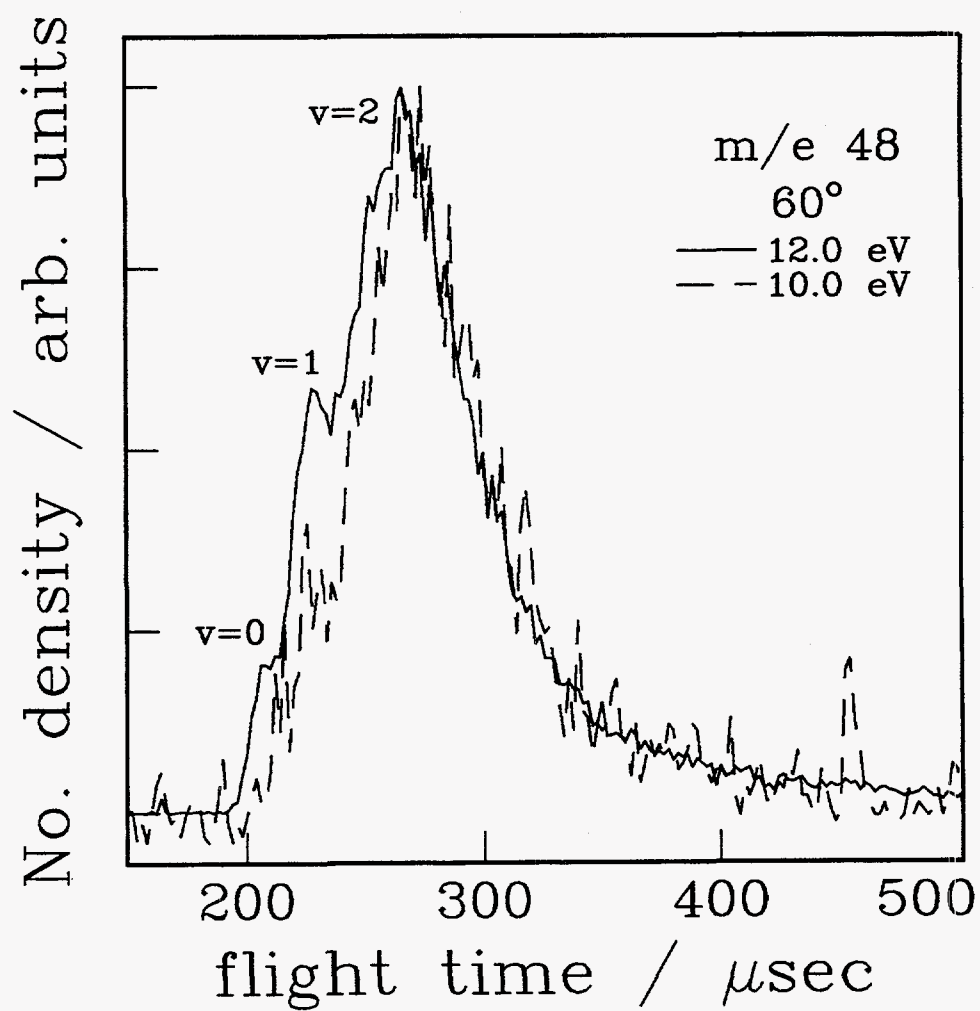
figure 9
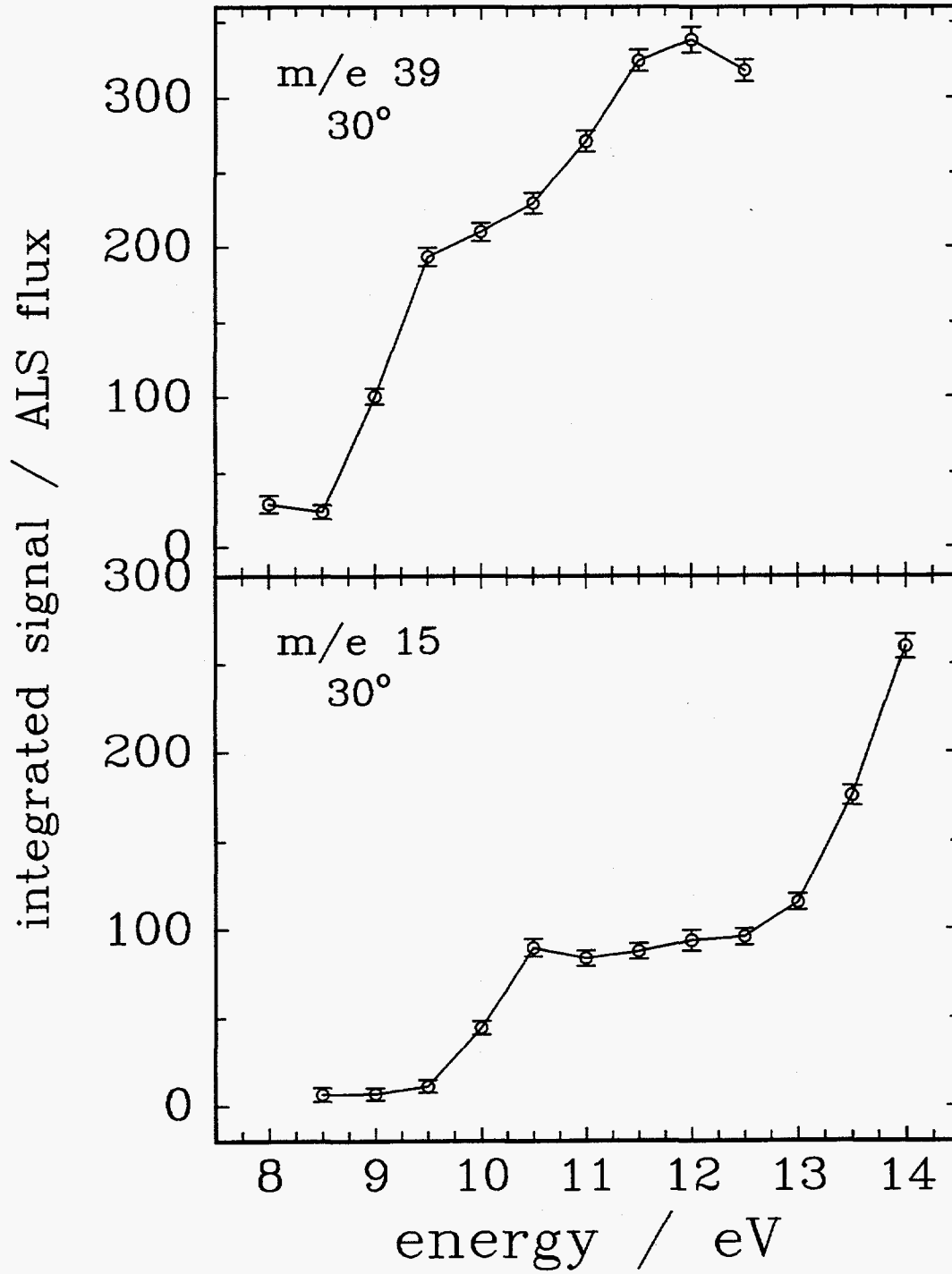
figure 10
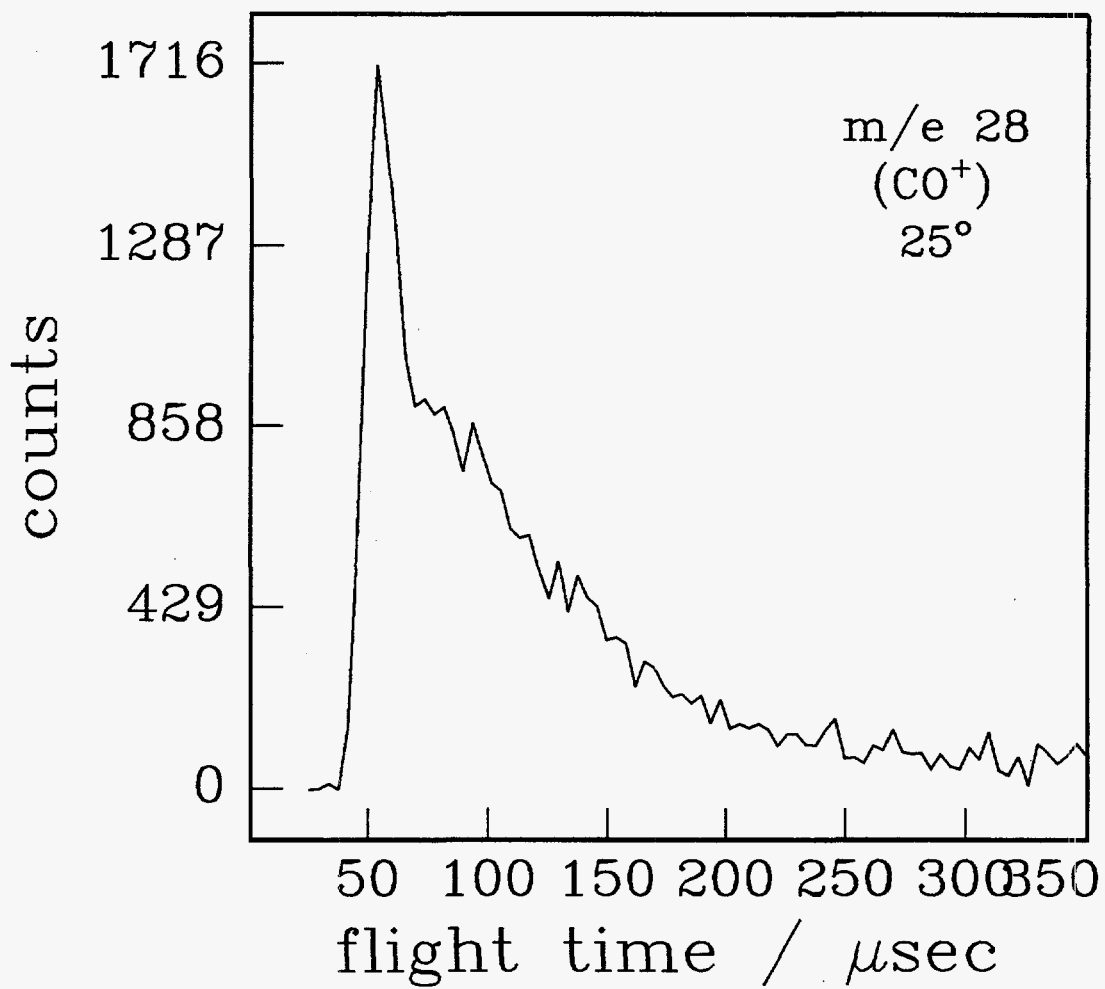
figure 11

figure 12

figure 13

Chapter 2

Photodissociation of Dimethyl Sulfoxide at 193 nm

Abstract

We have studied the photodissociation of dimethyl sulfoxide, DMSO-h_6 and DMSO-d_6, at 193 nm using the technique of photofragment translational spectroscopy with a tunable VUV product probe provided by undulator radiation on the Chemical Dynamics Beamline at the Advanced Light Source. In contrast to previous investigations we have found the dissociation to proceed *via* a stepwise mechanism involving multiple reaction channels. The primary dissociation, S-C bond cleavage to eliminate a methyl radical, was found to have two competing channels with distinct translational energy distributions. The translational energy distribution for the major primary dissociation channel suggests that it proceeds in a statistical manner on the ground electronic surface following internal conversion. In competition with this channel is a primary dissociation which exhibits a translational energy distribution suggestive of dissociation on an excited electronic surface with most of the available energy partitioned into translational and electronic degrees of freedom. Secondary decomposition of the CD_3SO intermediate was

found to proceed exclusively *via* C-S bond cleavage, $CD_3SO \rightarrow CD_3 + SO$. However, secondary decomposition of the CH_3SO intermediate was found to exhibit competition between $CH_3SO \rightarrow CH_3 + SO$ and $CH_3SO \rightarrow CH_2SO + H$. The dissociation to CH_3 and SO was the major secondary decomposition channel with the translational energy distribution indicating a barrier to recombination of >8 kcal/mol. While a minor hydrogen atom elimination channel was found to play a role in secondary decomposition of CH_3SO intermediates, no analogous secondary C-D bond cleavage was detected from the CD_3SO intermediates indicating the importance of tunneling in the secondary decomposition of CH_3SO.

1. Introduction

When a molecule with two equivalent chemical bonds is excited above the threshold for dissociation of both bonds, how the rupture of the two bonds are temporally coupled becomes a salient question. For discussions of the temporal correlation of the dissociating bonds we adopt here the convenient experimental definitions of concerted and stepwise mechanisms, where concerted refers to cleavage of both bonds prior to rotation of the intermediate, and stepwise refers to cleavage of the bonds in two distinct steps with the lifetime of the intermediate exceeding its rotational period.[1] Recently the question of a concerted verses stepwise dissociation has been addressed in our laboratory for such three-body dissociation processes as azomethane[2] and acetone[3], where the technique of

photofragment translational spectroscopy (PTS) was demonstrated to be particularly adept at resolving the dissociation dynamics. Characterization of such correlations between dissociating bonds is difficult using time resolved techniques for cases where the first step is predissocative rather than direct owing to the uncertainty in the determination of time zero.[4] Here we have continued the investigation of this class of photodissociation using PTS to study the UV dissociation of dimethyl sulfoxide, DMSO. At 193 nm there is sufficient energy to break both of the C-S bonds in DMSO. The dissociation can proceed in either a concerted (reaction 1) or stepwise (reaction 2) manner:[5,6]

$$CH_3SOCH_3 \rightarrow CH_3 + SO + CH_3 \qquad \Delta H = 103 \text{ kcal/mol} \qquad (1)$$

$$CH_3SOCH_3 \rightarrow CH_3SO + CH_3 \qquad \Delta H = 51 \text{ kcal/mol} \qquad (2a)$$

$$CH_3SO \rightarrow CH_3 + SO \qquad \Delta H = 52 \text{ kcal/mol} \qquad (2b)$$
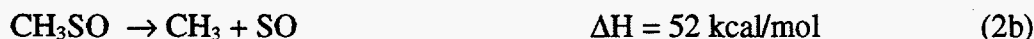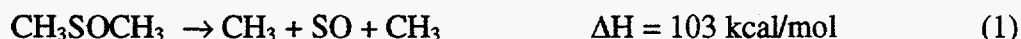
In addition to dissociation to two methyl radicals and sulfur monoxide, the following dissociation channels are also thermodynamically accessible at 193 nm:[5,6]

$$CH_3SOCH_3 \rightarrow CH_3SO + CH_3 \rightarrow CH_2SO + H + CH_3 \quad \Delta H = 106 \text{ kcal/mol} \quad (3)$$

$$CH_3SOCH_3 \rightarrow C_2H_6 + SO \qquad \Delta H = 13 \text{ kcal/mol} \qquad (4)$$

$$CH_3SOCH_3 \rightarrow CH_2SO + CH_4 \qquad \Delta H = 2 \text{ kcal/mol} \qquad (5)$$
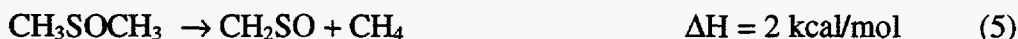
The room temperature UV absorption spectrum of DMSO was recorded by Gollnick and Stracke.[7] The absorption at 188 nm was attributed to a $(\pi^* \leftarrow \pi)$ transition on the SO moiety and the absorption at 205 nm to either a $(\sigma^* \leftarrow n)$ or $(d \leftarrow n)$

transition. The only published investigations of the gas phase UV photodissociation of DMSO have been reported by Chen *et al.* dissociating at 193 nm.[8] They used LIF (laser induced fluorescence) on both the (A-X) and (B-X) transitions to probe the the SO products, and 2+1 REMPI (resonance enhanced multiphoton ionization) to probe the methyl radical products. They found the SO vibrational distribution to be inverted, peaked at v=2. They also assigned rotational temperatures for the SO products at 750-1450 K and reported the SO quantum yield at 1.02 ± 0.12. The results of the 2+1 REMPI measurements made on the methyl radical products found them to be internally cold with only 1.9 kcal/mol of internal energy on average in each methyl. Based on their measurements of the partitioning of the available energy the authors concluded that the dissociation of DMSO at 193 nm proceeds along a single reaction path to produce SO + $2CH_3$ in a concerted three body elimination, reaction 1. The inverted SO vibrational distribution was attributed to an elongated S-O bond length in the electronically excited DMSO. Since concerted elimination processes represent the exception for three body dissociations, the suggestion that DMSO dissociates in a concerted manner at 193 nm presents it as a particularly interesting dynamical system for investigation.

In this study we have used PTS with VUV product ionization to investigate the dissociation dynamics of DMSO-h_6 and DMSO-d_6 following absorption at 193 nm. We have observed direct evidence that the dissociation to form SO and two methyl radicals proceeds via a stepwise mechanism. Our SO photoionization measurements agree with the internal energy measured for the SO product by Chen *et al.*, however, our measured

translational energy distributions suggest a much larger fraction of the available energy is partitioned into internal excitation of the methyl radical products than reported from the 2+1 REMPI results. In contrast to the conclusions of Chen *et al.* we have found the dissociation to be considerably more complex involving multiple decomposition channels. We have identified competing dissociation channels in both the primary dissociation involving C-S bond cleavage to eliminate a methyl radical as well as the secondary decomposition of the sufonyl intermediate. This study represents one of the first applications of VUV undulator radiation as a photofragment probe in PTS experiments and demonstrates this technique to be a powerful new tool for investigations in chemical dynamics.

2. Experimental

For detection of all neutral photofragments except hydrogen atoms the experiments were carried out on the Chemical Dynamics Beamline at the Advanced Light Source (ALS) at Lawrence Berkeley National Laboratory. A complete discription of the experimental apparatus and setup is provided in Chapter 1 of this thesis. We present here only the details specific to this experiment. A continuous molecular beam of either DMSO-h_6 or DMSO-d_6, <1% in He, was generated by bubbling 40-60 torr of He through a room temperature liquid sample and expanding the resulting mixture through a 0.25 mm stainless steel nozzle into a source chamber maintained at 1×10^{-4} torr. The nozzle was heated to 80°C to inhibit cluster formation and the resulting molecular beam typically had

a r.m.s. velocity of 1080 m/s with FWHM of 15%. After being skimmed twice the molecular beam was intersected at 90° by the output of a Lambda Physik LPX200 excimer laser operating on the ArF transition (193.3 nm) with laser fluence ranging 1-500 mJ/cm^2.

For detection of hydrogen atoms a similar apparatus was used with modifications designed to increase sensitivity for m/e 1 photofragments which have been discussed previously.[9] In this configuration a pulsed molecular beam of <1% DMSO-h$_6$ in He, the dissociation laser, and the detector axis are all fixed mutually perpendicular. The dissociation laser intersects the unskimmed molecular beam 5 mm above the pulsed nozzle exit. Neutral photofragments which recoil at 90° from the molecular beam pass through two defining apertures and travel 37.0 cm where they are ionized by electron impact, mass selected, and counted as a function of time.

DMSO-h$_6$, 99%, and DMSO-d$_6$, 99.9% isotopic purity, were obtained from Aldrich and used without further purification.

3. Results

For all of the TOF spectra presented the open circles represent the data, the dashed lines are single channel contributions to the forward convolution fit, and the solid line is the overall fit to the data. Data analysis was accomplished using the forward convolution technique that is described in detail in the "Data analysis" section of Chapter 1 of this thesis.

3.1 DMSO-d_6

The TOF spectra for m/e 66 (CD_3SO^+) at source angles of 12° and 22.5° are shown in figure 1. Each spectrum is the result of $2x10^6$ laser shots with the undulator radiation set at 11.0 eV. Not only do these spectra directly identify CD_3SO as a primary dissociation product, reaction 2a, but the spectra suggest that there is more than one dissociation channel resulting in CD_3SO photoproducts. The spectrum at 12° exhibits a clear shoulder ~80 μsec and the spectrum has been fitted with two separate contributions. The presence of the contribution at earlier flight times is confirmed in the 22.5° spectrum. The c.m. translational energy distribution for each of the two contributions are shown in figure 2. The primary dissociation channel that produces slow photofragments, fig. 2a, is peaked around 8 kcal/mol and has a tail that extends beyond 30 kcal/mol. The primary dissociation channel which produces fast photofragments, fig. 2b, is peaked at 26 kcal/mol and extends to 42 kcal/mol. Additional evidence for two channels leading to CD_3SO can be seen in figure 3, the TOF spectrum for m/e 64 (CD_2SO^+) at 12°, which was taken under the same photoionization conditions as the m/e 66 spectra. Different dissociation channels leading to CD_3SO products will demonstrate different dissociative ionization patterns as a result of the distinct internal energy distributions in the CD_3SO products. Figure 3 has been fitted with the $P(E_T)$s in figure 2 and it is clear that while the primary dissociation channel which produces slow photofragments is still evident with dissociative ionization slightly favoring the translationally slower, and therefore internally warmer, fragments, the

primary dissociation channel which produces fast photofragments is not observed at the CD_2SO mass. The failure to detect any of the primary channel which produces fast photofragments at m/e 64 demonstrates that the CD_3SO fragments from that channel are vibrationally much cooler than the primary channel which produces slow photofragments, with an internal energy distribution distinct from the slow photofragment dissociation channel.

The TOF spectra for m/e 18 (CD_3^+) at source angles of 20°, 35°, and 50° are shown in figure 4 and were taken with the undulator radiation set at 12.0 eV and without the use of the harmonic filter. The spectra have been fitted with three contributions. The contribution at the earliest flight times is fitted with the $P(E_T)$ for the primary channel which produced fast photofragments observed at m/e 66, figure 2b, confirming the fast methyl photofragments as the momentum matched dissociation partners of the fast CD_3SO fragments. There are two remaining contributions. One is the broad contribution peaked at ~80 μsec that are the methyl products from the slow photofragment primary dissociation channel, reaction 2a. The other is the contribution peaked ~55 μsec representing methyl products that result from secondary decomposition of those primary CD_3SO fragments produced with sufficient internal energy to undergo secondary dissociation, reaction 2b. The $P(E_T)$ for the primary dissociation channel which results in slow photofragments is shown in figure 5a. It is peaked near zero with an exponential decrease extending beyond 30 kcal/mol. Since methyl radical products do not undergo secondary decomposition, the $P(E_T)$ in figure 5a represents the complete $P(E_T)$ for the slow photofragment primary

dissociation channel. Figure 6 shows the $P(E_T)$ from figure 5a along with the $P(E_T)$ from figure 2a which is the $P(E_T)$ for the slow photofragment primary CD_3SO dissociation products which survive. The primary $P(E_T)$ for CD_3SO intermediates which undergo secondary decomposition is the difference between figures 5a and 2a which is the crossed-hatched region in figure 6. For a discussion of the truncation in the primary $P(E_T)$ for the surviving CD_3SO photofragments see section 4.2. The $P(E_T)$ for the secondary decomposition of CD_3SO intermediates, reaction 2b, produced in the slow photofragment primary dissociation is shown in figure 5b. It is peaked at 8 kcal/mol and extends to 32 kcal/mol.

TOF spectra for m/e 48 (SO^+) at source angles of 25°, 40°, and 50° are shown in figure 7 and were taken under the same photoionization conditions as the m/e 18 spectra. The fit to the TOF consists predominantly of the signal from the secondary decomposition of the CD_3SO intermediates produced in the slow photofragment primary dissociation channel. There is a small contribution to the m/e 48 TOF spectra from dissociative ionization of CD_3SO intermediates which is peaked at ~130 μsec and is most evident in the 25° spectrum. As mentioned above for the secondary CD_3 products, the primary $P(E_T)$ for CD_3SO intermediates which undergo secondary decomposition is represented by the difference between figure 5a and 2a, see figure 6. The m/e 48 (SO^+) spectra were fitted using the secondary $P(E_T)$ in figure 5b confirming the secondary methyl contribution in the m/e 18 TOF spectra to be the momentum matched partner of the SO. Although the fits to the secondary decomposition of the CD_3SO intermediates at m/e 18 (CD_3^+) and m/e 48

(SO^+) were not sensitive to the precise shape of the secondary angular distribution, the fits did require that the secondary angular distribution maintain forward/backward symmetry.

Branching Ratios. The branching ratios are depicted in figure 8. The branching ratios were obtained from the fitting ratios of the three contributions to the m/e 18 (CD_3^+) TOF spectra. We therefore assumed that under the experimental photoionization conditions the photoionization cross-section for the methyl radical products was independent of their internal energy. All kinematic considerations are accounted for in the fitting procedure. The ratio of the three channels used to obtain the best fit to the m/e 18 spectra was 19(primary, fast photoframents):52(primary, slow photofragments) :29(secondary). This yields a ratio of 27:73 for the fast photofragments primary dissociation channel to the slow photofragment primary dissociation channel. With the secondary dissociation proceeding exclusively from the slow photofragment primary dissociation, the fitting ratios indicate that 56% of the CD_3SO fragments produced in the slow photofragment primary dissociation undergo secondary decomposition. The best fits to the CD_3SO spectra, m/e 66, were obtained with a ratio of 44(primary, fast photframents):56(primary, slow photofragments). This ratio of the fast primary CD_3SO products to the surviving slow primary CD_3SO intermediates is consistent with the measured ratios for the m/e 18 spectra. With 56% of the slow photofragment primary channel undergoing secondary decomposition the result is a ratio of 45:55 for the fast photofragment primary channel to the surviving slow secondary CD_3SO products that is consistent with the fitting ratio for the m/e 66 TOF spectra. The majority of the error in the branching ratios obtained in this fashion results from the ability to adjust the fitting

ratios while maintaining a reasonable fit to all of the TOF data. We estimate this error to be <10%.

3.2 DMSO-h_6

We were not able to observe TOF spectra for m/e 63 (CH_3SO^+). The inability to directly detect the CH_3SO intermediate is the result of a number of experimental factors. As will be shown, in comparison with the CD_3SO intermediates, a greater percentage of the CH_3SO intermediates produced in the slow photofragment primary dissociation undergo secondary decomposition. In addition, the fast photofragment primary dissociation is less prevalent in the case of DMSO-h_6. Although this accounts for a reduction of ~30% in the yield of CH_3SO intermediates in the dissociation, the most substantial reduction in signal results from the necessity to increase the resolution of the quadrupole mass filter to permit sufficient discrimination between m/e 62 and m/e 63. The increased resolution is accompanied by a severe reduction in transmission of the quadrupole. The low signal at m/e 66 (CD_3SO^+) from the the CD_3SO intermediate was likely the result of preferential photodissociation rather than photoionization, and the additional reductions in signal for the CH_3SO rendered it unobservable under the experimental conditions.

Although we were not able to detect any signal at m/e 63 (CH_3SO^+), we observed a substantial signal at m/e 62. The TOF spectrum for m/e 62 (CH_2SO^+) at a source angle of 15 degrees is shown in figure 9. The spectrum was taken with the undulator radiation

set at 12 eV without the harmonic filter. The signal at m/e 62 can be attributed to either

dissociative ionization of CH_3SO intermediates or to secondary decomposition of the

CH_3SO intermediates involving hydrogen atom elimination, reaction 3. Direct evidence for

reaction 3 is shown in figure 10, the TOF spectrum for m/e 1 (H^+). The fit to the m/e 1

TOF spectrum contains three contributions. The slow contribution, peaked at 110 µsec, is

the contribution from dissociatively ionized methyl radical products scattered to 90°. The

contribution at early times, peaked at 30 µsec, exhibits a near quadratic dependence on the

dissociation laser fluence and has been fitted as a two photon dissociation with the first

photon yielding methyl radical products and the second photon dissociating the methyl

radicals to methylene and hydrogen atoms. The $P(E_T)$ for methyl radical photodissociation

at 193 nm has been previously determined in this laboratory[14] and was used in the fitting

for the secondary step in the two photon dissociation. The remaining middle feature,

peaked at 50 µsec, had a linear dependence on the laser power and was fitted assuming a

stepwise mechanism for reaction 3. The translational energy distributions for the primary,

$CH_3SOCH_3 \rightarrow CH_3 + SOCH_3$, and the secondary dissociation, $SOCH_3 \rightarrow SOCH_2 + H$,

are shown in figure 11. The $P(E_T)$s in figure 11 were also used to fit the TOF spectrum for

m/e 62 in figure 9 providing strong evidence that the m/e 62 TOF signal is the result of

reaction 3. The primary $P(E_T)$ is peaked at 6 kcal/mol and exponentially declines beyond

30 kcal/mol, and the secondary $P(E_T)$ is peaked at 4 kcal/mol and extends to 18 kcal/mol.

TOF spectra for m/e 15 (CH_3^+) at source angles of 20° and 35° are shown in figure

12. The undulator radiation was set at 11 eV and the harmonic filter was used with

argon.[11] The fitting is analogous to the m/e 18 (CD_3^+) spectra described above with the same three individual contributions. Owing to reasons discussed above, we were not able to observe spectra for the CH_3SO fragment and we have therefore assumed the $P(E_T)$ in figure 2b from the fast photofragment primary dissociation channel of DMSO-d_6 in fitting the fast contribution peaked ~30 μsec. The remaining two contributions are the slow photofragment primary dissociation, the slowest and broadest contribution peaked around 70 μsec, and subsequent secondary decomposition of the CH_3SO intermediate, reaction 2b, peaked ~40 μsec. The $P(E_T)$ for fitting the slow photofragment primary dissociation, reaction 2a, is shown in figure 13a and is identical to the analogous $P(E_T)$ for the deuterated case, figure 5a. The $P(E_T)$ used to fit the secondary decomposition, reaction 2b, is shown in figure 13b. The TOF spectra for the momentum matched secondary SO fragments, m/e 48 (SO^+), at source angles of 20°, 30°, and 45° are shown in figure 14. The dominant contribution is from decomposition of the CH_3SO intermediates, reaction 2b, fitted with the secondary $P(E_T)$ in figure 13b. At 20° and 30° there is a small contribution on the slow side from dissociative ionization of CH_3SO photofragments. Although the secondary $P(E_T)$ is very similar to the analogous $P(E_T)$ for the deuterated dissociation, figure 5b, it is slightly broader. This difference in the shape results from competition in the secondary dissociation with hydrogen atom elimination in DMSO-h_6. As with the fits to the DMSO-d_6 data, the secondary angular distribution was not sensitive to the exact shape of the distribution, however the fits did require that forward/backward symmetry be maintained.

Photoionization spectrum of the SO product: Figure 15 shows the relative intensity of the TOF signal at m/e 48 and a source angle of $20°$ as a function of the photoionization energy from 8.25 eV to 11.0 eV. For this measurement, in addition to the rare gas harmonic filter, the undulator radiation passed through a 3 mm thick MgF_2 window to further reduce background from residual high energy photons above the transmission cutoff for MgF_2 of about 11.2 eV. The energy distribution of the undulator radiation had a FWHM of 2.5%. From figure 15 the ionization onset for the SO products is ~9.5 eV. Taking into consideration the bandwidth of the undulator radiation, this corresponds to an onset of ~9.8 eV. The vertical I.P. for sulfur monoxide is 10.32 ± 0.02 eV.[10] The difference between the ionization onset for the SO product and the vertical I.P. reflects an internal energy content in the SO of 0.50 ± 0.15 eV.

Branching Ratios. The branching ratios are depicted in figure 8. The ratio between the fast photofragment primary channel, slow photofragment primary channel, and secondary C-S bond cleavage was obtained from the fits to the m/e 15 (CH_3^+) spectra. The best fit to the data resulted from a ratio of 11:54:35 respectively indicating 65% of the CH_3SO intermediates produced in the slow primary step undergo secondary decomposition. The error in the ratios between the contributions in the m/e 15 fits is analogous to the case of DMSO-d_6, <10%. In order to estimate the percentage of the secondary hydrogen elimination, reaction 3, we must compare the signal intensity of the m/e 62 and m/e 15 TOF spectra. Since there is no current information on the photoionization cross-section for CH_2SO at 12 eV we make the assumption that the

photoionization cross-sections of CH_3 at 11.0 eV and CH_2SO at 12.0 eV are equal and we estimate the contribution of reaction 3 at <5% overall.

4. Discussion

4.1 Primary dissociation, reaction 2a. Detection of the CD_3SO product at m/e 66, figure 1, provides strong evidence that the dissociation to sulfur monoxide and two methyl radicals does not exclusively proceed via a three body process. The TOF spectrum for m/e 66 at 12° in figure 1 exhibits a shoulder on the fast side suggesting two contributions to the spectrum, a contribution peaked at 80 μsec and a slower broad contribution peaked at 100 μsec. The existence of two separate contributions is confirmed by the differing dissociative ionization at m/e 64 (CD_2SO^+), figure 3, indicating the production of two different m/e 66 photoproducts with distinct vibrational energy distributions. As discussed above we were not able to detect the CH_3SO photoproducts due to experimental limitations, see section 3.2, however the fits to the TOF spectra at m/e 15 confirm the analogous fast and slow primary dissociations in the case of DMSO-h_6.

4.1.1 Fast photofragment primary dissociation. The $P(E_T)$ for the fast photofragment primary dissociation, reaction 2a, shown in figure 2b is peaked at 24 kcal/mol and extends to a maximum of 42 ± 5 kcal/mol. Assuming the maximum in the $P(E_T)$ reflects the production of vibrationally/rotationally cold products and neglecting the internal energy of the DMSO reactant[11], the maximum in the $P(E_T)$ represents the available energy following photodissociation at 193 nm (148 kcal/mol). Given an available energy

of of 42 ± 5 kcal/mol and using $\Delta H_f(DMSO) = -31.4$ kcal/mol and $\Delta H_f(CH_3) = 34.8$

kcal/mol[5] the result is $\Delta H_f(CH_3SO) = 40 \pm 5$ kcal/mol. Comparison of this value to the

value obtained from group additivity of $\Delta H_f(CH_3SO) = -15$ kcal/mol[6] suggests that the

fast primary dissociation might result in the production of an excited electronic state of

CH_3SO which lies ~55 kcal/mol above the ground electronic state. The lack of dissociative

ionization of the fast m/e 66 (CD_3SO^+) product to m/e 64 (CD_2SO^+) as compared with the

slow photofragment primary dissociation, see figures 1 and 2, indicates the fast CD_3SO

product is vibrationally much cooler than the slow CD_3SO product. This also indicates

that the electronically excited CD_3SO products must undergo radiative relaxation during

the ~30 μsec collisionless flight to the detector since nonradiative relaxation would result

in vibrational excitation which is not evident in the dissociative ionization at m/e 64

(CD_2SO^+). The large fraction of available energy partitioned into translation, $<E_{trans}> = 26$

kcal/mol, and the fact that the distribution is peaked at 24 kcal/mol suggests either direct

dissociation on a repulsive electronic surface or electronic predissociation on a surface

with a large barrier to recombination.

From the absorption spectrum of Gollnick and Stracke[7] the dominant absorption at

193 nm should be a ($\pi^* \leftarrow \pi$) transition on the SO moiety. The fast photofragment primary

dissociation may then be the result of electronic predissociation involving a repulsive

electronic surface. Comparison of TOF spectra taken at m/e 18 (CD_3^+) and 35° with the

dissociation laser polarized at -45°, 0°, 45°, and 90° with respect to the detector axis

demonstrated no difference in the overall TOF spectra. Assuming an isotropic angular

distribution for the slow photofragment primary dissociation, a reasonable assumption for a statistical dissociation on the ground electronic surface, see section 4.1.2, no change in the relative intensity of the fast photofragment channel to slow photofragment channel contributions in the TOF with polarization suggests a near isotropic angular distribution for the fast photofragment primary dissociation. A first order approximation of the dipole moment for a $(\pi^* \leftarrow \pi)$ transition within C_{2v} symmetry places the dipole moment in the plane of the molecule along the S=O bond. Based on a ground state CSC bond angle of 96.4° (ref. 7) the angle between the dipole and the C-S bond is 48.2° which leads to an anisotropy parameter[12] of $\beta = 0.34$ in the limit of a prompt dissociation. While in the excited state the CSC bond angle might be expected to increase, this would only lead to a decrease in the limiting value of β. In addition, any rotational averaging of the reactant molecule prior to dissociation will also serve to decrease the value of β. Our data for m/e 18 at various laser polarization angles is not sufficient to distinguish within this small range of values for β, $0 > \beta > 0.3$. Therefore our measurement of an angular distribution for the fast photofragment primary dissociation channel which appears nearly isotropic in the laboratory frame is consistent with electronic predissociation from the π^* surface on even a very rapid timescale owing to our lack of sensitivity to the degree to which the distribution is anisotropic.

4.1.2 Slow photofragment primary dissociation. The $P(E_T)$ for the slow photofragments primary dissociation, reaction 2a, is shown in figures 5a and 13a for DMSO-d_6 and DMSO-h_6 respectively. Within experimental error figure 5a and 13a are the

same. Note that the $P(E_T)$ in figure 2a determined from the slow m/e 66 (CD_3SO^+)

photoproducts differs from figures 5a and 13a on the low energy side. As will be discussed

below, a significant fraction of the slow CD_3SO products undergo secondary

decomposition and therefore the $P(E_T)$ in figure 2a represents only those CD_3SO

photofragments which survive. The $P(E_T)$ in figures 5a and 13a were determined from the

methyl radical product which does not secondarily decompose and therefore represents the

complete $P(E_T)$ for the slow photofragment primary dissociation.

The $P(E_T)$ for the slow photofragment primary dissociation, figure 5a or 13a, is

peaked at 2 kcal/mol and decreases exponentially out beyond 30 kcal/mol. Translational

energy distributions of this type, peaked near zero with an exponentially decreasing tail,

are characteristic of statistical dissociation on the ground electronic surface involving little

or no recombination barrier. From the endothermicity of the primary C-S bond cleavage,

$D_o(CH_3-SOCH_3) = 51$ kcal/mol[5,6], the available energy following absorption at 193 nm

(148 kcal/mol) is 97 kcal/mol. In the case of a statistical translational energy distribution

the extremely low probabililty for formation of products with a translational energy release

greater than half of the available energy severely limits our sensitivity to the $P(E_T)$ above

50 kcal/mol. For comparison, figure 16 shows a prior distribution for dissociation of a

rotationally cold molecule into two polyatomic fragments of 4 and 6 atoms each within the

rigid rotor, harmonic oscillator, and spherical top approximations and given 97 kcal/mol of

available energy.[13] The prior distribution represents a completely statistical prediction

against which the experimentally determined distribution may be compared. From figure

16 it is clear that the measured $P(E_T)$, dashed line in figure 16, is in excellent agreement

with the prior translational energy distribution, solid line in figure 16. Our results indicate that in the case of the slow photofragment primary dissociation the initial electronic excitation is followed by internal conversion to the ground electronic surface and C-S bond cleavage to produce two open shell molecules with little or no barrier to recombination.

4.2 Secondary decomposition of the sulfonyl intermediate, CD₃SO/CH₃SO.

Following the primary dissociation, reaction 2a, the sufonyl intermediates containing sufficient internal energy will undergo secondary decomposition. We found no evidence for the secondary dissociation of intermediates produced in the fast photofragment primary dissociation. The fast photofragment primary dissociation, see section 4.1.1, results in the production of electronically excited sulfonyl radicals with a substantial fraction of the available energy appearing in translation. The predominant partioning of the available energy into translational and electronic degrees of freedom and the lack of dissociative ionization of the fast m/e 66 (CD_3SO^+) photoproduct at m/e 64 (CD_2SO^+) are consistent with the persistence of the sulfonyl radicals produced in the fast photofragment primary dissociation.

In contrast with the fast photofragment primary dissociation, sulfonyl intermediates produced in the slow photofragment primary dissociation should contain ample internal energy to undergo secondary dissociation. As discussed in section 4.1.2, the slow photofragment primary dissociation is a statistical, near prior, dissociation on the ground electronic surface. Figure 6 shows the overall slow photofragment primary channel $P(E_T)$ with the $P(E_T)$ for the surviving CD_3SO fragments overlaid. The distributions are the same

above ~20 kcal/mol but at lower translational energy, and thus higher internal energy of the products, the distribution for the surviving CD_3SO fragments begins to fall off. The difference between the two distributions, the cross-hatched area in figure 6, represents the CH_3SO/CD_3SO fragments which undergo secondary decomposition. The gradual decline in the $P(E_T)$ for the surviving CD_3SO fragments toward lower translational energy reflects the broad internal energy distribution of the methyl partner fragment. In the case of atomic elimination a given translational energy release reflects a well defined internal energy in the polyatomic partner fragment and the result is an abrupt truncation of the $P(E_T)$ for the surviving polyatomic fragment.[14] In this case the broad internal energy distribution in the methyl partner fragment allows a broad distribution of internal energy in the CD_3SO fragments for a given translational energy release yielding a gradual truncation of the $P(E_T)$.

The onset of the truncation in the $P(E_T)$ for surviving CD_3SO photofragments occurs at the point where internally cold methyl radicals are produced along with sulfonyl radicals with internal energy equal to the height of the barrier to secondary sulfonyl radical decomposition. The recombination barrier for secondary C-S bond cleavage is > 8 kcal/mol, see section 4.2.1. Adding the recombination barrier to the C-S bond energy for the sulfonyl radical of ~52 kcal/mol the barrier to secondary C-S bond cleavage is ~60 kcal/mol. The onset of the truncation in the primary $P(E_T)$ should therefore occur at ~37 kcal/mol since the available energy following primary C-S bond cleavage is ~97 kcal/mol. With the onset of the truncation reflecting production of internally cold methyl radicals,

the portion of the $P(E_T)$ measured for the surviving sulfonyl intermediates below ~37 kcal/mol directly reflects the internal energy distribution of methyl radicals produced with surviving sulfonyl radicals. As can be seen in figure 2a the $P(E_T)$ lies almost entirely below 37 kcal/mol.

Using the prior model, figure 16, to predict the internal excitation in the sulfonyl intermediate following the slow photofragment primary dissociation, $<E_{int}(CD_3SO/CH_3SO)>_{prior}$ = 58 kcal/mol with the distribution extending beyond 90 kcal/mol. Both cleavage of the C-S bond, reaction 2b, and cleavage of the C-H/C-D bond, reaction 3, are, therefore, thermodynamically accessible pathways for secondary decomposition of the sulfonyl intermediate.

4.2.1 Secondary decomposition of the CD$_3$SO/CH$_3$SO intermediate: C-S bond cleavage. Cleavage of the C-S bond, reaction 2b, was the dominant secondary dissociation channel for the CH$_3$SO intermediates, and the only secondary decomposition pathway detected for the CD$_3$SO intermediates. As discussed above in section 4.2 the difference between the the overall $P(E_T)$ for the slow photofragment primary dissociation and the $P(E_T)$ for surviving sulfonyl intermediates, the cross-hatched area in figure 6, represents primary $P(E_T)$ for the CH$_3$SO/CD$_3$SO fragments which undergo secondary decomposition. In figure 6 the difference between the two distributions represents 55% of the total distribution, consistent with 56±10% secondary decomposition determined from the CD$_3$ TOF spectra fitting ratios. For reasons discussed in section 3.2 we were unable to directly detect the surviving CH$_3$SO photofragments, however in the fitting we assumed the

primary $P(E_T)$ for CH_3SO intermediates which secondarily dissociate to be the same as that for the CD_3SO photofragments. From the fitting ratios in the CH_3 TOF spectra we find that $64\pm10\%$ of the CH_3SO intermediates undergo secondary decomposition. This corresponds to a quantum yield for the SO of 0.6 ± 0.1 compared to the quantum yield reported by Chen *et al.* for SO of 1.02 ± 0.12.[8]

The $P(E_T)$ determined for secondary C-S bond cleavage is shown in figure 5b for CD_3SO and figure 13b for CH_3SO. The distributions are very similar, however the $P(E_T)$ for CH_3SO decomposition is slightly broader and a little flatter at the top of the distribution. This difference is likely the result of competing C-H bond cleavage in the case of CH_3SO decomposition which is discussed in the following section. In addition, stiffer modes in the CH_3 product as compared to the CD_3 product might result in less vibrational excitation of the CH_3 product and, therefore, a slightly faster $P(E_T)$ for the CH_3SO decomposition. The translational energy distributions, figure 5b and 13b, are peaked at ~8 kcal/mol suggesting a barrier to recombination of >8 kcal/mol. If one considers a dissociation model for simple bond rupture over an exit barrier where the available energy is partitioned in an impulsive fashion up to the height of the barrier to recombination and statistically above the barrier[3], then the maximum probability in the translational energy distribution will reflect the barrier to recombination. The success of this model for different chemical systems with widely differing available energies has shown that the barrier to recombination is predominantly responsible for energy partitioned into translation, even when the available energy greatly exceeds the barrier height.[4] The

limiting case results if all the potential energy of the recombination barrier appears in translation. Since it is possible for some portion of that potential energy to evolve into internal degrees of freedom as the dissociation proceeds, our measured maximum in the $P(E_T)$ represents a lower limit to the recombination barrier. In the case of both the deuterated and nondeuterated DMSO the fits to the data were not sensitive to the exact shape of the secondary angular distribution, however the fits did require that the secondary angular distribution maintain forward/backward symmetry, demonstrating rotational averaging of the CD_3SO intermediate prior to secondary C-S bond dissociation and providing direct evidence that reaction 2 proceeds via a stepwise mechanism[15] In the case of a concerted three body elimination we would have measured a strong correlation between the primary and secondary recoil velocity vectors.[2]

Our measurement of the SO internal energy found 11.5 ± 3.5 kcal/mol on average which agrees well with the more accurate measurement of Chen *et al.* who found an average of 8.9 kcal/mol with the vibrational distribution peaked at $v=2$.[8] From our results we conclude that SO products result from a stepwise dissociation, reaction 2, with a statistical primary dissociation followed by secondary decomposition over a recombination barrier of > 8 kcal/mol. This suggests that the dynamical partitioning of available energy into SO internal degrees of freedom results from strong exit channel effects in the secondary decomposition of the sulfonyl intermediate.

From the measured branching ratios we find a quantum yield for CH_3/CD_3 of 1.4 ± 0.1. This is in excellent agreement with recent diode absorption gain measurements

made by Rudolph and coworkers who determined a quantum yield of 1.4±0.1 for CD_3

from the dissociation of DMSO-d_6 at 193 nm.[15] In addition, Rudolph and coworkers

determined the fraction of nacent methyl radical products formed in the vibrational ground

state. Their measurements suggest an internal energy content of the CD_3 products in

excess of the REMPI measurements of Chen *et al.*[8] and below the internal energy content

which had been previously determined for CD_3 products in the dissociation of acetone-d_6

at 193 nm.[16] For comparison we can make a qualitative estimate of the vibrational energy

in the methyl radical products based on our overall picture of the dissociation of DMSO-d_6

at 193 nm. The fast primary dissociation accounts for 19% of the total methyl radical

yield. Using the soft fragment impulsive model[4] with 42 kcal/mol of available energy, see

section 4.1.1, we estimate $<E_{int}(CH_3/CD_3)> \sim 4$ kcal/mol for the fast photofragment

primary dissociation. For the slow photofragment primary dissociation, which accounts for

52% of the total methyl radical yield, we use the prior model, see section 4.1.2, to

estimate $<E_{int}(CH_3/CD_3)> \sim 32$ kcal/mol. The remaining 29% of the methyl radical

products are the result of secondary decomposition of sulfonyl intermediates. As discussed

earlier in this section, the forward barrier to C-S bond cleavage in the sulfonyl radical

intermediates is ~60 kcal/mol. For sulfonyl radicals produced in the slow photofragement

primary dissociation we can again use the prior model as an estimate of the internal energy

distribution, see figure 16. Truncating the distribution below 60 kcal/mol to represent only

those sulfonyl intermediates which undergo secondary decomposition yields

$<CH_3SO/CD_3SO>_{int} \sim 67$ kcal/mol. With $D_o(CH_3-SO) \sim 52$ kcal/mol[5,6], $<E_T> = 11$

kcal/mol for secondary C-S bond cleavage, and $<E_{int}(SO)> \sim 9$ kcal/mol[8] suggests very little energy remaining in internal energy of the methyl radical. Based on these estimates, overall the methyl radical products will contain ~ 17 kcal/mol of internal energy each on average. While we aknowledge the severity of the approximations made in this estimation it clearly suggests a larger internal energy content in the methyl products than the REMPI measurements of Chen *et al.*

4.2.2 Secondary decomposition of the CH$_3$SO intermediate: C-H bond cleavage. The primary and secondary translational energy distributions for reaction 3 which were determined from the fitting of the m/e 62 (CH$_2$SO$^+$) and m/e 1 (H$^+$) TOF spectra are shown in figure 11. Our inability to detect any evidence of C-D bond cleavage in the CD$_3$SO intermediates suggests that secondary C-H bond cleavage involves tunneling through the dissociation barrier. The secondary P(E$_T$), figure 11b, is peaked at ~ 4 kcal/mol. Since the C-H bond cleavage appears to involve tunneling, the barrier to recombination should be slightly higher than the 4 kcal/mol reflected by the maximum in the P(E$_T$). This places the barrier to secondary dissociation for reaction 2b and reaction 3 in very close proximity of one another, see figure 17. Figure 11a shows the P(E$_T$) for the primary C-H bond cleavage and although it is similar to the overall slow photofragment primary P(E$_T$), figure 13a, it is missing a portion of the low energy side. In contrast, the primary P(E$_T$) for sulfonyl intermediates which undergo secondary C-S bond cleavage, the region cross-hatched in figure 6, is missing the high energy side in comparison to the overall slow photofragment primary P(E$_T$). This indicates that CH$_3$SO intermediates that go on to break a C-H bond are internally cooler, and therefore translationally warmer, on

average compared with those that break the C-S bond. The resulting overall picture for the secondary decomposition of the CH_3SO intermediates shows that the fraction of CH_3SO intermediates with substantial internal energy above the barriers to secondary dissociation result almost exclusively in C-S bond cleavage. However, a small portion of the CH_3SO intermediates with internal energy near the dissociation barriers are able to break the C-H bond with tunneling playing an important role.

5. Conclusion

We have used the technique of photofragment translational spectroscopy with VUV synchrotron radiation for product ionization to investigate the photodissociation of $DMSO-h_6$ and $DMSO-d_6$ at 193 nm. A picture of the overall dissociation including all of the observed dissociation channels and the estimated barriers is shown in figure 17. In contradiction to previous studies we found direct evidence that dissociation to sulfur monoxide and two methyl radicals occurs via a stepwise dissociation on the ground electronic surface. In addition we also found competing dissociation channels in both the primary and secondary steps. A small fraction of the primary dissociation results in a very large translation energy release and appears to involve dissociation on an excited electronic surface to form methyl radical and an electronically excited state of the sulfonyl radical. With the majority of the available energy partitioned into electronic and translational degrees of freedom the sulfonyl radicals from the fast photofragment primary dissociation lack sufficient internal energy to undergo secondary decomposition. The

majority of the primary dissociation occurs following an initial ($\pi^* \leftarrow \pi$) excitation and internal conversion to the ground electronic surface. Primary C-S bond cleavage then proceeds over little or no barrier resulting in a statistical, near prior, partitioning of the available energy. In the case of DMSO-d_6 all of the CD_3SO intermediates with sufficient internal energy to overcome the barrier to C-S bond cleavage, 56% of the $SOCD_3$ produced in the slow photofragment primary dissociation, dissociate via reaction 2b. In the case of DMSO-h_6 those sulfonyl intermediates with internal energy well above the barrier to secondary C-S bond cleavage go on to dissociate via reaction 2b, however a small fraction of CH_3SO intermediates with internal energy near the dissociation barriers are able to break the C-H bond with tunneling playing a significant role.

References

---

[1] C. E. M. Strauss and P. L. Houston, *J. Phys. Chem.* **94**, 8751 (1990).

[2] S. W. North, C. A. Longfellow, and Y. T. Lee, *J. Chem. Phys.* **99**, 4423 (1993).

[3] S. W. North, D. A. Blank, J. D. Gezelter, C. A. LongFellow, and Y. T. Lee, *J. Chem. Phys.* **102**, 4447 (1995).

[4] S. W. North, Ph.D.Thesis, University of California, Berkeley, 1995.

[5] The heat of formation for DMSO was taken from *Phys. Chem. Ref. Data* **17**, (1988) Supl. No. 1.

The heats of formation for SO, CH_3, H, C_2H_6, and CH_4 were taken form the Handbook of Chemistry and Physics, D. R. Lide (CRC, Boca Raton, 1995).

[6] The heat of formation for CH_3SO and CH_2SO were based on group additivity from S. W. Benson, *Chem. Rev.* **78**, 23 (1978).

[7] K. Gollnick and H. U. Stracke, *Pure Appl. Chem.* **33**, 217 (1973).

[8] X. Chen, F. Asmar, H. Wang, and B. R. Weiner, *J. Phys. Chem.* **95**, 6415 (1991); X. Chen, H. Wang, B. R. Weiner, M. Hawley, and H. H. Nelson, *J. Phys. Chem.* **97**, 12269 (1993).

[9] S. W. North, D. A. Blank, P. M. Chu, and Y. T. Lee, *J. Chem. Phys.* **102**, 791 (1995).

[10] Handbook of Chemistry and Physics, D. R. Lide (CRC, Boca Raton, 1995).

[11] DMSO at 298 K contains ~2.3 kcal/mol of internal energy on average and should experience substantial cooling following supersonic expansion.

[12] R. N. Zare. *Mol. Photochem.* **4**, 1 (1972).

[13] R. D. Levine and R. B. Bernstein, *Acc. Chem. Res.* **7**, 393 (1974); J. T. Muckerman, *J. Phys. Chem.* **93**, 179 (1989).

[14] T. K. Minton, P. Felder, R. J. Brudzynski, and Y. T. Lee, *J. Chem. Phys.* **81**, 1759 (1984); S. W. North, D. A. Blank, and Y. T. Lee, *Chem. Phys. Lett.* **222**, 38 (1994).

[15] R. N. Rudolph, S. W. North, G. E. Hall, T. J. Sears, *manuscript in preparation.*

[16] G. E. Hall, D. Vanden Bout, and T. J. Sears, *J. Chem. Phys.* **94**, 4182 (1991).

Figure Captions

Figure 1:   TOF spectra for m/e 66 (CD_3SO^+) at source angles of 12° and 22.5°. The

forward convolution fit contains two contributions representing the fast

and slow channels for reaction 2a and fit with the $P(E_T)$s in figure 2.

Figure 2:   (a) c.m. translational energy distribution used to fit the slow contribution in

the m/e 66 (CD_3SO^+) TOF spectra, figure 1. (b) c.m. translational energy

distribution used to fit the fast contribution in the m/e 66 (CD_3SO^+) TOF

spectra, figure 1.

Figure 3:   TOF spectrum for m/e 64 (CD_2SO^+) at a source angle of 12°. The fit

shown is from the two $P(E_T)$s in figure 2 with the same fitting ratio used to

fit the m/e 66 (CD_3SO^+) spectra in figure 1. Note absence of the fast

feature in the experimental data.

Figure 4:   TOF spectra for m/e 18 (CD_3^+) at source angles of 20°, 35°, and 50°. The

forward convolution fit has three components. The fastest component,

peaked ~40 μsec, is fit with the $P(E_T)$ in figure 2b and represents the fast

channel for reaction 2a. The slowest and broadest component, peaked ~80

μsec, is fitted with the $P(E_T)$ in figure 5a and represents the slow channel

for reaction 2a. The middle contribution, peaked ~55 μsec, is fitted with the secondary $P(E_T)$ in figure 5b and represents products from reaction 2b.

Figure 5:   (a) Primary c.m. translation energy distribution used to fit the slowest contribution to the m/e 18 (CD_3^+) TOF spectra in figure 4, slow channel for reaction 2a. (b) Secondary c.m. translation energy distribution for reaction 2b used to fit the middle contribution to the m/e 18 (CD_3^+) TOF spectra in figure 4 and the dominant contribution to the m/e 48 (SO^+) TOF spectra in figure 7.

Figure 6:   The c.m. translational energy distribution from figure 2a overlaid on the c.m. translation energy distribution from figure 5a. The area with the cross-hatches is the difference between figure 5a and figure 2a and represents the primary c.m. translation energy distribution for sulfonyl intermediates which undergo secondary C-S bond cleavage.

Figure 7:   TOF spectra for m/e 48 (SO^+) from dissociation of DMSO-d_6 at source angles of 25°, 40°, and 50°. The dominant contribution to the forward convolution fit is the result of reaction 2b and is fitted with the $P(E_T)$ in figure 5b. The small contribution to the fit at 25°, peaked ~125 μsec, is from dissociative ionization of CD_3SO photoproducts.

Figure 8:   Branching ratios for the dissociation of DMSO-d_6 and DMSO-h_6 at 193 nm. Determination of the values is discussed in the text. The error in the values is estimated to be <10%.

Figure 9:   TOF spectrum for m/e 62 (CH_2SO^+) at a source angle of 15°. The forward convolution fit is from the primary and secondary $P(E_T)$s in figure 11a and 11b according to reaction 3.

Figure 10:   TOF spectrum for m/e 1 (H^+) with the detector, molecular beam, and dissociation laser mutually perpendicular. The forward convolution fit contains three contributions. The fastest contribution, peaked ~40 μsec, is a two photon dissociation involving C-S bond cleavage followed by secondary photodissociation of the methyl radical products. The slowest contribution, peaked ~105 μsec, is from dissociative ionization of methyl radical products. The middle contribution, peaked ~60 μsec is fit with the primary and secondary $P(E_T)$s in figures 11a and 11b according to reaction 3.

Figure 11:   (a) Primary c.m. translation energy distribution used to fit the m/e 62 (CH_2SO^+) TOF spectrum in figure 9 and the middle contribution to the m/e 1 (H^+) TOF spectrum in figure 10, reaction 3. (b) Secondary c.m. translation energy distribution for reaction 3 used to fit the m/e 62 (CH_2SO^+) TOF spectrum in figure 9 and the middle contribution to the m/e 1 (H^+) TOF spectrum in figure 10.

Figure 12:   TOF spectra for m/e 15 (CH_3^+) at source angles of 20° and 35°. The forward convolution fit has three components. The fastest component, peaked ~40 µsec, is fit with the $P(E_T)$ in figure 2b and represents the fast channel for reaction 2a. The slowest and broadest component, peaked ~75 µsec, is fit with the $P(E_T)$ in figure 13a and represents the slow channel for reaction 2a. The middle contribution, peaked ~45 µsec, is fit with the secondary $P(E_T)$ in figure 13b and represents products from reaction 2b.

Figure 13:   (a) Primary c.m. translation energy distribution used to fit the slowest contribution to the m/e 15 (CH_3^+) TOF spectra in figure 12, slow channel for reaction 2a. (b) Secondary c.m. translation energy distribution for reaction 2b used to fit the middle contribution to the m/e 15 (CH_3^+) TOF spectra in figure 12 and the dominant contribution to the m/e 48 (SO^+) TOF spectra in figure 14.

Figure 14:   TOF spectra for m/e 48 (SO$^+$) from dissociation of DMSO-h$_6$ at source

angles of 20°, 30°, and 45°. The dominant contribution to the forward

convolution fit is the result of reaction 2b and is fit with the P(E$_T$) in figure

13b. The small contribution to the fit at 20°, peaked ~125 μsec, is from

dissociative ionization of CH$_3$SO photoproducts.

Figure 15:   Photoionization spectrum for m/e 48 (SO$^+$) photofragments from DMSO-

h$_6$ at a source angle of 20° for undulator radiation energies of 8.25-10.75

eV. The VUV had a roughly gaussian shape with FWHM of 0.5 eV.

Figure 16:   Calculated prior distributions for dissociation of a rotationally cold reactant

into 4 and 6 atom fragments within the rigid rotor, harmonic oscillator, and

spherical top approximations with 97 kcal/mol of available energy. The

solid line is the calculated translational energy distribution. The dotted line

is the internal energy distribution of the 4 atom product. The dot-dash-dot

line is the internal energy distribution of the 6 atom product. The dashed

line is the primary P(E$_T$) for the slow channel of reaction 2a from figures 5a

and 13a.

Figure 17:   A summary of the dissociation channels which we observed for DMSO

following absorption at 193 nm. Thermodynamic values are from ref. 5 and

ref. 6 and estimations for the energy of S1, T1, and S2 are from ref. 7.

Relative contributions of each channel are shown in figure 8.
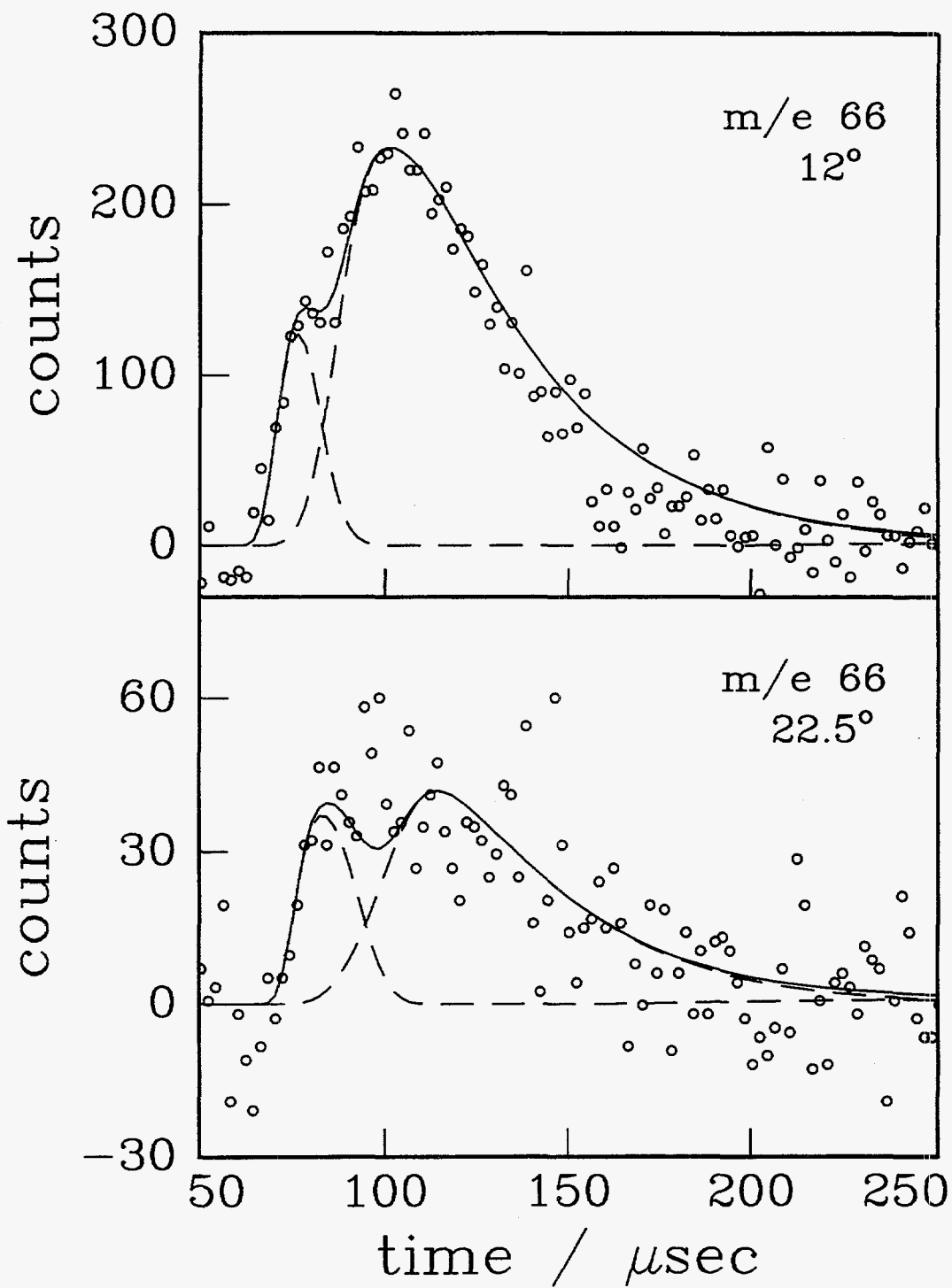
figure 1
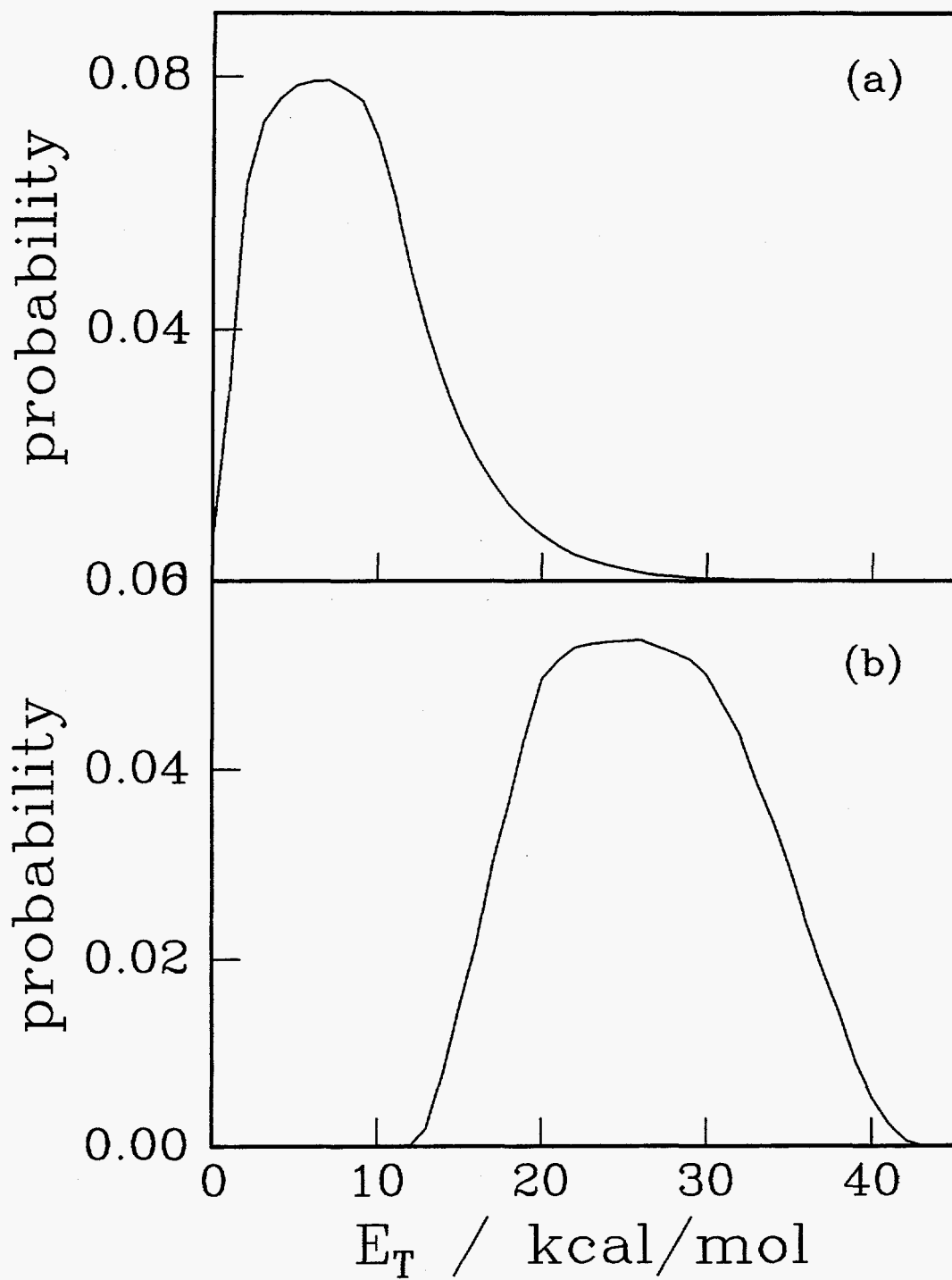
figure 2
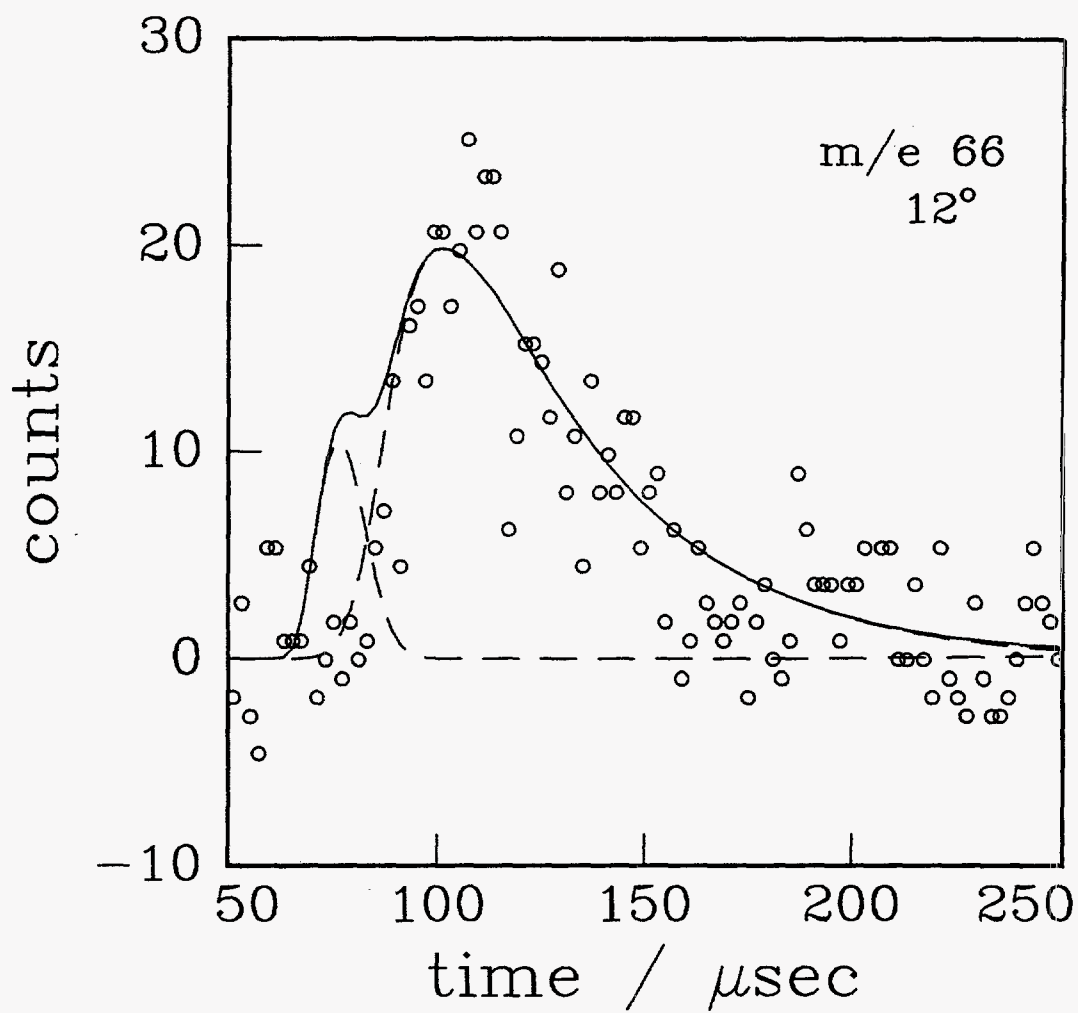
figure 3
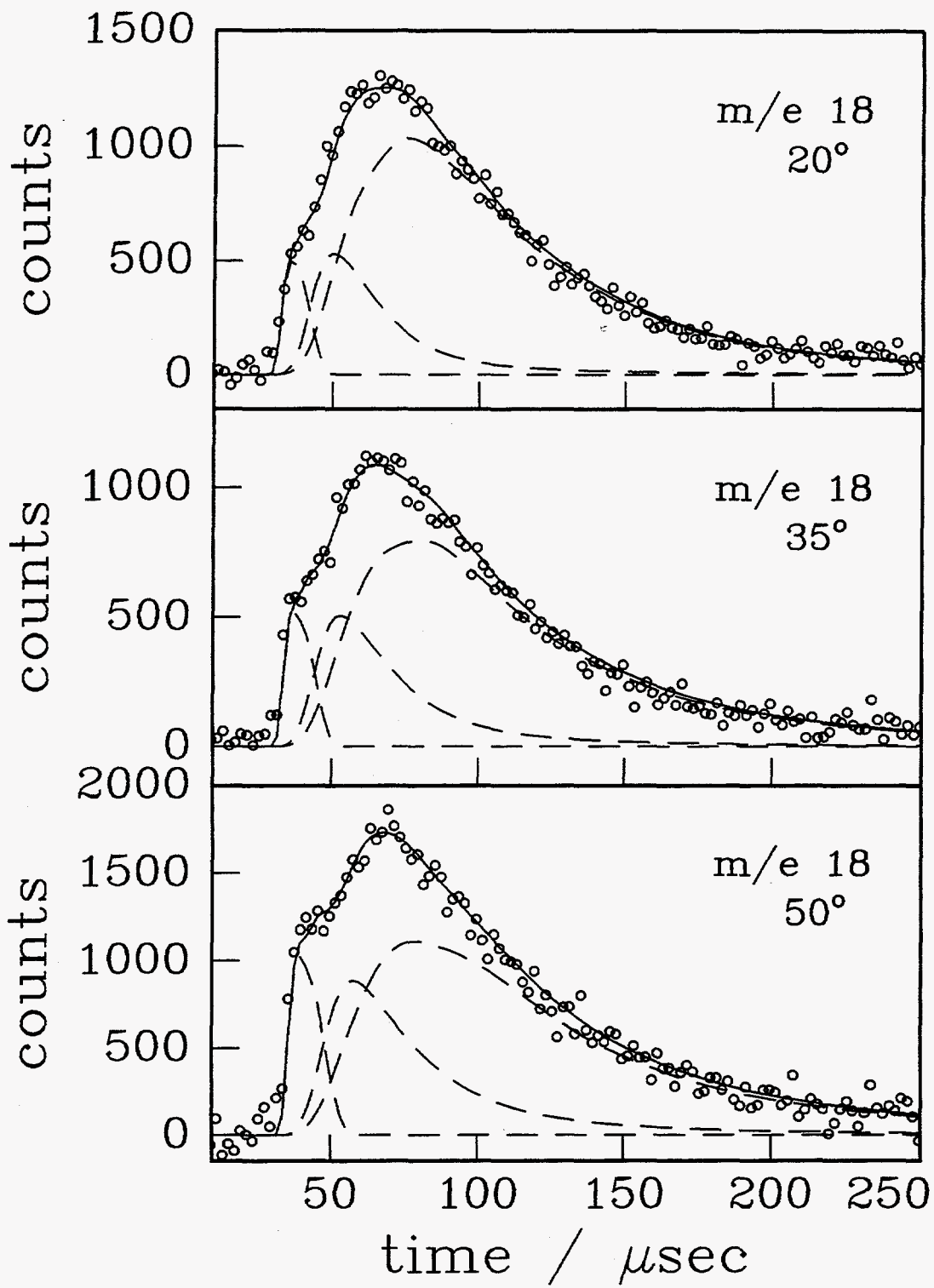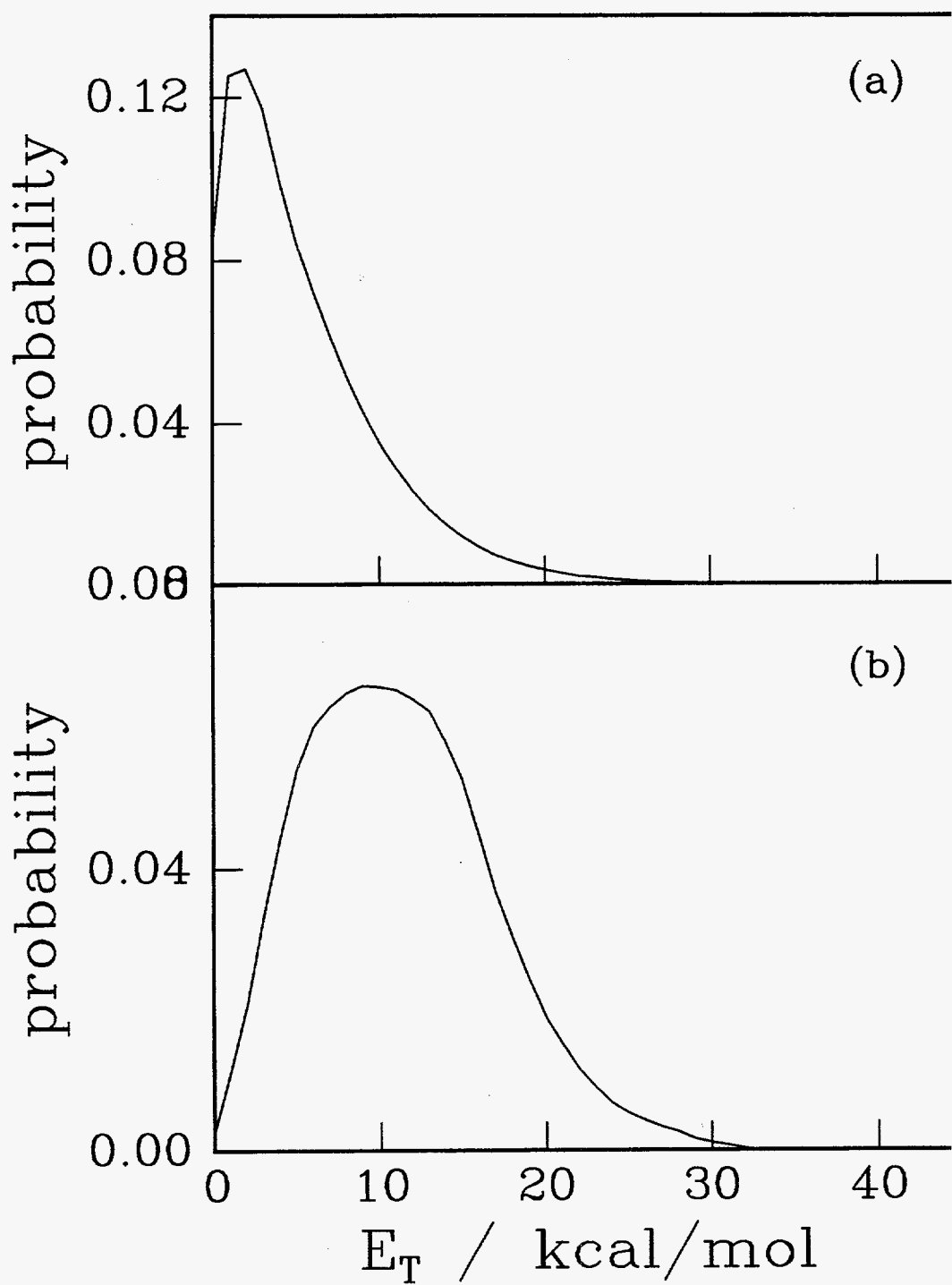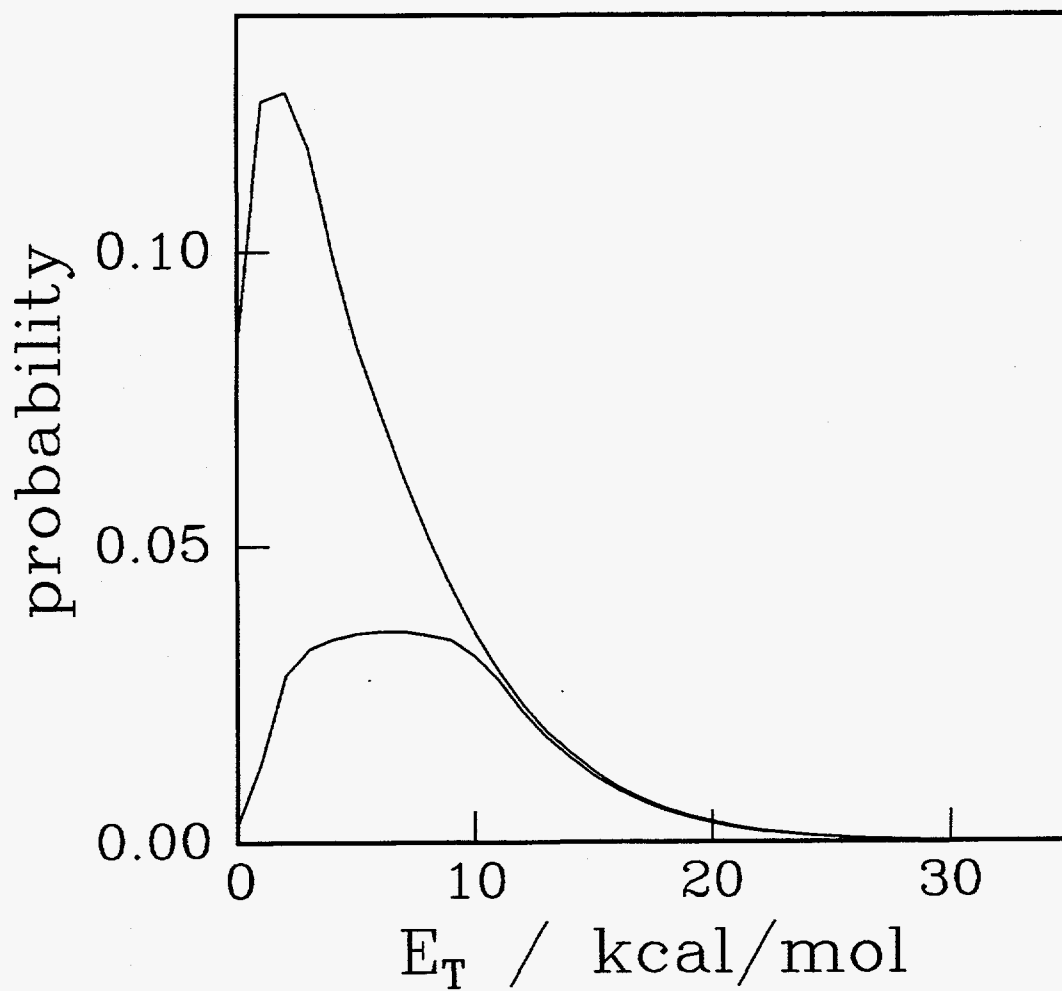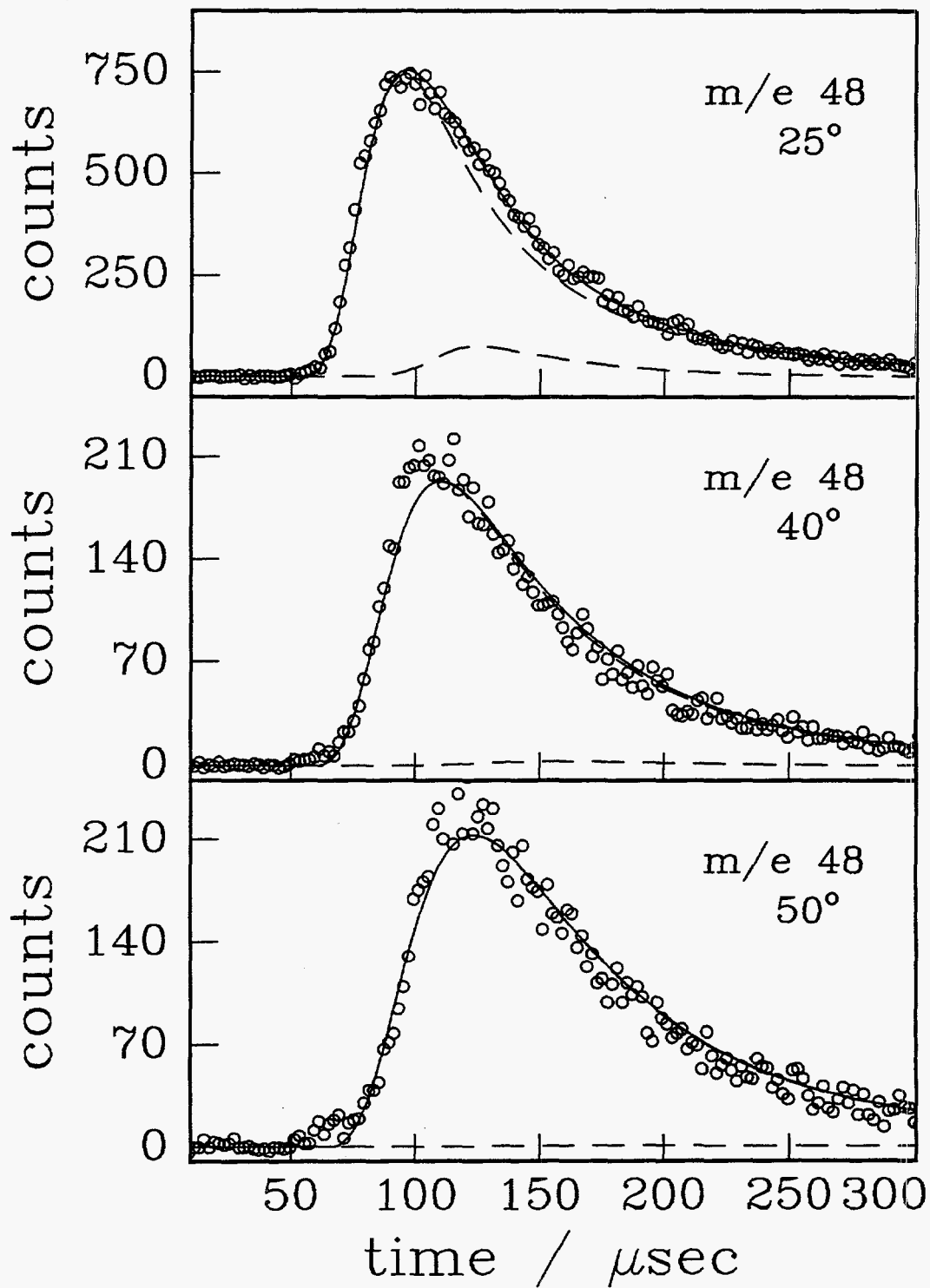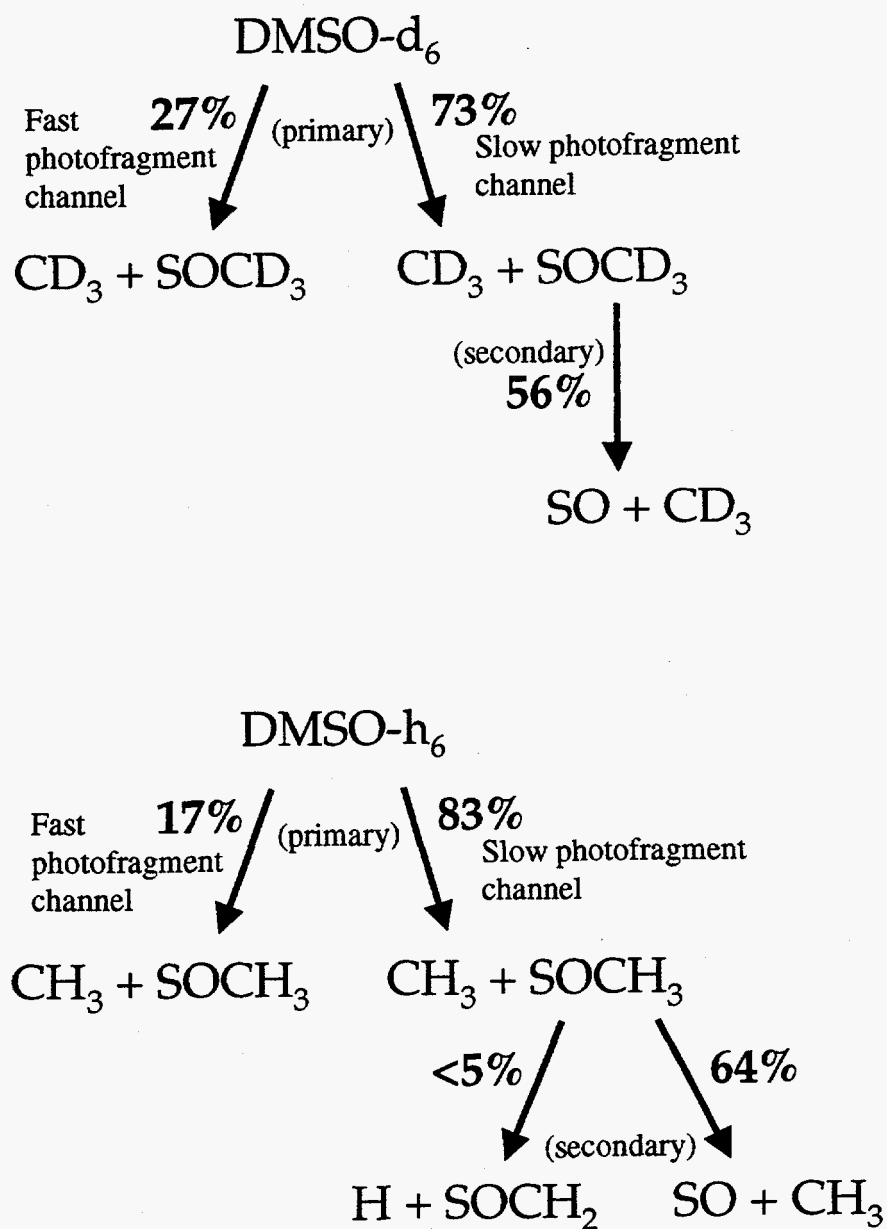
figure 4

figure 5

figure 6

figure 7

$$DMSO\text{-}d_6$$

Fast photofragment channel **27%** (primary) **73%** Slow photofragment channel

$$CD_3 + SOCD_3 \qquad CD_3 + SOCD_3$$

(secondary) **56%**

$$SO + CD_3$$

$$DMSO\text{-}h_6$$

Fast photofragment channel **17%** (primary) **83%** Slow photofragment channel

$$CH_3 + SOCH_3 \qquad CH_3 + SOCH_3$$

<5% (secondary) **64%**

$$H + SOCH_2 \qquad SO + CH_3$$
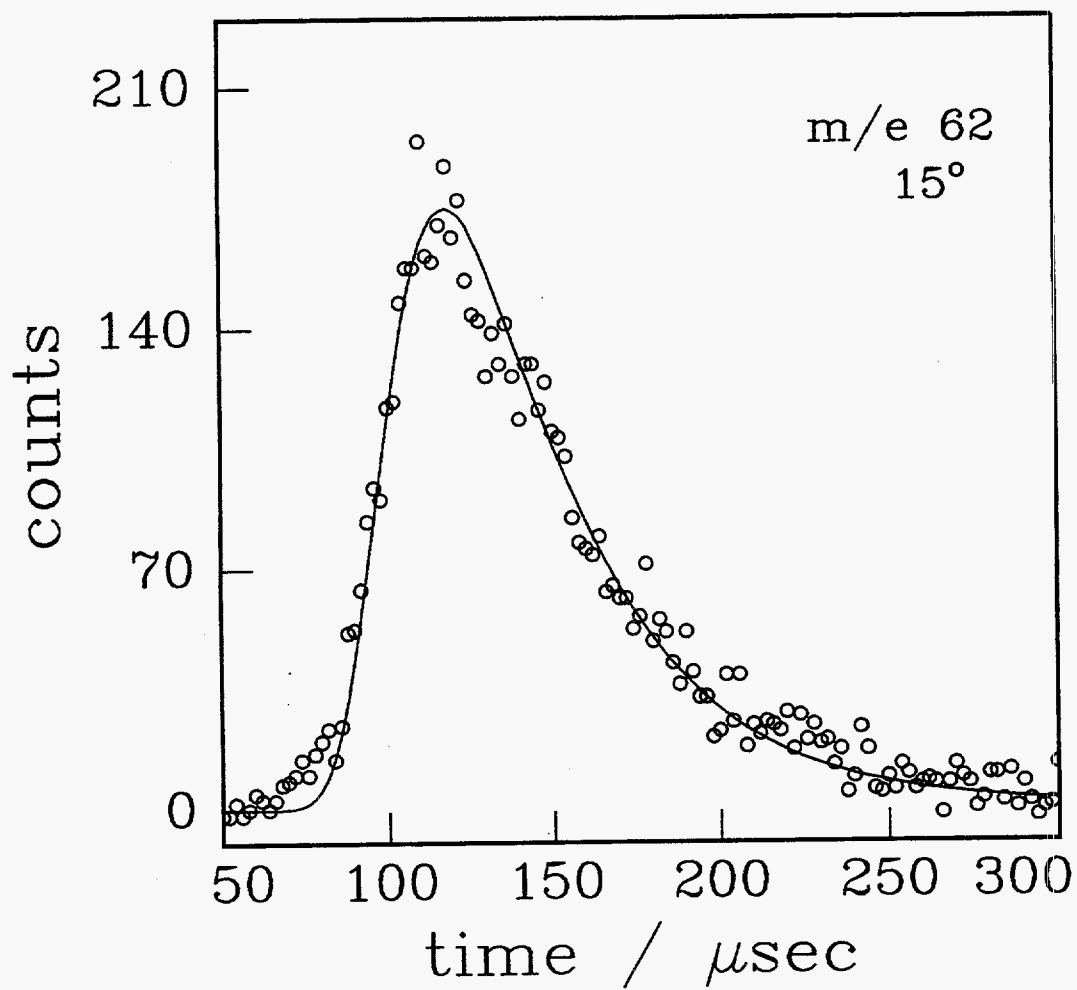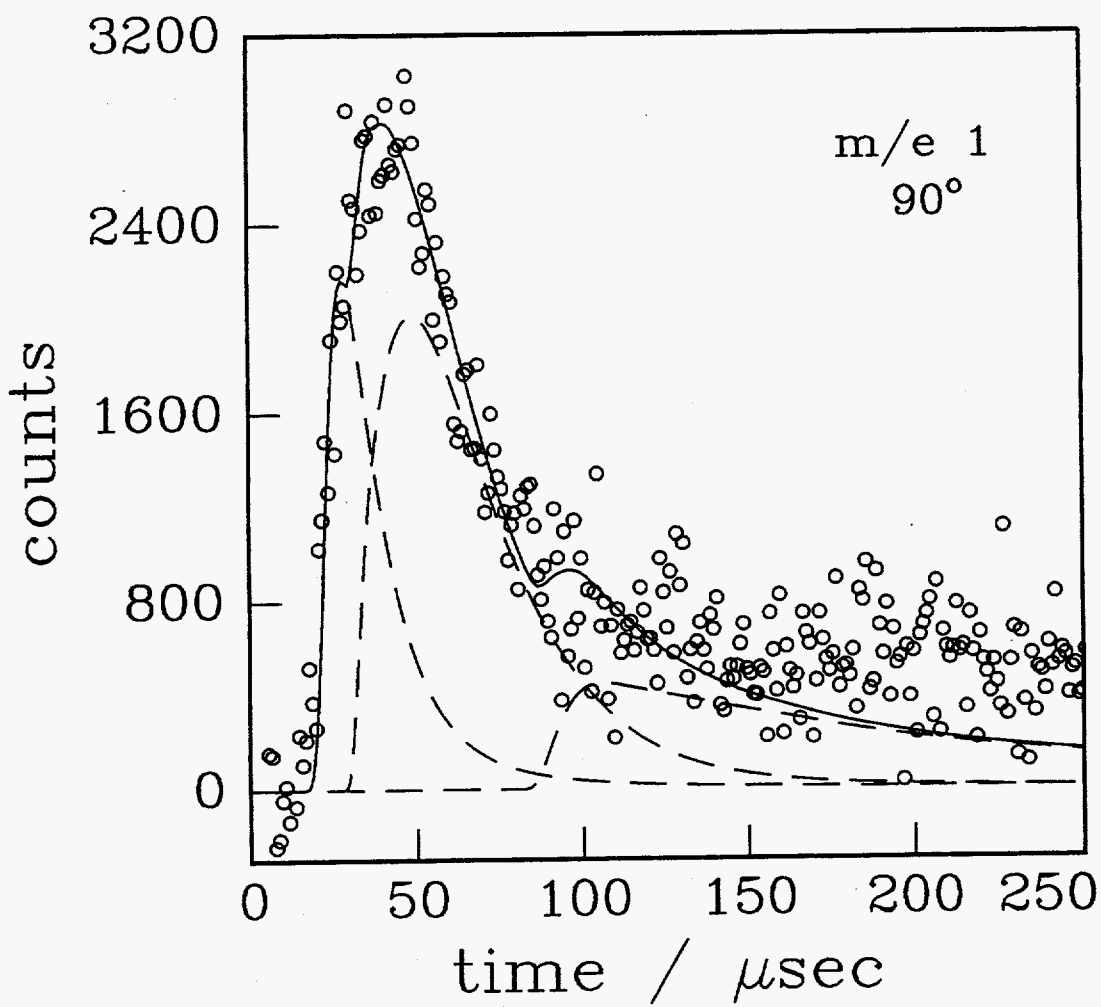
figure 8
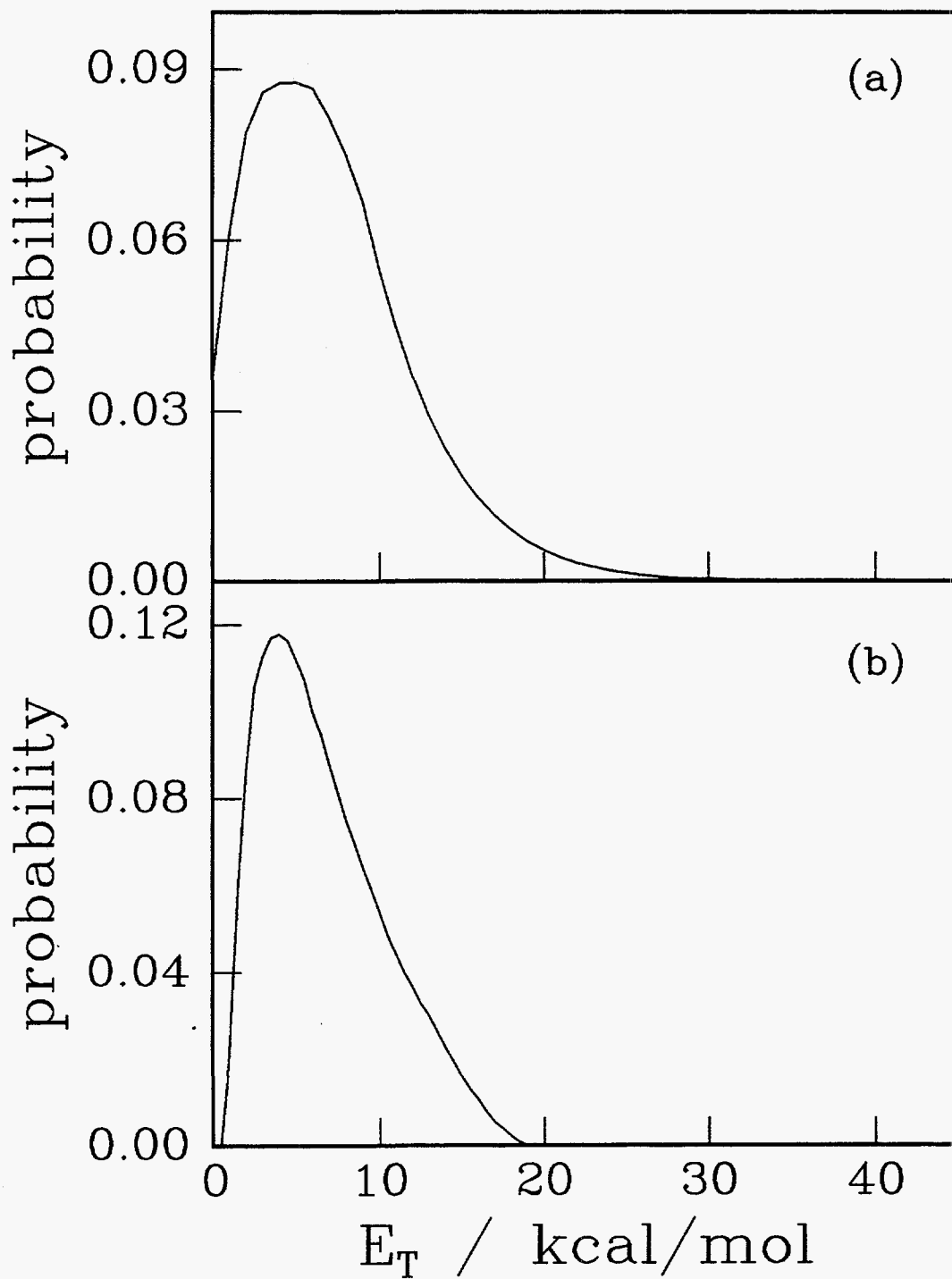
figure 9
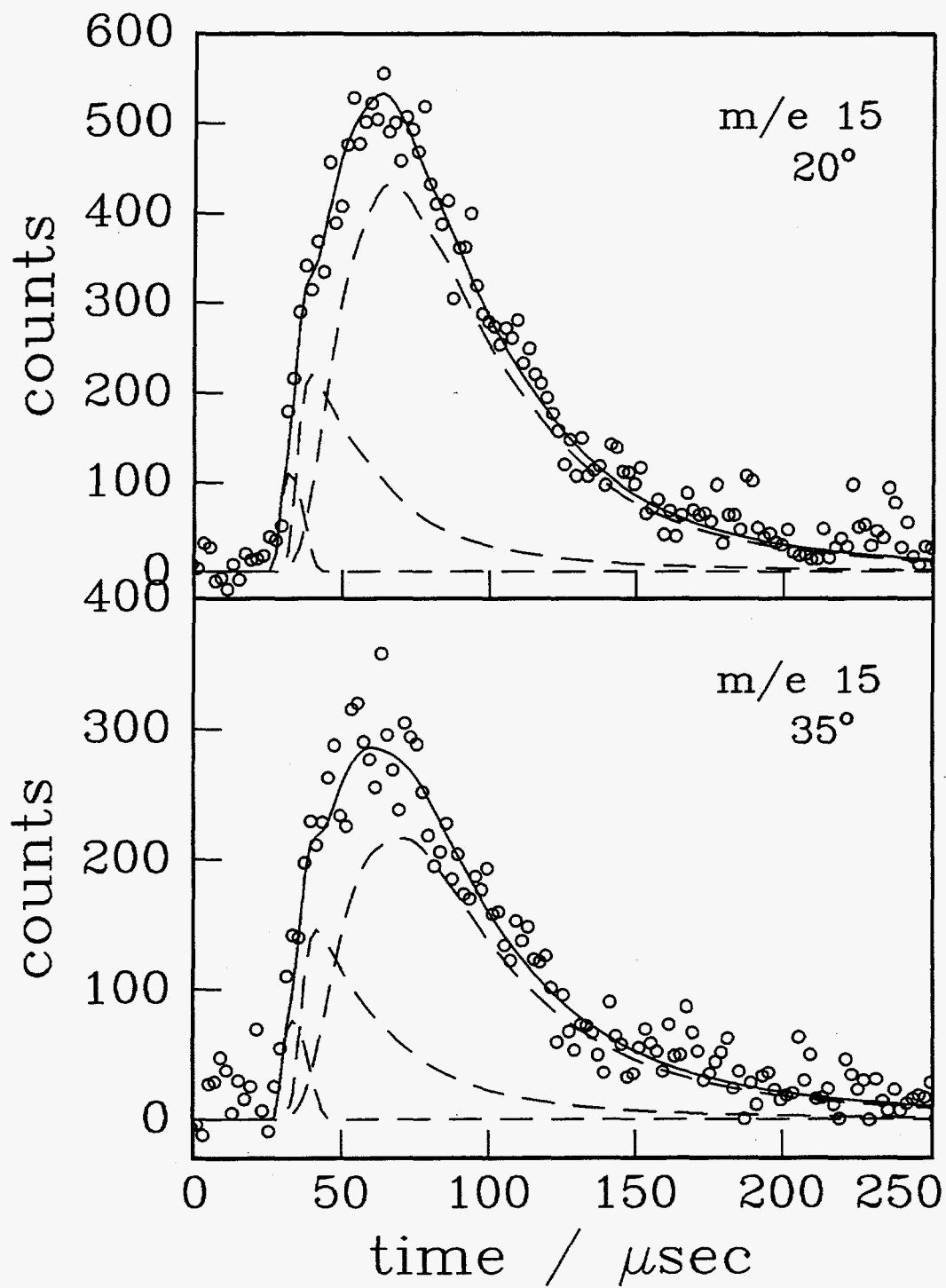
figure 10
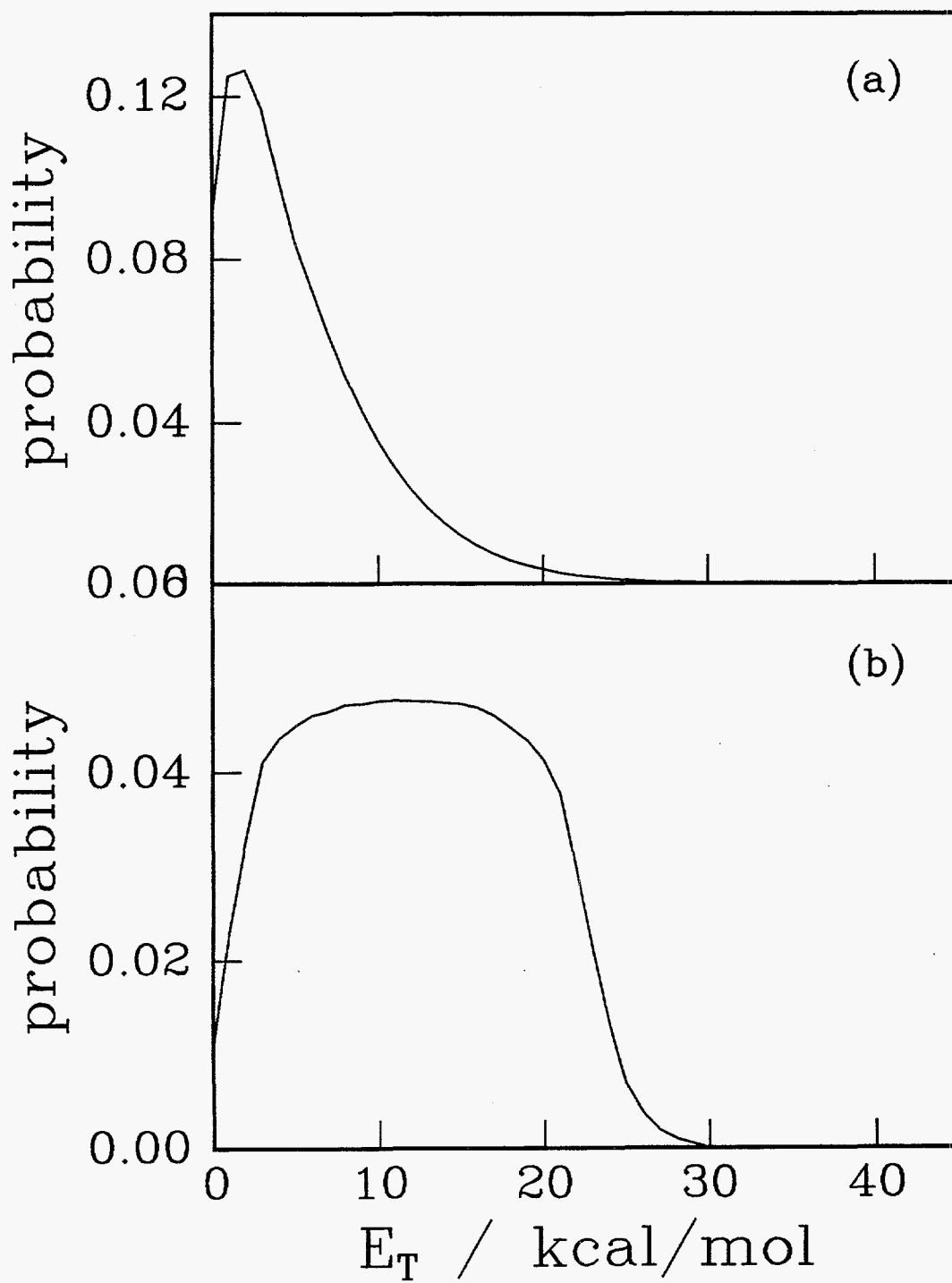
figure 11
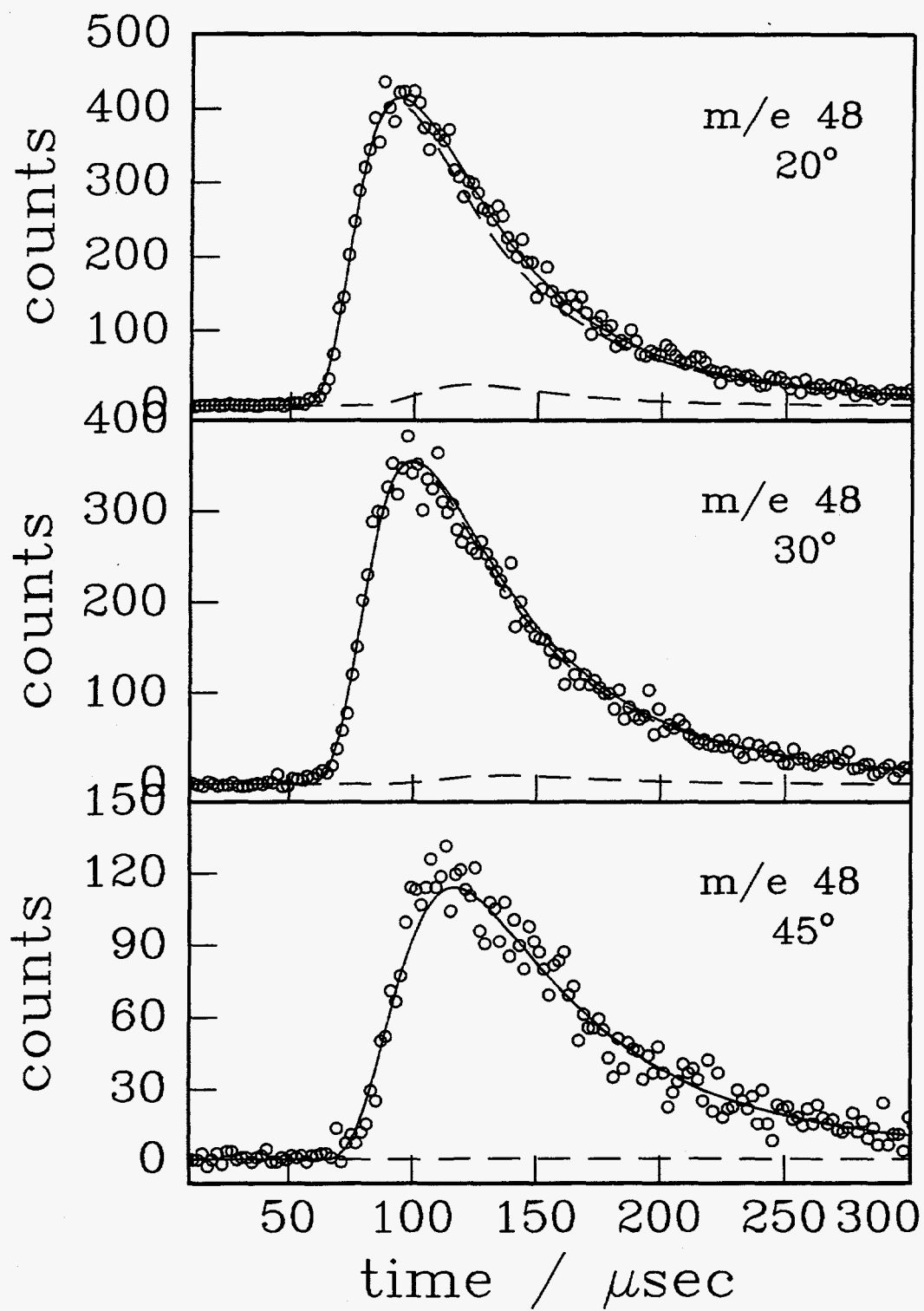
figure 12
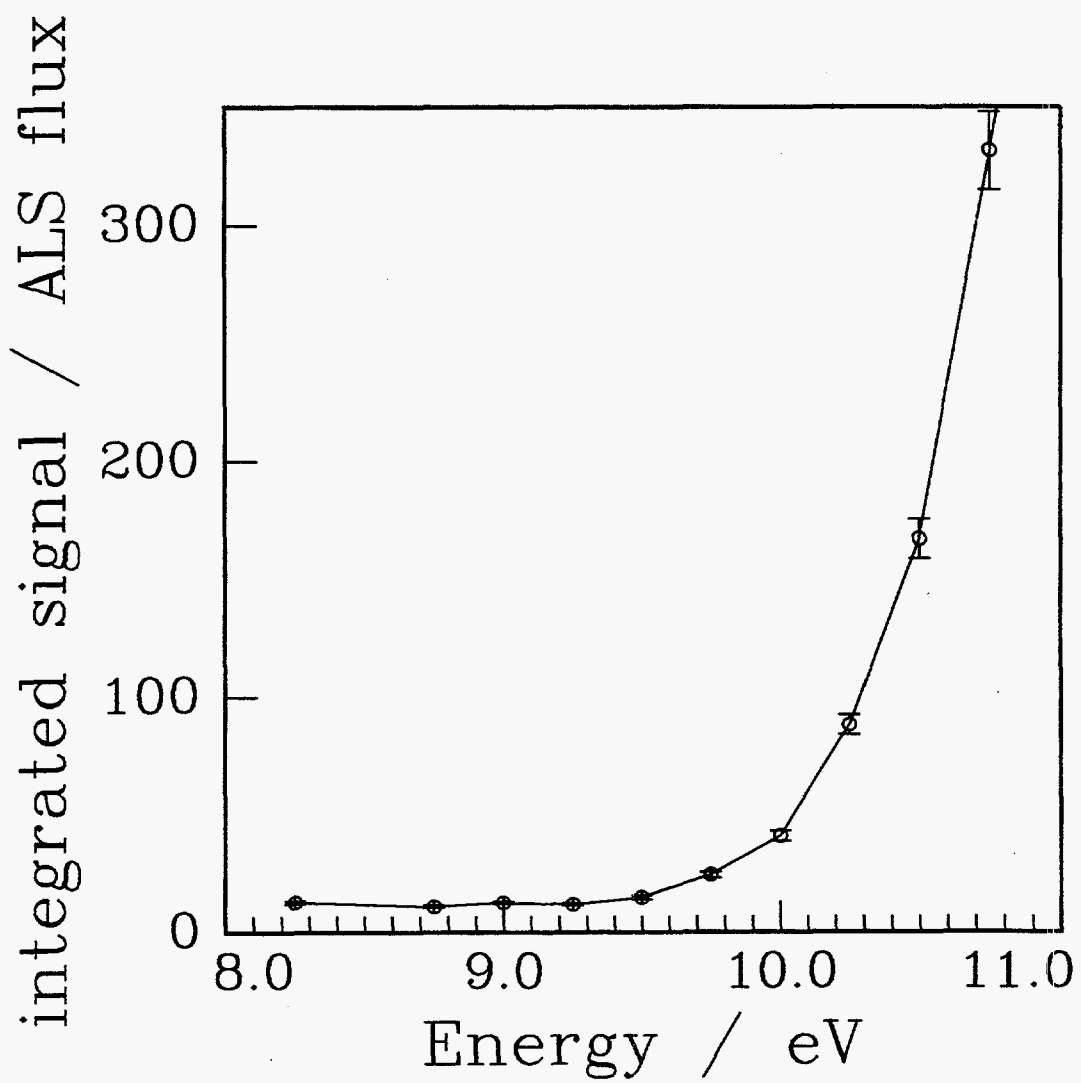
figure 13
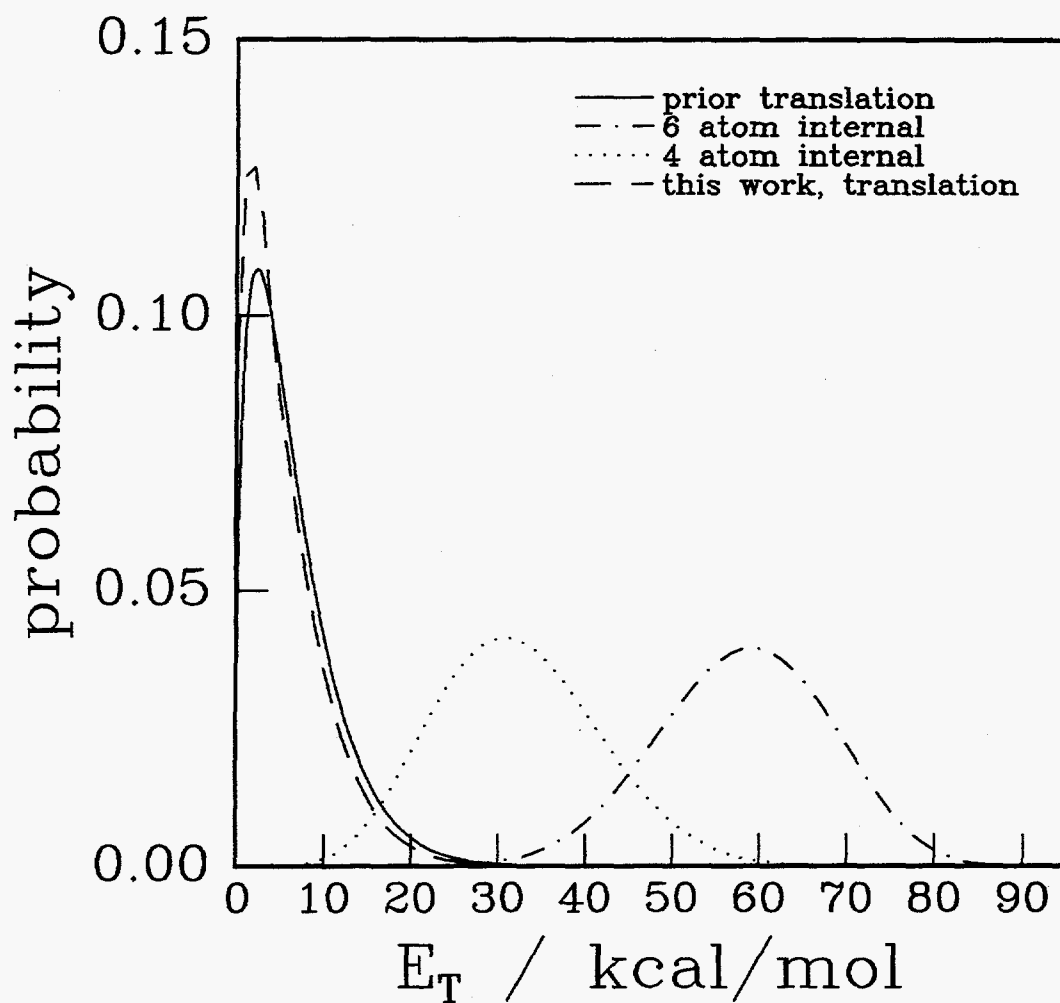
figure 14
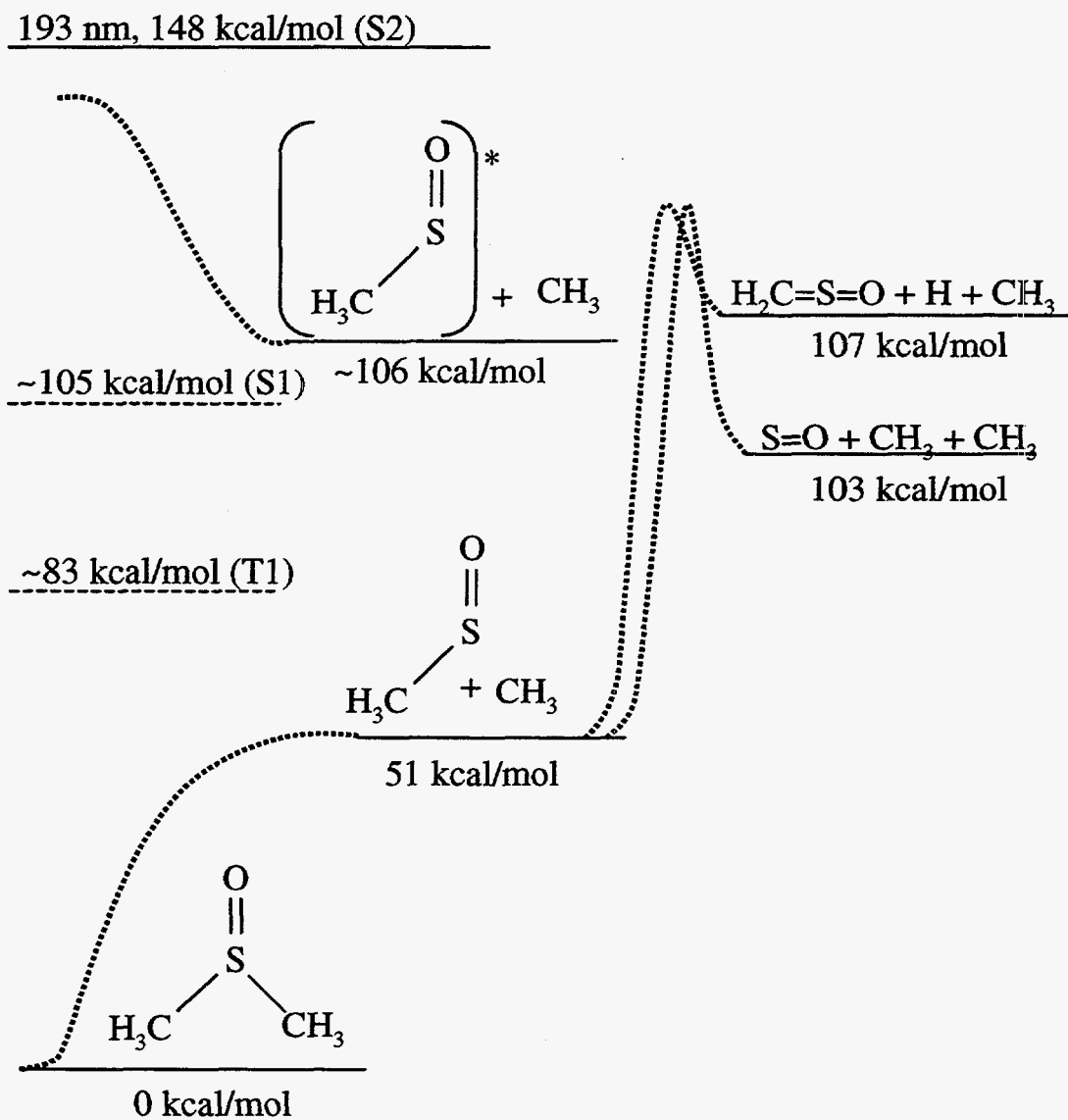
figure 15

figure 16

figure 17

Chapter 3

Photodissociation of Acrylonitrile at 193 nm

Abstract

We have investigated the photodissociation of acrylonitrile (H_2CCHCN) at 193 nm using the technique of photofragment translational spectroscopy. The experiments were performed at the Chemical Dynamics Beamline at the Advanced Light Source and used tunable vacuum ultraviolet synchrotron radiation for product photoionization. We identified four primary dissociation channels including atomic and molecular hydrogen elimination, HCN elimination, and CN elimination. All of the dissociation channels appear to occur on the ground electronic surface following internal conversion from the initially excited $\pi\pi^*$ electronic state. The product translational energy distributions reflect near statistical simple bond rupture for the radical dissociation channels, while substantial recombination barriers mediate the translational energy release for the two molecular elimination channels. Photoionization onsets have provided additional insight into the chemical identities of the products and their internal energy content. In addition, we have investigated the dissociation of acrylonitrile-1d to further elucidate the H_2 and HCN elimination mechanisms.

1. Introduction

As the simplest π-bonded hydrocarbons ethylene and its substituted analogues serve as prototypical systems for the study of this important class of molecules. These compounds exhibit a strong $\pi^* \leftarrow \pi$ transition around 190 nm and their photochemistry following excitation has been the subject of considerable literature. At excitation wavelengths <200 nm there is sufficient available energy for both radical (eq. 1 and 2) and molecular (eq. 3 and 4) elimination channels.

$$H_2CCHX \Rightarrow C_2H_2X + H \qquad\qquad (rxn\ 1)$$

$$H_2CCHX \Rightarrow C_2H_3 + X \qquad\qquad (rxn\ 2)$$

$$H_2CCHX \Rightarrow C_2H_2X + H_2 \qquad\qquad (rxn\ 3)$$

$$H_2CCHX \Rightarrow C_2H_2 + HX \qquad\qquad (rxn\ 4)$$
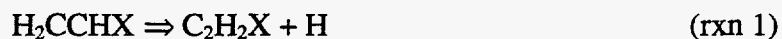
Understanding the competition between these channels as well as the underlying dynamics of each channel has been central to previous experimental investigations.

The photochemistry of ethylene has been the subject of numerous studies.[1] Balko *et al.* used the technique of photofragment translational spectroscopy (PTS) to study the dissociation of ethylene at 193 nm. The authors characterized both the atomic and molecular hydrogen elimination channels which were found to occur with nearly equal yields. Both dissociation channels followed internal conversion (IC) to the ground electronic surface. The hydrogen atom loss exhibited a center of mass (c.m.) translational

energy distribution ($P(E_T)$) consistent with statistical bond rupture involving little or no barrier to recombination. The $P(E_T)$ for the molecular hydrogen elimination channel was peaked at 20 kcal/mol reflecting a substantial recombination barrier. From the dissociation of selectively deuterated ethylene isotopomers a 2:3 ratio of 1,1 verses 1,2 H_2 elimination was determined. Based on thermodynamic considerations, the 1,1 elimination was assigned predominantly to the production of singlet vinylidene contrary to previous reports.[2] In addition, the authors also measured the $P(E_T)$ for hydrogen atoms which resulted from the subsequent dissociation of the nascent vinyl radical photoproducts.

Of the mono-substituted ethylenes, the photodissociation of vinyl chloride has received the greatest attention. A comprehensive review of the photodissociation of vinyl chloride at 193 nm can be found in reference 3. We mention here only a few of the key points from the results of those investigations. Gordon and coworkers have pursued an extensive series of studies investigating the dissociation of vinyl chloride at 193 nm using Doppler spectroscopy. The authors have measured Doppler profiles for hydrogen atom products with an average translational energy of 17 kcal/mol assuming a Maxwell-Boltzmann distribution. The main focus of these investigations, however, has been the Cl and HCl elimination channels. The bimodal translational energy distribution for the radical Cl elimination channel was originally assigned as two dissociation channels based on the results of Umemoto *et al.* for 1,1 dichloroethylene. The faster fragments were thought to originate from the σ^*(C-Cl) electronic surface while the slower fragments originated from a ground state dissociation.[4] The state resolved $P(E_T)$'s for HCl measured by Gordon and

coworkers were qualitatively similar to the $P(E_T)$ measured by Balko _et al._ for H_2 elimination from ethylene.[1] The HCl rotational population was found to be biexponential for v=0 and was fit well with a single Boltzmann rotational temperature for v=1 and v=2. Gordon and coworkers also dissociated vinyl chloride-1d at 193 nm and found a 25:75 ratio of HCl:DCl. While this might suggest a 25:75 ratio of 1,2 verses 1,1 HCl elimination, this conclusion was contradicted by the identical internal energy distributions of the HCl and DCl products. A complex mechanism involving partial H-atom scrambling followed by a concerted 1,1 HCl elimination and isomerization of the singlet vinylidene product to acetylene was invoked to explain the experimental results.

The photodissociation of acrylonitrile (H_2CCHCN) has received comparably less attention. The vacuum ultraviolet absorption spectrum was measured by Mullen and Orloff who assigned the following transitions: $n \rightarrow \pi^*$ at 217.0 nm, $\pi \rightarrow \pi^*$ at 203.0 nm, and $\sigma \rightarrow \sigma^*$ at 172.5 nm.[5] Gandini and Hacket photolyzed acrylonitrile at 213.9 nm and identified end products consistent with the molecular elimination channels, reactions 3 and 4, with a ratio of HCN to H_2 loss of 1.6.[6] The authors noted a drop in the H_2 quantum yield when photolyzing at 206.5 nm and suggested the onset of a competitive radical dissociation channel. Dissociation of acrylonitrile-1d resulted in a ratio of 1.5±0.2 for both HD/H_2 and C_2HD/C_2H_2 and while the evidence was not conclusive, the authors favored a dissociation mechanism where randomization of the H/D atoms precedes dissociation and dissociation involves 1,2 elimination for both HCN and H_2. Nishi _et al._ have performed PTS experiments on acrylonitrile at 193 nm.[7] The authors identified two single photon

dissociation pathways, CN and HCN elimination. The translational energy distributions for both channels were obtained by a direct inversion of the TOF spectra, and each was fitted with a Boltzmann distribution. The lower energy contribution, T_{bolt}=2500 K, was assigned to the CN elimination channel, and the higher energy contribution, T_{bolt}=6000 K, was assigned to HCN elimination with a ratio of CN/HCN >3. Experiments employing VUV flash photolysis of acrylonitrile-1d followed by spectroscopic VUV detection of the products suggested that molecular HCN elimination channel results predominantly from 1,1 elimination on an excited electronic surface to give HCN and *triplet* vinylidene.[8] The authors also placed an upper limit on the CN elimination channel of 5%. Bird and Donaldson investigated the CN elimination channel at 193 nm using laser-induced fluorescence (LIF) to probe the CN product state distributions.[9] Only v=0 and v=1 vibrational states were populated with a ratio of (v=1/v=0) = 0.14. The nascent rotational distributions for both v=0 and v=1 were fitted with a Boltzmann rotational temperature of T_{bolt}=1450 K. Based on the non-statistical vibrational distribution, the level of rotational excitation, and the translational energy distribution reported by Nishi *et al.* the authors concluded that the CN elimination channel proceeds *via* a prompt dissociation on an excited electronic surface. Recently, North and Hall investigated the CN elimination channel at 193 nm using transient frequency-modulated spectroscopy to measure nascent CN Doppler profiles.[10] The measured CN v=1 to v=0 branching ratio was in good agreement with the results of Bird and Donaldson. The CN Doppler profiles, however, were consistent with a prior translational energy distribution and showed no detectable

vector correlations suggesting that the dissociation proceeds *via* simple bond rupture on the ground electronic surface. The authors also determined a quantum yield of <0.01 for the CN elimination channel.

We have recently demonstrated the power of the technique of photofragment translational spectroscopy with tunable VUV synchrotron radiation used for product photoionization to resolve a complete picture of complex photodissociation dynamics in small molecular systems.[11] In this study we have used this method to investigate the photodissociation of acrylonitrile and acrylonitrile-1d at 193 nm. Figure 1 shows the thermodynamically available dissociation channels following absorption at 193 nm. We have identified four primary dissociation channels including both of the radical dissociation channels, reactions 1 and 2, and both of the molecular elimination channels, reactions 3 and 4. The dissociation is consistent with competition on the ground electronic surface following IC from the initially excited $\pi\pi^*$ state. Translational energy distributions have been determined for all of the observed dissociation channels. We have measured the photoionization onsets for all of the dissociation products with the exception of H and H_2 and these measurements have provided additional information about the identity and internal excitation of the scattered dissociation products. The selective photoionization also enabled us to distinguish between signals generated by molecular HCN elimination and radical CN elimination, eventhough both of these dissociation channels result in the same product mass combination, m/e 27 + m/e 26. We have also investigated the

photodissociation of acrylonitrile-1d at 193 nm and measured the product ratios for $C_3HN:C_3DN$ and $C_2HD:C_2H_2$.

2. Experimental

These experiments were carried out at the Chemical Dynamics Beamline at the Advanced Light Source (ALS) at Lawrence Berkeley National Laboratory. A complete description of the experimental apparatus and setup is provided in Chapter 1 of this thesis. We present here only the details specific to this experiment. A continuous molecular beam was generated by expanding 100 Torr of 3% or 11% acrylonitrile in He through a 0.125 mm nozzle into a source chamber maintained at 4×10^{-4} Torr. The nozzle was heated to ~200 °C to inhibit cluster formation. The velocity distribution of the resulting beam was measured by chopping the beam with a slotted mechanical wheel. The beam velocity for the 3% acrylonitrile in He was 1710 m/s with a FWHM of 12% and for the 11% acrylonitrile in He was 1330 m/s with a FWHM of 13%. The molecular beam was skimmed twice and intersected at 90° with the output of a Lambda Physik LPX-200 excimer laser operating on the ArF transition (193.3 nm). Laser fluence ranged 10-300 mJ/cm^2. In all of the experiments presented here the photodissociation laser was unpolarized which has the experimental result of an isotropic laboratory photofragment distribution in the plane defined by the molecular beam and detector axis regardless of the degree to which an individual dissociation channel may be anisotropic.

Acrylonitrile, 99+%, was obtained from Aldrich and used without further purification. Acrylonitrile-1d was prepared according to the method of Mathias and Colletti.[12] The sample was confirmed by ^{1}H NMR to be 77% deuterated at the 1 position.

3. Results

For all of the TOF spectra presented, the circles represent the data, the dashed lines represent contributions of individual dissociation channels to the forward convolution fit, and the solid line is the total forward convolution fit to the data. While TOF spectra were taken at multiple laser fluences to insure that dissociation signals were the result of single photon processes, all TOF spectra presented were taken with a laser fluence of ~100 mJ/cm^2. Center of mass translational energy distributions were generated from the laboratory TOF spectra using the forward convolution technique. The forward convolution technique is described in detail in the "Data analysis" section of Chapter 1 of this thesis.

Hydrogen atom elimination. Figure 2 shows the TOF spectra for m/e 52 ($C_3H_2N^+$) at source angles of 5° and 7.5° and a photoionization energy of 14.0 eV. The spectra contain a single feature which was fitted with the $P(E_T)$ shown as the solid line in figure 3. The $P(E_T)$ is exponentially decreasing from 4 kcal/mol out to a maximum of about 40 kcal/mol. Due to background from the molecular beam, 5° was the minimum scattering angle at which we were able to collect TOF data. As a result we were not

sensitive to the $P(E_T)$ below 4 kcal/mol which is the minimum energy required to scatter a C_3H_2N photoproduct to $5°$. The photoionization spectrum for the C_3H_2N photoproducts collected at a scattering angle of $7.5°$ is shown as the circles in figure 4. Taking into consideration the width of the undulator radiation, the photoionization onset is 9.3 ± 0.3 eV.

We use the following expression to calculate the available energy,

$$E_{available} = E_{h\nu} - D_o(H-C_3H_2N) + E_{reactant, internal} \qquad \text{(eqn. 1)}$$

In equation 1 we make the assumption that the internal excitation of the acrylonitrile reactant is negligible.[13] Estimating $D_o(H-C_3H_2N) \sim 108$ kcal/mol based on the C-H bond strength in ethylene[23] the available energy following H-atom elimination at 193 nm (148 kcal/mol) is ~40 kcal/mol. A minimum of 13 kcal/mol of translational energy is required to scatter a C_3H_2N photoproduct to $7.5°$. By truncating the $P(E_T)$ at 13 kcal/mol and calculating the average translational energy we find that the portion of the measured $P(E_T)$ above 13 kcal/mol has an average of $<E_T>_{(>13\ kcal/mol)} = 20$ kcal/mol. Since this channel results from atomic elimination and there is no evidence for electronic excitation of the products, any portion of the available energy not partitioned into translation must be partitioned into internal degrees of freedom in the C_3H_2N products. Subtracting the average translational energy from the available energy leaves an average internal energy in the C_3H_2N photoproducts detected at $7.5°$ of 20 kcal/mol. Therefore, the photoionization spectrum for m/e 52 photoproducts in figure 4 represents C_3H_2N radicals containing a very broad internal energy distribution with $<E_{int}>$~20 kcal/mol. Without quantitative

information about the affect of internal energy in the neutral on the photoionization process we are unable to report a corrected value for the photoionization onset of internally cold C_3H_2N radicals. However, additional internal energy will most likely lead to a red shift in the photoionization onset and therefore our measured value of 9.3 ±0.3 eV should represents a lower limit to the true photoionization threshold for internally cold C_3H_2N radicals.

Molecular hydrogen elimination. Figure 5 shows TOF spectra for m/e 51 (C_3HN^+) at a source angle of 7.5° and photoionization energies of 12.0 eV and 14.0 eV and at a source angle of 10° and a photoionization energy of 12.0 eV. There are two contributions to the forward convolution fit to the TOF spectra. The major component in the fit is the result of H_2 elimination and was fitted with the $P(E_T)$ in figure 6. The $P(E_T)$ has a maximum probability at 18 kcal/mol and extends beyond 47 kcal/mol with $<E_T>=23\pm1$ kcal/mol. The minor component in the fit is the result of dissociative photoionization of C_3H_2N products which resulted from atomic hydrogen elimination and was fitted with the $P(E_T)$ in figure 3. Compared with the spectra at 12.0 eV, the 14.0 eV spectrum was well fitted by increasing the contribution of the dissociative ionization channel from the atomic hydrogen elimination products with respect to the H_2 elimination channel. Fitting spectra taken at both 12.0 eV and 14.0 eV, where the ratio of the two contributions to the signal is significantly different, provided additional confidence in the fit to the H_2 elimination channel. The photoionization spectrum for C_3HN photoproducts collected at a scattering angle of 10° is shown as the triangles in figure 4. The spectrum

shows a photoionization onset of 10.8±0.3 eV. This is consistent with the I.P. for cyanoacetylene of 11.6 eV[23] with the red shift in the photoionization onset resulting from internal excitation in the HCCCN photoproducts.

HCN and CN elimination. There are two possible product channels which can result in a photoproduct mass combination of m/e 27 + m/e 26; HCN (m/e 27) + C_2H_2 (m/e 26) and CN (m/e 26) + C_2H_3 (m/e 27). In traditional PTS experiments, that employ electron impact product ionization, it is often difficult or impossible to distinguish between dissociation channels that generate the same mass combination. The selectivity afforded by tunable VUV photoionization provides a significant advantage in such cases. The photoionization spectrum for m/e 27 photoproducts collected at a scattering angle of 15° is shown in figure 7. The spectrum has a dominant feature with an onset around 11.0 eV and a small shoulder with an onset around 8.5 eV. The two possible photoproducts at m/e 27 are HCN and the vinyl radical which have ionization potentials of 13.6 eV and 8.6 eV respectively.[23] The shoulder with a phototionization onset around 8.5 eV is consistent with the I.P. for vinyl radicals and it cannot result from HCN photoproducts since a red shift of 5.1 eV from the HCN I.P. of 13.6 eV exceeds the available energy following photodissociation at 193 nm. The dominant feature in figure 7, with a photoionization onset around 11.0 eV, can be assigned to HCN photoproducts with the red shift of the photoionization onset reflecting substantial internal excitation in the HCN products. Additional evidence for the presence of two distinct dissociation channels leading to m/e 27 photoproducts is shown in figure 8. Figure 8 shows TOF spectra for m/e 27 at a source

angle of 20° at photoionization energies of 10.0 eV and 15.0 eV. The two spectra have

been arbitrarily scaled together, however the kinematically corrected integrated signal at a

photoionization energy of 10.0 eV is <1% of the signal at 15.0 eV. It is clear in figure 8

that at photoionization energies well above the I.P. for both HCN and the vinyl radical the

m/e 27 TOF spectrum is dominated by HCN photoproducts. However, when the

photoionization energy is set below the onset for ionization of HCN products and above

the I.P. for vinyl radical products we obtain a TOF spectrum for the vinyl radical products

which exhibits very different kinematics from the HCN elimination process. It should be

noted that without the ability to selectively ionize the products the kinematic difference

between the channels would be insufficient to separate them in a traditional PTS

experiment. The slow products from the CN elimination channel would be lost in the tail

of the dominant HCN elimination signal.

HCN elimination. Figure 9 shows TOF spectra for m/e 27 photoproducts at

source angles of 30° and 50° and a photoionization energy of 15 eV. As discussed above,

at a photoionization energy of 15.0 eV the spectra in Figure 9 represent HCN

photoproducts. Figure 10 shows TOF spectra for m/e 26 at source angles of 30° and 50°

and a photoionization energy of 15 eV. The TOF spectra in figures 9 and 10 were fitted

with the $P(E_T)$ in figure 11 confirming the TOF spectra in figure 10 to be the momentum

matched C_2H_2 partner fragment to HCN photoproducts. While 15.0 eV is sufficient to

photoionize both C_2H_2 and CN photoproducts, the ionization potentials are 11.4 eV and

14.1 eV respectively[23], no difference in the shape of the m/e 26 TOF spectra was found

when decreasing the photoionization energy to 12.0 eV. Since 12.0 eV is well below the I.P. for CN products this confirms that the m/e 26 TOF spectra consist almost exclusively of C_2H_2 photoproducts from HCN elimination. The $P(E_T)$ for HCN elimination in figure 11 has a maximum probability at 8 kcal/mol, $<E_T> = 15$ kcal/mol, and decreases out beyond 47 kcal/mol. The photoionization spectrum for the m/e 26 (C_2H_2) photoproducts scattered to 15° is shown as the circles in figure 12. For comparison the photoionization spectrum of jet cooled acetylene was obtained by sending a neat molecular beam of acetylene directly into the detection region of the instrument and is shown as the triangles in figure 12. The two ionization spectra in figure 12 have been arbitrarily scaled to the integrated signal at a photoionization energy of 13.0 eV. The photoionization spectrum for acetylene, triangles in figure 12, has an abrupt onset at the I.P. for acetylene of 11.4 eV.[23] A comparatively more subtle onset is exhibited by the C_2H_2 photoproducts, circles in figure 12, at 10.5±0.3 eV.

CN elimination. As discussed above, by tuning the photoionization energy below the onset for HCN photoproducts it was possible to discriminate against HCN photoproducts at m/e 27 enabling us to obtain TOF spectra for vinyl radical photoproducts which result from CN elimination. Figure 13 shows TOF spectra for m/e 27 ($C_2H_3^+$) photoproducts at source angles of 10° and 20° and a photoionization energy of 10.0 eV. The TOF spectra in figure 13 were fitted with the $P(E_T)$ shown as the solid line in figure 14. The $P(E_T)$ has a maximum probability at 1 kcal/mol and exponentially decreases out to a maximum translational energy of ~12 kcal/mol. Since CN has an I.P. of 14.1 eV[23]

which lies above the I.P. of all of the possible C_2H_2 photoproducts, we were not able to discriminate against the C_2H_2 photoproducts from HCN elimination at m/e 26 in order to obtain TOF spectra for CN photoproducts.

The endothermicity, available energy, and average translational energy release for each of the observed dissociation channels is shown in table 1.

Acrylonitrile-1d. We measured product ratios for the dissociation of acrylonitrile-1d (H_2CCDCN) at 193 nm. The sample was determined by ^1H NMR and mass spectrometry to be 77% deuterated at the 1 position. For H_2/HD elimination we measured the integrated signal for m/e 52 (C_3DN^+) and m/e 51 (C_3HN^+) scattered to 12.5° at a photoionization energy of 14.0 eV. Due to kinematic considerations the signal from atomic hydrogen elimination in the 23% nondeuterated portion of the reactant sample producing C_3H_2N, m/e 52, is negligible at a scattering angle of 12.5°. We assumed the amount of dissociative ionization for both C_3DN and C_3HN to be the same and obtained a measured ratio of $C_3DN/C_3HN = 0.60^{+0.04}_{-0.06}$. For HCN/DCN elimination we measured the integrated signal for m/e 26 ($C_2H_2^+$) and m/e 27 (C_2HD^+) at a scattering angle of 20° and a photoionization energy of 11.5 eV. In this case we must also correct for dissociative ionization of both the C_2H_2 and C_2HD products. Dissociative ionization of C_2H_2 will decrease the m/e 26 signal while dissociative ionization of C_2HD to C_2D^+ will enhance the m/e 26 signal and dissociative ionization of C_2HD to either C_2H^+ or C_2D^+ will decrease the signal at m/e 27. In order to correct for dissociative ionization, we measured the relative signal for m/e 26 ($C_2H_2^+$) and m/e 25 (C_2H^+) from the photodissociation of non-deuterated

acrylonitrile under the same experimental conditions and found a ratio of (m/e 26)/(m/e25) = 7.0. We found dissociative ionization at all other possible masses to be negligible. In the case of the C_2HD products we assumed a 1:1 ratio of $C_2D^+:C_2H^+$ from the dissociative ionization and obtained a measured ratio of $C_2HD/C_2H_2 = 0.60^{+0.07}_{-0.06}$. With the photoionization energy set at 11.5 eV there was no significant interfering signal at m/e 27 from HCN photoproducts when measuring C_2HD photoproducts.

4. Discussion

A. Radical elimination (reactions 1 and 2).

Hydrogen atom elimination. The $P(E_T)$ for hydrogen atom elimination shown by the solid line in figure 3 has a maximum probability ≤ 4 kcal/mol and decreases out to ~40 kcal/mol. Translational energy distributions of this type are indicative of simple bond rupture on the ground electronic surface involving little or no barrier to recombination and near statistical partitioning of the available energy. For comparison, the statistical prediction from a prior distribution[14] is shown as the dashed line in figure 3. Since we do not measure the complete $P(E_T)$, we cannot measure below 4 kcal/mol, we were not able to normalize the measured $P(E_T)$ with respect to the statistical prediction. We have arbitrarily scaled the two distributions in figure 3 to have the same probability at 6 kcal/mol.

We have established an available energy of 40 kcal/mol for this channel. The prior distribution at this available energy predicts $<E_T> = 4$ kcal/mol. The measured $P(E_T)$ does not fall off above 4 kcal/mol as rapidly as the prior model which indicates that slightly more energy is partitioned into the translational degrees of freedom than the statistical expectation. One possible explanation for this observation could be the result of a small recombination barrier. The repulsive interaction implied by such a barrier would be expected to partition a significant fraction of this potential energy into translational degrees of freedom. Another reason the distribution shows a greater translational energy release than the prior prediction may come from the classical treatment of the oscillators in the prior calculation. The higher frequency modes in the C_3H_2N product are probably not well represented classically, and will therefore not receive a statistical portion of the available energy leaving more energy in translation.

While there have been no previous reports of measurements of this dissociation channel, our measured $P(E_T)$ is very similar to the $P(E_T)$ measured by Balko *et al.*[1] for hydrogen atom elimination from ethylene at 193 nm. Interestingly, Mo *et al.* reported a translational energy distribution based on hydrogen atom Doppler profiles from the dissociation of vinyl chloride at 193 nm which were consistent with a Maxwell-Boltzmann distribution and contained an average translational energy of 17 kcal/mol.[15] This very large fraction of the available energy, 35% on average, in translation would seem to indicate a nonstatistical partitioning of the available energy suggesting a significant difference in the mechanism of hydrogen atom elimination from vinyl chloride as compared with

acrylonitrile and ethylene. The hydrogen atom Doppler profiles were isotropic which the authors suggested to indicate internal conversion prior to dissociation. This result is consistent with our results for acrylonitrile and the results for ethylene which indicate internal conversion to the ground electronic surface prior to C-H bond cleavage. While we are unable to offer an explanation for the large translational energy release for H atom fragments in vinyl chloride, we are currently pursuing the dissociation of vinyl chloride at 193 nm using PTS and we hope to address this issue in a forthcoming publication.[16]

CN elimination. The minor CN elimination channel in acrylonitrile has been reinvestigated recently.[9,10] North and Hall[10] measured a CN quantum yield of 0.003 ±0.001 in stark contrast to the earlier PTS study of Nishi *et al.* who had assigned a CN quantum yield of 0.75 based on indirect TOF evidence.[7] We are not able to determine absolute quantum yields in the present study due to a lack of available quantitative information concerning the photoionization cross sections of the products. However, we estimate this channel to account for <1% of the total dissociation yield at 193 nm in clear agreement with the results of North and Hall. The CN elimination channel is substantially smaller than the analogous Cl elimination channel in vinyl chloride, which may account for as much as 50% of the dissociation products at 193 nm.[16] In vinyl chloride, the large Cl elimination channel is due to the participation of a direct dissociation channel which crosses the initially excited $\pi\pi^*$ state in the Franck-Condon region.[4,3] The absence of such a repulsive electronic surface correlating to CN elimination in acrylonitrile forces this channel to compete with other more energetically favorable dissociation pathways on the

ground state potential energy surface. As a result, the molecular elimination channels dominate and the radical channels are relatively minor.

The translational energy distribution determined in this experiment is consistent with the statistical randomization of the available energy followed by a barrierless dissociation on the ground electronic state. A prior translational energy distribution[14], which approximates a statistical partitioning of energy, is shown as the dash-dot line in figure 14 and is qualitatively very similar to the measured distribution (solid line). For comparison, an impulsive model[17] which has been invoked to fit the fast Cl elimination channel in vinyl chloride, would result in an average translational energy of ~9 kcal/mole rather than the 2.4 kcal/mole observed. Furthermore, in such cases the $P(E_T)$ most often resembles a Gaussian distribution centered at the impulsive average, qualitatively different than is experimentally observed.

State-dependent translational distribution from the analysis of Doppler profiles over the full range of populated CN rotational states in v=0 have been recently measured by North and Hall.[10] The state-dependent distributions were indistinguishable, suggesting that the $P(E_T)$ derived from a single CN state can be compared to the present, state-averaged, measurements. The $P(E_T)$ obtained from CN Doppler profiles for N=24, v=0 is shown as the dashed line in figure 14. The present experimental distribution is slightly colder than the Doppler measurement. However, in light of the nascent CN vibrational distribution, which shows greater than statistical excitation, the difference in the two experiments is not surprising. The state-averaged translational energy distribution should be less energetic than the v=0 distribution since it includes $v \geq 1$ CN channels which were

unable to be measured in the previous study.

B. Molecular elimination (reactions 3 and 4).

HCN elimination. Thermodynamically there are three C_2H_2 isomers which can be produced from the elimination of HCN following absorption at 193 nm (148 kcal/mol), see figure 1:

$$H_2CCHCN \Rightarrow HCCH + HCN \qquad \Delta H_0 = 43.0 \text{ kcal/mol} \qquad \text{(rxn 5)}$$

$$H_2CCHCN \Rightarrow :CCH_2 \, (^1A_1) + HCN \qquad \Delta H_0 = 86 \text{ kcal/mol} \qquad \text{(rxn 6)}$$

$$H_2CCHCN \Rightarrow :CCH_2 \, (^3B_2) + HCN \qquad \Delta H_0 = 134 \text{ kcal/mol} \qquad \text{(rxn 7)}$$
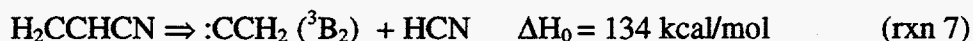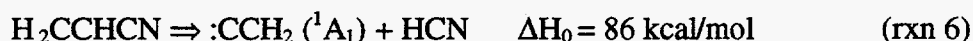
The $P(E_T)$ in figure 11 has a maximum probability at 8 kcal/mol, extends beyond 47 kcal/mol, and has a FWHM of ~20 kcal/mol. The available energy for reaction 7 is 14 kcal/mol. With only 50% of the $P(E_T)$ below 14 kcal/mol we can place an upper limit on the contribution of reaction 7 at half of the total HCN elimination based on thermodynamic arguments. The photoionization spectra for the C_2H_2 photoproducts, circles in figure 12, demonstrates a photoionization onset of 10.5±0.3 eV. The ionization potential for singlet and triplet vinylidene is not well determined. We adopt a value of 11.4 eV for the IP of singlet vinylidene based on the recommended value from Romus *et al.*[18] If we assume that the IP for triplet vinylidene is just the I.P. for singlet vinylidene suppressed by the singlet/triplet splitting energy of 2.0 eV[21] we obtain an estimate of 9.4 eV for the I.P. of triplet vinylidene. Our measured photoionization onset is 1 eV above

this estimate for the I.P. of triplet vinylidene. Considering the thermodynamic restrictions, we believe that reaction 7 is not a significant channel in HCN elimination. This is contrary to the conclusion of Fahr and Laufer who reported the dissociation to form triplet vinylidene was the major dissociation channel following VUV flash photolysis.[8]

The $P(E_T)$ is consistent with the energetics of both reactions 5 and 6. Based on linewidth analysis from negative ion photodetachment experiments, Lineberger and coworkers estimated a lifetime of 40-200 femtoseconds for singlet vinylidene.[21] Ab initio investigations have placed the isomerization barrier for singlet vinylidene to acetylene at 2-4 kcal/mol in agreement with experimental estimate of the lifetime.[19] Therefore, singlet vinylidene will isomerize to vibrationally excited acetylene prior to reaching the photoionization probe radiation (flight time is ~50 μsec), and we will detect acetylene in the case of either 1,1 or 1,2 HCN elimination. The recombination barrier for reaction 6 should be substantially smaller than the 1,2 elimination, reaction 5. We estimate the recombination barrier for reaction 6 at ~5 kcal/mol and for reaction 5 at ~50 kcal/mol based on calculations by Riehl *et al.* on the analogous HCl elimination channels in vinyl chloride.[20] However, in the case of 1,1 elimination, reaction 6, the short lifetime for singlet vinylidene means isomerization will be competitive with the rate of separation of the two photofragments. This is analogous to the elimination of HCl from vinyl chloride discussed by Gordon and coworkers.[3] With isomerization proceeding rapidly enough to leave the HCN and acetylene photoproducts in close proximity, the strong repulsion between these two closed shell molecules will give a translational kick to the photoproducts. In other

words, some fraction of the isomerization energy, ΔH_I = 43 kcal/mol[21], should be available for partitioning into relative translation. Our measure photoionization onset of 10.5±0.3 eV is 0.9 eV below the I.P. for 11.4 eV for acetylene[23], note the photoionization spectrum for acetylene cooled in a supersonic jet shown as the triangles in figure 11 for comparison. This suppression of the I.P. provides a qualitative estimate of ~21 kcal/mol of internal excitation in the acetylene photoproducts. In the case of 1,1 elimination, this suggest that only about half of the energy of isomerization, 43 kcal/mol (2 eV), went into internal excitation of the acetylene. This is consistent with the proposal of a dissociation involving a concerted isomerization allowing partitioning of some of the isomerization energy into degrees of freedom other than internal excitation of the acetylene fragment.

With $\langle E_T \rangle$ = 15 kcal/mol and an available energy of 104 kcal/mol, including the isomerization energy in the case of 1,1 HCN elimination, there is still an average of 89 kcal/mol in internal energy of the HCN and acetylene products. Using the 21 kcal/mol suppression of the acetylene photoionization onset to estimate the internal energy in the acetylene products leaves 68 kcal/mol in the HCN products indicating a partitioning of more than half of the available energy into internal excitation in the HCN photoproducts. The onset for the HCN photoionization, the major feature in figure 7, is ~11 eV. This is a red shift of 2.6 eV, 60 kcal/mol, from the I.P. of HCN = 13.6 eV[23]. The good agreement of this value with the internal energy estimated from the average translation, the available energy, and the photoionization red shift in the acetylene photoproducts, supports using

the red shift of the photoionization onset as a qualitative estimate of photofragment internal energy.

We can address the question of 1,1 vs. 1,2 HCN elimination using our measured ratio of $C_2HD/C_2H_2 = 0.60^{+0.07}_{-0.06}$ from the dissociation of 77% H_2CCDCN, 23% H_2CCHCN. We consider the two limiting cases of total H/D randomization prior to dissociation and of no H/D randomization prior to dissociation. There are three dissociation channels that can lead to the formation of either C_2HD or C_2H_2 products:

$$H_2CCDCN \Rightarrow C_2HD + HCN \qquad\qquad \text{(rxn 8)}$$

$$H_2CCDCN \Rightarrow C_2H_2 + DCN \qquad\qquad \text{(rxn 9)}$$

$$H_2CCHCN \Rightarrow C_2H_2 + HCN \qquad\qquad \text{(rxn 10)}$$

First we consider the limiting case of complete H/D atom randomization prior to dissociation. We can calculate the predicted ratio of C_2HD/C_2H_2 using equations 2 and 3. Since there is a ratio of 2:1 for H:D in the deuterated portion of the sample, reaction 8 is twice as likely as reaction 9.

$$P_{rxn8} = 2 \cdot P_{rxn9} \cdot \frac{i_{HCN}}{i_{DCN}} \qquad\qquad \text{(eqn. 2)}$$

$P_{rxn\,X}$ represents the relative probability of the given reaction and i_{HCN}/i_{DCN} is the isotope effect. We estimate the isotope effect $i_{HCN}/i_{DCN}=2.0/1.5$ based on the isotope effect for H_2 and HD elimination from ethylene.[22] The reactant composition must be conserved:

$$P_{rxn8} + P_{rxn9} = R_{H_2CCDCN} \qquad\qquad P_{rxn10} = R_{H_2CCHCN} \qquad\qquad \text{(eqn. 3)}$$

Where R represents the percent of each reactant, $R_{H2CCDCN}$ = 0.77, $R_{H2CCHCN}$ = 0.23. We assume the difference in kinematics for reactions 8-10 to be negligible and the result is a predicted ratio of C_2HD/C_2H_2 = 1.27 which is well outside the error bounds of our measured value. Therefore, we can rule out the complete randomization of H/D atoms prior to dissociation.

Assuming no randomization of H/D atoms prior to dissociation we can use

$$\frac{C_2HD}{C_2H_2} = \frac{rxn\ 8}{rxn\ 9 + rxn\ 10} = \frac{P_{12} \cdot R_{H_2CCDCN}}{\left[P_{11} \cdot \frac{i_{DCN}}{i_{HCN}} \cdot R_{H_2CCDCN} \right] + \left[(P_{11} + P_{12}) \cdot R_{H_2CCHCN} \right]} \qquad (eqn.\ 4)$$

equation 4 to calculate the ratio of 1,1/1,2 HCN elimination.

From our measured ratio of C_2HD/C_2H_2 = $0.60^{+0.07}_{-0.06}$ we obtain a ratio of P_{11}/P_{12} = 1.3±0.2. This indicates that 1,1 HCN elimination is favored by nearly 3:2 over 1,2 elimination.

Comparing our measured P(E_T) to the previous PTS experiments of Nishi *et al.*[7] we first note that the authors suggested that the m/e 27 TOF spectra were a combination of both HCN photoproducts and C_3H_3 photoproducts from CN elimination with the CN elimination channel favored by > 3:1. The authors then decomposed the P(E_T) determined from the TOF spectra into two Boltzmann components assigning the translationally colder distribution to CN elimination and the translationally hotter component to HCN elimination. Based on the quantum yield measurement of North and Hall[10] for the CN elimination of <0.01 it is clear that the TOF spectra measured by Nishi *et al.* for m/e 27

must consist almost entirely of HCN photoproducts. Therefore, the $P(E_T)$ determined from those TOF spectra is a single distribution representing HCN elimination. The $P(E_T)$ has a maximum probability at ~3 kcal/mol compared to 8 kcal/mol in our measured distribution and overall the $P(E_T)$ of Nishi _et al._ appears shifted to lower energy with respect to our measured $P(E_T)$. One possible explanation for the slower $P(E_T)$ presented by Nishi _et al_ could come from the long tails on their TOF spectra which they attributed to residual gas buildup following the pulsed molecular beam. Direct inversion of these TOF spectra to obtain translational energy distributions may have been biased toward lower energy as a result of the tail in the TOF spectra at long times. Gordon and coworkers measured the state selected $P(E_T)$ for HCl(v=0, v=1, and v=2) from vinylchloride dissociation at 193 nm using Doppler spectroscopy.[3] The shape of the distributions are very similar to our measured $P(E_T)$ from HCN elimination with a slightly higher average translational energy which is consistent with the higher available energy in the dissociation of vinylchloride of 124 kcal/mol compared to 104 kcal/mol for acrylonitrile. The agreement between the analogous HCN and HCl translational energy distributions suggests the two dissociations proceed via a very similar mechanism on the ground electronic surface.

**Molecular hydrogen elimination.** Thermodynamically there are three C_3HN isomers that can be produced from the elimination of H_2 following absorption at 193 nm (148 kcal/mol), see figure 1:

$$H_2CCHCN \Rightarrow HCCCN + H_2 \qquad \Delta H_0 = 50 \text{ kcal/mol} \qquad \text{(rxn 11)}$$

$$H_2CCHCN \Rightarrow \, ^1(:CCHCN) + H_2 \qquad \Delta H_0 \sim 90 \text{ kcal/mol} \qquad \text{(rxn 12)}$$

$$H_2CCHCN \Rightarrow \, ^3(:CCHCN) + H_2 \qquad \Delta H_0 \sim 140 \text{ kcal/mol} \qquad \text{(rxn 13)}$$
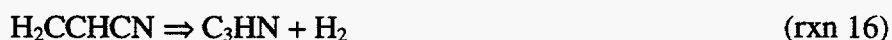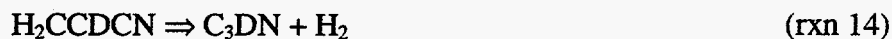
We estimate the endothermicity for dissociation to give of H_2 and singlet cyanovinyl radical, reaction 12, based on the endothermicity of the analogous H_2 elimination from ethylene and vinyl chloride.[1,20] We assume that the singlet/triplet splitting in the cyanovinyl radical is similar to the singlet/triplet splitting in vinylidene of 48 kcal/mol[21] to obtain the estimated endothermicity of reaction 13. The $P(E_T)$ for molecular hydrogen elimination is shown in figure 6. Using equation 1 the available energy following reaction 13 is ~8 kcal/mol. Since the photofragments from this channel have translational energy in excess of the energetic limit of reaction 13 it is unlikely that this reaction plays a significant role in H_2 elimination. The $P(E_T)$ is consistent with the energetics of both remaining channels. The measured distribution is quite broad, FWHM~20 kcal/mol, with a maximum probability at 18 kcal/mol and clearly reflects the presence of a large recombination barrier.

The 1,1 elimination of H_2 to give the singlet cyanovinyl radical would be expected to have a much smaller recombination barrier than 1,2 elimination to cyanoacetylene. For example Riehl *et al.* have calculated the recombination barrier for the analogous 1,1 dissociation in vinyl chloride to be about 6 kcal/mol.[20] However, they also calculate the barrier to isomerization of the chlorovinyl radical to chloroacetylene to be ~1 kcal/mol which would mean a sub-picosecond lifetime for the chlorovinyl radical. Very rapid isomerization of cyanovinyl radicals to cyanoacetylene following a 1,1 elimination of H_2

would allow the two photofragments to experience part of the strong repulsive potential between H_2 and cyanoacetylene at close proximity. As in the case of HCN elimination, this concerted isomerization/dissociation is analogous to elimination of HCl from vinyl chloride discussed by Gordon and coworkers.[3] The magnitude of the repulsive kick between H_2 and cyanoacetylene will be strongly dependent on the rate of isomerization with the result of such a concerted process being the partitioning of some of the energy of isomerization into translation of the dissociating fragments. It is also the strong repulsion between H_2 and cyanoacetylene at small distances that is responsible for the large recombination barrier in 1,2 H_2 elimination, reaction 11. We would expect a larger translational energy release from the 1,2 elimination since direct formation H_2 and cyanoacetylene will leave them closer to one another and, therefore, higher on the strongly repulsive potential energy surface. However, while we would expect a larger translational energy release from 1,2 elimination, 1,1 elimination with a concerted isomerization of the C_2HCN photofragment could generate a comparable translational energy release. As a result, the measured $P(E_T)$ in figure 6 is insufficient to address the question of the contributions to H_2 elimination from reaction 11 and 12. In the study of ethylene dissociation at 193 nm isotopically labeled reactants demonstrated a ratio of 3:2 for 1,1 vs. 1,2 H_2 elimination while the measured $P(E_T)$ was a single broad feature peaked around 20 kcal/mol. The relative heights of the recombination barriers for 1,1 and 1,2 elimination should be similar to those in acrylonitrile. This demonstrates that 1,1 elimination involving a concerted isomerization can result in a translational energy release which exceeds

expectation based on the height of the recombination barrier becoming comparable to the $P(E_T)$ for 1,2 elimination.

To further investigate whether or not this channel is the result of 1,1 H_2 elimination, 1,2 H_2 elimination, or a combination of the two we photodissociated acrylonitrile-1d and measured a ratio of $C_3DN/C_3HN = 0.60^{+0.04}_{-0.06}$ from a 77% deuterated sample. In order to address the ratio of 1,1 and 1,2 H_2 elimination we must consider the following three possible dissociation channels from the dissociation of a 77% H_2CCDCN, 23% H_2CCHCN sample:

$$H_2CCDCN \Rightarrow C_3DN + H_2 \qquad\qquad\qquad\text{(rxn 14)}$$

$$H_2CCDCN \Rightarrow C_3HN + HD \qquad\qquad\qquad\text{(rxn 15)}$$

$$H_2CCHCN \Rightarrow C_3HN + H_2 \qquad\qquad\qquad\text{(rxn 16)}$$

We now compare the two limiting cases involving complete H/D atom randomization prior to dissociation and no H/D atom randomization prior to dissociation. If complete randomization precedes dissociation we can calculate the expected product ratio using equations 5 and 6. With a ratio of H:D = 2:1 in the deuterated reactant, reaction 15 is twice as likely as reaction 14.

$$P_{rxn14} = \frac{1}{2} \cdot P_{rxn15} \cdot \frac{i_{H2}}{i_{HD}} \qquad\qquad\qquad\text{(eqn. 5)}$$

P_{rxn} x represents the relative probability of the given reaction. For the isotope effect between H_2 and HD elimination we adopt the value determined by Okabe and coworker

for the dissociation of deuterated ethylene of $i_{H2}/i_{HD} = 2.0/1.5$.[22] The authors note a reduction in the isotope effect for 1,2 elimination compared to 1,1 elimination, however the difference is small and we will assume the isotope effect to be the same in both cases. The reactant composition must be conserved.

$$P_{rxn14} + P_{rxn15} \cdot \frac{k_{rxn14}}{k_{rxn15}} = R_{H_2CCDCN} \qquad P_{rxn16} \cdot \frac{k_{rxn14}}{k_{rxn16}} = R_{H_2CCHCN} \qquad \text{(eqn. 6)}$$

Where R is the percent of each reactant, $R_{H2CCDCN} = 0.77$, $R_{H2CCHCN} = 0.23$, and k is the kinematic correction relative to reaction 14 which results from the difference in the reduced mass of the products, $k_{rxn\ 14} = 1.00$, $k_{rxn\ 15} = 0.69$, $k_{rxn\ 16} = 0.98$. The result is a predicted value of $C_3DN/C_3HN = 0.61$ assuming complete H/D atom randomization prior to dissociation. This is certainly in good agreement with with our measured ratio of $C_3DN/C_3HN = 0.60^{+0.04}_{-0.06}$. However, it is also possible that this result is simply coincidental with the ratio of 1,1/1,2 elimination in a dissociation mechanism that involves no H/D randomization prior to dissociation. In the case of HCN elimination we demonstrated that H/D randomization does not precede dissociation. Since both of these dissociation channels occur on the ground PES it is difficult to invoke a dissociation mechanism that allows H/D randomization to precede one dissociation channel and not the other. If we assume no H/D atom randomization prior to dissociation we can calculate the 1,1 to 1,2 elimination ratio from our measure C_3DN/C_3HN ratio using equation 7. In equation 7, P_{11} and P_{12} represent the probability of 1,1 and 1,2 elimination respectively.

$$\frac{C_3DN}{C_3HN} = \frac{rxn14}{rxn15 + rxn16} = \frac{P_{11} \cdot k_{rxn14} \cdot R_{H_2CCDCN}}{\left[P_{12} \cdot \frac{i_{HD}}{i_{H2}} \cdot k_{rxn15} \cdot R_{H_2CCDCN} \right] + \left[(P_{11} + P_{12}) \cdot k_{rxn16} \cdot R_{H_2CCHCN} \right]} (eqn.7)$$

Using equation 7 we obtain a ratio of P_{11}/P_{12} = 0.59 ± 0.05 assuming no H/D randomization prior to dissociation. This would suggest a much greater preference for 1,2 elimination compared to P_{11}/P_{12} = 1.5 determined for ethylene.[1]

The photoionization spectrum for C_3HN photoproducts, triangles in figure 4, has a photoionization onset of 10.8±0.3 eV. With such a short lifetime for any cyanovinyl radicals in comparison to the photofragment flight time, ~50 μsec, isomerization to cyanoacetylene will occur before the photoproducts reach the photoionization region. Therefore, in the case of either 1,1 or 1,2 H_2 elimination cyanoacetylene will be detected as the final product. The photoionization onset for cyanoacetylene is red shifted from its I.P. of 11.6 eV[23]. The red shift of the photoionization onset provides a qualitative indication of the internal energy in the cyanoacetylene photoproducts. If the red shift of 0.8 eV can be associated with the internal energy it would appear that even in the case of 1,1 H_2 elimination, reaction 12, only about half of the isomerization energy from the cyanovinyl radical to cyanoacetylene, ΔH_I~2 eV[21], is partitioned into internal energy of the cyanoacetylene product on average. As mentioned above the 1,2 elimination would be expected to have a larger translational energy release then 1,1 elimination, however with $<E_T>$=23 kcal/mol in figure 6 there is still ~75 kcal/mol of available energy on average to be partitioned into internal energy of the H_2 and cyanoacetylene. Using 0.8 eV (18

kcal/mol) as a qualitative estimate of the internal energy content in cyanoacetylene leaves over half of the available energy partitioned into internal excitation of the H_2 products on average, ~56 kcal/mol.

5. Conclusion

Using the technique of photofragment translational spectroscopy with VUV photoionization of the products we have identified four dissociation channels following absorption at 193 nm, reactions 1-4. All four dissociation channels are consistent with internal conversion to the ground electronic surface following the initially excited $\pi\pi^*$ state. The elimination of HCN involves both 1,1 and 1,2 HCN elimination with 1,1 elimination favored by a ratio of ~3:2. The 1,1 elimination proceeds to give singlet vinylidene in a dissociation that involves concerted isomerization to acetylene analogous to HCl elimination from vinyl chloride. The isomerization proceeds on the time scale of photofragment separation allowing some portion of the isomerization energy to be partitioned into degrees of freedom other than internal energy of the acetylene product. For both 1,1 and 1,2 HCN elimination there is a very large fraction of the available energy, >50%, partitioned into internal energy of the HCN photoproduct. In the case of H_2 elimination, if we assume no H/D randomization prior to dissociation, we find the 1,2 elimination channel to be favored over the 1,1 elimination channel by ~ 2:1. Akin to the 1,1 HCN elimination, 1,1 H_2 elimination appears to result in formation of the singlet

cyanovinyl radical with rapid isomerization to cyanoacetylene. The concerted isomerization/dissociation again allows the energy of isomerization to be partitioned into all of the available degrees of freedom. Analogous to the HCN elimination, over 50% of the available energy is partitioned into internal degrees of freedom in the H_2 product. Atomic hydrogen elimination also exhibits a $P(E_T)$ which is consistent with statistical simple bond rupture. The distribution maximum is shifted to slightly higher energy than the prediction of a prior distribution, which may indicate the presence of a small recombination barrier. The radical CN elimination channel accounts for a very small fraction of the dissociation, <1%. The measured translational energy release is similar to the statistical prediction of a prior distribution indicating a barrierless dissociation on the ground electronic surface. These results for the CN elimination channel are in excellent agreement with the recent Doppler measurements of North and Hall.

Table 1. Summary of translational energy release from the four observed dissociation channels. All values are in kcal/mol. Thermodynamic values were taken from reference 23 and available energies were calculated using equation 1.

Reaction Channel	ΔH_0	E_{avail} at 193 nm	$<E_T>$	$<E_T> / E_{avail}$
$H_2CCHCN \rightarrow H + H_2CCCN$	~108	~40	na	na
$H_2CCHCN \rightarrow CN + H_2CCH$	131	17	2.4	14
$H_2CCHCN \rightarrow H_2 + HCCCN$	50	97	23	24
$H_2CCHCN \rightarrow HCN + HCCH$	43.0	104.4	15	14

References

[1] B. A. Balko, J. Zhang, and Y. T. Lee, *J. Chem. Phys.* **97**, 935 (1992) *and references therein;* E. F. Cromwell, A. Stolow, M. J. J. Vrakking, and Y. T. Lee, *J. Chem. Phys.* **97**, 4029 (1992).

[2] A. Fahr and A. H. Laufer, *J. Photochem.* **34**, 261 (1989).

[3] M. J. Berry, *J. Chem. Phys.* **61**, 3114 (1974); Y. Huang, Y. Yang, G. He, S. Hashimoto, and R. J. Gordon, *J. Chem. Phys.* **103**, 5476 (1995) *and references therin.*

[4] M. Umemoto, K. Seki, H. Shinohara, U. Nagashima, M. Kinoshita, and R. Shimada, *J. Chem. Phys.* **83**, 1657 (1985).

[5] P. A. Mullen and M. K. Orloff, Theoret. *Chim. Acta* **23**, 278 (1971).

[6] A. Gandini and P. A. Hackett, *Can. J. Chem.* **56**, 2069 (1978).

[7] N. Nishi, H. Shinohara, and I. Hanazaki, *J. Chem. Phys.* **77**, 246 (1982).

[8] A. Fahr and A. H. Laufer, *J. Phys. Chem.* **96**, 4217 (1992).

[9] C. A. Bird and D. J. Donaldson, *Chem. Phys. Lett.* **249**, 40 (1996).

[10] S. W. North and G. E. Hall, *Chem. Phys. Lett.* **263**, 148 (1996).

[11] D. A. Blank, S. W. North, D. Stranges, A. G. Suits, and Y. T. Lee, *J. Chem. Phys.* **106**, 539 (1997).

[12] L. J. Mathias and R. F. Colletti, *Macromolecules* **21**, 857 (1988).

[13] At 273 K acrylonitrile will contain an average of 0.9 kcal/mol in rotation and 0.8 kcal/mol in vibration and the acrylonitrile reactant will experience substantial cooling upon supersonic expansion.

[14] R. D. Levine and R. B. Bernstein, _Acc. Chem. Res._ **7**, 393 (1974); J. T. Muckerman, _J. Phys. Chem._ **93**, 179 (1989).

[15] Y. Mo, K. Tonokura, Y. Matsumi, M. Kawasaki, T. Sato, T. Arikawa, P. T. A. Reilly, Y. Xie, Y. Yang, Y. Huang, and R. J. Gordon, _J. Chem. Phys._ **97**, 4815 (1992).

[16] See Chapter 4 of this thesis.

[17] G. E. Busch and K.R. Wilson, _J. Chem. Phys._ **56**, 3626 (1972).

[18] P. Romus, P. Botschwina, and J. P. Maier, _Chem. Phys. Lett._ **84**, 71 (1981).

[19] T. Carrington, L. M. Hubbard, H. F. Schaefer III, and W. H. Miller, _J. Chem. Phys._ **80**, 4347 (1984); M. M. Gallo, T. P. Hamilton, and H. F. Schaefer III, _J. Am. Chem. Soc._ **112**, 8714 (1990).

[20] J. Riehl and K. Morokuma, _J. Chem. Phys._ **100**, 8976 (1994).

[21] K. M. Ervin, J. Ho, and W. C. Lineberger, _J. Chem. Phys._ **91**, 5974 (1989).

[22] H. Okabe and J. R. McNesby, _J. Chem. Phys._ **36**, 601 (1962).

[23] Handbook of Chemistry and Physics, D. R. Lide (CRC, Boca Raton, 1995).

Figure Captions

Figure 1: The relative energy of possible dissociation channels from acrylonitrile following absorption at 193 nm. The origin of the thermodynamic values are in reference 23.

Figure 2: TOF spectra for m/e 52 ($C_3H_2N^+$) photoproducts at source angles of 5° and 7.5° and a photoionization energy of 14.0 eV. The solid line is the forward convolution fit using the $P(E_T)$ shown as the solid line in figure 3.

Figure 3: The solid line is the $P(E_T)$ used to fit the TOF spectra in figure 2 for hydrogen atom elimination, $C_3H_3N \Rightarrow H + C_3H_2N$. The dotted line is the calculated prior distribution given an available energy of 40 kcal/mol for comparison.

Figure 4: The circles are the photionization spectrum for the m/e 52 ($C_3H_2N^+$) photoproducts from hydrogen atom elimination, $C_3H_3N \Rightarrow H + C_3H_2N$, at a source angle of 7.5°. The triangles are the photionization spectrum for the m/e 51 (C_3HN^+) photoproducts from molecular hydrogen elimination, $C_3H_3N \Rightarrow H_2 + C_3HN$, at a source angle of 10°.

Figure 5:   TOF spectra for m/e 51 (C_3HN^+) photoproducts at source angle of 7.5° and a

photoionization energies of 14.0 eV and 12.0 eV and at a source angle of

10° with a photoionization energy of 12.0 eV. The dotted line representing

the larger contribution to the fits is the forward convolution fit using the

$P(E_T)$ shown in figure 6 for molecular hydrogen elimination, $C_3H_3N \Rightarrow H_2 +$

C_3HN. The dotted line representing the smaller contribution to the fit is the

result of dissociative ionization of C_3H_2N photoproducts resulting from

hydrogen atom elimination, $C_3H_3N \Rightarrow H + C_3H_2N$, and was fitted with the

$P(E_T)$ in figure 3. The solid line is the total forward convolution fit to the

data.

Figure 6:   The $P(E_T)$ for molecular hydrogen elimination, $C_3H_3N \Rightarrow H_2 + C_3HN$, used

for the forward convolution fits to the TOF spectra in figure 5.

Figure 7:   The photoionization spectrum for m/e 27 photoproducts at a source angle of

15°. The major component with an onset ~11 eV is from HCN

photoproducts, $C_3H_3N \Rightarrow HCN + C_2H_2$, and the small shoulder with an onset

at 8.5 eV is from vinyl radical photoproducts generated by CN elimination,

$C_3H_3N \Rightarrow CN + C_2H_3$.

Figure 8:   TOF spectra for m/e 27 photoproducts at a source angle of 20° and

photoionization energies of 10.0 eV, solid line, and 15.0 eV, dashed line. The

TOF spectrum at 10.0 eV represents vinyl radical products from CN

elimination and the spectrum at 15.0 eV is dominated by HCN

photoproducts, see text. The two TOF spectra have been arbitrarily scaled

together, however the TOF spectrum at 10.0 eV has a corrected signal

intensity <1% of the TOF spectrum at 15.0 eV.

Figure 9:   TOF spectra for m/e 27 at source angles of 30° and 50° and a photoionization

energy of 15.0 eV. The solid line is the forward convolution fit for HCN

elimination, $C_3H_3N \Rightarrow HCN(m/e\ 27) + C_2H_2(m/e\ 26)$, using the $P(E_T)$ in

figure 11.

Figure 10:   TOF spectra for m/e 26 at source angles of 30° and 50° and a photoionization

energy of 15.0 eV. The solid line is the forward convolution fit for HCN

elimination, $C_3H_3N \Rightarrow HCN(m/e\ 27) + C_2H_2(m/e\ 26)$, using the $P(E_T)$ in

figure 11.

Figure 11:   The $P(E_T)$ for HCN elimination, $C_3H_3N \Rightarrow HCN + C_2H_2$, used for the

forward convolution fits to the TOF spectra in figures 9 and 10.

Figure 12: The circles are the photoionization spectrum for m/e 26 photoproducts at a source angle of 15°. The triangles are the photoionization spectrum for a molecular beam of acetylene.

Figure 13: TOF spectra for m/e 27 at source angles of 10° and 20° and a photoionization energy of 10.0 eV. The solid line is the forward convolution fit for CN elimination, $C_3H_3N \Rightarrow CN(m/e\ 26) + C_2H_3(m/e\ 27)$, using the $P(E_T)$ represented by the solid line in figure 14. Note that 10.0 eV is below the I.P. for HCN thereby descriminating against the HCN elimination channel at m/e 27.

Figure 14: The solid line is the $P(E_T)$ for CN elimination, $C_3H_3N \Rightarrow CN + C_2H_3$, used for the forward convolution fits to the TOF spectra in figure 13. The dashed line is the $P(E_T)$ for CN elimination determined by Doppler spectroscopy by North et al.. The dash-dot-dash line is the calculated prior distribution assuming 18 kcal/mol of available energy.
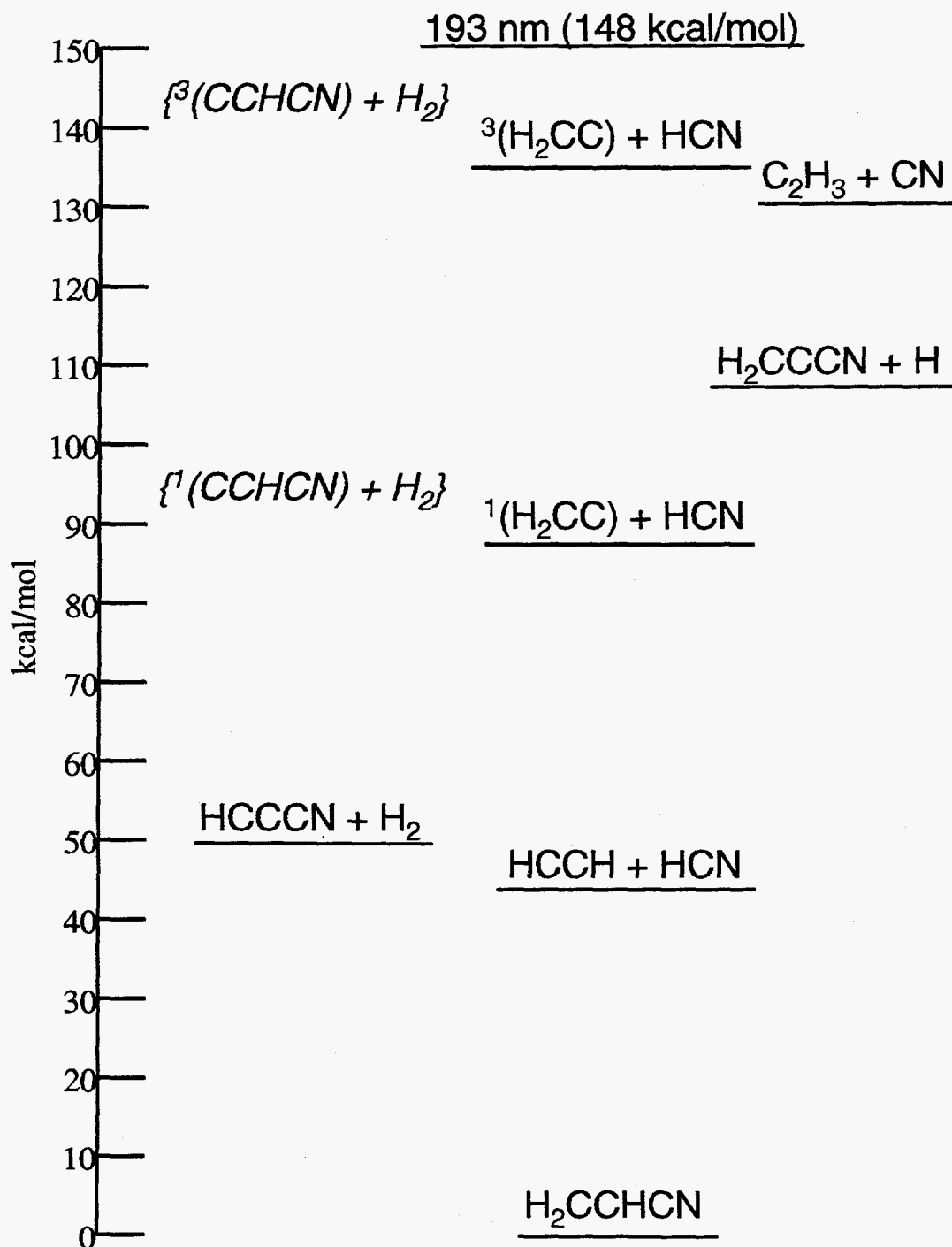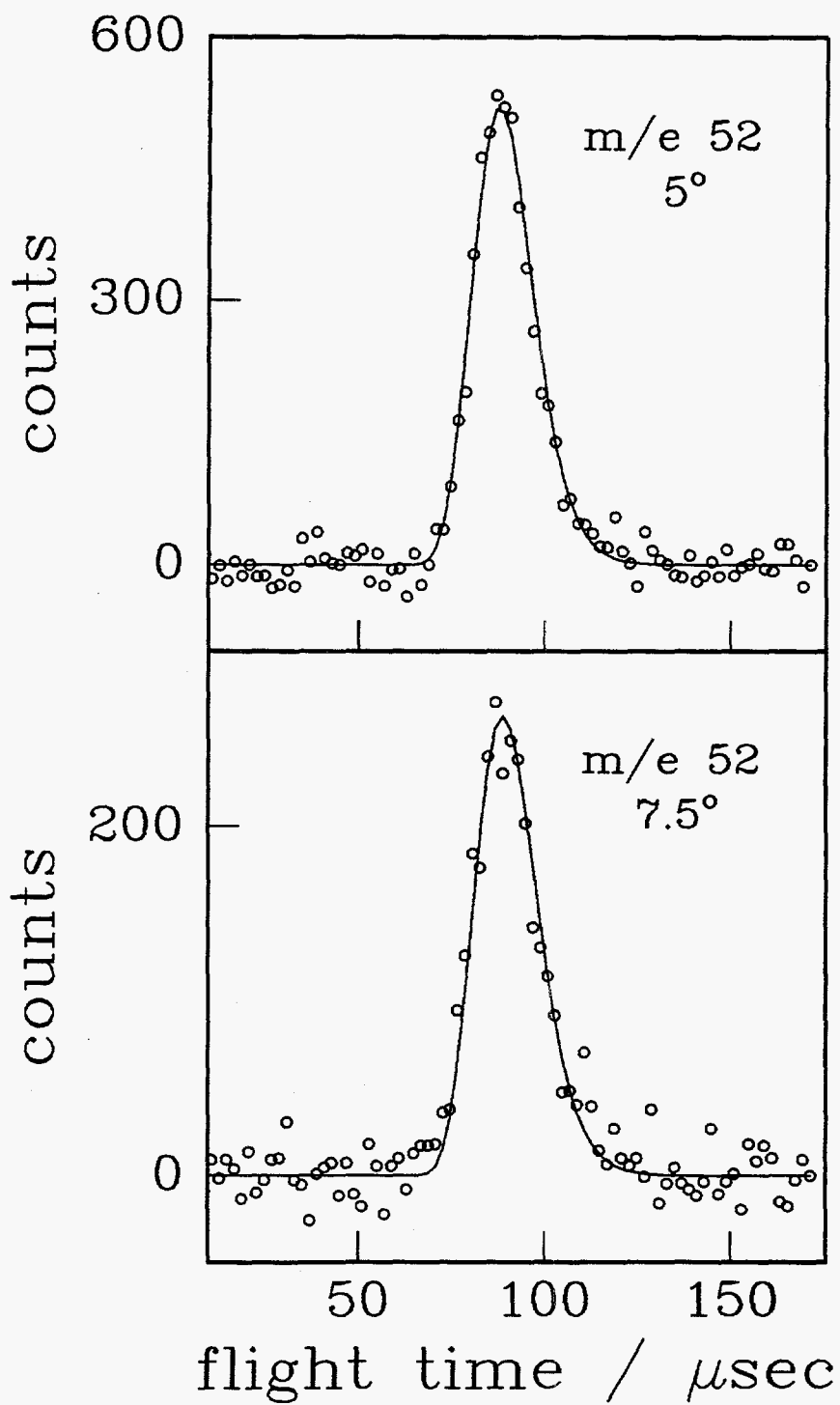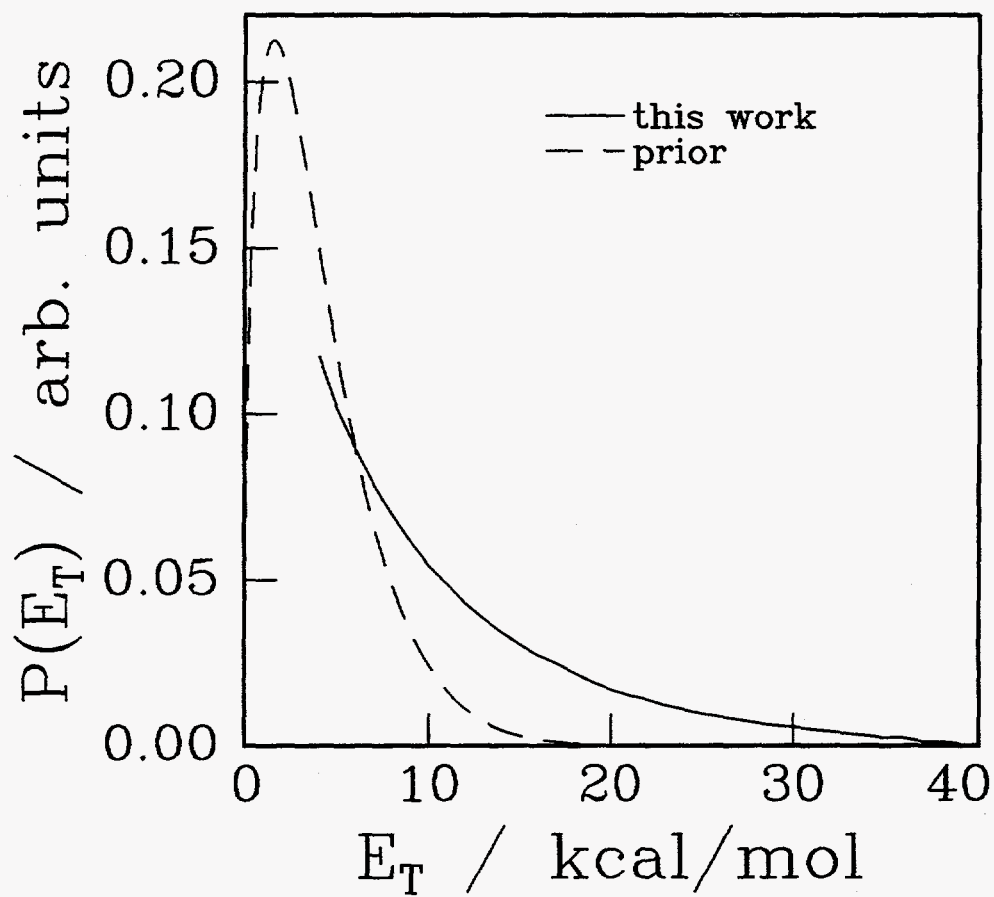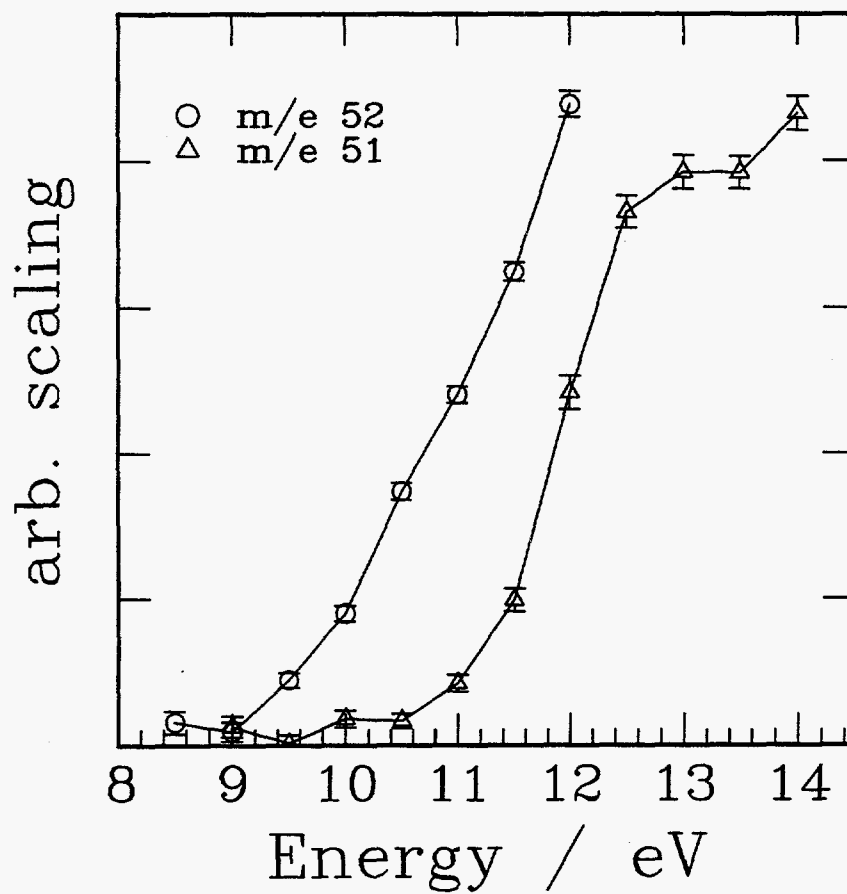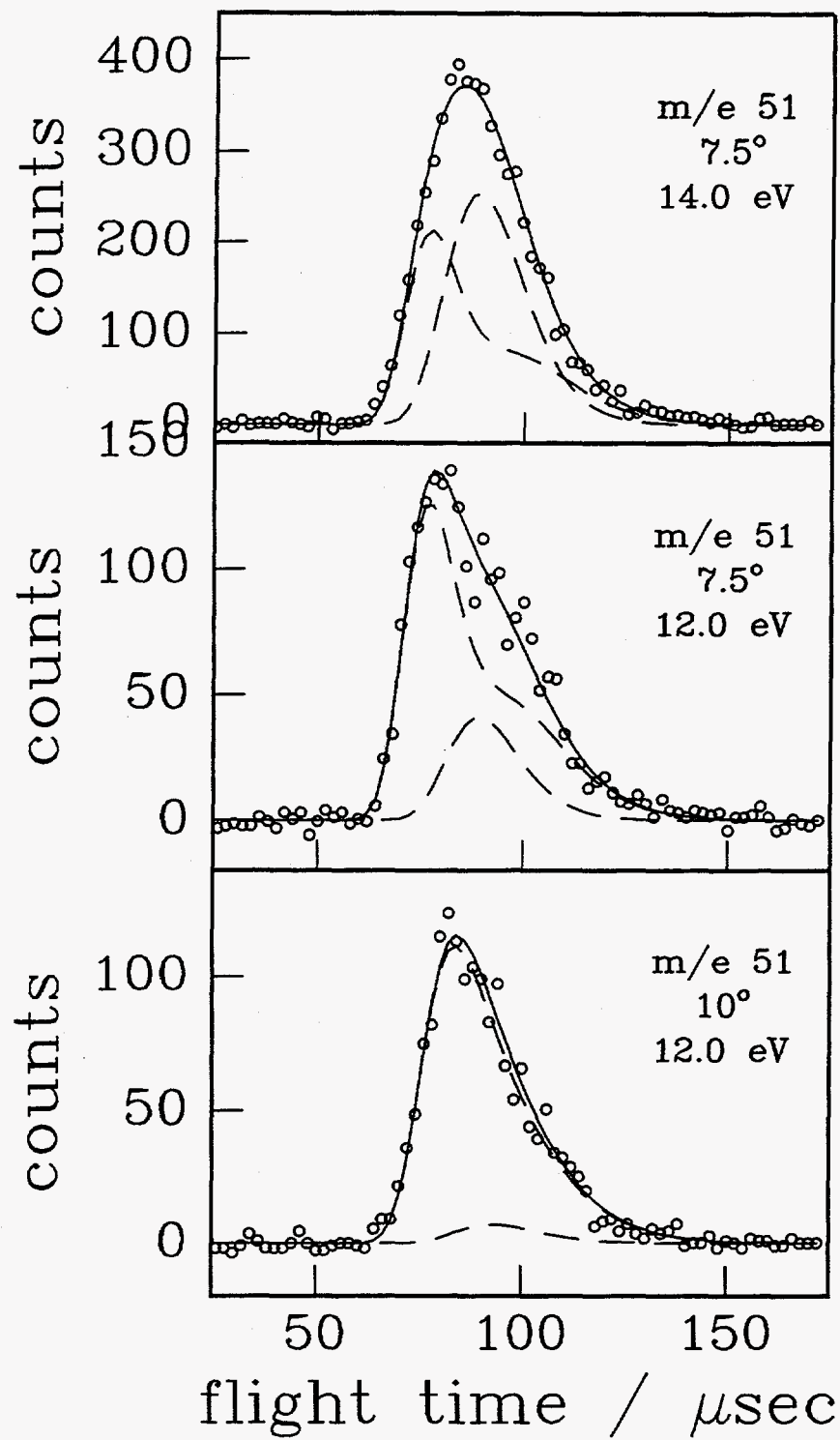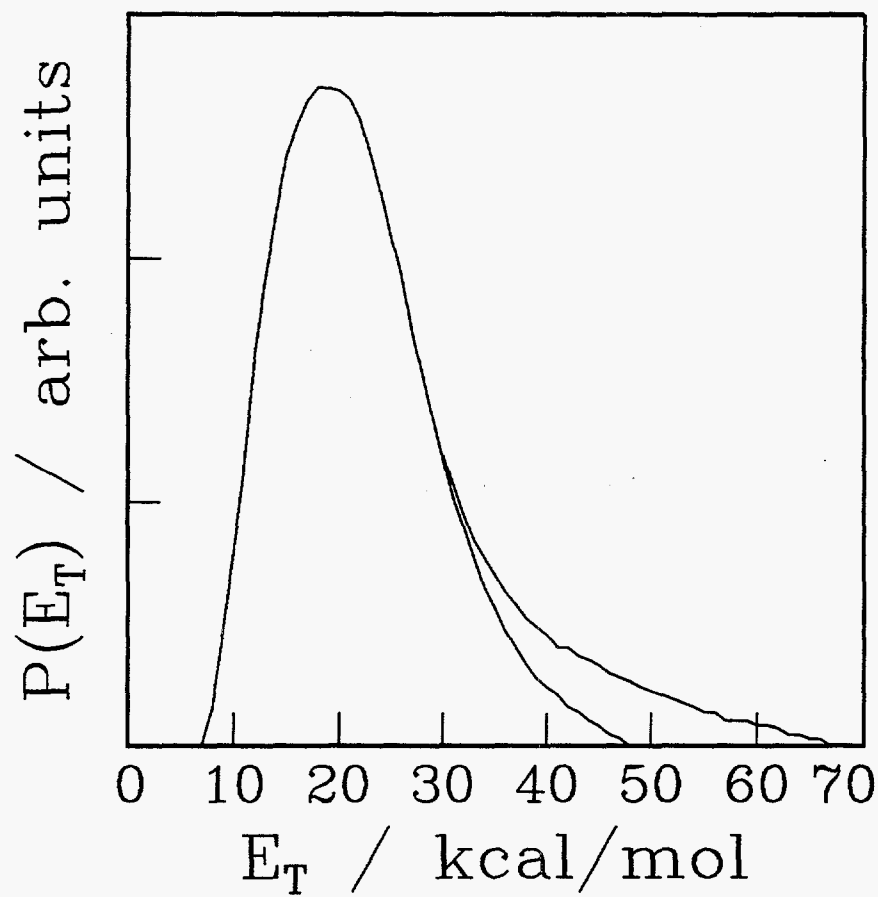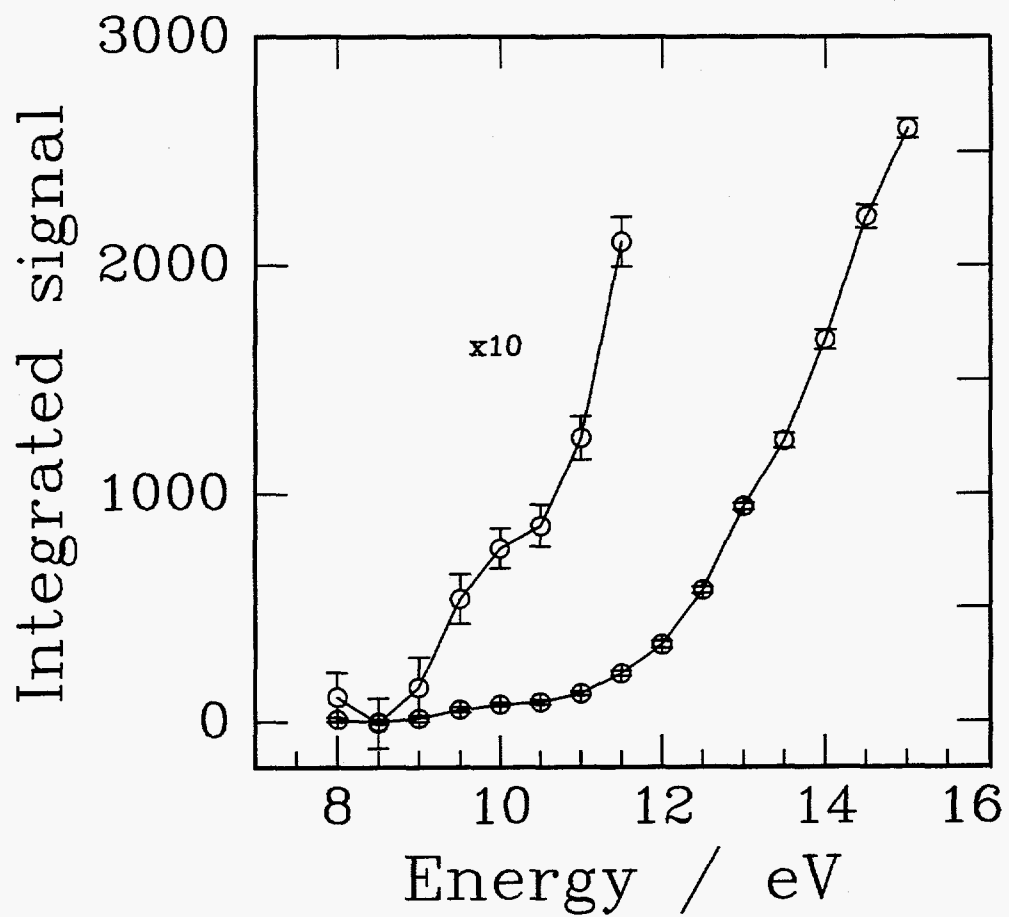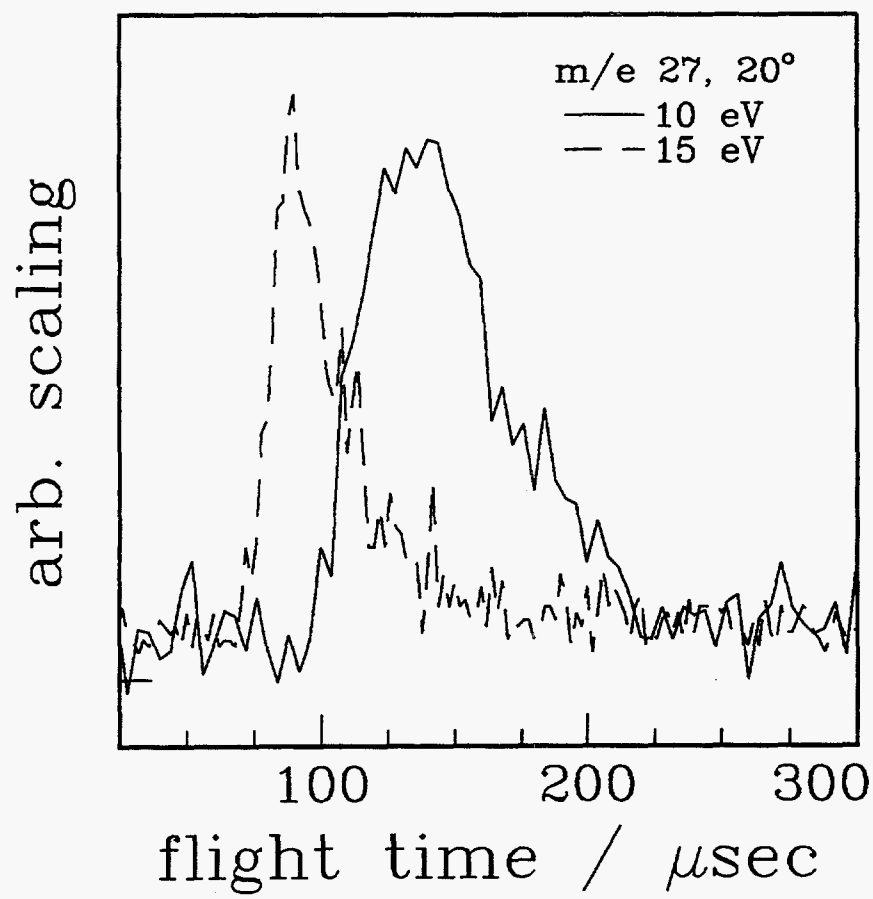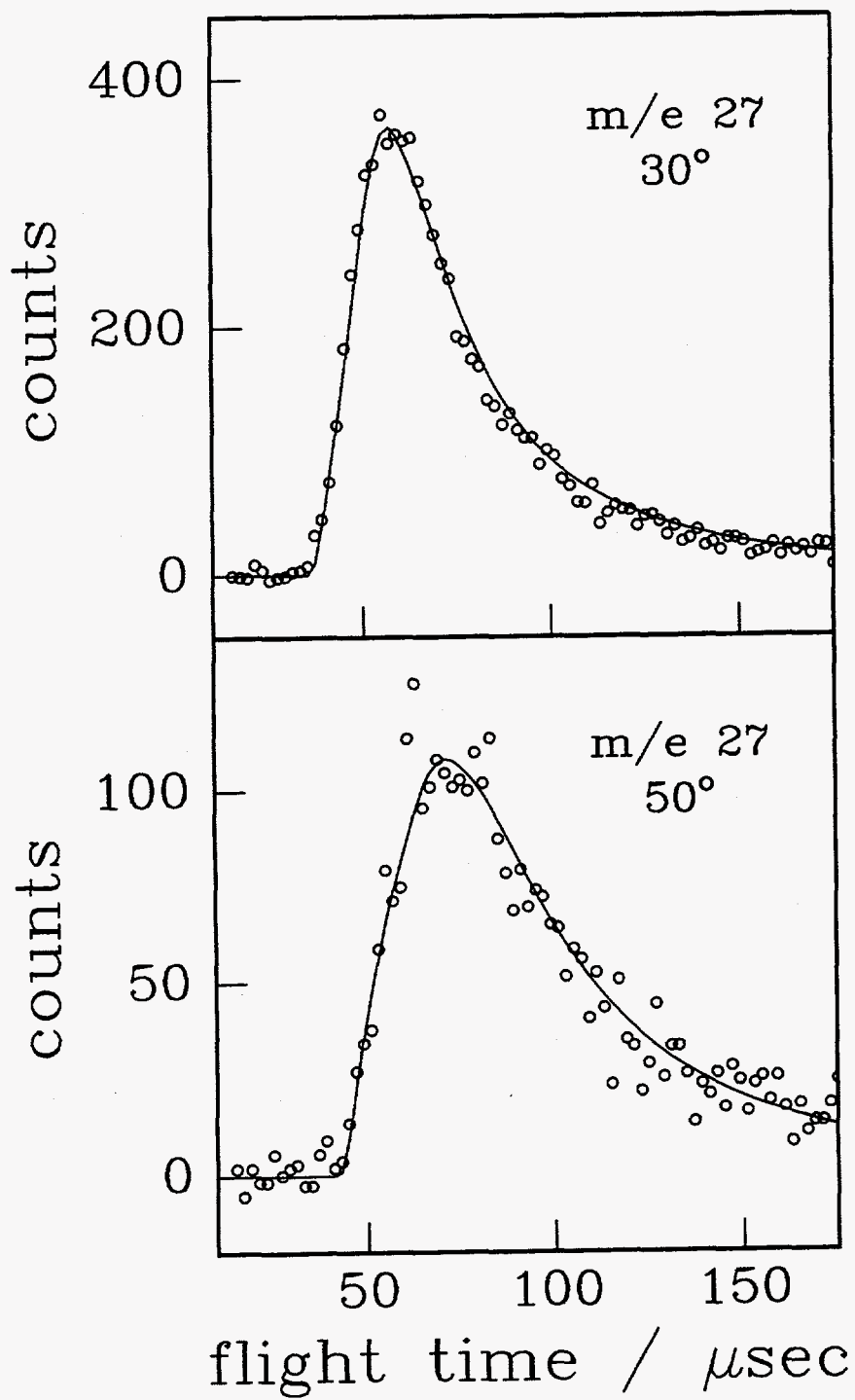
figure 1

figure 2
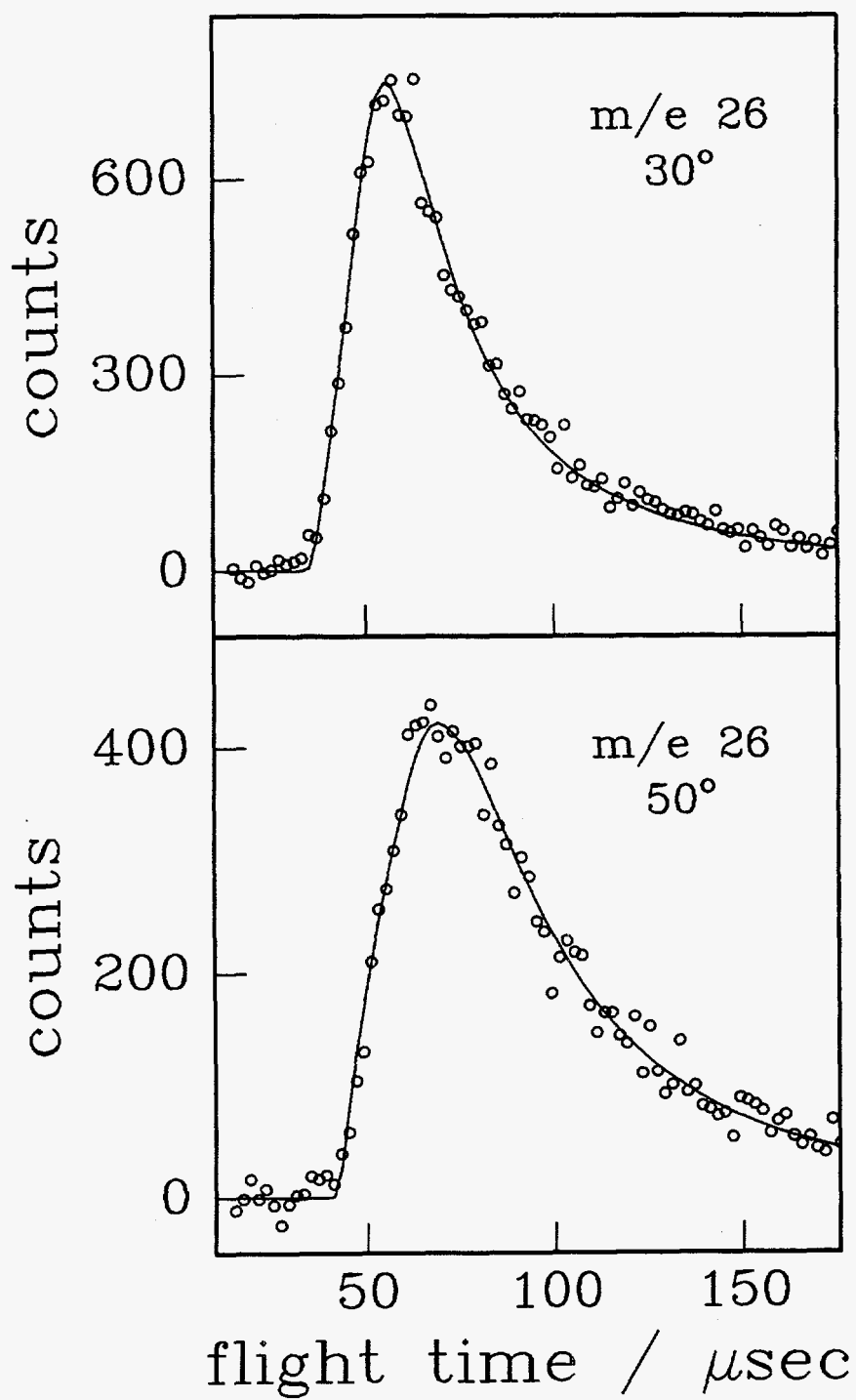
figure 3

figure 4

figure 5

figure 6

figure 7

figure 8
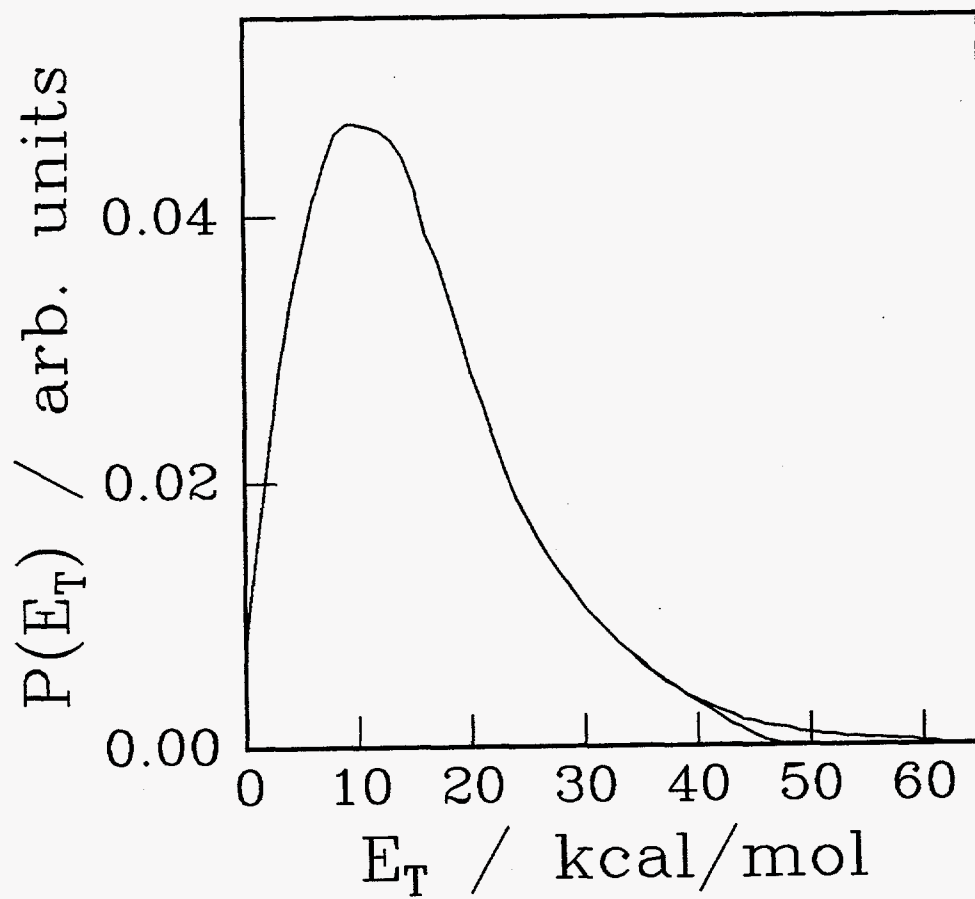
figure 9
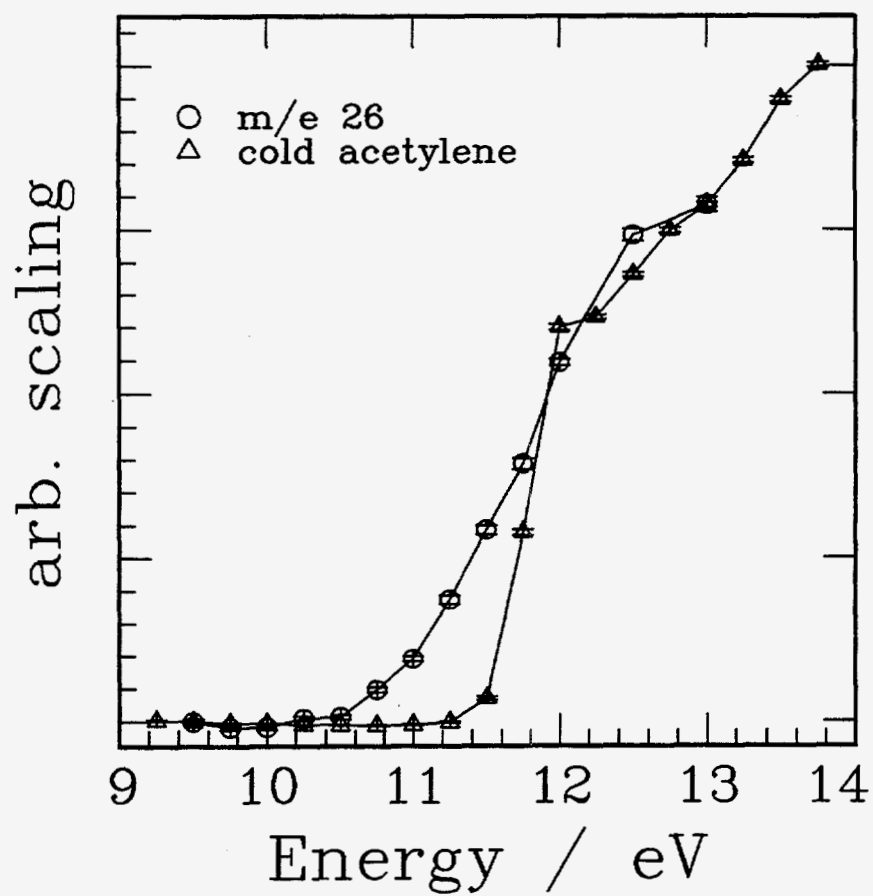
figure 10
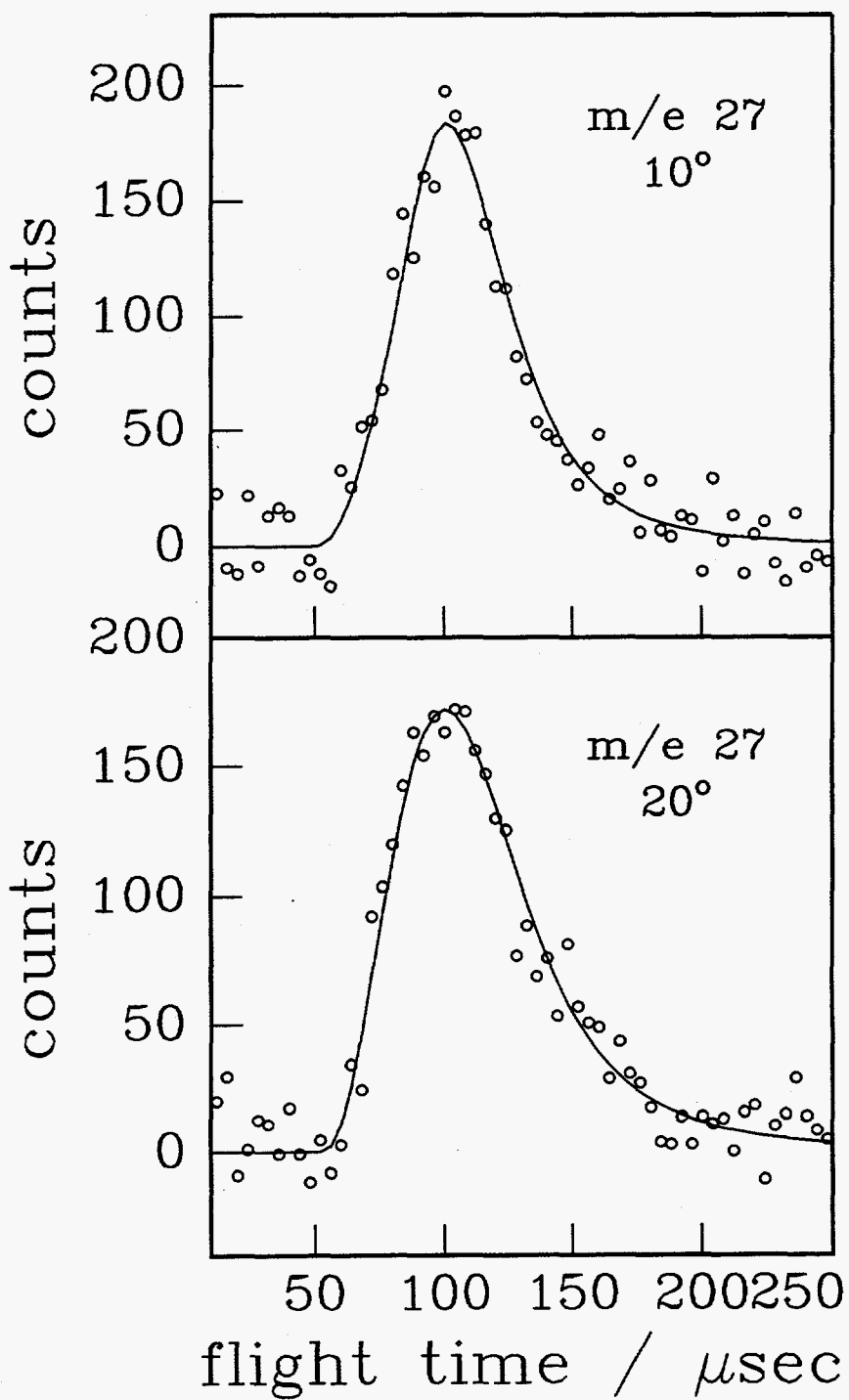
figure 11
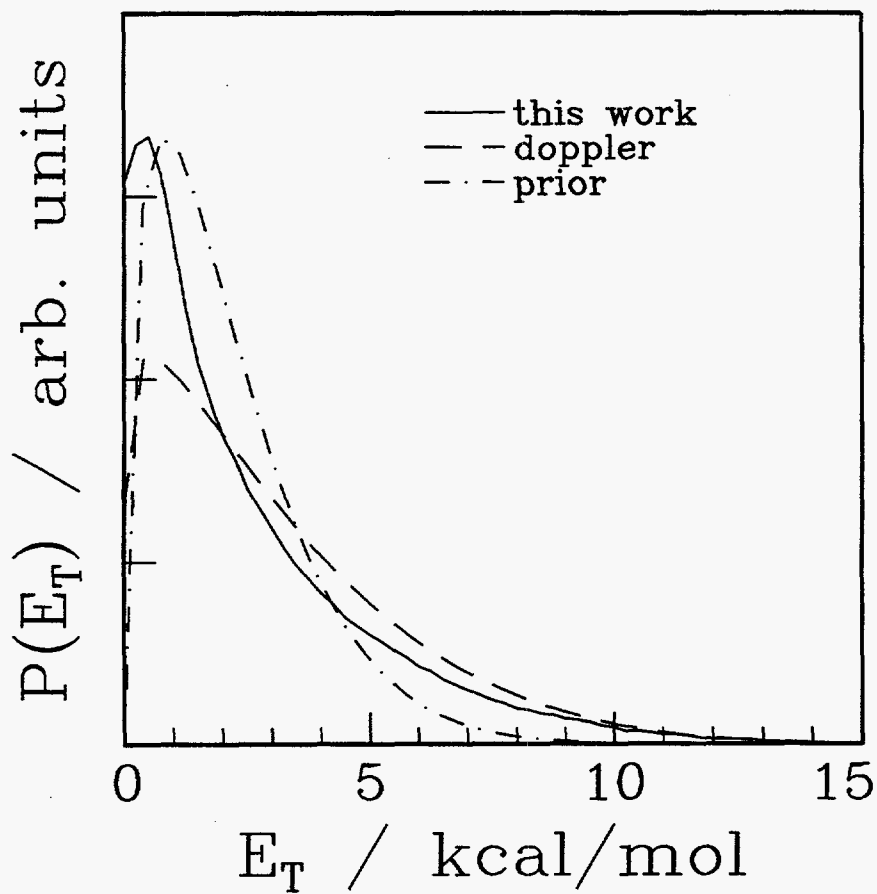
figure 12

figure 13

figure 14

Chapter 4

Photodissociation of Vinyl Chloride at 193 nm

Abstract

We have investigated the photodissociation of vinyl chloride (H_2CCHCl) at 193 nm using the technique of photofragment translational spectroscopy. The experiments were performed at the Chemical Dynamics Beamline at the Advanced Light Source and used vacuum ultraviolet synchrotron radiation for product photoionization. We have observed five primary dissociation channels following the initial $\pi^* \leftarrow \pi$ excitation. With the exception of a translationally hot atomic chlorine elimination channel, the dissociation channels are consistent with competition on the ground electronic surface following internal conversion from the initially excited $\pi\pi^*$ surface. These channels include atomic and molecular hydrogen elimination, HCl elimination, and a translationally slow Cl elimination channel. We have also observed two secondary decomposition channels which involve elimination of Cl from chlorovinyl radicals following the primary atomic hydrogen elimination channel and hydrogen atom elimination from vinyl radicals following the primary atomic Cl elimination on the ground electronic surface. By measuring the truncation in the translational energy distribution for C_2H_2Cl products from primary atomic hydrogen elimination we have made a direct measurement of the barrier for Cl +

acetylene of 11 ± 2 kcal/mol. And finally, we report the photoionization spectrum for the vinyl radical between 7 eV and 10 eV.

1. Introduction

The ultraviolet photodissociation of chloroethylenes has received considerable attention. The ultraviolet absorption in these molecules is characterized by a strong band around 190 nm that is the result of a $\pi^* \leftarrow \pi$ transition. The previous investigations have concentrated on the major dissociation channels involving HCl elimination and atomic chlorine elimination. Broad band photolysis in photochemical laser studies found that the HCl products were highly vibrationally excited following photolysis at wavelengths $\lambda > 155$ nm.[1] Berry invoked a dissociation model where the potential energy of the dissociation barrier was localized in HCl product vibration with the rest of the available energy partitioned among the remaining degrees of freedom. Based on a comparison of HCl yields from vinyl chloride and vinyl chloride-1d Berry also concluded that the elimination of HCl in chloroethylenes predominantly occurs via 1,2 elimination. Using FTIR emission spectroscopy Donaldson and Leone measured HCl vibrational distributions that were very similar to the photochemical laser measurements following photolysis at 193 nm.[2] The authors demonstrated good agreement with their results using a dissociation model involving a statistical partitioning of the available energy near the transition state. Infrared emission spectroscopy following 193 nm dissociation by Moss *et al.* found substantial

vibrational excitation in the acetylene/chloroacetylene partner fragments and a high degree of rotational excitation in the HCl products.[3]

Umemoto *et al.* used photofragment translational spectroscopy (PTS) to investigate both the HCl and Cl elimination channels in chloroethylenes following absorption at 193 nm.[4] The translational energy distribution for HCl photoproducts were non-statistical with maximum probability at 5-10 kcal/mol. The distributions converged to energies representing about half of the available energy, which the authors discussed in the context of localized available energy analogous to the model employed by Berry.[1] The nearly isotropic angular distribution of the HCl photofragments indicated internal conversion from the initially excited $\pi\pi^*$ electronic surface prior to dissociation. Translational energy distributions from atomic chlorine elimination in the dichlorothylenes were clearly bimodal consisting of a contribution from fast Cl fragments and from a slow Cl fragment channel. The Cl elimination from vinyl chloride appeared to be dominated by the fast Cl fragment elimination channel. The measured anisotropy for the fast Cl elimination channel indicated a prompt dissociation on the time scale of rotation. The authors suggested that the fast Cl elimination was the result of crossing from the initially excited $\pi\pi^*$ PES to the low lying $n\sigma^*_{(C-Cl)}$ PES followed by direct dissociation. The slow Cl channel was suggested to result from internal conversion (IC) followed by dissociation on the ground PES. The competition between IC and dissociation on the $n\sigma^*_{(C-Cl)}$ surface was quantitatively reflected in the measured ratio of ~1.1 for HCl:Cl product yields from the dissociation of vinyl chloride.

More recently, Suzuki *et al.* have used the technique of photofragment ion imaging to investigate the Cl elimination channel in the photodissociation of trans-dichloroethylene at 193 nm, 210 nm, and 235 nm.[5] The authors obtained state-resolved speed and angular distributions for the Cl photofragments. The translational energy distributions were bimodal and when averaged over the two spin orbit states of the Cl fragments were in agreement with the earlier results of Umemoto *et al.* The ratio of the fast Cl to slow Cl fragment channels was found to vary with wavelength with enhancement of the fast Cl fragment component at longer wavelengths. This result was interpreted based on the effect of C=C twist in the initial excitation on the competition between IC and crossing to the $n\sigma^*_{(C-Cl)}$ dissociative surface. While the ratio of the fast fragment Cl elimination channel to the slow Cl fragment elimination channel was found to be very similar for $Cl(^2P_{1/2})$ and $Cl(^2P_{3/2})$, the authors did mention results from cis-dichloroethylene which demonstrated significant enhancement of the fast Cl fragment channel for $Cl(^2P_{1/2})$ compared to $Cl(^2P_{3/2})$.

In an extensive set of investigations, Gordon and coworkers have used Doppler spectroscopy to obtain state-resolved translational energy distributions for the dissociation of chloroethylenes at 193 nm.[6] The authors measured Doppler profiles for hydrogen atom photoproducts which were consistent with Boltzmann distributions containing 25%-33% of the available energy. They also measured nacent rotational state distributions for H_2 photoproducts in the first 5 vibrational levels and extracted average translational energy releases for a couple of the rovibrational states. The main focus of the investigations was the Cl and HCl elimination channels from vinyl chloride. The state resolved translational

energy distributions for HCl elimination from vinyl chloride were consistent with the state averaged measurement of Umemoto _et al._ The observed rotational distribution for HCl (v=0) was biexponential while the distributions for HCl (v>0) were well represented by a single Boltzmann temperature. The authors measured a yield of HCl from vinyl chloride-1d that was 25% of the yield from vinyl chloride suggesting a preference for 1,1 HCl elimination over 1,2 HCl elimination. However, this was complicated by the fact the measured internal state distribution for HCl from both vinyl chloride and vinyl chloride-1d were identical. To explain the data the authors invoked a dissociation model involving exclusive 1,1 HCl elimination with isomerization of the vinylidene fragment to acetylene on the timescale of fragment separation. The HCl yield from vinyl chloride-1d was explained by partial H atom randomization prior to dissociation, and the HCl rotational distributions were discussed in the context of HCl vibrational adiabaticity. The Cl elimination channel demonstrated a bimodal translational energy distribution in accordance with previous studies. The $Cl(^2P_{1/2})$ photofragments were found to account for a greater fraction of the Cl products produced from the excited state dissociation compared with the ground PES dissociation channel which was explained by adiabatic correlation with partial spin-orbit scrambling in the asymptotic region.

The most recent experimental investigation on chloroethylenes is the PTS study of the photodissociation of three dichloroethylenes and trichloroethylene at 193 nm and 157 nm by Sato _et al._[7] At 193 nm they measured $P(E_T)$'s for primary HCl and Cl elimination that were in good agreement with previous measurement by Gordon and coworkers[6] and Suzuki _et al._[5] In addition, they found it necessary to invoke the secondary decomposition

of the chlorovinyl radical intermediates in order obtain satisfactory fits to the Cl^+ and

$C_2H_2^+$ TOF data. The $P(E_T)$ for secondary C-Cl bond cleavage required to fit the data was

found to be peaked away from zero in all of the systems studied which the authors

interpreted this as the result of a substantial centrifugal barrier and not the result of a

barrier on the dissociating electronic PES.

Reihl and Morokuma have investigated the dissociation of vinyl chloride using *ab*

initio molecular orbital methods.[8] HCl elimination was found to have the lowest barrier to

dissociation on the ground PES with 1,1 HCl elimination favored over 1,2 elimination

based on a lower dissociation barrier in agreement with experimental observation.[6] The

barrier to H atom migration was determined to be just below the 1,1 HCl elimination

barrier which suggests H atom scrambling may precede dissociation. The authors also

concluded that 1,1 HCl elimination would be favored over the loss of H_2 since the barrier

to H_2 elimination lies ~30 kcal/mol above the barrier to 1,1 HCl elimination. In the case of

both H_2 and HCl elimination the vinylidene/chlorovinylidene product formed following 1,1

elimination was calculated to have a very small barrier to H atom migration indicating very

rapid isomerization to acetylene/chloroacetylene. The calculated endothermicity of atomic

H and Cl elimination was close to the barrier for 1,1 H_2 elimination. Elimination of an H

atom from the β carbon was determined to be favored over loss from the α carbon in

accordance with the results of Gordon and coworkers.[6]

In this investigation we have used the technique of photofragment translational

spectroscopy with tunable vacuum ultraviolet product photoionization to study the

dissociation of vinyl chloride at 193 nm. Figure 1 shows the thermodynamically available

product channels for vinyl chloride following absorption at 193 nm. We have measured

state averaged center of mass (c.m.) translational energy distributions ($P(E_T)$'s) for the

primary HCl, Cl, and H_2 elimination channels at substantially higher resolution than

previously reported. We also report the first direct measurements of the secondary

decomposition of both vinyl radical and chlorovinyl radical primary dissociation products

from the photodissociation of vinyl chloride. The secondary decomposition of primary

vinyl radical photoproducts is evident through comparison of the measured $P(E_T)$ for the

Cl and momentum matched vinyl radical fragments. Secondary decomposition of the

chlorovinyl radicals exhibits itself as an abrupt truncation in the measured $P(E_T)$ for

chlorovinyl radicals. The truncation provides a direct measurement for the barrier to the

addition of atomic chlorine to acetylene. And finally we report the photoionization

spectrum for the vinyl radical photoproduct between 7 eV and 10 eV.

2. Experimental

These experiments were performed at the Chemical Dynamics Beamline at the

Advanced Light Source (ALS) at Lawrence Berkeley National Laboratory. A complete

description of the experimental apparatus and setup is provided in Chapter 1 of this thesis.

We present here only the details specific to this experiment. A continuous molecular beam

of 4.5% vinyl chloride in helium was generated by expanding 100 torr of the gas mixture

through a 0.125 mm nozzle into a source chamber maintained at 8×10^{-4} torr. The velocity

distribution of the resulting molecular beam was determined by chopping the beam with a slotted mechanical wheel. The beam had a maximum probability at 1270 m/s with a FWHM of 10%. The molecular beam was skimmed twice and intersected at 90° with the output of a Lambda Physik LPX-200 excimer laser operation on the ArF transition (193.3 nm). The laser fluences ranged 30-300 mJ/cm^2.

Vinyl chloride 99.5% was obtained from Aldrich Chemical Co. and used without further purification.

3. Results

For all of the time of flight (TOF) spectra presented the circles represent the raw data, the dashed lines are single channel contributions to the forward convolution fit, and the solid lines are the combined overall fit to the data. There was no change in the shape of any of the TOF spectra over a laser fluence range 30-300 mJ/cm^2 providing strong evidence that all of the observed signals are the result of single photon absorptions. The TOF spectra presented were taken with a laser fluence of ~100 mJ/cm^2. In all of the experiments presented here the photodissociation laser was unpolarized which results in an isotropic laboratory photofragment distribution in the plane defined by the molecular beam and detector axis. Center of mass translational energy distributions were generated from the laboratory TOF spectra using the forward convolution technique. The forward convolution technique is described in detail in the "Data analysis" section of Chapter 1 of this thesis.

Atomic hydrogen elimination and secondary decomposition of chlorovinyl

intermediates. The TOF spectrum for m/e 61 ($C_2H_2Cl^+$) at a scattering angle of 7.0° and a

photoionization energy of 11.0 eV is shown in figure 2. The TOF spectrum was fitted with

the $P(E_T)$ in figure 3. The $P(E_T)$ decreases out to ~43 kcal/mol and at low energy exhibits

a sudden truncation at 11 kcal/mol. The truncation results from secondary decomposition

of chlorovinyl intermediates that have sufficient internal energy to overcome the barrier to

C-Cl bond cleavage, $C_2H_2Cl^{\ddagger} \rightarrow C_2H_2 + Cl$. The solid line in figures 2 and 3 represents the

best fit to the data and the dashed lines demonstrate the sensitivity of the forward

convolution fit to the position of truncation of the $P(E_T)$. Based on these fits we assign a

confidence of 11±2 kcal/mol to the point of truncation.

We can calculate the available energy using equation 1.

$$E_{avail} = E_{h_\nu} + E_{reactant\ internal} - D_o(C_2H_2Cl\text{-}H) \qquad\qquad (\text{eqn. 1})$$

We assume the internal energy in the vinyl chloride reactant to be negligible[9] and given E_{h_ν}

=148 kcal/mol (193 nm) and $D_o(C_2H_2Cl\text{-}H)$ = 101 kcal/mol (ref 10) the result is an

available energy of 47 kcal/mol following H atom elimination. With no evidence of any

electronic excitation of the products, any available energy not partitioned into translation

must be partitioned into internal degrees of freedom in the chlorovinyl radical. Therefore,

our measured $P(E_T)$ is a direct measurement of the internal energy distribution in the

chlorovinyl photoproducts, and the truncation is a direct measurement of the barrier to

secondary decomposition of chlorovinyl radical intermediates. The only

thermodynamically available secondary decomposition pathway is C-Cl bond cleavage to

give acetylene and a chlorine atom. Figure 4 shows a schematic representation of the relationship between the truncation in the primary $P(E_T)$ for H atom elimination and the barrier to secondary C-Cl bond cleavage in primary chlorovinyl radical photoproducts. A truncation of the $P(E_T)$ at 11 ± 2 kcal/mol corresponds to a barrier height of 137 ± 2 kcal/mol relative to vinyl chloride. This is a dissociation barrier of 36 ± 2 kcal/mol for C-Cl bond cleavage in the chlorovinyl radical and provides a direct measurement of 11 ± 2 kcal/mol for the barrier to recombination, $Cl + HCCH \rightarrow C_2H_2Cl$, given the endothermicity of $C_2H_3Cl \rightarrow H + Cl + HCCH$, $\Delta H_0 = 126.1$ kcal/mol.[10] Any rotational excitation of the C_2H_2Cl intermediates following the primary C-Cl bond cleavage could result in rotationally metastable C_2H_2Cl molecules. The result would be an increase in the energy for the point of truncation and a corresponding higher reported value for the barrier to recombination. For this reason the value of 11 ± 2 kcal/mol should be considered an upper limit to the barrier for the reaction of $Cl + HCCH$. However, in this case the effect of such a centrifugal barrier is expected to be negligible since the primary dissociation is a statistical elimination of atomic hydrogen. The statistical elimination of such a light photofragment will generate very little torque on the C_2H_2Cl partner fragment making the production of highly rotationally excited C_2H_2Cl intermediates unlikely.

As a result of the secondary decomposition of chlorovinyl photoproducts, we are not able to measure the $P(E_T)$ for the H-atom elimination channel below 11 kcal/mol from the m/e 61 photofragments.

Molecular hydrogen elimination. Figure 5 shows TOF spectra for m/e 60 (C_2HCl^+) at scattering angles of $10°$ and $15°$ and a photoionization energy of 12.0 eV. The dominant component in the $10°$ spectrum and the only component in the $15°$ spectrum is the result of H_2 elimination and was fitted the $P(E_T)$ shown in figure 6. The minor component in the $10°$ spectrum is from dissociative photoionization of C_2H_2Cl photoproducts and was fitted with the $P(E_T)$ in figure 3 for H atom elimination. The $P(E_T)$ in figure 6 has a roughly Gaussian shape with $<E_T> = 18\pm2$ kcal/mol, a maximum probability at ~20 kcal/mol, and a FWHM of ~20 kcal/mol. The dependence of the integrated signal for m/e 60 on the laser fluence is shown in figure 7 for a scattering angle of $10°$. The power dependence in figure 7 has a slope of <1 and the slope decreases with increasing power. The TOF spectra did not change shape over the fluence range shown in figure 7 demonstrating the signal at m/e 60 to be the result of a single photon dissociation and indicating that any contribution from secondary photodissociation of primary chlorovinyl photoproducts is negligible.

HCl elimination. The TOF spectra for m/e 36 ($H^{35}Cl^+$) at scattering angles of $20°$ and $40°$ and a photoionization energy of 14.0 eV are shown in figure 8. The TOF spectra in figure 8 were fitted with the $P(E_T)$ in figure 9. The $P(E_T)$ in figure 9 has a maximum probability at 12 kcal/mol, extends to ~70 kcal/mol, and has $<E_T> = 18\pm1$ kcal/mol. The photoionization spectrum for m/e 36 photoproducts at a scattering angle of $20°$ is shown in figure 10. Taking into consideration the energy width of the undulator radiation, figure 10 shows a photoionization onset of 10.5 ± 0.3 eV for the HCl photoproducts. Comparison

of this value with the HCl ionization potential (IP) of 12.75 eV[11] demonstrates a red shift

of ~2.2 eV (51 kcal/mol) in the photoionization onset with respect to the HCl IP. The red

shift is the result of internal excitation in the HCl photofragments. Quantitative evaluation

of the internal energy from the measured photoionization spectrum is a difficult question

that we are currently unable to address. A qualitative interpretation of the internal energy

in the HCl photofragments from the depression of the photoionization onset is presented

in the discussion section.

   Atomic chlorine elimination and secondary decomposition of the vinyl radical

intermediates. The TOF spectra for m/e 35 ($^{35}Cl^+$) at scattering angles of 7°, 15°, and 25°

and a photoionization energy of 14.0 eV are shown in figure 11. The TOF spectra have

been fitted with two components, the dashed lines in figure 11. The narrow component at

earlier times, peaked ~55 μsecs, was fitted with the $P(E_T)$ in figure 12. The $P(E_T)$ has a

roughly Gaussian shape with maximum probability at 22 kcal/mol and $<E_T> = 23\pm1$

kcal/mol. The slow broad component, ~75-200 μsecs, was fitted with the $P(E_T)$ in figure

13. Note that the $P(E_T)$ in figure 13 is the translational energy distribution of Cl products

and *not* the c.m. translational energy distribution reported in all of the other figures

presented in this manuscript. The $P(E_T)$ exhibits a maximum probability ~0.5 kcal/mol

which decreases to a plateau from 2-4 kcal/mol and then decreases out to a maximum

energy of ~7 kcal/mol. The shape indicates that the $P(E_T)$ in figure 13 contains

contributions from at least two separate components.

We can decompose the $P(E_T)$ for the slow Cl photofragments shown in figure 13 into two dissociation channels. We assign the slower portion of the $P(E_T)$ to statistical C-Cl bond cleavage, $H_2CCHCl \rightarrow H_2CCH + Cl$, and we use a slightly modified prior translational energy distribution to model the experimental distribution. The $P(E_T)$ is shown as the solid line in the top of figure 14 with the dashed line showing a prior distribution for comparison. The resulting fits to the TOF spectra are shown as the dotted line at the slowest product arrival times, peaked around 120 μsecs. The $P(E_T)$ has a maximum probability ~1 kcal/mol and $<E_T> = 3\pm1$ kcal/mol. The faster portion of the $P(E_T)$ in figure 13 we attribute to secondary C-Cl bond cleavage in the chlorovinyl intermediates following primary H atom elimination, $H_2CCHCl \rightarrow C_2H_2Cl^\ddagger + H \rightarrow C_2H_2 + Cl + H$. We demonstrated the existence of this channel above with our measured truncation in the $P(E_T)$ for C_2H_2Cl photoproducts that resulted from primary H atom elimination, see figure 4. The $P(E_T)$'s used in the forward convolution fits to the TOF data are shown in the bottom of figure 14. The dashed line is the $P(E_T)$ for the primary H atom elimination, $H_2CCHCl \rightarrow C_2H_2Cl + H$. The solid line is the $P(E_T)$ for the secondary decomposition of the chlorovinyl radical intermediates, $C_2H_2Cl^\ddagger \rightarrow C_2H_2 + Cl$. We are unable to measure the portion of the primary $P(E_T)$ for H atom elimination resulting from C_2H_2Cl intermediates that undergo secondary decomposition. We assume that the shape is similar to the measured $P(E_T)$ for the H atom elimination channel in ethylene[12] truncated at 11 kcal/mol as determined from the surviving C_2H_2Cl photofragments. The large discrepancy in the masses of the C_2H_2Cl and H atom products in the primary dissociation

results in little c.m. velocity of the C_2H_2Cl intermediates. Therefore, the forward convolution fits are not sensitive to the shape of the $P(E_T)$ used to represent the primary H atom elimination, given by the dotted line in the bottom of figure 14. The fits are, however, very sensitive to the $P(E_T)$ for secondary decomposition of the C_2H_2Cl intermediates shown as the solid line in figure 14. The resulting fits to the TOF data are shown as the faster of the two dotted line components in figure 11, peaked around 70 μsecs. The secondary $P(E_T)$ has a maximum probability at ~8 kcal/mol and $<E_T> = 8\pm1$ kcal/mol. The maximum in the secondary $P(E_T)$ is consistent with our measured recombination barrier for the secondary decomposition process of 11 ± 2 kcal/mol assuming a significant fraction of the exit barrier potential energy is partitioned into fragment recoil.[13]

We obtained the ratio of the three dissociation channels that result in atomic chlorine photoproducts from the ratios used to fit the TOF data in figure 11. The fast primary Cl elimination channel, $P(E_T)$ in figure 12, accounts for 86% of the total Cl photoproducts. The slow primary Cl elimination channel, $P(E_T)$ is the solid line in the top of figure 14, accounts for 7% of the Cl photoproducts, and the secondary decomposition of chlorovinyl intermediates, bottom of figure 14, accounts for the remaining 7% of Cl photoproducts.
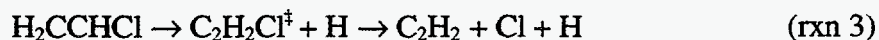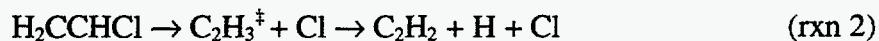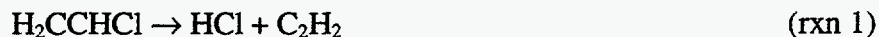
The TOF spectra for m/e 27 ($C_2H_3^+$) at scattering angles of 15° and 25° and a photoionization energy of 11.0 eV are shown in figure 15. The TOF spectra were fitted with the $P(E_T)$ in figure 12 and represents the momentum matched vinyl radicals for the

fast primary Cl fragments. It is immediately apparent from figure 15 that the vinyl radical photoproducts that would be momentum matched with the slow Cl elimination channel are not present. We attributed half of the slow Cl photoproducts to secondary decomposition of chlorovinyl radical intermediates, a process that does not produce a photoproduct at m/e 27. The other half of the slow Cl photoproducts we attribute to a statistical Cl elimination channel that would result in a momentum matched vinyl radial photoproduct at m/e 27. The absence of the slow momentum matched vinyl radical product in figure 15 is a direct indication of secondary decomposition of the vinyl radical intermediates produced in the slow Cl elimination channel, $C_2H_3^{\ddagger} \rightarrow C_2H_2 + H$. The dependence of the integrated signal for m/e 27 at a scattering angle of 20° on the photodissociation laser fluence is shown in figure 16. The power dependence has a slope of <1 and decreases with increasing fluence providing strong evidence that the m/e 27 signal is the result of a single photon process.

The photoionization spectrum for m/e 27 ($C_2H_3^+$) photoproducts at a scattering angle of 20° is shown in figure 17. The vinyl radical photoproducts are the result of the fast Cl elimination channel, $P(E_T)$ shown in figure 12. Taking into consideration the energy width of the ALS, figure 17 shows a photoionization onset of 8.3±0.3 eV. This is consistent with the I.P. for the vinyl radiacal of 8.6 eV[11] with the small red shift resulting from internal excitation on the vinyl radical photoproducts.

Photoproducts at m/e 26. TOF spectra for m/e 26 ($C_2H_2^+$) at a scattering angle of 10° and photoionization energy of 11.0 eV, and scattering angles of 10° and 20° at a

photoionization energy of 14.0 eV are shown in figure 18. Three of the dissociation channels we have mentioned above result in production of C_2H_2 photoproducts:

$$H_2CCHCl \rightarrow HCl + C_2H_2 \qquad\qquad (rxn\ 1)$$

$$H_2CCHCl \rightarrow C_2H_3^{\ddagger} + Cl \rightarrow C_2H_2 + H + Cl \qquad\qquad (rxn\ 2)$$

$$H_2CCHCl \rightarrow C_2H_2Cl^{\ddagger} + H \rightarrow C_2H_2 + Cl + H \qquad\qquad (rxn\ 3)$$

The forward convolution fits to the TOF spectra at 14 eV, bottom two TOF in figure 18, include contributions from all three of these dissociation channels. The $P(E_T)$ for reaction 1 is shown in figure 9 and the $P(E_T)$'s for both steps in reaction 3 are shown in the bottom of figure 14. The primary dissociation step in reaction 2 is the slow Cl elimination and the $P(E_T)$ is shown in the top of figure 14. For the secondary decomposition of the vinyl radical intermediates, the second step in reaction 2, we assumed a prior translational energy distribution consistent with a statistical simple bond rupture. As a result of the large difference in the masses of the products from the second step in reaction 2, the c.m. velocity imparted to the C_2H_2 fragment is very small and the forward convolution fit was not sensitive to the shape of the $P(E_T)$. In addition to reactions 1-3, it was also necessary to include a contribution to the m/e 26 TOF spectra from dissociative ionization of C_2H_3 photofragments from the fast Cl elimination channel. This contribution was fitted with the $P(E_T)$ in figure 12 and it is the narrow component peaked ~48 μsecs in the TOF spectra. The necessity to include reactions 2 and 3 to obtain a satisfactory fit to the TOF spectra provides additional confirmation of these two secondary decomposition processes.

The TOF spectrum at 11.0 eV was fitted with only reaction 1 and the dissociative

ionization signal from C_2H_3 photoproducts. In reactions 1-3 the C_2H_2 product will be

acetylene by the time it arrives in the photoionization region as the result of either direct

formation of acetylene in the dissociation or rapid isomerzation of singlet vinylidene

products, see discussion section. By using 11.0 eV photoionization radiation, which is

slightly below the I.P. of acetylene at 11.4 eV[11], we significantly enhance the signal from

acetylene products that contain substantial internal energy which can red shift the

photoionization onset. The disappearance of contributions from reactions 2 and 3 from the

TOF at 11.0 eV demonstrates that the C_2H_2 products from these reactions contain less

internal energy than the C_2H_2 products from reaction 1. This is consistent with the much

lower available energies for reactions 2 and 3 of 20 kcal/mol as compared with 124

kcal/mol for reaction 1. The ability to discriminate between dissociation channels that

produce products with the same chemical identity but result from different dissociation

dynamics is another significant advantage of this technique over traditional PTS

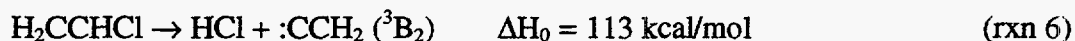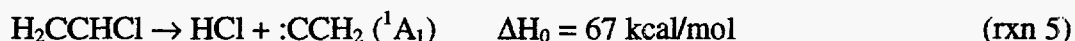experiments that employ electron impact ionization.
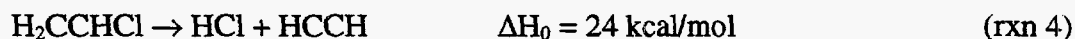

4. Discussion

A. Molecular elimination

HCl elimination. Our measured $P(E_T)$ for HCl elimination is shown in figure 9.

The shape of our measured $P(E_T)$ is similar the $P(E_T)$ reported by Umemoto *et al.* using

traditional PTS techinques at a fixed scattering angle of $90°$.[4] However, our distribution has a higher average translation, $\langle E_T \rangle = 18 \pm 1$ kcal/mol compared to $\langle E_T \rangle = 15 \pm 1$ kcal/mol reported by Umemoto _et al._, with the tail of our $P(E_T)$ extending almost 10 kcal/mol beyond the $P(E_T)$ of Umemoto _et al._ Our state averaged $P(E_T)$ is also in good agreement with the state selected measurements of Huang _et al._[6] The state selected $P(E_T)$ measurements of Huang _et al._ show narrowing and shifting toward lower energy with increasing HCl vibrational excitation. Their measured average energies range from $\langle E_T \rangle = 25 \pm 2$ kcal/mol for HCl(v''=0) to $\langle E_T \rangle = 18 \pm 1$ kcal/mol for HCl (v''=2). Assuming the trend continues with increasing vibrational levels of the HCl photoproduct, and with substaintial population in HCl v>2 as suggested by Berry's chemical laser studies[1], averaging over all of the HCl vibrational levels should yield a state averaged value for $\langle E_T \rangle$ in good agreement with our measured value.

Thermodynamically there are three C_2HCl isomers that can be formed following the elimination of HCl, reactions 4-6. The origins of the thermodynamic values are listed in reference 10.

$$H_2CCHCl \rightarrow HCl + HCCH \qquad \Delta H_0 = 24 \text{ kcal/mol} \qquad \text{(rxn 4)}$$

$$H_2CCHCl \rightarrow HCl + :CCH_2 \, (^1A_1) \qquad \Delta H_0 = 67 \text{ kcal/mol} \qquad \text{(rxn 5)}$$

$$H_2CCHCl \rightarrow HCl + :CCH_2 \, (^3B_2) \qquad \Delta H_0 = 113 \text{ kcal/mol} \qquad \text{(rxn 6)}$$

Although we are not able to rule out reaction 6 based on thermodynamic considerations alone, the fact that our measured $P(E_T)$ extends smoothly beyond the available energy for reaction 6, $E_{avail} = 45$ kcal/mol, suggests that reaction 6 does not play a significant role in

HCl elimination. In addition, Umemoto _et al._ found the HCl photofragment distribution to be nearly isotropic, $\beta=0.088\pm0.015$, providing strong evidence that the dissociation proceeds on the ground PES following IC from the initially excited $\pi\pi^*$ PES.[4] Dissociation on the ground electronic surface does not correlate with formation of triplet vinylidene.[6] However, dissociation on the ground PES does correlate with formation of singlet vinylidene, reaction 5, as well as linear acetylene, reaction 6.
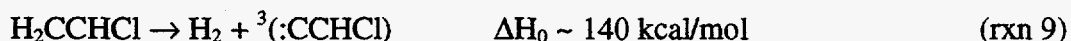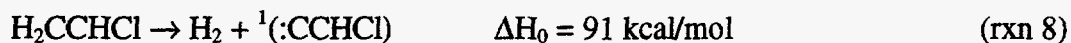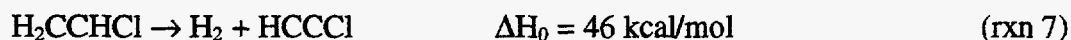
The recombination barriers for reactions 4 and 5 were calculated by Reihl _et al._ to be 3 kcal/mol and 63 kcal/mol respectively.[8] With such a small recombination barrier, 1,1 elimination to produce singlet vinylidene would be expected to result in a near statistical translational energy release with a maximum probability around 3 kcal/mol. A maximum probability of 12-13 kcal/mol in our measured $P(E_T)$, figure 9, suggests a larger recombination barrier such as that calculated for reaction 4. Huang _et al._ measured the ratio of the yield for HCl from vinyl chloride versus vinyl chloride-1d (H_2CCDCl). The results indicated that 1,1 HCl elimination was favored over 1,2 HCl elimination by 3:1 assuming no H/D scrambling prior to dissociation. However, the results also demonstrated identical internal state distributions for the HCl and DCl photoproducts indicating that both products resulted from the same dissociation process. To explain these results the authors invoked a dissociation mechanism involving partial H/D scrambling prior to exclusive 1,1 elimination, reaction 5. The idea that H/D scrambling is competitive with HCl elimination was supported by the calculations of Reihl _et al._ that placed the barriers to the two processes in very close proximity. In order to explain the larger than expected

translational energy release, Huang *et al.* suggested a dissociation mechanism where isomerization of singlet vinylidene to acetylene occurs on a timescale comparable to the separation of the two photofragments. Lineberger and coworkers have estimated the lifetime of singlet vinylidene at 40-200 fs from linewidth analysis of negative ion photodetachment experiments.[14] This is consistent with the calculated barrier to isomerization of singlet vinylidene to acetylene of 2-4 kcal/mol.[15] Huang *et al.* termed the mechanism concerted. With the isomerization proceeding in concert with the photofragment separation the energy of isomerization would be available for partitioning into degrees of freedom other than internal energy of the acetylene product alone. The creation of acetylene and HCl in close proximity would leave the photofragments experiencing some portion of the large recombination barrier for reaction 4 and explain the additional translational energy release.

The photoionization spectrum for the HCl photoproducts is shown in figure 10. The photoionization onset onset of 10.5 ± 0.3 eV is red shifted from the IP of HCl, 12.75 eV[11], by ~2.2 eV (~51 kcal/mol). We have previously demonstrated that the red shift of the photoionization onset from the IP provides a good qualitative indication of the internal energy of the photofragments.[16] With an available energy for reaction 4 of 124 kcal/mol, the red shift in the photoionization onset suggests that ~40% of the available energy is partitioned into internal degrees of freedom in the HCl photoproducts. The large internal excitation is consistent with the chemical laser studies of Berry and the time-resolved FTIR measurements by Donaldson and Leone.[1,2] In both studies the authors found highly

nonstatistical vibrational population for the HCl photoproduct. In addition Huang *et al.* also found a very highly rotationally excited component in the HCl(v''=0) state distributions. Our measured $\langle E_T \rangle$ = 18±1 kcal/mol only accounts for 14% of the available energy leaving ~46% of the available energy, ~57 kcal/mol, on average in internal degrees of freedom in the acetylene photoproduct. This is in good agreement with infrared emission experiments by Moss *et al.* that reported the acetylene products to be very highly vibrationally excited following dissociation at 193 nm.[3]

Molecular hydrogen elimination. Thermodynamically the C_2H_2 product formed following the elimination of molecular hydrogen can be either acetylene or vinylidene, reactions 7-9. The origins of the thermodynamic values are listed in reference 10.

$$H_2CCHCl \rightarrow H_2 + HCCCl \qquad \Delta H_0 = 46 \text{ kcal/mol} \qquad \text{(rxn 7)}$$

$$H_2CCHCl \rightarrow H_2 + {}^1(:CCHCl) \qquad \Delta H_0 = 91 \text{ kcal/mol} \qquad \text{(rxn 8)}$$

$$H_2CCHCl \rightarrow H_2 + {}^3(:CCHCl) \qquad \Delta H_0 \sim 140 \text{ kcal/mol} \qquad \text{(rxn 9)}$$

The $P(E_T)$ for H_2 elimination is shown in figure 6. Using equation 1, the available energy for reaction 9 is ~8 kcal/mol. With less than 5% of the $P(E_T)$ below 8 kcal/mol it is unlikely that reaction 9 makes any significant contribution to H_2 elimination.

Riehl *et al.* calculated the recombination barrier for 1,1 elimination, reaction 8, to be 6 kcal/mol.[8] Such a relatively small recombination barrier is not consistent with our measured $P(E_T)$ which has a maximum probability at ~20 kcal/mol. The large translational energy release that we measure would be more consistent with the higher recombination barrier expected for 1,2 elimination, reaction 7. The ab initio study of Riehl *et al.* was not
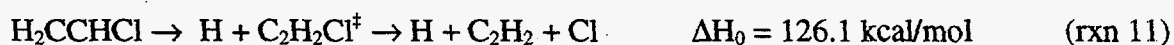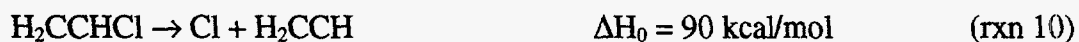
able to locate the transition state for 1,2 elimination, however the recombination barrier would be expected to be substantially higher than the recombination barrier for reaction 8 and the dissociation barrier should also be higher than the 1,1 elimination pathway. If the dissociation barrier for reaction 7 is above the dissociation barrier for reaction 8, then we would expect 1,1 H_2 elimination to be preferred over 1,2 H_2 elimination. However, He *et al.* concluded based on the maximum product recoil that the major dissociation channel was 1,2 elimination.[6] We offer an alternative picture of the dissociation based on the mechanism later proposed by the same authors (Huang *et al.*[6]) to explain the elimination of HCl from vinyl chloride. The authors termed this mechanism *concerted* and it is consistent with our large observed translational energy release. The mechanism involves isomerization of the chlorovinylidene in concert with 1,1 H_2 elimination. The barrier to isomerization of the singlet chlorovinylidene to chloroacetylene was calculated by Reihl *et al.* to be <1 kcal/mol. Such a small calculated barrier left the authors to question whether or not there is actually a minimum associated with this structure. The extremely small barrier would result in very rapid isomerization of singlet chlorovinylidene to chloroacetylene on the timescale of separation of the H_2 and C_2HCl photoproducts. The isomerization energy would then be available for partitioning into degrees of freedom other than internal excitation in the chloroacetylene products. Reaction 8 would generate H_2 and chloroacetylene photoproducts in very close proximity where they would experience the strongly repulsive recombination potential associated with reaction 7. The result would be a large translational energy release consistent with our measured $P(E_T)$.

B. Atomic elimination

Atomic hydrogen elimination. The $P(E_T)$ we measured for atomic hydrogen elimination is shown in figure 3. As a result of secondary decomposition of the chlorovinyl radical photoproducts, we are only able to measure the $P(E_T)$ below the truncation point at 11 kcal/mol. Our measured $P(E_T)$ has a maximum probability at the truncation point and decreases out to ~45 kcal/mol. Mo *et al.* reported isotropic Doppler profiles for the H atom photoproducts following 193 nm providing evidence that the dissociation occurs on the ground PES following IC from the initially excited $\pi\pi^*$ PES.[6] The authors also reported an average translational energy release of 17±2 kcal/mol for the H atom photofragements. This large translational energy release, 35% of the available energy for H atom elimination, is seemingly contradictory with simple bond rupture on the ground PES. Our measured $P(E_T)$, which only includes the portion of the distribution above 11 kcal/mol, provides a rigorous upper limit of $<E_T> = 18$ kcal/mol. From our measurements of the Cl photoproducts that result from secondary decomposition of chlorovinyl radical intermediates, we have direct evidence that the $P(E_T)$ must extent below the truncation point. Therefore, the average translational energy release must be significantly lower than our upper limit of 18 kcal/mol. In the analogous H atom elimination channels for ethylene[12] and acrylonitrile[16] at 193 nm the $P(E_T)$s were found to be consistent with statistical simple bond rupture. Although we are not able to measure the complete $P(E_T)$ for H atom elimination, the majority of the evidence suggests that the complete distribution is consistent with statistical simple bond rupture on the ground PES. We are

unable to offer an explanation for the anomalously high average translation measured by Mo *et al.*

Atomic chlorine elimination. Both Umemoto *et al.* and Gordon and coworkers previously observed bimodal translational energy distributions for Cl photoproducts from the dissociation of vinyl chloride at 193 nm. [4,6] Umemoto *et al.* originally suggested two dissociation channels originating from primary C-Cl bond cleavage on two different potential energy surfaces. The translationally colder channel was assigned to dissociation on the ground PES following IC, and the translationally hotter channel was assigned to dissociation on the low lying $n\sigma^*_{(C-Cl)}$ PES. In addition to the two atomic chlorine elimination channels from primary C-Cl bond cleavage, reaction 10, we have identified a third reaction channel that produces Cl photofragments from secondary decomposition of primary chlorovinyl intermediates, reaction 11.

$$H_2CCHCl \rightarrow Cl + H_2CCH \qquad \Delta H_0 = 90 \text{ kcal/mol} \qquad (\text{rxn } 10)$$

$$H_2CCHCl \rightarrow H + C_2H_2Cl^\ddagger \rightarrow H + C_2H_2 + Cl \qquad \Delta H_0 = 126.1 \text{ kcal/mol} \qquad (\text{rxn } 11)$$

The translationally hotter Cl elimination channel accounts for 86% of Cl photofragments and our measured $P(E_T)$ is shown in figure 12. Our average translational energy $\langle E_T \rangle = 23 \pm 1$ is in good agreement with that reported by Huang *et al* of $\langle E_T \rangle = 22$ kcal/mol. The large translational energy release and the large anisotropy reported for this channel, $\beta = 0.40 \pm 0.03$[4], are consistent with Umemoto *et al.*'s original suggestion that this channel involves dissociation on the $n\sigma^*_{(C-Cl)}$ PES. Following the initial $\pi\pi^*$ excitation the excited vinyl chloride reactants cross out of the Franck-Condon region to an avoided

crossing with the low lying $n\sigma^*_{(C-Cl)}$ PES surface. Using Gaussian 92 computations, Myers _et al._ found the splitting at the avoided crossing to be 261 cm^{-1}.[17] Reactants that remain on the lower adiabatic surface go through the avoided crossing region and dissociate on the $n\sigma^*_{(C-Cl)}$ PES. Reactants that hop to the upper adiabatic surface at the avoided crossing turn around and return to the Franck-Condon region where they undergo IC and dissociate on the ground electronic surface. Based on the branching ratios reported by Umemoto _et al_ for HCl, the dominant dissociation channel on the ground PES, and Cl, it appears that ~50% of the total dissociation yield at 193 nm occurs via C-Cl bond cleavage on the $n\sigma^*_{(C-Cl)}$ PES. Huang _et al._ reported 21%-59% of the Cl photoproducts from dissociation on $n\sigma^*_{(C-Cl)}$ PES the were in the $^2P_{1/2}$ state and the authors suggested the distribution of j=3/2 and j=1/2 Cl atoms to be the result of scrambling in the asymptotic region.

TOF spectra for the momentum matched vinyl radical photoproducts (m/e 27) are shown in figure 15 and they have been fitted with the $P(E_T)$ in figure 12 for C-Cl bond cleavage on the $n\sigma^*_{(C-Cl)}$ PES. With an available energy of 58 kcal/mol for reaction 10, it is interesting to note the survival of vinyl radical photoproducts corresponding to a c.m. translational energy release of <21.5 kcal/mol. Balko _et al._ measured a $P(E_T)$ for decomposition of vinyl radicals produced in the 193 nm photodissociation of ethylene that indicated there to be little or no barrier to recombination.[12] Therefore the barrier to C-H bond cleavage in the vinyl radical photoproducts is just the endothermicity of 34 kcal/mol, reaction 12.

$$H_2CCH^{\ddagger} \rightarrow H + HCCH \qquad \Delta H_0 = 34 \text{ kcal/mol} \qquad \text{(rxn 12)}$$

Any available energy following C-Cl bond cleavage, reaction 10, not partitioned into electronic excitation of the Cl photoproducts or translational degrees of freedom must be partitioned into internal degrees of freedom in the vinyl radical photoproducts. With the Cl produced in its excited spin orbit state, $^2P_{1/2}$, the endothermicity of reaction 10 becomes 92.5 kcal/mol leaving an available energy of 55.5 kcal/mol to be partitioned between translation and internal excitation in the vinyl radical photoproducts. A barrier of 34 kcal/mol to secondary C-H bond cleavage, reaction 12, leads to a minimum c.m. translational energy release corresponding to survival of vinyl radical photoproducts of 21.5 kcal/mol. The extension of our measured $P(E_T)$ below 21.5 kcal/mol down to a minimum of 8 kcal/mol indicates the formation of metastable vinyl radical photoproducts. The lifetime of these metastable products must be at least comparable to their neutral flight time of ~50 μsecs. In an investigation of the photodissociation of vinyl bromide at 193 nm, Wodtke *et al.* suggested the formation of vinyl radical products in a metastable electronic state following atomic bromine elimination based on a similar analysis of the TOF data.[18] Their measurements found the metastable electronic state of the vinyl radical, $^2A"$, 42 kcal/mol above the ground electronic state. The available energy for reaction 10 if the vinyl radical product is generated in this excited electronic state is only 16 kcal/mol. Therefore, although production of H_2CCH $(A,^2A")$ could account for stable vinyl radical products corresponding to the portion of the $P(E_T)$ below 16 kcal/mol, this channel can not account for the stable vinyl radical products corresponding to the $P(E_T)$ between 16

kcal/mol and 21.5 kcal/mol. A more likely explanation is rotational metastability of the vinyl radical products. Rotational excitation of the vinyl radical products following the impulsive C-Cl bond cleavage on the $n\sigma^*_{(C-Cl)}$ PES, reaction 10, could easily reach the 13.5 kcal/mol (24% of the available energy) needed to explain the metastable H_2CCH products.

The high resolution afforded by our experiments allowed us to resolve structure in the $P(E_T)$ for the translationally colder Cl photofragments, figure 13. With our direct evidence for reaction 11 and our measured recombination barrier for Cl + HCCH we were able to deconvolute the $P(E_T)$ in figure 13 into two channels from reactions 10 and 11. The $P(E_T)$s for the two channels are shown in figure 14 and the two channels each account for 7% of the total Cl photofragment yield. As a result of limited translational energy resolution the previous studies fail to resolve any structure in the translationally colder component.[4,6] The authors attribute the entire translationally colder component to reaction 10 on the ground PES and make no reference to Cl photoproducts from reaction 11. Our results demonstrated that half of the translationally colder component consists of Cl photoproducts from reaction 11.

Our measured $P(E_T)$ for the primary Cl elimination channel on the ground PES, reaction 10, is shown in the top of figure 14, solid line. For comparison, the $P(E_T)$ from a prior prediction with an available energy of 25 kcal/mol is shown as the dashed line in the top of figure 14. The statistical distribution is consistent with simple bond rupture on the ground electronic surface. However, the agreement with a prior prediction with less than half of the available energy for reaction 10 ($E_{avail} = 56$ kcal/mol) suggests that there may

not be complete randomization of energy in all the vibrational modes prior to dissociation. The $P(E_T)$ previously reported for this channel by Gordon and coworkers neglected the contribution from reaction 11 and therefore overestimated the translational energy release from reaction 10 on the ground PES. In addition Gordon and coworkers reported that >85% of the Cl photofragments were in the $^2P_{3/2}$ state. This agrees with the correlated states of the products from reaction 10 or 11 on the ground PES. The absence in figure 15 of momentum matched vinyl radical products for the C-Cl bond cleavage channel on the ground PES is the result of secondary decomposition of the vinyl radical intermediates, reaction 12.

Secondary decomposition of chlorovinyl radical intermediates and the barrier to Cl + acetylene. As mentioned above, the third source of Cl photofragments, which has gone unmentioned in previous work on vinyl chloride, is secondary decomposition of chlorovinyl radical intermediates generated by primary H atom elimination, reaction 11. The $P(E_T)$ for the second step in reaction 11, C-Cl bond cleavage in the chlorovinyl radical intermediates, is shown as the solid line in the bottom of figure 14. The $P(E_T)$ is peaked away from zero with a maximum probability of 8 kcal/mol. This is in excellent agreement with our measured upper bound to the recombination barrier of 11±2 kcal/mol for the reaction Cl + acetylene from the truncation in our measured $P(E_T)$ for C_2H_2Cl photofragments, see figure 4. This represents the first direct measurement of the barrier for the reaction Cl + acetylene. In the dissociation of dichloroethylenes, Sato *et al.* found it necessary to include secondary decomposition of the chlorovinyl photofragments and

also found the $P(E_T)$ for secondary C-Cl bond cleavage peaked away from zero very similar to our reported $P(E_T)$.[7] However, since kinetic studies[19] have reported no activation energy in the reaction of Cl + acetylene, the author concluded that the peaking away from zero was the result of a centrifugal barrier from rotational excitation in the C_2H_2Cl intermediate following the primary C-Cl bond cleavage. In our investigation of vinyl chloride the primary dissociation is a statistical elimination of an H atom instead of a direct elimination of a much heavier Cl atom. The C_2H_2Cl intermediate in our study should have almost no rotational excitation leaving little if any centrifugal barrier to dissociation. Therefore, our measured 11 ± 2 kcal/mol barrier is a barrier on the ground PES for the addition of Cl to C_2H_2.

5. Conclusion

Using the technique of PTS with tunable VUV undulator radiation we have investigated the dissociation of vinyl chloride following $\pi^*\leftarrow\pi$ excitation at 193 nm. We have identified one dissociation channel which occurs following crossing to the $n\sigma^*_{(C-Cl)}$ PES resulting in Cl elimination with a large translational energy release. We have identified four primary dissociation channels that occur on the ground PES following IC from the initially excited $\pi\pi^*$ PES including HCl elimination, H atom elimination, Cl elimination, and H_2 elimination. In addition, we have directly measured secondary decomposition of primary chlorovinyl radical and vinyl radical photoproducts. We have measured c.m. translational energy distributions for all of the dissociation channels. From

the truncation of the $P(E_T)$ for surviving chlorovinyl radical photoproducts we have made

a direct measurement of the recombination barrier for Cl + acetylene of 11 ± 2 kcal/mol.

We have measured the photoionization spectrum for HCl photoproducts providing a

qualitative indication that ~40% of the available energy for the HCl elimination channel is

partitioned into internal degrees of freedom in the HCl photofragments, in agreement with

previous work. We have also reported the photoionization spectrum for vinyl radical

intermediates resulting in a direct measurement of the photoionization onset at 8.3 ± 0.3

eV.

References

[1] M. J. Berry, *J. Chem. Phys.* **61**, 3114, (1974); M. J. Molina and G. C. Pimentel, *J. Chem. Phys.* **56**, 3988 (1972).

[2] D. J. Donaldson and S. R. Leone, *Chem. Phys. Lett.* **132**, 240 (1986).

[3] M. G. Moss, M. D. Ensminger, and J. D. McDonald, *J. Chem. Phys.* **74**, 6631 (1981).

[4] M. Umemoto, K. Seki, H. Shinohara, U. Nagashima, N. Nishi, M. Kinoshita, and R. Shimada, *J. Chem. Phys.* **83**, 1857 (1985).

[5] T. Suzuki, K. Tonokura, L. S. Bontuyan, and N. Hashimoto, *J. Phys. Chem.* **98**, 13447(1994).

[6] P. T. A. Reilly, Y. Xie, and R. J. Gordon, *Chem. Phys. Lett.* **178**, 511 (1991); Y. Mo, K. Tonokura, Y. Matsumi, M. Kawasaki, T. Sato, T. Arikawa, P. T. A Reilly, Y. Xie, Y. Yang, Y. Huang, and R. J. Gordon, *J. Chem. Phys.* **97**, 4815 (1992); Y. Huang, Y. Yang, G. He, and R. J. Gordon, *J. Chem. Phys.* **99**, 2752 (1993); Y. Huang, G. He, Y. Yang, S. Hashimoto, R. J. Gordon, *Chem. Phys. Lett.* **229**, 621 (1994); Y. Huang, Y. Yang, G. He, S. Hashimoto, R. J. Gordon, *J. Chem. Phys.* **103**, 5476 (1995); G. He, Y. Yang, Y. Huang, S. Hasimoto, and R. J. Gordon, *J. Chem. Phys.* **103**, 5488 (1995).

[7] K. Sato, S. Tsunashima, T. Takayanagi, G. Fujisawa, and A. Yokoyama, *J. Chem. Phys.* **106**, 10123 (1997).

[8] J. Riehl and K. Morokuma, *J. Chem. Phys.* **100**, 8976 (1994).

[9] At room temperature the vinyl chloride reactant will contain 1-2 kcal/mol of internal energy on average and will experience substantial cooling of the internal degrees of freedom following supersonic expansion.

[10] The heats of formation for vinyl chloride, acetylene, vinyl radical, chlorovinyl radical, H, H2, HCl, and Cl were taken from Handbook of Chemistry and Physics, D. R. Lide (CRC, Boca Raton, 1995). The isomerization energy for acetylene/vinylidene and the singlet/triplet splitting for vinylidene were taken from reference 14. The dissociation energy for elimination of H_2 along with either chloroacetylene or singlet chlorovinylidene was taken from reference 8. The singlet/triplet splitting for chlorovinyldene was esitmated based on the singlet/triplet splitting in vinylidene.

[11] Handbook of Chemistry and Physics, D. R. Lide (CRC, Boca Raton, 1995).

[12] B. A. Balko, J. Zhang, and Y. T. Lee, *J. Chem. Phys.* **97**, 935 (1992).

[13] This assumption has previously been shown to be reasonable: S. W. North, D. A. Blank, J. D. Gezelter, C. A. Longfellow, and Y. T. Lee, *J. Chem. Phys.* **102**, 4447 (1995).

[14] K. M. Ervin, J. Ho, and W. C. Lineberger, *J. Chem. Phys.* **91**, 5974 (1989).

[15] T. Carrington, L. M. Hubbard, H. F. Schaefer III, and W. H. Miller, *J. Chem. Phys.* **80**, 4347 (1984); M. M. Gallo, T. P. Hamilton, and H. F. Schaefer III, *J. Am. Chem. Soc.* **112**, 8714 (1990).

[16] See chapter 3 of this thesis.

[17] T. L. Myers, D. C. Kitchen, B. Hu, and L. J. Butler, *J. Chem. Phys.* **104**, 5446 (1996).

[18] A. M. Wodtke, E. J. Hintsa, J. Somorjai, and Y. T. Lee, _Israel Journal of Chemistry_, **29**, 383 (1989).

[19] W. B. DeMore, S. P. Sander, D. M. Golden, M. J. Molina, R. F. Hampson, M. J. Kurylo, C. J. Howard, A. R. Ravishankara, _Chemical kinetics and photochemical data for use in stratospheric modeling_, Evaluation number 9, JPL Publicaiton 90-1, Pasadena, CA, 1990.

Figure Captions

Figure 1:   Thermodynamically available dissociation channels for vinyl chloride following absorption at 193 nm. The origins of the thermodynamic values can be found in reference 9.

Figure 2:   TOF spectrum for m/e 61 ($C_2H_2Cl^+$) photoproducts at a scattering angle of 7° and a photoionization energy of 11.0 eV. The forward convolution fits are from the $P(E_T)$ in figure 3.

Figure 3: $P(E_T)$ used to fit the TOF spectra in figure 2. The dotted lines represent the uncertainty in the point of truncation.

Figure 4:   A schematic representation of the relationship between the truncation in the $P(E_T)$ for surviving chlorovinyl radical intermediates and the recombination barrier for Cl + HCCH.

Figure 5:   TOF spectra for m/e 60 (C_2HCl^+) photoproducts at scattering angles of 10° and 15° and a photoionization energy of 12.0 eV. The dominant component in the forward convolution fits is from H_2 elimination, $H_2CCHCl \rightarrow H_2 +$ HCCCl, and was fitted with the $P(E_T)$ shown in figure 6. The minor component in the 10° spectrum is from dissociative ionization of C_2H_2Cl photoproducts and was fitted with the $P(E_T)$ shown in figure 3.

Figure 6: $P(E_T)$ for H_2 elimination, $H_2CCHCl \rightarrow H_2 + HCCCl$, used to fit the TOF

spectra shown in figure 5.

Figure 7:   The dependence of the integrated signal for m/e 60 at a scattering angle of

10° on the photodissociation laser fluence.

Figure 8:   TOF spectra for m/e 36 (HCl^+) at scattering angles of 20° and 40° and a

photoionization energy of 14.0 eV. The forward convolution fits to the

TOF spectra were done with the $P(E_T)$ shown in figure 9.

Figure 9: $P(E_T)$ for HCl elimination, $H_2CCHCl \rightarrow HCl + C_2H_2$, used to fit the TOF

spectra shown in figure 8.

Figure 10:   Integrated signal intensity for m/e 36 (HCl^+) photoproduct at a scattering

angle of 20° plotted as a function of the undulator photoionization energy.

Figure 11:   TOF spectra for m/e 35 ($^{35}Cl^+$) photoproducts at scattering angles of 7°,

15°, and 25°, and a photoionization energy of 14.0 eV. The sharp

component at early arrival times, dashed line, was fitted with the $P(E_T)$ in

figure 12 for C-Cl bond cleavage on the $n\sigma^*_{(C-Cl)}$ PES. The products at later

arrival times, dashed line, were fitted with the $P(E_T)$ in figure 13. The

slower component was then broken into two components, dotted lines,

involving C-Cl bond on the ground PES, $P(E_T)$ shown in top of figure 14,

and secondary decomposition of primary chlorovinyl radical intermediates,

$P(E_T)$s shown in bottom of figure 14.

Figure 12: $P(E_T)$ for C-Cl bond cleavage, $H_2CCHCl \rightarrow Cl + C_2H_3$, on the $n\sigma^*_{(C-Cl)}$

PES used in the forward convolution fits for the TOF in figures 11 and 15.

Figure 13:   Translational energy distribution for the slow Cl photoproducts. The

forward convolution fit to the TOF data in figure 11 is the dashed line

representing the component from ~60-200 msecs. Note that this is the

translational energy distribution for Cl fragments alone and NOT the c.m.

translational energy distribution.

Figure 14: $P(ET)$s for the two product channels that make up the slow Cl

photofragments for which the $P(E_T)$ is shown in figure 13. **TOP:** $P(E_T)$ for

C-Cl bond cleavage, $H_2CCHCl \rightarrow Cl + C_2H_3$, on the ground PES, solid

line. Prior distribution calculated given 25 kcal/mol of available energy,

dashed line. **BOTTOM:** $P(E_T)$ for primary chlorovinyl radical

intermediates that undergo secondary decomposition, $H_2CCHCl \rightarrow H +$

$C_2H_2Cl^{\ddagger}$, dashed line. $P(E_T)$ for secondary decomposition of chlorovinyl

radical intermediates, $C_2H_2Cl^{\ddagger} \rightarrow Cl + HCCH$, solid line.

Figure 15:   TOF spectra for m/e 27 ($C_2H_3^{+}$) photoproducts at scattering angles of 15°

and 25° and a photoionization energy of 11.0 eV. The forward convolution

fits to the spectra were done using the $P(E_T)$ in figure 12.

Figure 16:   The dependence of the integrated signal for m/e 27 ($C_2H_3^{+}$) at a scattering

angle of 20° on the photodissociation laser fluence.

Figure 17:   The dependence of the integrated signal at m/e 27 ($C_2H_3^{+}$) and scattering

angle of 20° on the unduator photoionization energy.

Figure 18:   TOF spectra for m/e 26 ($C_2H_2^{+}$) at a scattering angle of 10° and a

photoionization energy of 11.0 eV and scattering angles of 10° and 20° and

a photoionization energy of 14.0 eV. The contributions to the forward

convolution fits are described in the text.
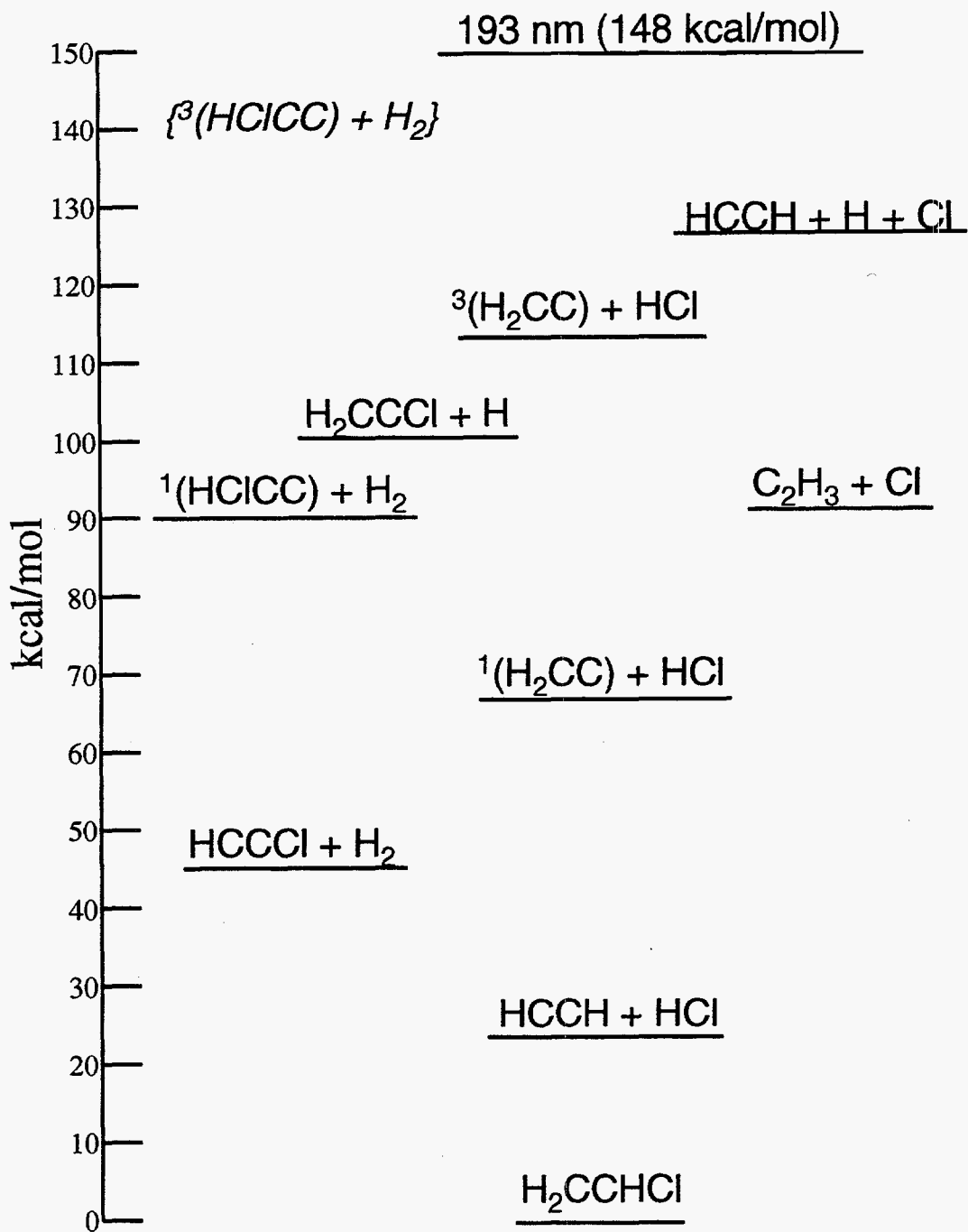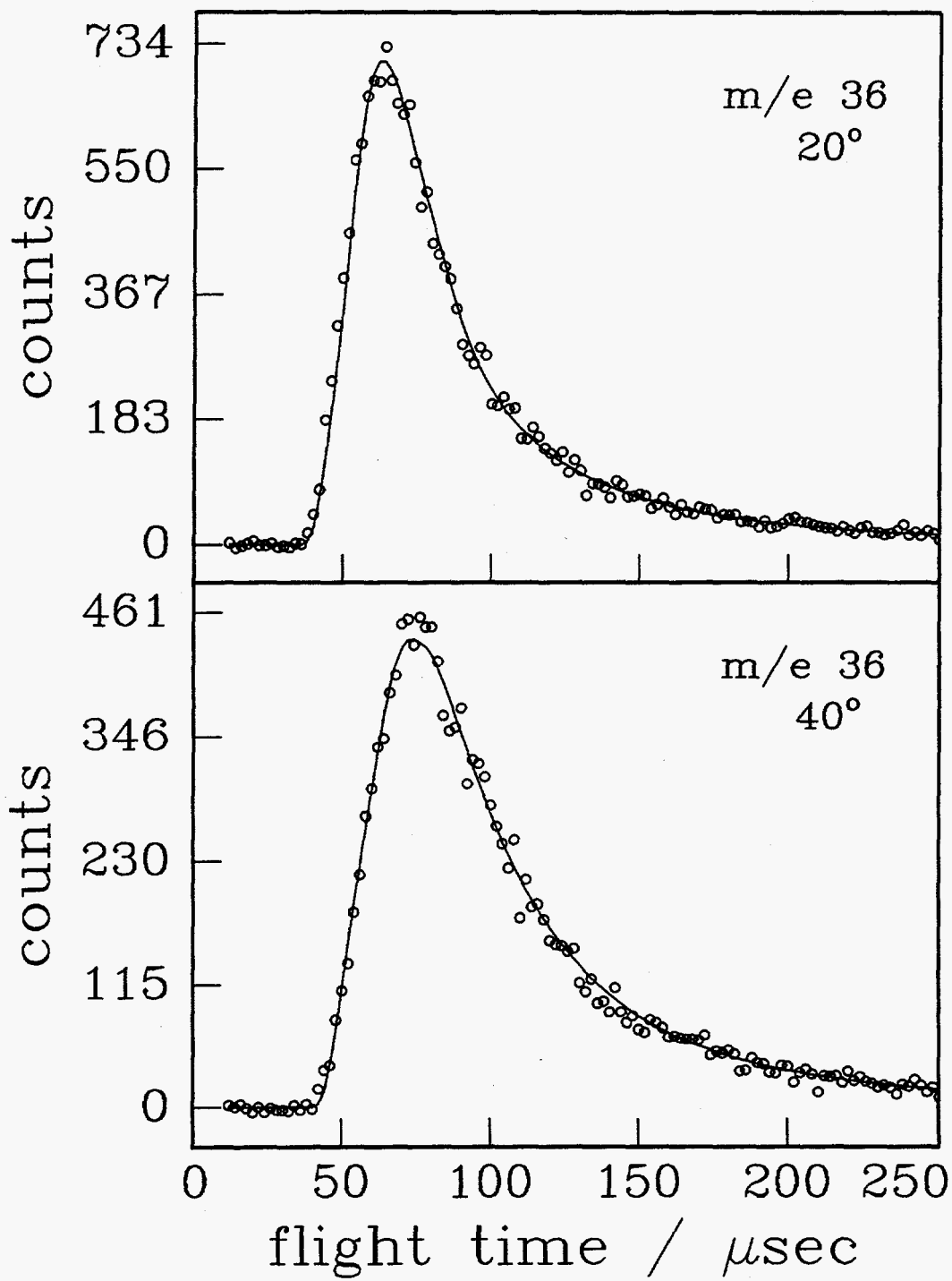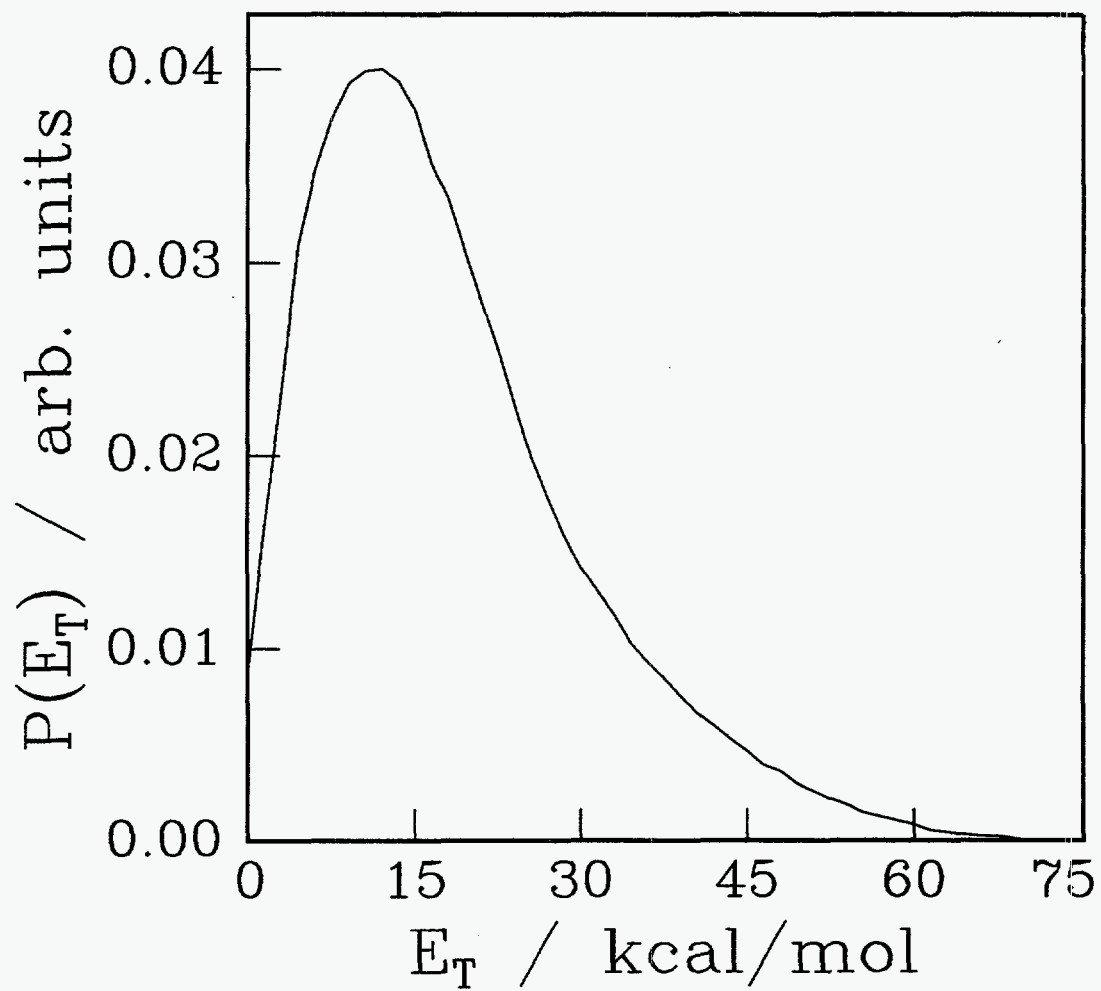
figure 1
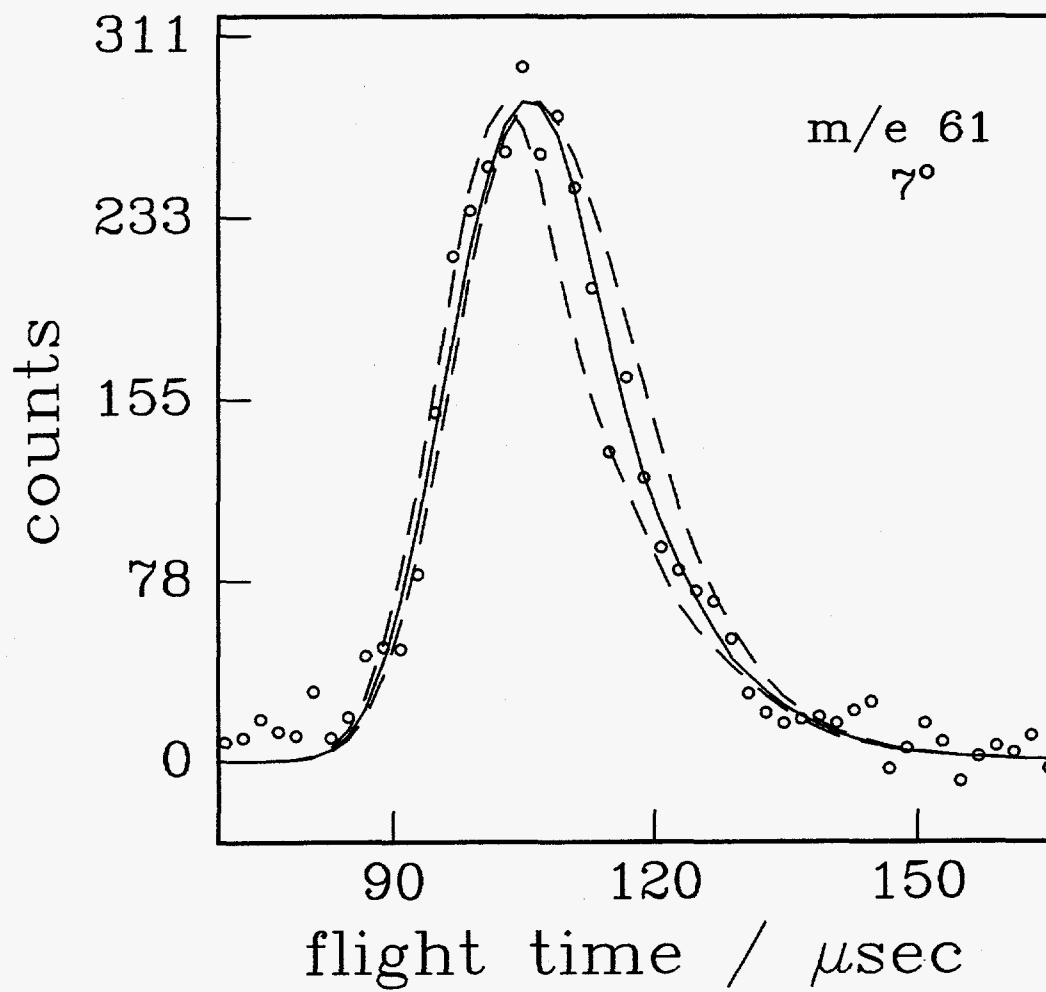
figure 2
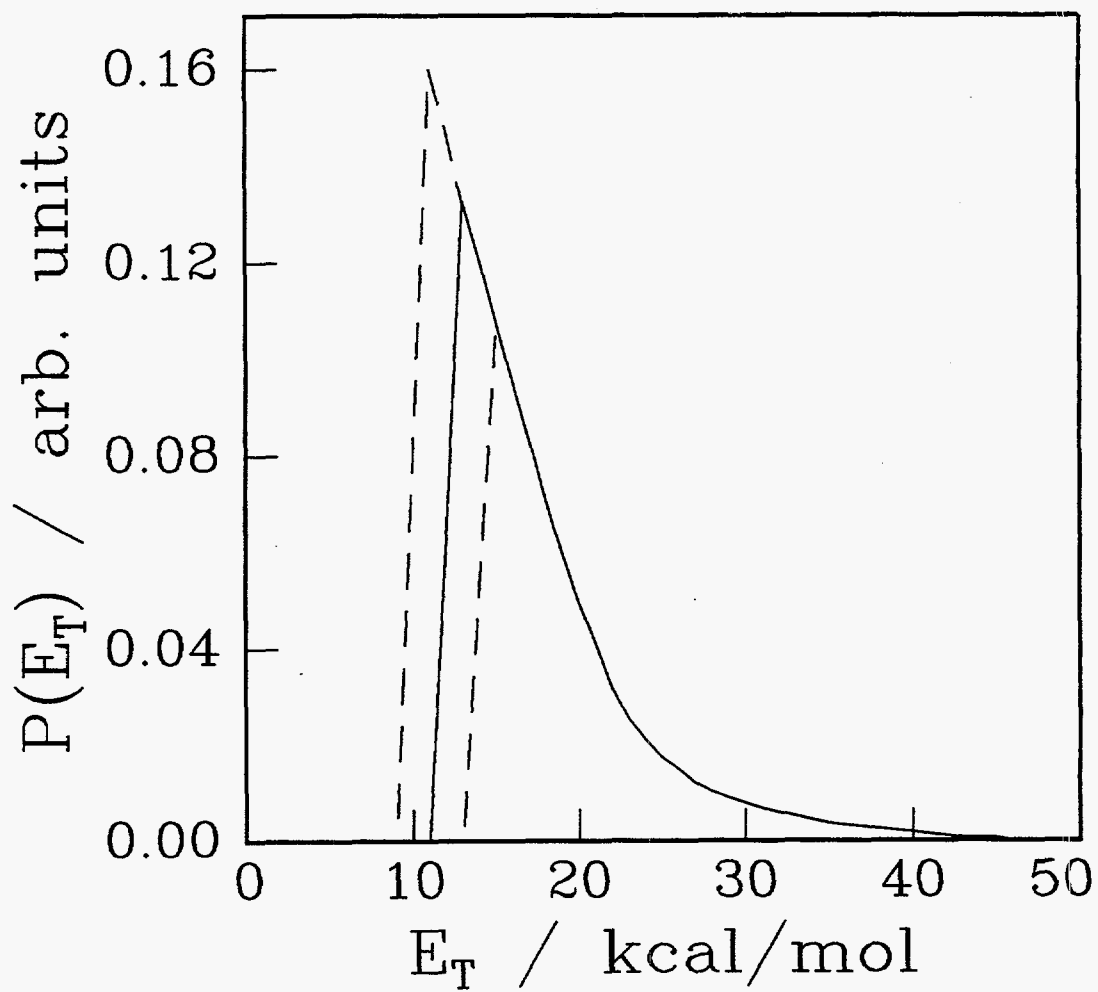
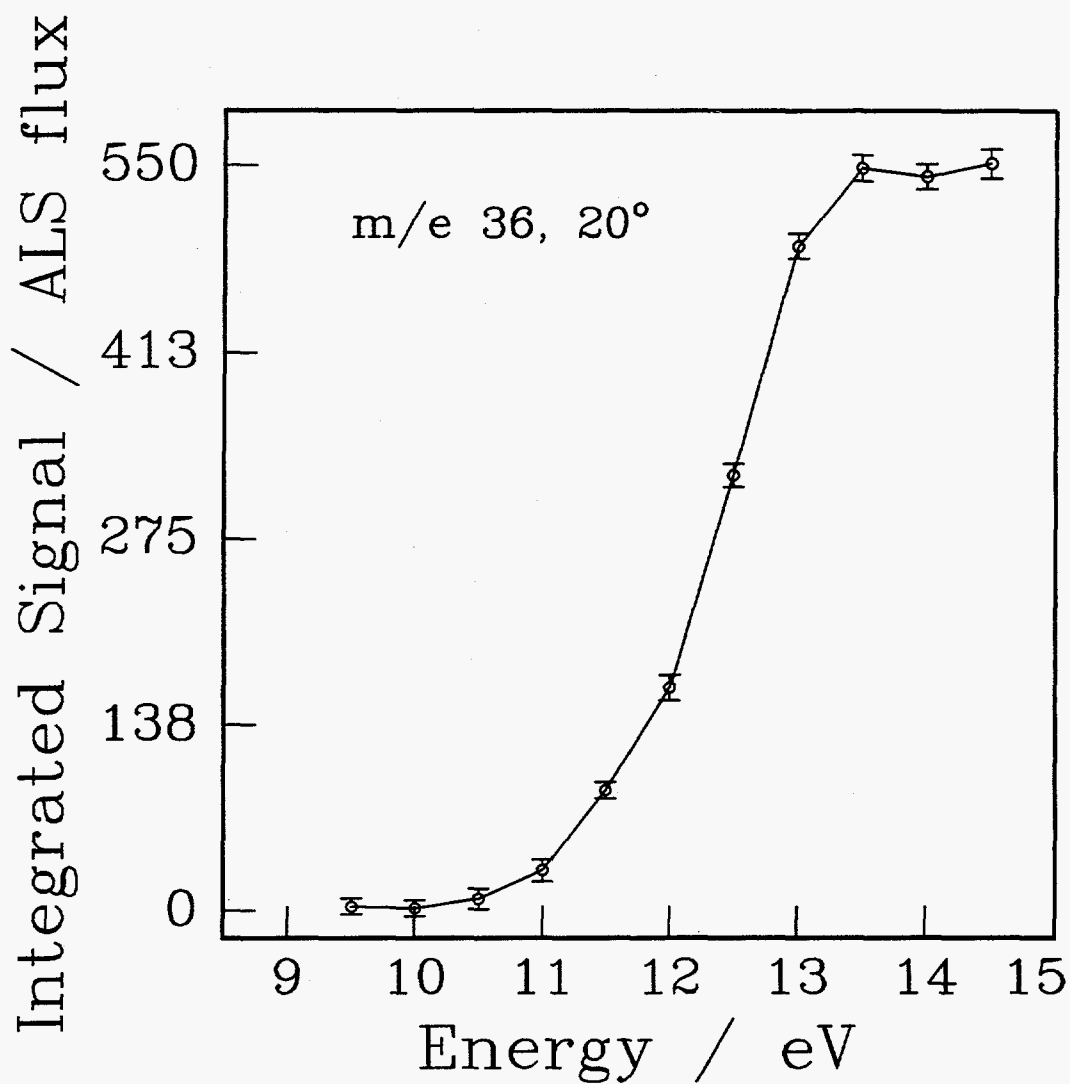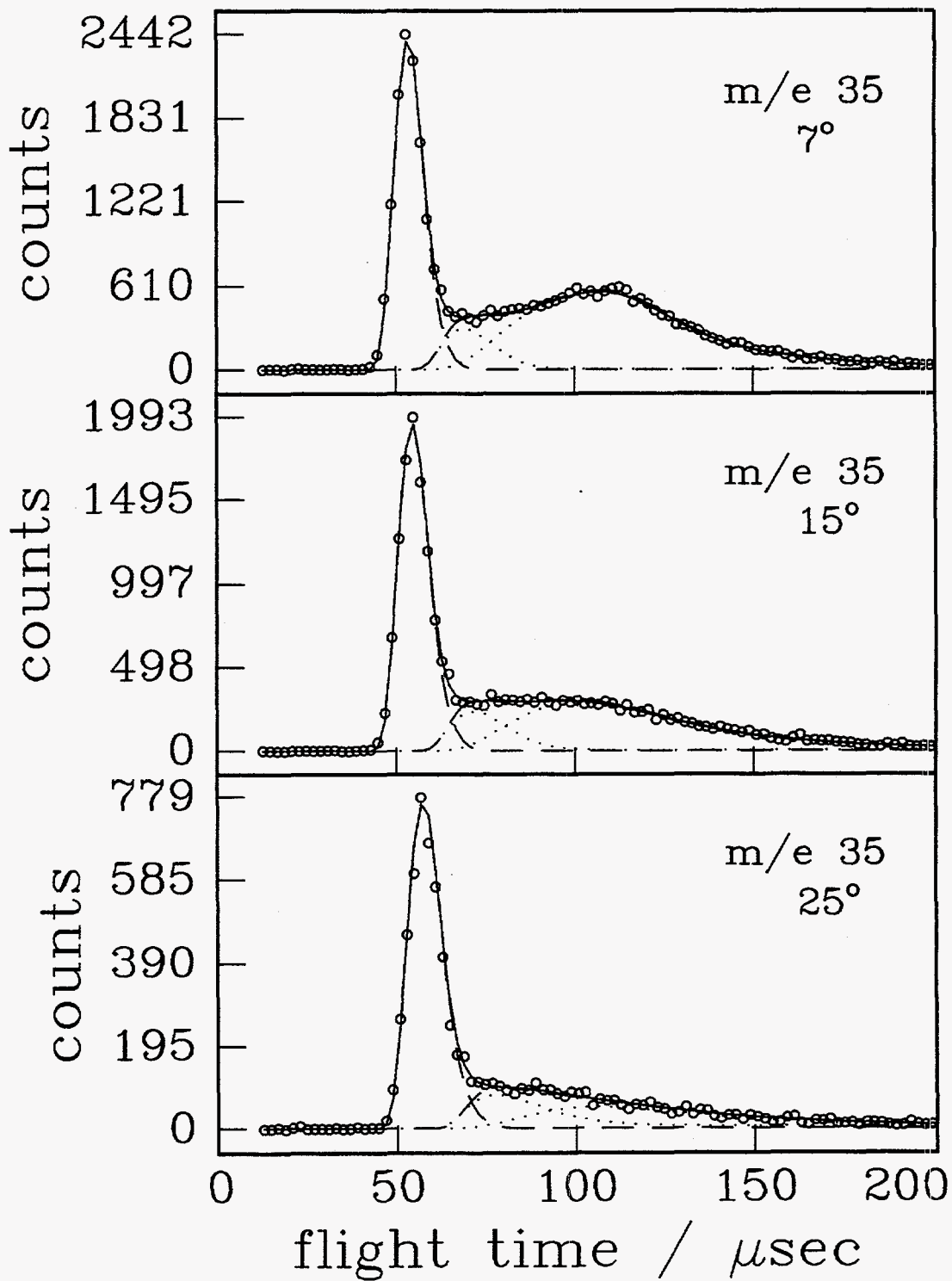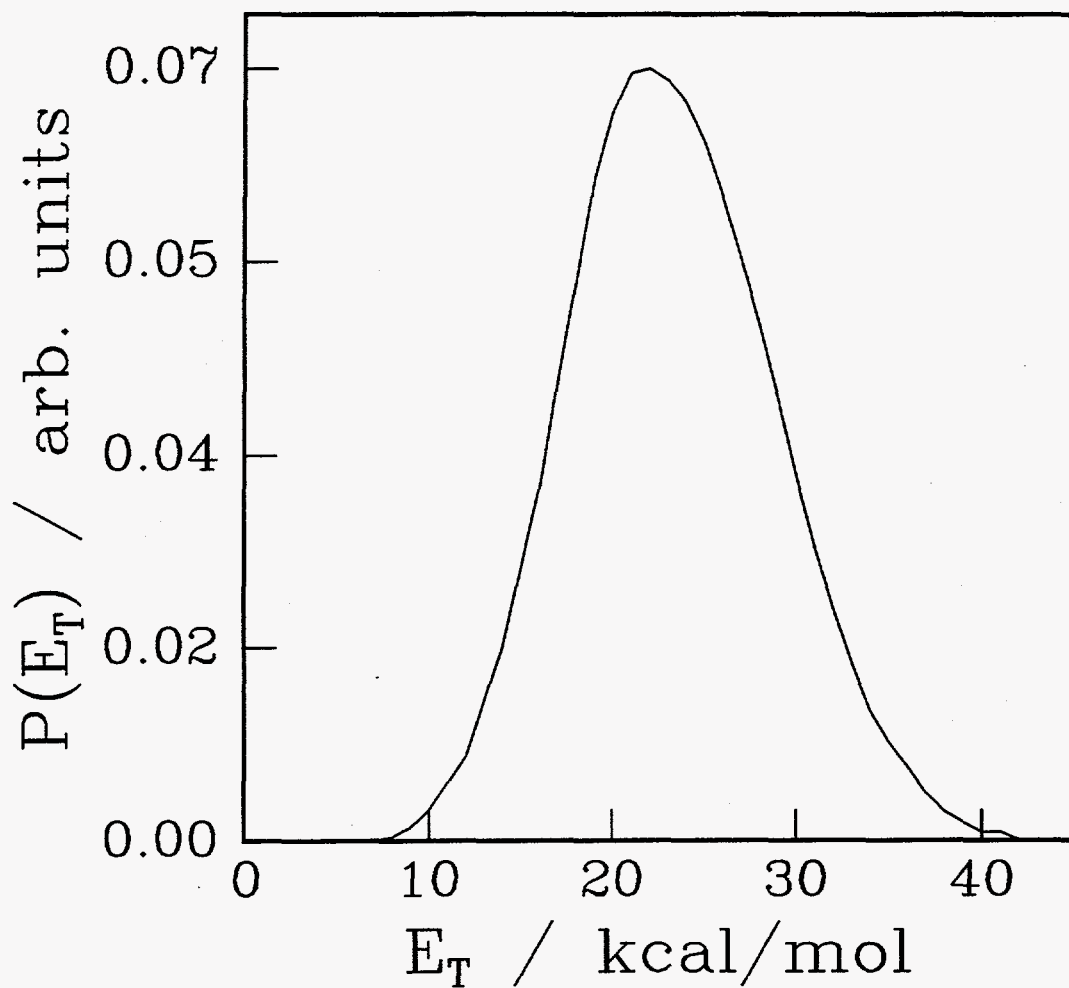figure 3
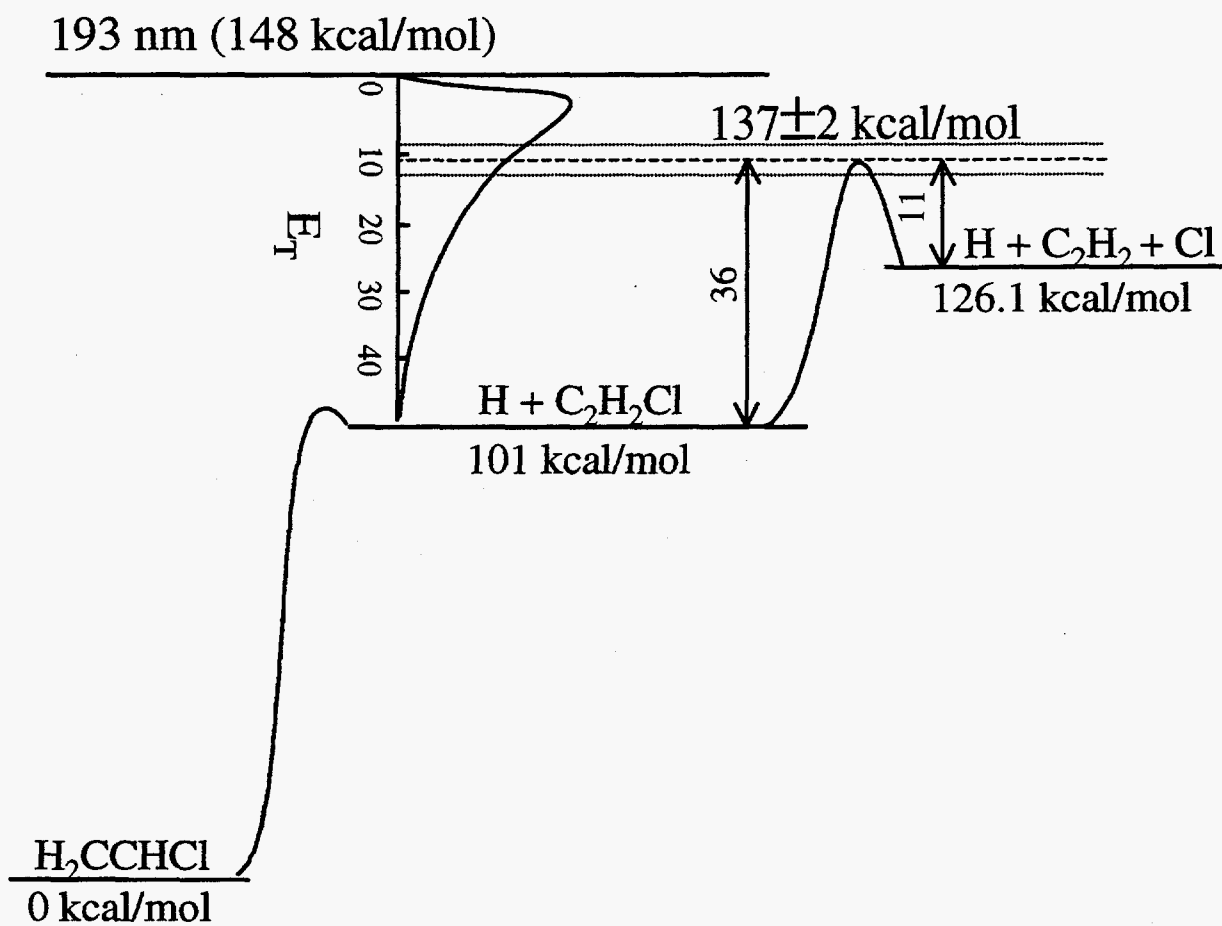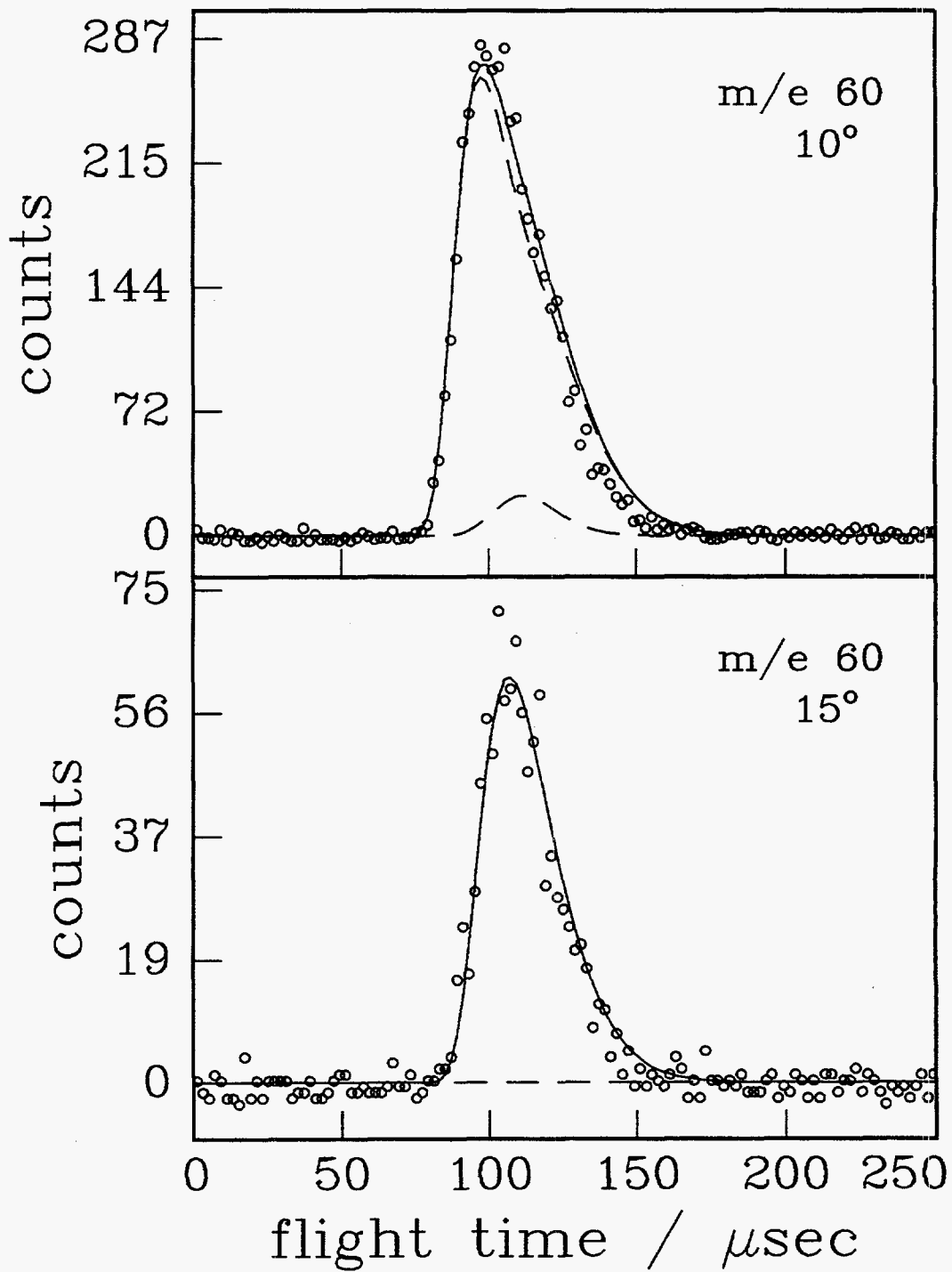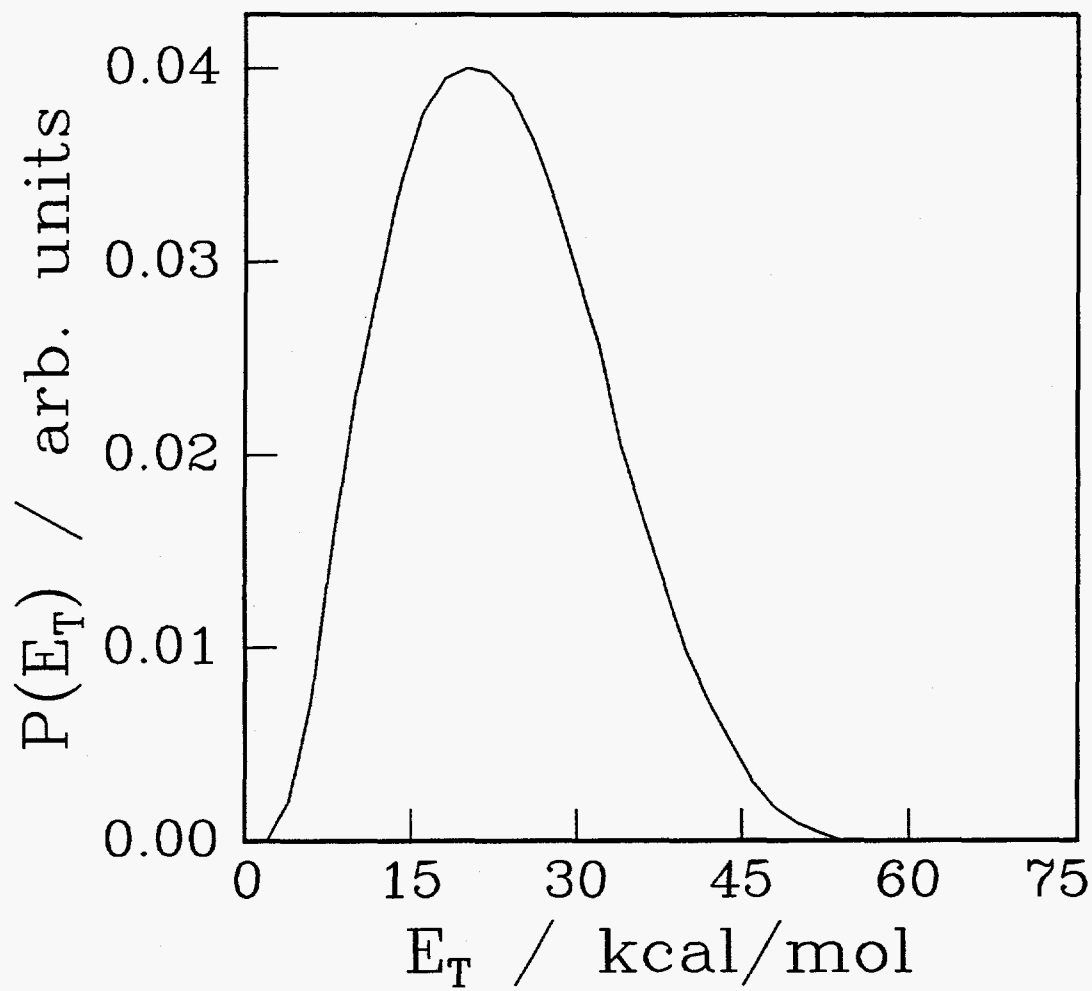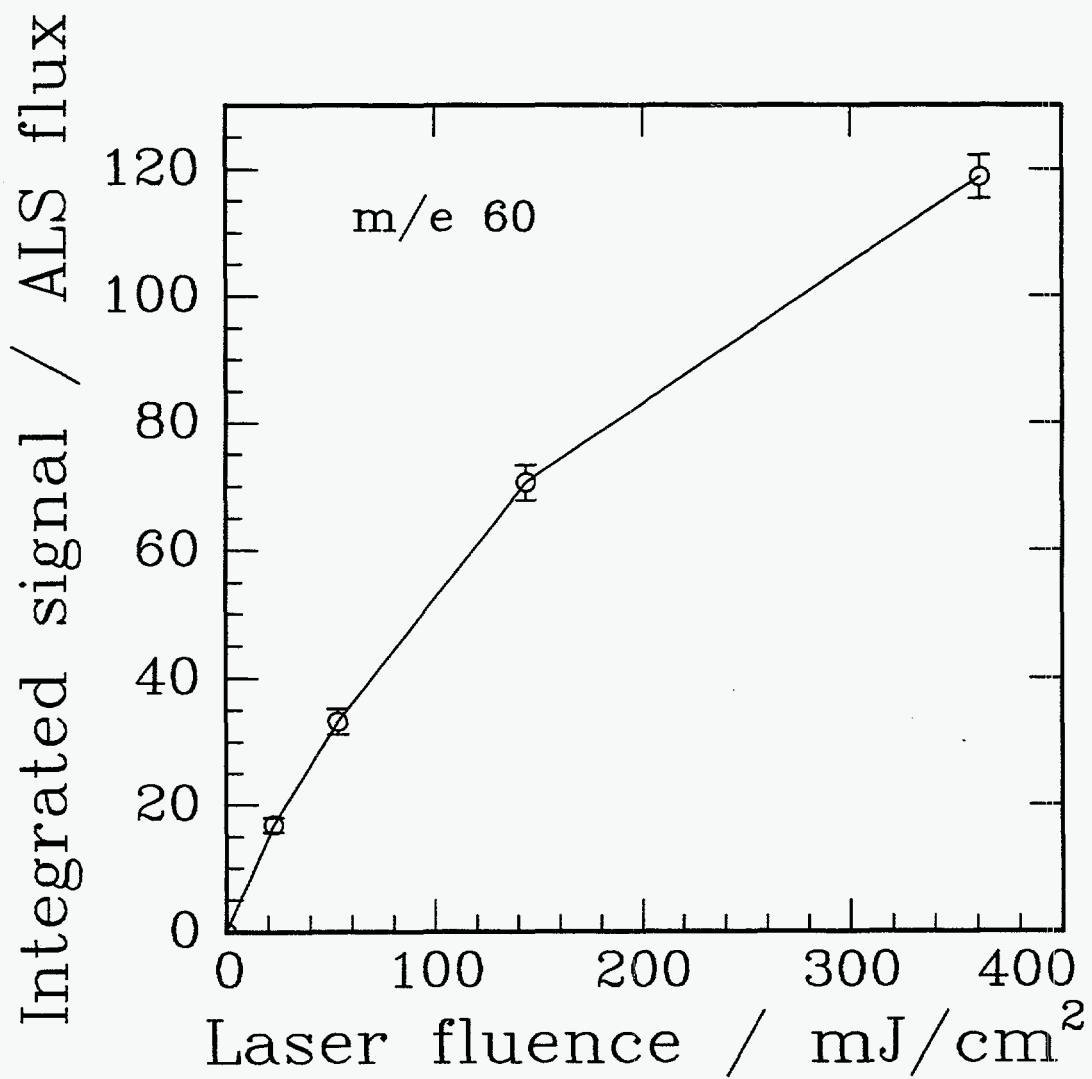
figure 4

figure 5

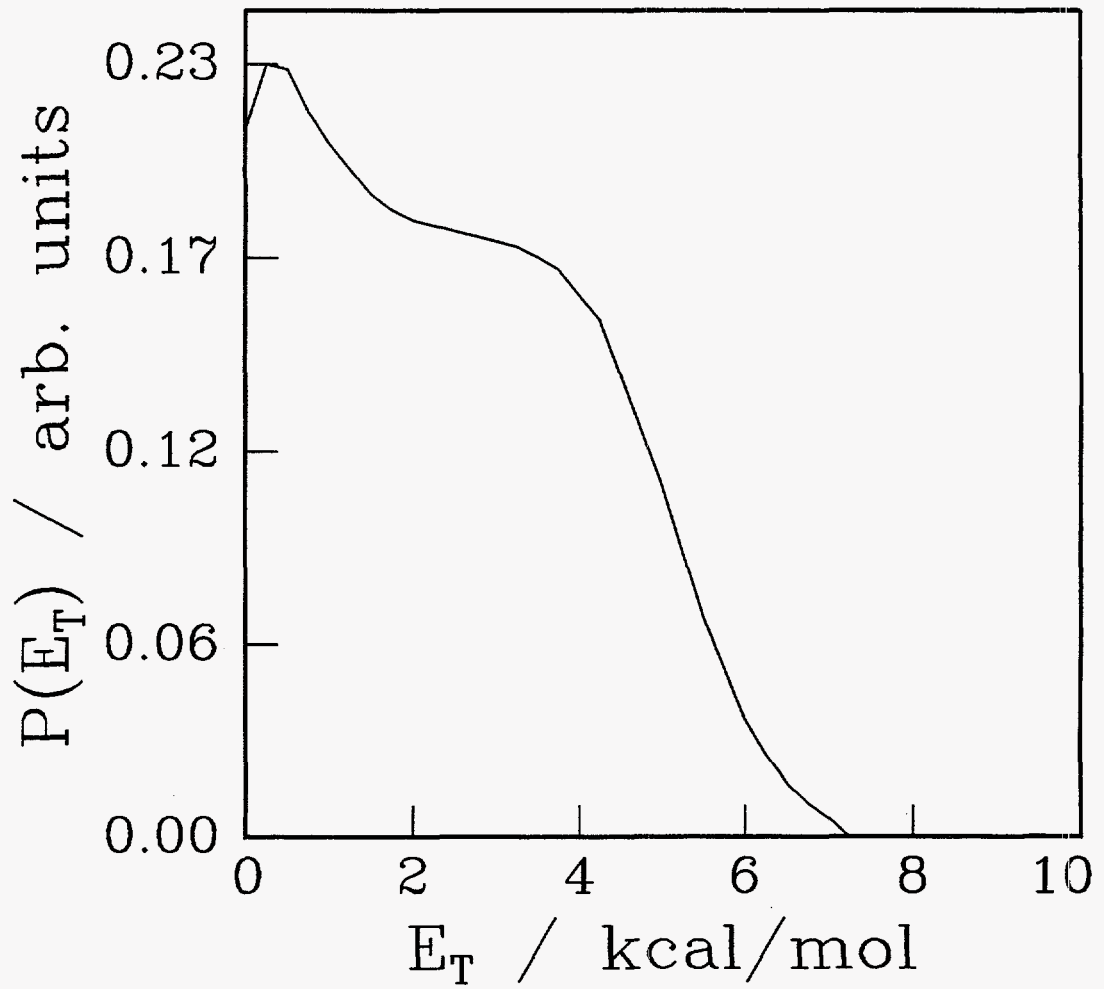figure 6

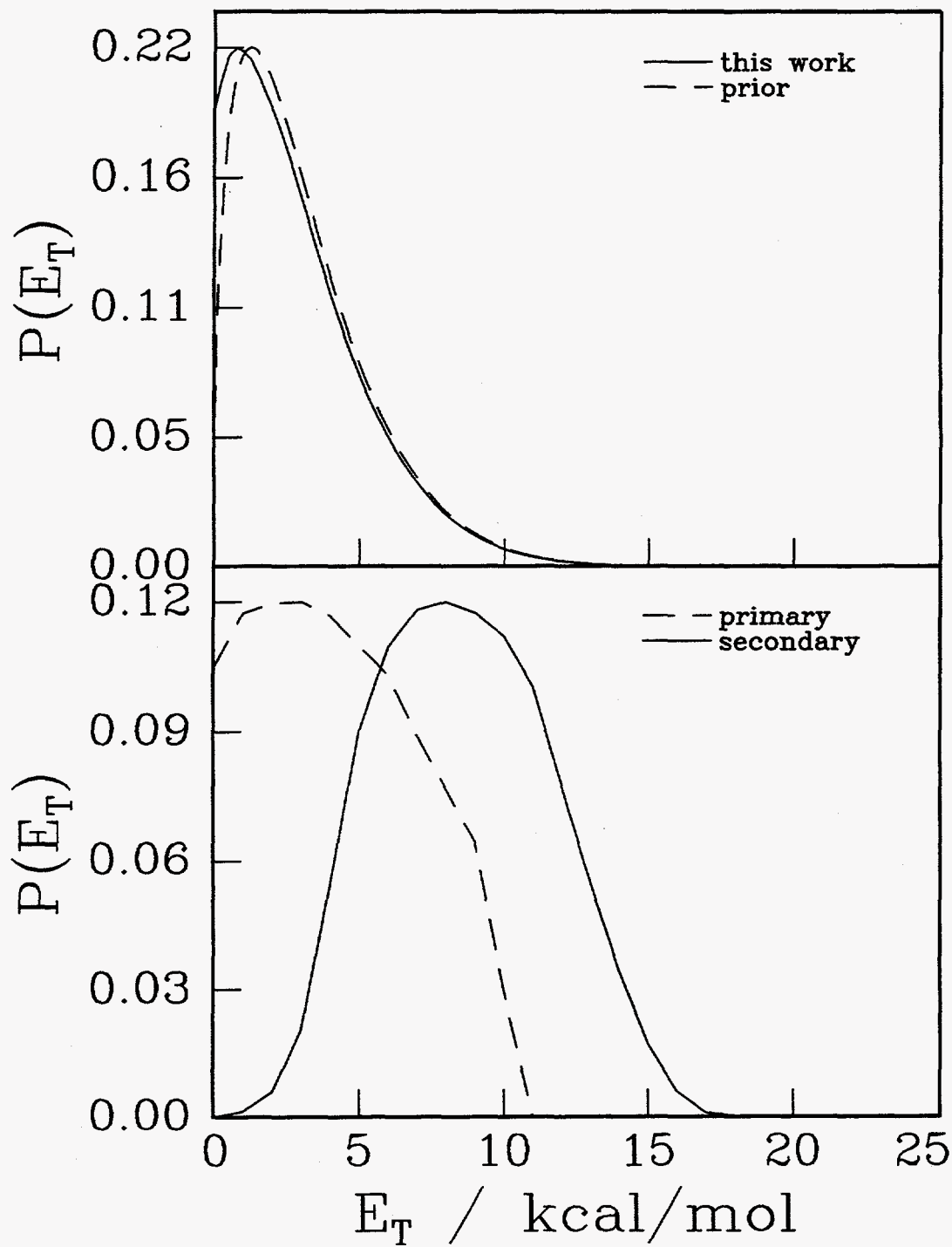figure 7

figure 8

figure 9

figure 10

figure 11

figure 12
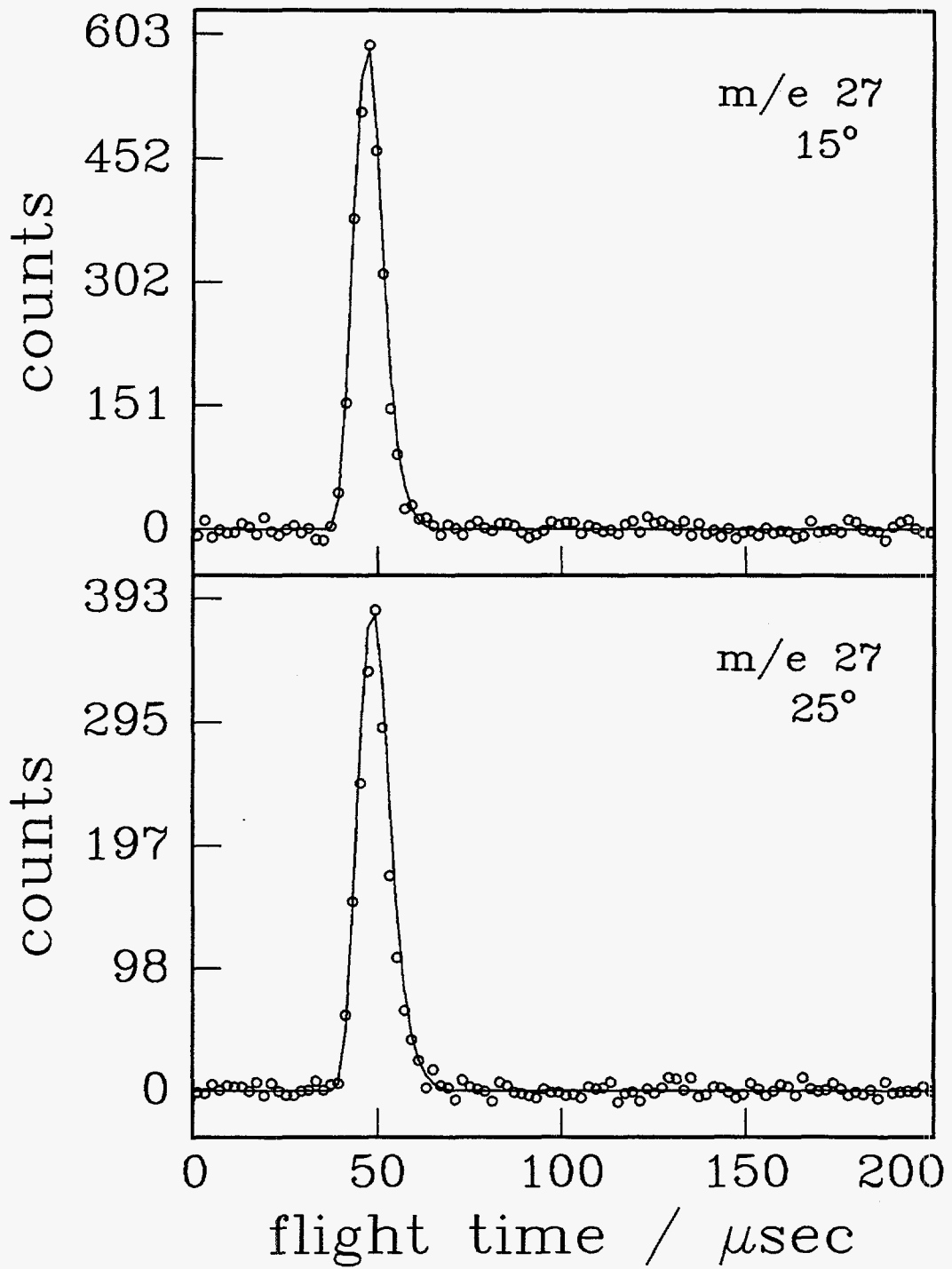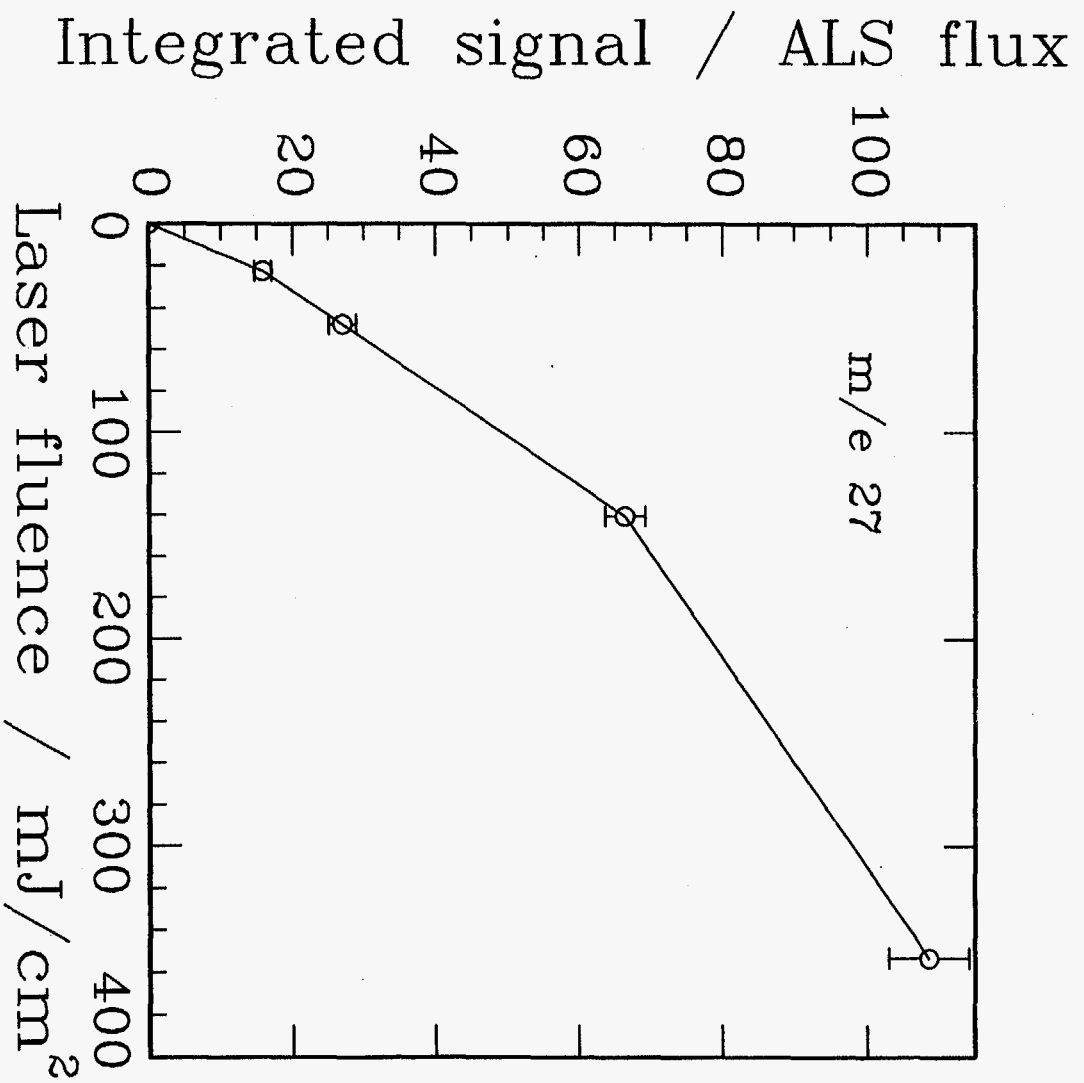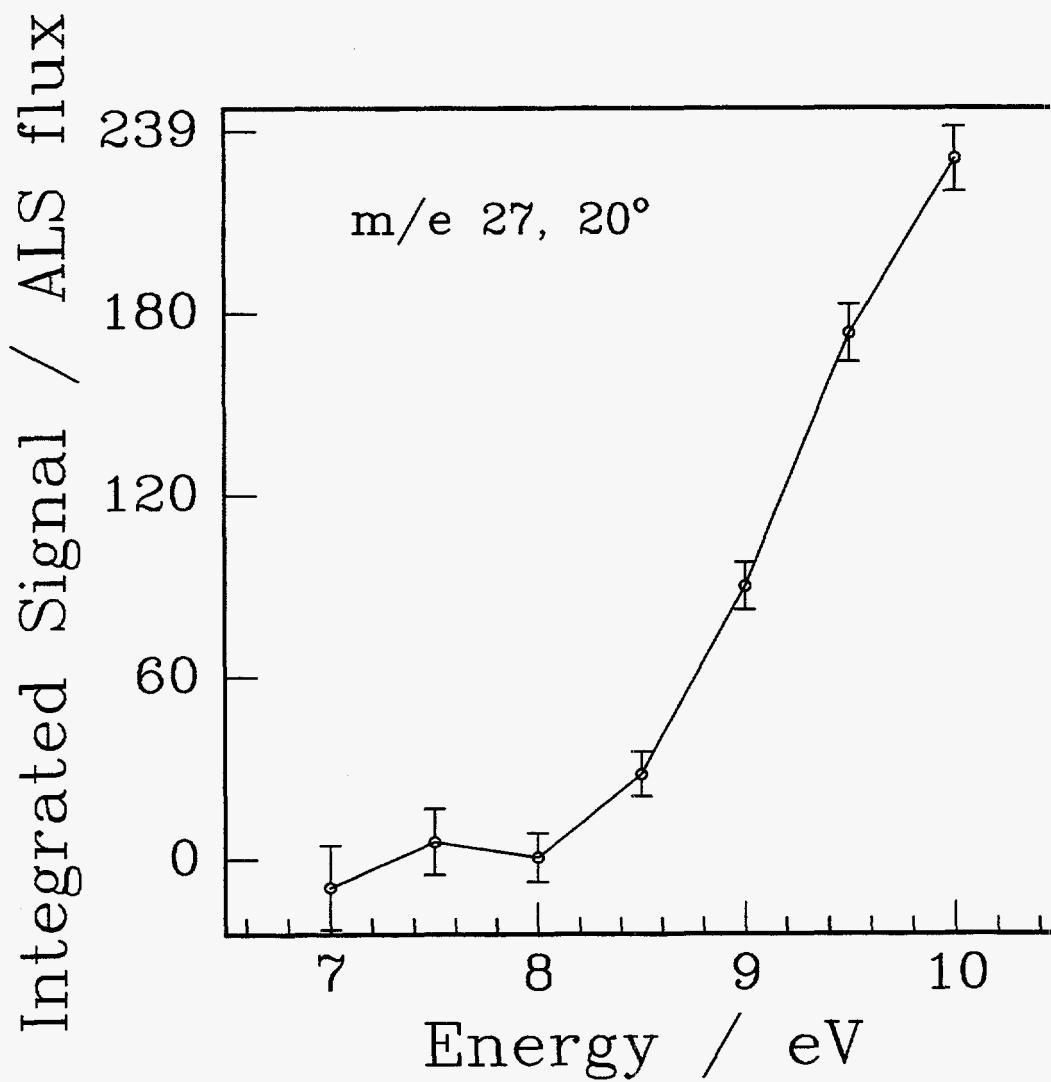
figure 13

figure 14

figure 15
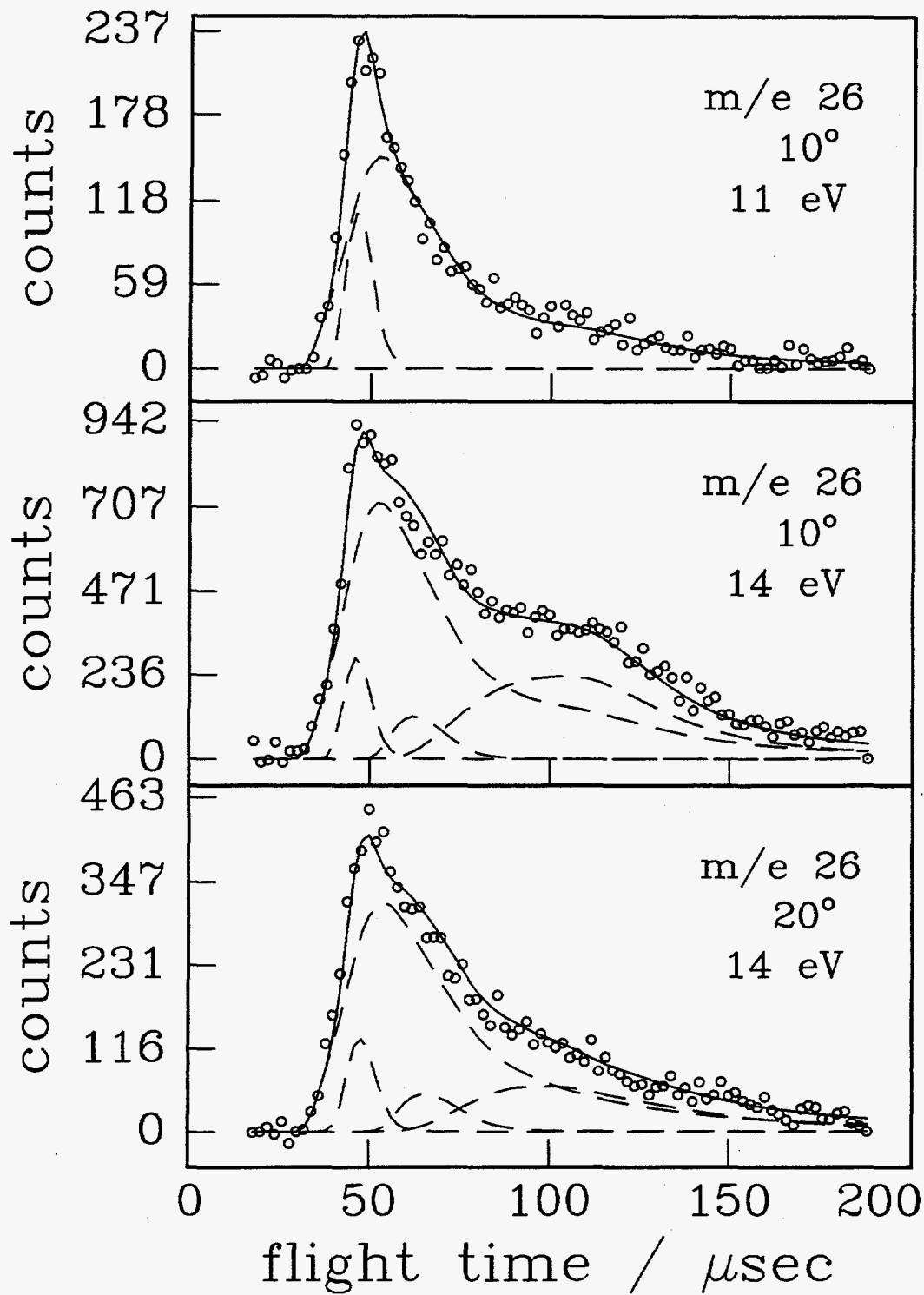
figure 16

figure 17

figure 18

Chapter 5

Reactive Scattering: Hydrogen atom abstraction from propane by atomic chlorine

Abstract

We have used the crossed molecular beam technique to study the hydrogen atom abstraction from propane by atomic chlorine over a wide range of collision energies. We have measured laboratory TOF spectra and angular distributions for E_{coll} = 8.0, 11.5, and 31.6 kcal/mol. Center-of-mass flux maps were generated from the measured laboratory distributions. The results demonstrate two distinct reaction mechanisms that depend on the impact parameter of the reactive collision. Large impact parameter collisions proceed *via* a stripping mechanism resulting in forward scattered products with very little momentum change in going from reactant to product. The stripping reactions are most likely dominated by abstraction of secondary hydrogen atoms. Smaller impact parameter collisions lead to direct reactions with an impulsive recoil and are consistent with a preference for a collinear transition state geometry, -C-H-Cl. The larger energy along the line of centers in smaller impact parameter collisions most likely makes the effect of a larger barrier to abstraction of primary hydrogen atoms negligible leaving the ratio of primary to secondary hydrogen abstraction to be dictated by simple statistics.

1. Introduction

Hydrogen atom abstraction from saturated hydrocarbons by free radicals are reactions of great importance in both atmospheric and combustion chemistry. While there is a wealth of available kinetic information about this class of reactions, by comparison studies investigating the detailed dynamics of these systems are considerably less abundant.

Using molecular beam methods and laser induced flourescence (LIF), Andresen and Luntz measured the internal state distributions of the OH products from the reaction of $O(^3P)$ with a number of alkanes.[1] The alkanes were chosen to provide a comparison between abstraction of a primary [RCH_2-H, $ex.$ $C(CH_3)_4$], secondary [R_2CH-H, $ex.$ c-C-$_6H_{12}$], or tertiary [R_3C-H, $ex.$ $(CH_3)_3CH$] hydrogen atoms. The authors reported only ~2% of the available energy was partitioned into rotation in the OH products. The abstraction of the different types of H atoms resulted in very little change in the rotational distributions. This was interpreted ás being indicative of a collinear intermediate configuration (R-H-O) for abstraction of all three types of H atoms. There was only slight broadening of the rotational distributions over a range of collision energies demonstrating the narrow cone of acceptance for reaction about the collinear geometry. Unlike the rotational distributions, the OH(v=1/v=0) population ratios showed a clear dependence on the type of H atom abstracted. Abstraction of primary hydrogen atoms almost exclusively produced OH(v=0) while secondary H atoms resulted in ~25% of the OH products in v=1

and abstraction of tertiary H atom produced slightly more OH(v=1) than OH(v=0). The difference in the vibrational distributions was attributed to the difference in energetics for abstraction of different hydrogen atoms. The exothermicity of the reactions increases from –2.3 kcal/mol for primary H atoms to -7.0 kcal/mol for secondary H atoms and –10.3 kcal/mol for tertiary H atoms. The activation energies increase in the order tertiary <secondary<primary. The argument invoked was that in the less exothermic primary H atom abstraction, which has a larger activation barrier, the transition state geometry should be more product like leading to less vibrational excitation. As the reaction becomes more exothermic with a lower activation energy, primary>secondary>tertiary, the transition state becomes more reactant like and the result is greater product vibrational excitation. The authors produced good agreement with the experimental results using quasiclassical trajectory calculations assuming a triatomic model for the reaction, R-H-O.[2] The agreement demonstrated the validity of treating the hydrocarbon radical, R, as a structureless particle in these abstraction reactions with the dynamics being dominated by the interaction between the $O(^3P)$ atom and the reactive C-H bond.

Recently, hydrogen atom abstraction from small alkanes by atomic chlorine has been investigated in detail under single collision conditions using resonance enhanced multiphoton ionization (REMPI) of the HCl products and core extracted ion time of flight (TOF) methods. These experiments take advantage of the anisotropic distribution of Cl photoframents in the photodissociation of Cl_2 to generate Cl reactants with a well know velocity and angular distribution. The REMPI ionization of HCl provides nascent rovibrational product state distributions and analysis of the core extracted ion TOF

profiles leads to laboratory velocity distributions. Making assumptions about the c.m. speed distribution, c.m. angular distributions can be obtained. These methods have been used by Zare and coworkers and Dagdigian and coworkers to measure state selected differential cross sections for HCl products in the reactions of Cl with a number of saturated hydrocarbons from methane to isobutane.[3,4,5,6,7,8]

The reaction of Cl with methane in its ground vibrational state is slightly endothermic with an activation energy ~2-3 kcal/mol. At a collision energy of 3.7 kcal/mol HCl(v=1) is not thermodynamically accessible and the HCl(v=0) rotational population was found to be very cold.[3] The HCl products were scattered exclusively in the backward direction with respect to the relative velocity of the Cl reactant. Using a hard sphere model, strongly back-scattered products are correlated with small impact parameter (b) collisions. The backward scattering can be intuitively explained within the line-of-centers model[9] where only the collisions at small b lead to sufficient energy along the reaction coordinate to overcome the barrier to reaction. Very low rotational excitation and the strong backward scattering indicate that the transition state for reaction is tightly constrained about a linear geometry, H$_3$C-H-Cl, analogous to the abstraction reactions of O(^{3}P) mentioned above.

At the same collision energy, vibrational excitation of the methane reactant, v_3=1, leads to a significant change in the reaction dynamics and a substantial enhancement in the total reactive cross-section.[4] The additional available energy provided by excitation of the methane reactant makes the reaction to produce HCl(v=0,J) exothermic by ~7 kcal/mol and opens up the HCl(v=1,J) product channel which is endothermic by ~2

kcal/mol. The HCl(v=0,J) products are backward scattered in analogy to the reaction with methane in its ground vibrational state, however the HCl(v=0,J) products from the reaction with $CH_4(v_3=1)$ show greater rotational excitation. This was interpreted as demonstrating a similar reaction mechanism in both cases with the additional energy in the methane reactant allowing some degree of relaxation from the strict collinear intermediate geometry. The reactant vibrational energy provides some available energy along the reaction coordinate lessening the energy that must be provided from relative translation and increasing the range of b for reactive collisions. The HCl(v=1,J) products were found to have lower rotational excitation than the HCl(v=0,J) products and exhibited very different scattering. For low J HCl(v=1,J) products the scattering was strongly in the forward direction exhibiting a stripping type mechanism with reactions resulting from large b collisions. With increasing J in the HCl(v=1,J) products, the scattering begins to exhibit an additional component in the backwards direction. The backwards scattering becomes comparable to the component in the forward direction for HCl(v=1, J=3). Lower rotational excitation in the forward scatter products is consistent with the relatively weak interaction experienced in a large b stripping reaction where the CH_3 acts as a spectator. The more backward scattered HCl(v=1,J) products have a slight increase in rotational excitation generated by recoiling from the more severe interaction in a smaller b collision providing an additional torque on the departing HCl product.
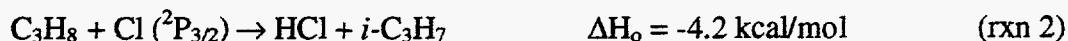
The reaction of Cl with C_2H_6 is slightly endothermic by ~2 kcal/mol and the authors again found only a small fraction (2%) of the available energy partitioned into HCl product rotation. Their analysis also determined that there was very little internal

excitation in the ethyl radical product. While these results were consistent with a developing picture of H atom abstraction that involved a direct reaction with a collinear intermediate reaction geometry, a nearly isotropic product angular distribution was seemingly at odds with the previous results for the $Cl + CH_4$ system. The authors explained the difference in the scattering as a result of the greatly reduced reaction barrier in the C_2H_6 reaction. The substantially lower barrier to reaction means that very little of the total translational energy is required along the reaction coordinate in order to produce a reactive collision. Therefore, the restriction on b for reactive collisions between Cl and $CH_4(v=0)$, which comes from the necessity to provide enough energy along the reaction coordinate to overcome the barrier, is almost completely relaxed for ethane. This allows almost every collision between Cl and C_2H_6 to lead to a reaction. The result is a nearly isotropic product angular distribution that is still consistent with the proposed direct reaction mechanism leading to very little internal excitation of the products.

Using the same technique, in addition to the reaction of Cl with methane, Varley and Dagdigian have extended their studies to include larger hydrocarbons investigating the reactions of Cl with propane and isobutane.[6-8] Collision energies were 7.4 kcal/mol and 8.1 kcal/mol respectively. The larger hydrocarbons are complicated by the addition of secondary, in the case of propane, and tertiary, in the case of isobutane, H atoms that compete for abstraction. Abstractions of all three types of H atoms are exothermic with the exothermicity increasing tertiary>secondary>primary. Using isotopically labeled reactants the authors were able to separate abstraction of the different H atoms. Both secondary and tertiary H-atoms, from propane and isobutane respectively, were

abstracted preferentially as compared with the neighboring primary H atoms. This result was noted previously for propane by Yen *et al.*[10] The HCl/DCl rotational distributions were found to be cold, in agreement with the previous hydrocarbons studied, again indicating a linear intermediate geometry. Abstraction of the primary hydrogen atoms in both molecules led to mostly backward scattered products, while secondary and tertiary H atom abstraction produced more isotropic and sideways scatter products respectively. In addition, slightly higher rotational excitation of the HCl/DCl products resulted from abstraction of secondary or tertiary H atoms compared with primary H atoms. The greater reactivity, slightly higher rotational excitation of the products, and more isotropic scattering reflects a larger acceptance about the collinear intermediate geometry that can lead to a reactive collision. Reactions over a large range of b are consistent with the very low activation barriers reported for both of these reactions from kinetic studies.[11] The greater propensity for backwards scattering and the slightly lower rotational excitation in the HCl/DCl products from abstraction of primary H atoms may also suggest a slightly higher barrier to reaction compared with the negligible barrier for abstraction of secondary or tertiary H atoms.

In this study we report the first crossed molecular beam investigation of chemical reaction dynamics using tunable VUV synchrotron radiation to probe the scattered reaction products. We have investigated the hydrogen abstraction reaction from propane by atomic chlorine $(Cl,^2P_{3/2})$ for collision energies ranging from 8.0 kcal/mol to 31.6 kcal/mol. As mentioned above there are two different possible reactions depending on whether a primary or secondary hydrogen atom is abstracted, reactions 1 and 2.[11]

$$C_3H_8 + Cl\ (^2P_{3/2}) \rightarrow HCl + n\text{-}C_3H_7 \qquad \Delta H_o = -2.0\ kcal/mol \qquad (rxn\ 1)$$

$$C_3H_8 + Cl\ (^2P_{3/2}) \rightarrow HCl + i\text{-}C_3H_7 \qquad \Delta H_o = -4.2\ kcal/mol \qquad (rxn\ 2)$$

The rate constant for this reaction has been reported at $(1.2\text{-}1.4)\times10^{-10}\ cm^3$ molecules^{-1} s^{-1} and the temperature dependence over a range 220-600 K produced a very small activation energy of 40 K.[11]

The crossed molecular beam technique using "universal" detection, electron impact ionization of the scattered reaction products followed by a quadrupole mass filter and Daly ion counter, has proven to be one of the most powerful tools in obtaining an complete picture of bimolecular reaction dynamics under single collision conditions for an extensive list of chemical reactions.[12,13] However, the hydrogen atom abstraction reaction provides a particular challenge to this technique. Crossed molecular beam reactive scattering experiments generate an extremely small number density of products at the detection region placing a premium on detection sensitivity for the reaction products. Discriminating against the large background from scattered reactant ^{35}Cl and ^{37}Cl when attempting to detect the signal from HCl products requires very high mass resolution. Very high mass resolution is associated with very low quadrupole transmission thus greatly reducing the product signal. There is also background from HCl contamination in the Cl beam. Detection of the C_3H_7 product is even more problematic since the scattered C_3H_8 reactant will dissociatively ionize to $C_3H_7^+$ (as well as all $C_{n\leq3}H_{n\leq8}^+$) in the electron bombardment ionizer generating tremendous background

that cannot be avoided with mass filtering. Using tunable VUV synchrotron radiation for photoionization of the product molecules in place of electron bombardment provides a solution to these problems. Tuning the VUV photoionization light to an energy above the ionization potential (IP) of the two C_3H_7 isomers but below the IP for the propane provides discrimination against any background generated from dissociative ionization of scattered propane reactants and allows detection of the C_3H_7 products with near background free conditions. In addition, the selective ionization also relaxes the need for mass discrimination between the scattered C_3H_8 reactants appearing at their parent mass, $C_3H_8^+$, and C_3H_7 products allowing much greater quadrupole transmission and thus increased product signal. This selectivity is provided without any spectroscopic knowledge about the products since this is a state independent single photon ionization of the products.

We have measured state average translational energy and angular distributions from the reaction of Cl + propane for collision energies ranging from 8.0 kcal/mol to 31.6 kcal/mol. At the lower collision energy we find a nearly isotropic scattering of the products. The forward scattered products show a larger translational energy release than the backward scattered products. This difference becomes more pronounced with increasing collision energy and there appears to be the emergence of two distinct scattering components at the higher collision energies. These experiments represent the first application of VUV synchrotron radiation for product ionization in a crossed molecular beam reactive scattering experiment and demonstrate the power and promise of this new technique for investigations of reactive collisions.

2. Experimental

The experiments were carried out at the Chemical Dynamics Beamline at the Advanced Light Source (ALS) at Lawrence Berkeley National Laboratory. A complete description of the experimental apparatus and setup is provided in Chapter 1 of this thesis. We present here only the details specific to this experiment.

The continuous propane beam was generated by expanding propane diluted in rare gas through a 0.25 mm stainless steel nozzle. Mixtures of 7% propane in He and 16% propane in He were used. The total stagnation pressure was typically 150 torr and the nozzle was fitted with a resistive heater and K-type thermocouple to allow heating up to 400 °C. The beam was skimmed once with a 0.5 mm stainless steel skimmer and the resulting beam had a full width at half maximum (FWHM) angular divergence of 0.7°.

The continuous molecular beam of atomic chlorine was generated by thermal dissociation of Cl_2 diluted in rare gas mixtures. Mixtures of 2% Cl_2 in He, 7% Cl_2:18% Ar:75% He, and 7% Cl_2 in Ar were used. The typical total stagnation pressure was 600 torr. The pyrolytic molecular beam source is shown in figure 1. The source consists of a high density graphite nozzle with a 0.15 mm opening that is spring loaded into a resistively heated silicon carbide (SiC) front plate. From the rear water cooled copper clamp to within 2 cm of the SiC heating element the wall of the graphite nozzle was 0.5 mm thick in order to reduce conduction of heat between the front and rear of the assembly. A ¼"

teflon line was attached to the rear of the graphite nozzle using a hand tightened cajon connection with a rubber O-ring seal for delivery of the Cl_2/rare gas mixture.

The top of figure 2 shows the integrated on axis signal for $^{35}Cl_2^+$(m/e 70) and $^{35}Cl^+$(m/e 35) as a function of the nozzle temperature for a mixture of 7% Cl_2 in He. The nozzle temperature was monitored using optical pyrometery and was found to be consistent with velocity analysis of supersonic rare gas beams to $\pm$ 75 °C. Under typical experimental conditions the nozzle was run at 1500-1550 °C providing dissociation of a large fraction of the Cl_2 as can be seen in the top of figure 2. Roughly 250 Watts (10 A, 25 V) across the SiC heating element was required to achieve a temperature of 1500°C. The Cl beam was skimmed twice, first by a water cooled nickel skimmer with a 1.0 mm opening and then again by a second 1.0 mm stainless steel skimmer. The resulting beam had a FWHM angular divergence of 1.0°. At 1500°C a Boltzmann distribution predicts that ~15% of the chlorine atoms will be in the exited spin-oribit state, $Cl(^2P_{1/2})$. With a large percentage of these being relaxed in the supersonic expansion, the majority of the Cl reactants will be in the ground spin-orbit state, $Cl(^2P_{3/2})$.

Periodic monitoring of the relative intensity of the Cl beam was performed using elastic scattering off a neat supersonic molecular beam of neon. A representative time of flight (TOF) spectrum is shown in the bottom of figure 2 for elastically scattered Cl using a mixture of 7% Cl_2 in He and a nozzle temperature of 1500 °C. The TOF spectrum was taken at a scattering angle of 50° with respect to the neon beam and the scattered Cl atoms were photoionized with 14.5 eV undulator radiation. A scattering angle of 50° is beyond the maximum elastic scattering angle for Cl_2, see the insert newton diagram in the

bottom of figure 2, allowing monitoring of the atomic Cl beam without interference from dissociative photoionization of Cl_2. The TOF spectrum in figure 2 was accumulated over only 3 minutes of signal averaging using the cross-correlation technique described below for product velocity analysis.

Instrument purity propane and high purity Cl_2 were obtained from Matheson and used without further purification.

The cross-correlation method was used for velocity analysis of the both reactant beams as well as the reactive scattering products.[14] A 17.8 cm diameter cross-correlation wheel with two identical 255-bit pseudorandom sequences of open an closed slots was used in front of the detector entrance to modulate the incident flux. The wheel was spun at 326.8 Hz resulting in a nominal resolution of 6 μsec in the TOF. The neutral flight length from the wheel to the undulator photoionization is 11.9 cm. For velocity analysis of either molecular beam, the beam being analyzed was placed on line with the detector axis, the aperture at the entrance to the detector was set to 0.075 mm, and the photoionization energy was set to 14.5 eV with Ar in the gas filter. The resulting beam parameters are listed in table1 and the most probable collision energies and spread in the collision energies are listed in table 2.

Detection of the scattered C_3H_7 reaction products was accomplished using a photoionization energy of 9.5 eV with Ar in the gas filter and using the MgF_2 filter. For an illustration of the importance of the MgF_2 filter see "The VUV PI Radiation" section in the first chapter of this thesis. The IP for propane is 10.9 eV and the IPs for the two C_3H_7 isomers are 8.1 eV (n-C_3H_7) and 7.5 eV (i-C_3H_7).[15,16] By using a photoionization

energy of 9.5 eV there is almost no background from ionization or dissociative ionization of the C_3H_8 reactants. We detect the C_3H_7 products at m/e 43 ($C_3H_7^+$) and the quadrupole is set with a mass resolution of ~1.2 amu FWHM to maximize ion transmission. TOF spectra were recorded for C_3H_7 products at laboratory scattering angles of –10° to 110° with respect to the propane beam. Signals were averaged for 1-3 hours at each angle and laboratory angular distributions were obtained by integration of the TOF spectra for each angle.

3. Results and Analysis

We measured laboratory angular and TOF distributions for C_3H_7 (at m/e 43, $C_3H_7^+$) products at three center of mass (cm) collision energies, E_c = 8.0, 11.5, 31.6 kcal/mol. The experimental conditions for each collision energy are listed in table 2. Newton diagrams for the three collision energies are shown in the bottom of figures 3, 9, and 15 respectively. The circles in the Newton diagrams represent the maximum recoil for C_3H_7 products given the available energy for the more exothermic abstraction channel, reaction 2.

CM angular distributions, $T(\Theta_{cm})$, and translational energy distributions, $P(E_T)$, were generated from the laboratory angular distributions and TOF spectra using the forward convolution technique. The forward convolution technique is discussed in detail in the "Data analysis" section of Chapter 1 of this thesis. The data demonstrated a strong dependence of the $P(E_T)$ on the cm scattering angle. In general, the forward scattered

C_3H_7 products involved a much larger translational energy release than the products scattered in the backwards direction. This effect was most apparent at the two higher collision energies. In order to obtain satisfactory fits to the experimental data using the forward convolution technique, four separate sets of decoupled $T(\Theta_{cm})$ and $P(E_T)$ were used. The effect of using multiple sets of decoupled $T(\Theta_{cm})$ and $P(E_T)$ is to provide an effective coupling of $T(\Theta_{cm})$ and $P(E_T)$ in the overall forward convolution fit to the data. The measured laboratory angular distributions and the forward convolution fits are shown in figures 3, 9, and 15 for the three different collision energies The TOF spectra and forward convolution fits are shown in figures 4, 10, and 16. The solid lines in figures 4, 10, and 16 are the forward convolution fits to the data.

As a result of only skimming the propane beam only once, there is a minor component in the TOF spectra from reactions of effusive propane reactants. This component is most apparent at a laboratory angle of 110° and at the lowest collision energy. We used the same forward convolution formalism to simulate the reactions of from the effusive propane reactants that was used for simulation of the scattering from the supersonic propane reactants. Since our current forward convolution software was not equipped to simulate an effusive reactant source, the effusive propane beam was modeled as a supersonic beam with a peak velocity of 300 m/s, $\Delta v/v = 1.0$, and a FWHM angular divergence of 7.0°. The contributions to the TOF spectra from effusive reactants are shown as the dash-dot-dash lines in figures 4, 10, and 16, and the dashed lines are the summed total of the products from both the supersonic propane reactants (solid line) and the effusive propane reactants. The forward convolution fits to the laboratory angular

distributions, the solid lines in figures 3, 9, and 15, are the summed total of contributions from both supersonic and effusive propane reactants. The inexact representation of the effusive propane reactants is the most likely reason behind our inability to obtain a satisfactory fit to the laboratory angular distributions at $110°$. It is at this laboratory angle, $110°$, where the products from the effusive propane reactants have the greatest relative contribution to the total measured product number density.

The result of the forward convolution analysis is a best fit cm flux distribution, $I_{cm}(\Theta, E_T)$. The best-fit total cm flux and average translational energy release, $<E_T>$, are shown as a function a cm angle in the bottom and top respectively of figures 5, 11, and 17 for the three collision energies. The $P(E_T)$ at three cm angles are shown in figures 6, 12, and 18, and the total cm velocity flux maps are shown in figures 7, 13, and 19 with both 2-D contour maps and 3-D wire plots. A summary of the cm translational energy release at four cm angles is provided in table 3.

At $E_{coll}=8.0$ kcal/mol the cm angular distribution is isotropic with $<E_T>$ largest in the forward direction, reaching a minimum at $\Theta_{cm}=90$, and increasing toward scattering in the backward direction, figure 5. At $E_{coll}=11.5$ kcal/mol the scattering is still nearly isotropic with small peaks appearing in the forward direction $(\Theta_{cm}\sim10°)$ and in the sideways direction $(\Theta_{cm}\sim100°)$. The $<E_T>$ is at a maximum in the forward direction and decreases out to $\Theta_{cm}=90°$. From $\Theta_{cm}=90°$ to $\Theta_{cm}=180°$ $<E_T>$ remains constant, figure 11. The angular distribution at $E_{coll}=31.6$ kcal/mol has similar features to $E_{coll}=11.5$ kcal/mol. Comparison of figures 11 and 17 shows the forward scattered component at $E_{coll}=31.6$ kcal/mol has increased relative to the sideways/backward scattering and demonstrates

broadening toward sideways angles. The sideways/backward scattering is nearly unchanged from E_{coll}=11.5 kcal/mol to E_{coll}=31.6 kcal/mol with $<E_T>$ remaining constant from Θ_{cm}=90°-180° and a small peak appearing in the angular distribution at Θ_{cm}~100°. The $P(E_T)$s are similar in shape at all of the collision energies, figures 6, 12, and 18. The $P(E_T)$s are all peak well away from 0 kcal/mol with the maximum probability occurring at higher energies for smaller cm scattering angles. All of the $P(E_T)$s are fairly broad with a FWHM ~25-30% of the available energy.

At the two higher collision energies we are able to separate the products into two scattering components based on the clear difference in translational energy release for the forward scattered products compared with the sideways/backwards scattered products. These two components are most apparent at E_{coll}=31.6 kcal/mol and can be seen in the contour plot at the bottom of figure 19. The separation of these two components is shown by the dashed lines in the angular distributions in figures 11 and 17. The two scattering components are also illustrated with 3-D flux maps in figures 14 and 20 showing the slower sideways/backward component at the bottom, the faster forward scattered component in the middle, and the total flux map at the top.

Photoionization spectrum of the propyl radical. We also report the photoionization spectrum for the propyl radical between 6.5 eV and 10.0 eV. Figure 8 shows the integrated signal as a function of the PI energy at m/e 43 ($C_3H_7^+$) for a collision energy of 8.0 kcal/mol and a laboratory scattering angle of 10°. The apertures defining the VUV undulator radiation were set at 5x4 mm resulting in an energy resolution of $\Delta E/E$=2.5% FWHM, see chapter 1 of this thesis. Taking into account the

width of the VUV PI radiation, figure 8 shows a photoionization onset of 7.5±0.3 eV in

excellent agreement with the reported value for the IP of 7.5 eV for i-C_3H_7.[16] From table

3, the average translation energy release for forward scattered products at E_{coll}=8.0

kcal/mol is ~60% of the 12.2 kcal/mol available energy or ~7.3 kcal/mol. This leaves

~4.9 kcal/mol on average in internal energy of the two products. Varley *et al.* have

reported very little internal excitation of the HCl products, ~2% of the available energy,

at a similar collision energy of 7.4 kcal/mol. Therefore, the majority of the 4.9 kcal/mol

of internal energy must be partitioned into the C_3H_7 products and the photoionization

onset in figure 8 represents i-C_3H_7 radicals with $<E_{int}>$~4.5 kcal/mol. Since it is possible

for internal energy to red shift the photoionization onset (examples of this effect can be

found throughout the rest of this thesis), our measure PI onset of 7.5±0.3 eV represents an

upper limit to the true vertical ionization energy of internally cold i-C_3H_7 radicals. While

the resolution of our measurement is not high, this does represent a direct measurement

of the photoionization onset for an unstable free radical with a known internal energy.

We are able to identify the presence of the i-C_3H_7 isomer at θ_{lab}=10° based on the

photoionization onset and we have demonstrated the ability of ES1 to measure the

photoionization onsets of reactive scattering products at given laboratory scattering

angles.

4. Discussion

Based on our measurements we can immediately eliminate the formation of a reaction complex with a lifetime comparable to or longer than its rotational period. Our measured angular distributions do not exhibit the forward/backward symmetry associated with a long lived complex and there is a strong dependence of $P(E_T)$ on $T(\Theta_{cm})$. The large partitioning of energy into translation is also contradictory to the statistical division of available energy traditionally found in the decomposition of a long lived reaction complex. All of our results are consistent with a direct reaction mechanism in agreement with the conclusions from previous investigations for H atom abstraction from saturated alkanes.[3-8] The transition states have been calculated by Bottoni *et al.* to be collinear (C-H-Cl) for abstraction of both primary and secondary hydrogen atoms from propane by a chlorine atom.[17] A collinear transition state is further supported by the small amount of rotational excitation in the HCl products measured by Varley and Dagdigian, ~2% of the available energy.[7]

Our measurements show very broad scattering at all measured collision energies with greater translational energy release for forward scattered products than sideways/backwards scattered products. At the two higher collision energies the difference in translational energy of the products is most apparent and suggests a separation of the scattering into two distinct reaction mechanisms. This separation is illustrated in figures 14 and 20.

Table 3 shows that the forward scattered products, $\Theta_{cm}=10°$, demonstrate an increase in the fraction of available energy partitioned into translation with an increase in

collision energy. As the collision energy is increased, the fraction of the available energy provided by the reaction exothermicity is decreased. In otherwords, the forward scattered products appear to have very little sensitivity to the energy released in the reaction. The contour maps in figures 7, 13, and 19 show that the forward scatter products have a maximum probability around the cm velocity of the incident propane reactants. With the small change in mass from propane reactant to propyl radical product, the lack of change in velocity reflects almost no change in momentum of the reactants as they pass through the transition state. The forward scattering and the lack of change in momentum of the reactants indicate reactions with large impact parameters and weak interactions at the transition state. These are hallmarks of the spectator/stripping reaction mechanism. The limited interaction of the reactants in a stripping mechanism is also consistent with the small rotational excitation in the HCl products measured by Varley and Dagdigian.[7]

The large impact parameters translate into a perpendicular approach (perpendicular to the C-H bond of the H atom being abstracted) and very little velocity along the reaction coordinate (C-H-Cl). Therefore, forward scattered products are limited to reactions with barriers that are small compared to the collision energy. Kinetic studies over a range 220-600 K found a very small activation energy of 40 K (~0.1 kcal/mol) consistent with our observed stripping mechanism.[11] This activation energy reflects abstraction of the H atoms with the smallest barrier. In accordance with the weaker C-H bond, _ab initio_ calculations found the barrier to abstraction of secondary H atoms, reaction 2, to be lower than the barrier to primary H atom abstraction, reaction 1. Our measured photoionization onset of 7.5±0.3 eV for forward scattered C_3H_7 products,

figure 8, is also consistent with production of i-C$_3$H$_7$ (IP=7.5 eV), reaction 2. From our results is likely that the forward scattering is dominated by reaction 2, particularly at lower collision energies.

As the collision energy is increased, the forward scattering component shows broadening to larger cm angles and an increase in intensity at the highest collision energy with respect to the sideways/backwards scattering, see figures 5, 11, and 17. This could indicate the opening/increase of a stripping mechanism for primary hydrogen atoms, reaction 1. Although the barrier to reaction 1 may only be ~1 kcal/mol above the near absent barrier for reaction 2 (*ab initio* values suggest the barrier could be as much as 4 kcal/mol above the barrier for reaction 2[11]), and our collision energies are 8.0 kcal/mol and above, the increase in forward scattering with collision energy is still consistent with an increase in stripping of primary hydrogen atoms. As mentioned above, the geometry of a stripping reaction leads to very little of the relative reactant translation along the C-H-Cl reaction coordinate. The situation is worse for primary H-atoms compared with secondary H-atoms. A collinear C-H-Cl approach in the case of primary H-atoms has an impact parameter that is ~1.5-2 times that of a collinear approach for secondary H-atoms. This means that the abstraction of a primary H-atom must also overcome a larger centrifugal barrier. With a stripping mechanism providing very little of the relative translational energy along the C-H-Cl reaction coordinate, we should still observe a limited increase in stripping of primary H-atoms with an increase in collision energy even for collision energies that are large compared to the small reaction barrier.

The sideways/backward scattered component is consistent recoiling from collisions at smaller impact parameters for reactions favoring a collinear approach, -C-H-Cl. The sideways/backward scattered component demonstrates a consistent partitioning of 50% of the available energy into translation at all three collision energies, see table 3. The strong coupling of internal energy in the products with the available energy is in clear contrast with the stripping seen in the forward direction and reflects the more sever interactions in a collision with a smaller impact parameter. Our measured translational energy release is consistent with an impulsive product recoil from a direct, exothermic reaction at smaller impact parameters. An impulsive recoil will impart a torque about the cm of the departing fragments with a larger collision energy leading to a larger impulse and greater internal excitation of the products. Initially, the cold HCl rotational distributions measured by Varley and Dagdiagian at a collision energy of 7.4 kcal/mol may appear to contradict an impulsive recoil from small b collisions.[7] However, a preferred collinear -C-H-Cl geometry would leave the impulse of the recoil primarily along the H-Cl bond with limited torque on the HCl product. Therefore, most of the available energy that is not partitioned into translation, 50%, is partitioned into internal energy of the C$_3$H$_7$ products. Note that a collinear C-H-Cl reaction geometry will have an impact parameter of ~0.6 Å for reaction 2 and 0.9-1.2 Å for reaction 1 leaving an impulsive recoil to impart a significant torque on the C$_3$H$_7$ products, consistent with our observed energy partitioning.[7]

As the collision energy is increased from 8.0 kcal/mol to 11.5 kcal/mol the backward scattering spreads to smaller cm angles and at the higher collision energies a

peak in the sideways direction, $\Theta_{cm} \sim 100°$, begins to emerge. We can use the line of

centers model which was successfully employed to explain the scattering from Cl +

vibrationally cold methane and ethane.[4,5] In this case we refer to the collinear C-H-Cl

coordinated as the line of centers, not the line between the cm of the reactants. As the

collision energy is increased, the range of impact parameters that impart sufficient energy

along the reaction coordinate to overcome the reaction barrier is increased leading to a

broader scattering distribution. With almost no effective barrier to abstraction of

secondary H-atoms, the spreading out of the backward scattering when increasing E_{coll}

from 8.0 kcal/mol to 11.5 kcal/mol suggests that a significant fraction of the

sideways/backward scattered products are the result of primary H-atom abstraction. Since

the impact parameter for sideways/backwards scattering (in a direct reaction) is relatively

small, there will be sufficient energy along the line of centers for reaction to occur in

almost every collision, especially for the higher collision energies. Therefore, it is likely

that abstraction of primary H-atoms will be the more dominant channel based simply on

the statistical advantage, outnumbering the secondary H-atoms 3:1. A preferred collinear

geometry, C-H-Cl, is also consistent with the peaking at $\Theta_{cm} \sim 100°$ for the two higher

collision energies. For abstraction of primary H-atoms, a preferred collinear C-H-Cl

geometry will have an impact parameter of 0.9-1.2 Å leading to preferred sideways

scattering of the products. The broad range of scattering in the sideways/backward

directions reflects the large range of impact parameters that lead to reaction.

In addition to measuring the HCl product state distributions Varley and Dagdigian

also measured the angular distributions for HCl and DCl products using $CD_3CH_2CD_3$.[7]

The DCl products showed sideways/backward scattering in good agreement with our conclusion that primary H-atom abstraction produces sideways/backward scattering, particularly at lower collision energies. The HCl products were more isotropically scattered. This is less consistent with our results. Although the secondary H-atom abstraction should proceed by both of the mechanisms we have observed, our results suggest that the stripping mechanism should be the more dominant mechanism for reaction 2. The Varley and Dagdigian results actually show a drop-off in scattering toward more forward angles. One possible explanation comes from the assumption made by Varley and Dagdigian of zero internal energy in the C_3H_7 product when analyzing the 1-D ion TOF spectra to generate cm angular distributions. The authors mention that increasing the internal energy to 5 kJ/mol had no significant effect on the resulting cm angular distribution. However, our results found 40-50% of the available energy partitioned into internal energy and this partitioning showed a strong dependence on the scattering angle. With the very small HCl internal energy measured by Varley and Dagdigian most of the internal energy must be in the C_3H_7 products. For their collision energy of 7.4 kcal/mol this corresponds to 3.0-3.7 kcal/mol of internal excitation in the C_3H_7 products or ~3 times the internal energy reported as having a minimal effect on the data analysis leading to the reported angular distributions.

As mentioned above, the sideways/backwards scattering we observe is consistent with the line of centers model used to describe the results of Zare and coworkers for Cl + vibrationally cold methane and ethane.[3-5] The reaction of Cl + $CH_4(v=0)$ produced exclusive backwards scattering since only small b collisions provided sufficient energy

along C-H-Cl to overcome the endothermic reaction barrier. In the case of ethane the

authors suggested that the sideways/isotropic scattering they observed was the result of a

greatly diminished reaction barrier compared with methane allowing nearly every

collision to lead to a reaction. There may also be a small effect the non-zero impact

parameter associated with a collinear reaction geometry also promoting sideways

scattering. However, this effect will be much less in Cl + ethane than Cl + propane since

a collinear geometry in ethane has an impact parameter of only ~0.17 Å compared with

0.9-1.2 Å for a primary hydrogen in propane. The smaller impact parameter for the

preferred geometry in ethane will also lead to significantly less rotational excitation of

the ethyl radical product in an impulsive recoil. A smaller internal energy helps avoid the

difficulty faced in the data analysis of Varley and Dagdigian for Cl + propane (see

paragraph above) when assuming near zero internal energy in the hydrocarbon radical for

analysis of the 1-D ion TOF spectra. Hydrogen atom abstraction in ethane should be

similar to abstraction of primary H-atoms from propane and the scattering from Cl +

ethane is similar to our sideways scattered products that we conclude are predominantly

from abstraction of primary H-atoms.

The stripping mechanism we observed is similar to the forward scattering

reported from $CH_4(v_3=1)$. The additional vibrational energy in the methane reactant was

suggested to significantly lower the barrier to reaction allowing reactions for large b

collisions. This is analogous to the smaller barrier for abstraction of secondary H-atoms

compared with primary H-atoms in propane. For H-atom abstraction from $CH_4(v_3=1)$ the

forward scattered HCl products were preferentially found in v=1 as a result of efficient

coupling between the v_3 vibration in the CH_4 reactants and the HCl products. With vibrationally cold propane reactants we expect the stripping reaction to lead to vibrationally cold HCl products, consistent with the measurements of Varley and Dagdigian.[7]

5. Conclusion

We have used the crossed molecular beam technique to investigate the reaction Cl + propane $\rightarrow$ HCl + C_3H_7 at three collision energies, 8.0, 11.5, and 31.6 kcal/mol. We have observed two distinct reaction mechanisms. Collisions with large impact parameters preferentially abstract a secondary hydrogen atom *via* a spectator/stripping reaction mechanism. There is an increase in the stripping component at the highest collision energy that may suggest stripping of primary hydrogen atoms when the collision energies is sufficiently high. The stripping mechanism is similar to the mechanism reported for forward scattering in the reaction Cl + $CH_4(v_3=1)$, however there have been no previous reports of a stripping mechanism for hydrogen atom abstraction from vibrationally cold saturated hydrocarbons. Collisions with smaller impact parameters involve a direct reaction mechanism with an impulsive product recoil and are consistent with a collinear C-H-Cl transition-state geometry. This channel is most likely dominated by abstraction of primary hydrogen atoms and is consistent with the reaction mechanism proposed for the analogous reactions Cl + $CH_4(v=0)$ and Cl + C_2H_6.

Table 1. Experimental beam parameters.

Beam Conditions	Peak Beam Velocity (m/s)	Speed Ratio (v/Δv)
Cl (2% Cl_2 in He)	3121	5.7
Cl (7%Cl_2,18%Ar,75%He)	1852	5.8
Cl (7% Cl_2 in Ar)	1382	7.0
C_3H_8 (7% C_3H_8 in He, nozzle at 270°C)	1931	8.6
C_3H_8 (16% C_3H_8 in He, nozzle at 20°C)	1200	11.0

Table 2. Experimental Conditions (cm collision energies).

Cl peak velocity (m/s)	C_3H_8 peak velocity (m/s)	cm collision energy (kcal/mol)	$\Delta E_{coll}/E_{coll}$
3121	1931	31.6	0.32
1852	1205	11.5	0.30
1382	1220	8.0	0.24

Table 3. Average Translational Energy Release

E_{coll} (kcal/mol)	E_{avail}[a] (kcal/mol)	$<E_T>/E_{avail}$ for given cm angle				$(\Delta<E_T>)_{max}$ (kcal/mol)
		$\Theta_{cm}=10°$	$\Theta_{cm}=50°$	$\Theta_{cm}=100°$	$\Theta_{cm}=160°$	
8.0	12.2	0.62	0.54	0.49	0.53	1.8
11.5	15.7	0.68	0.58	0.52	0.52	2.6
31.6	35.8	0.74	0.69	0.51	0.48	9.3

(a) Available energy for abstraction of the secondary hydrogen atom, reaction 2.

References

[1] P. Andresen and A. C. Luntz, *J. Chem. Phys.* **72**, 5842 (1980).

[2] A. C. Luntz and P. Andresen, *J. Chem. Phys.* **72**, 5851 (1980).

[3] W. R. Simpson, T. P. Rakitzis, S. A. Kandel, T. Lev-On, and R. N. Zare, *J. Phys. Chem.* **100**, 7938 (1996).

[4] W. R. Simpson, T. P. Rakitzis, S. A. Kandel, A. J. Orr-Ewing, and R. N. Zare, *J. Chem. Phys.* **103**, 7313 (1995).

[5] S. A. Kandel, T. P. Rakitzis, T. Lev-On, and R. N. Zare, *J. Chem. Phys.* **105**, 7550 (1996).

[6] D. F. Varley and P. J. Dagdigian, *J. Phys. Chem.* **99**, 9843 (1995).

[7] D. F. Varley and P. J. Dagdigian, *Chem. Phys. Lett.* **255**, 393 (1996).

[8] D. F. Varley and P. J. Dagdigian, *J. Phys. Chem.* **100**, 4365 (1995).

[9] R. D. Levine and R. B. Bernstein, *Molecular Reaction Dynamics and Chemical Reactivity*; Oxford University Press: New York, 1987.

[10] Y. Yen, Z. Wang, B. Xue, and B. Koplitz, *J. Phys. Chem.* **98**, 4 (1994).

[11] R. Atkinson, D. L. Baulch, R. A. Cox, R. F. Hampson, J. A. Kerr, and J. Troe, *J. Phys. Chem. Ref. Data* **21**, 1125 (1992).

[12] Y. T. Lee, J. D. McDonald, P. R. LeBreton and D. R. Hershback, *Rev. Sci Instrum.* **40**, 1402 (1969).

[13] Y. T. Lee, *Science* **236**, 793 (1987).

[14] K. Skold, Nucl. *Inst. Methods* **63**, 114 (1968); V. L. Hirshy and J. P. Aldridge, *Rev. Sci. Instrum.* **42**, 381 (1971); G. Comsa, R. David, and b. J. Schumacher, *Rev. Sci. Instrum.* **52**, 789 (1981).

[15] Handbook of Chemistry and Physics, D.R. Lide (CRC, Boca Raton, 1995).

[16] J. L Franklin, J. G. Dillard, H. M. Ronstock, J. T. Herron, K. Draxl, and F. H. Field, *Ionization Potentials, Appearance Potentials, and Heats of Formation of Gaseous Positive Ions*, Nat. Stand. Ref. Data Ser., Nat. Bur. Stand. (U.S.), June 1969.

[17] A. Bottoni and G. Poggi, *J. Mol. Struct.* **337**, 161 (1995).

Figure Captions

Figure 1:   Schematic drawing of the continuous pyrolytic molecular beam source used for generation of the atomic chlorine beam.

Figure 2:   Atomic chlorine beam diagnostics. (Top) Plot of the Cl and Cl_2 on axis intensities as a function of the nozzle temperature. (Bottom) Elastic scattering of the atomic chlorine beam off a neat beam of neon. See the inserted newton diagram.

Figure 3:   Laboratory angular distribution for C_3H_7 products and Newton diagram for a collision energy of 8.0 kcal/mol. The solid line is the forward convolution fit and the circles are the data.

Figure 4:   TOF spectra for C_3H_7 at 10 laboratory angles for a collision energy of 8.0 kcal/mol. Circles are the data, solid line is the forward convolution fit, dash-dot-dash line is the forward convolution fit for the effusive component (see text) and the dashed line is the total fit to the data.

Figure 5:   Average translational energy release (top) and total flux (bottom) as a function of cm angle. Collision energy is 8.0 kcal/mol.

Figure 6: $P(E_T)$ at three cm angles, 10°, 40°, and 120°, for a collision energy of 8.0

                kcal/mol.

Figure 7:   CM flux map for a collision energy of 8.0 kcal/mol.

Figure 8:   Photoionization spectrum for the C_3H_7 product at a laboratory angle of 10°

                and a collision energy of 8.0 kcal/mol.

Figure 9:   Laboratory angular distribution for C_3H_7 products and Newton diagram

                for a collision energy of 11.5 kcal/mol. The solid line is the forward

                convolution fit and the circles are the data.

Figure 10:   TOF spectra for C_3H_7 at 10 laboratory angles for a collision energy of 11.5

                kcal/mol. Circles are the data, solid line is the forward convolution fit,

                dash-dot-dash line is the forward convolution fit for the effusive

                component (see text) and the dashed line is the total fit to the data.

Figure 11:   Average translational energy release (top) and total flux (bottom) as a

                function of cm angle. Collision energy is 11.5 kcal/mol.

Figure 12: $P(E_T)$ at three cm angles, 10°, 50°, and 120°, for a collision energy of 11.5 kcal/mol.

Figure 13:   CM flux map for a collision energy of 11.5 kcal/mol.

Figure 14:   Separation of the two reaction mechanisms for a collision energy of 11.5 kcal/mol shown as 3-D flux maps. Bottom map is the sideways/backward scattered component, middle is the forward scattered stripping component, and the top is the total flux map.

Figure 15:   Laboratory angular distribution for C_3H_7 products and Newton diagram for a collision energy of 31.6 kcal/mol. The solid line is the forward convolution fit and the circles are the data.

Figure 16:   TOF spectra for C_3H_7 at 10 laboratory angles for a collision energy of 31.6 kcal/mol. Circles are the data, solid line is the forward convolution fit, dash-dot-dash line is the forward convolution fit for the effusive component (see text) and the dashed line is the total fit to the data.

Figure 17:   Average translational energy release (top) and total flux (bottom) as a function of cm angle. Collision energy is 31.6 kcal/mol.

Figure 18:   P(E$_T$) at three cm angles, 10°, 50°, and 120°, for a collision energy of 31.6 kcal/mol.

Figure 19:   CM flux map for a collision energy of 31.6 kcal/mol.

Figure 20:   Separation of the two reaction mechanisms for a collision energy of 31.6 kcal/mol shown as 3-D flux maps. Bottom map is the sideways/backward scattered component, middle is the forward scattered stripping component, and the top is the total flux map.

Continuous Pyrolytic Molecular Beam Source

High density graphite nozzle

SiC heating element

molybdenum bands

water cooled copper

Stainless mount

1 inch
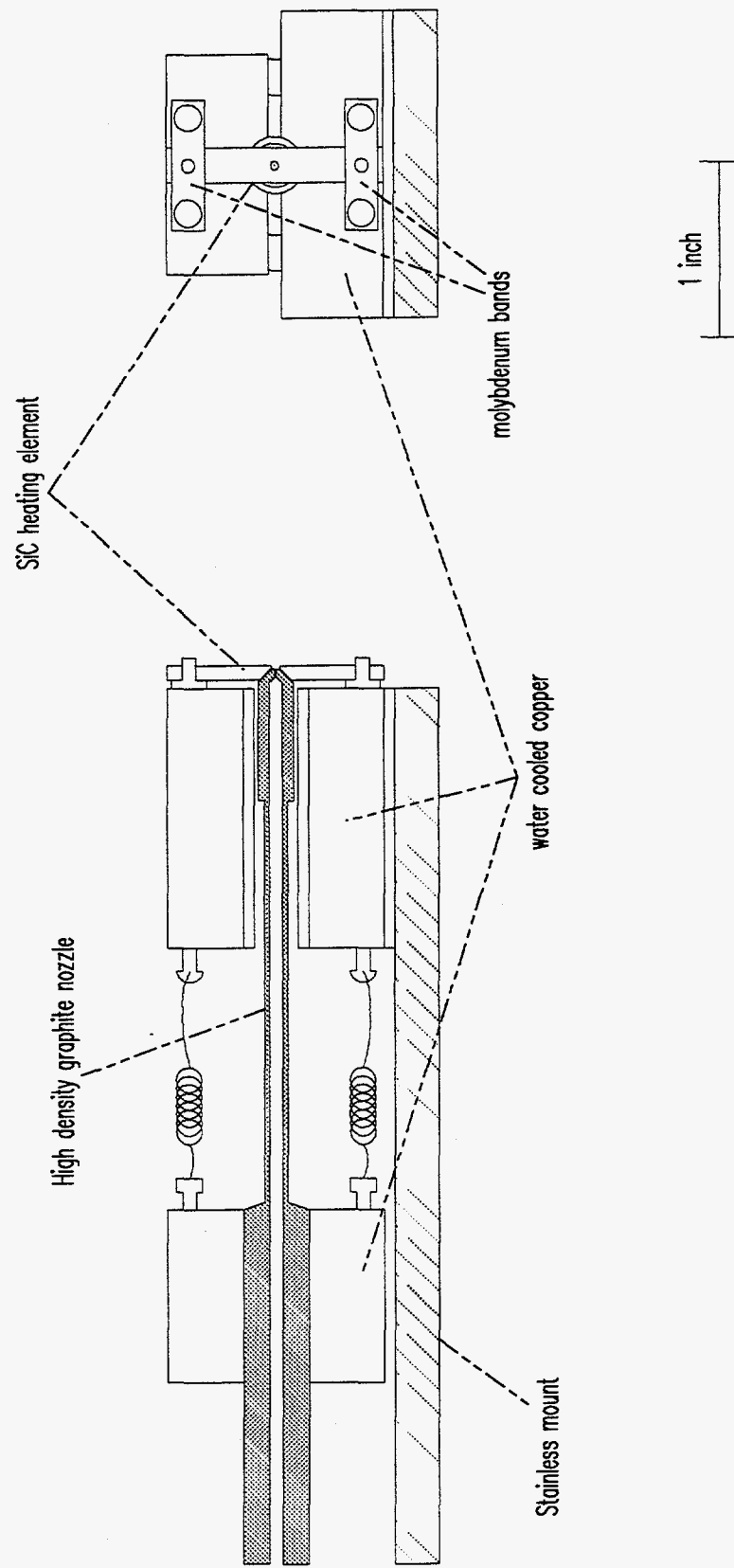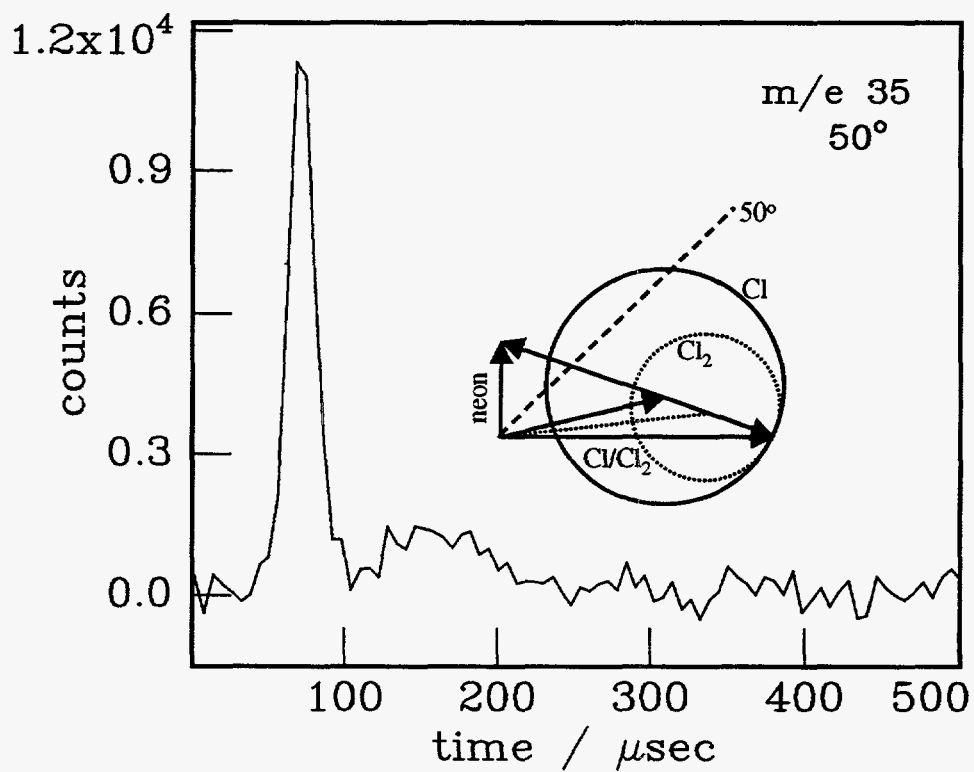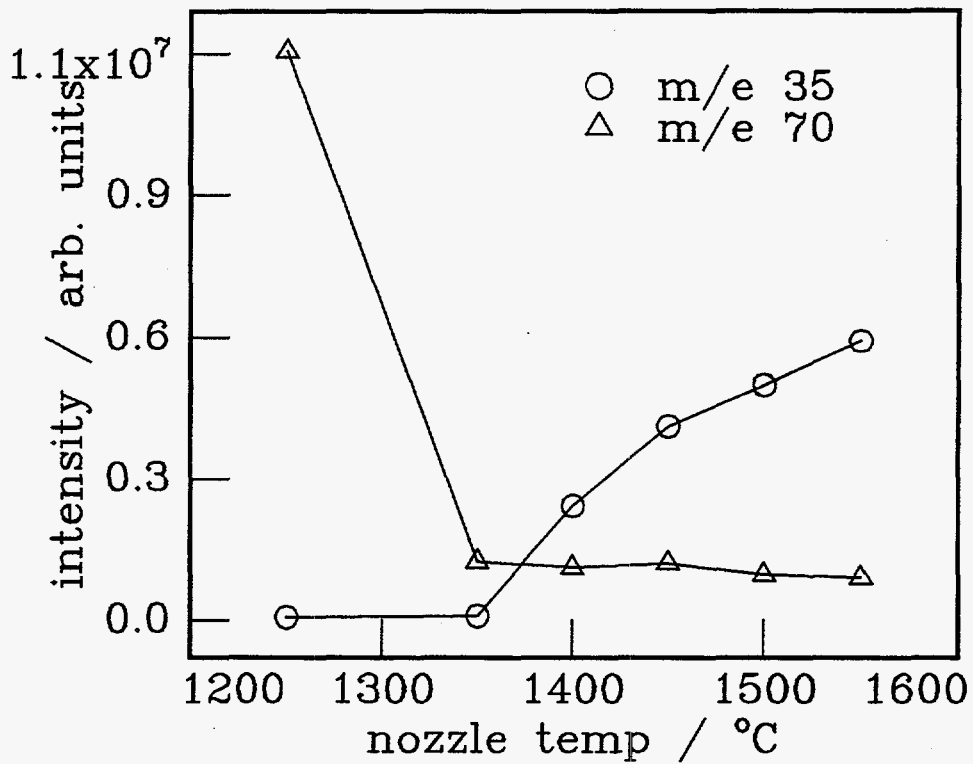
figure 1

figure 2

8.0 kcal/mol collision energy
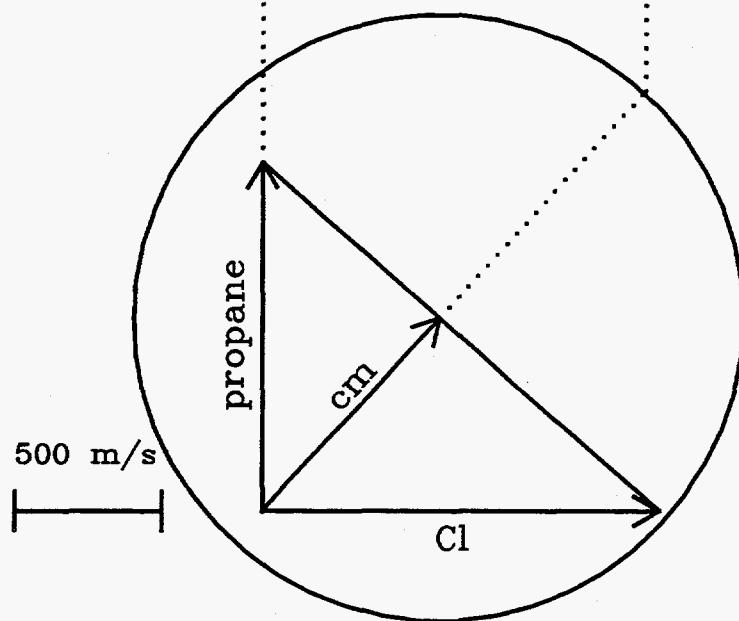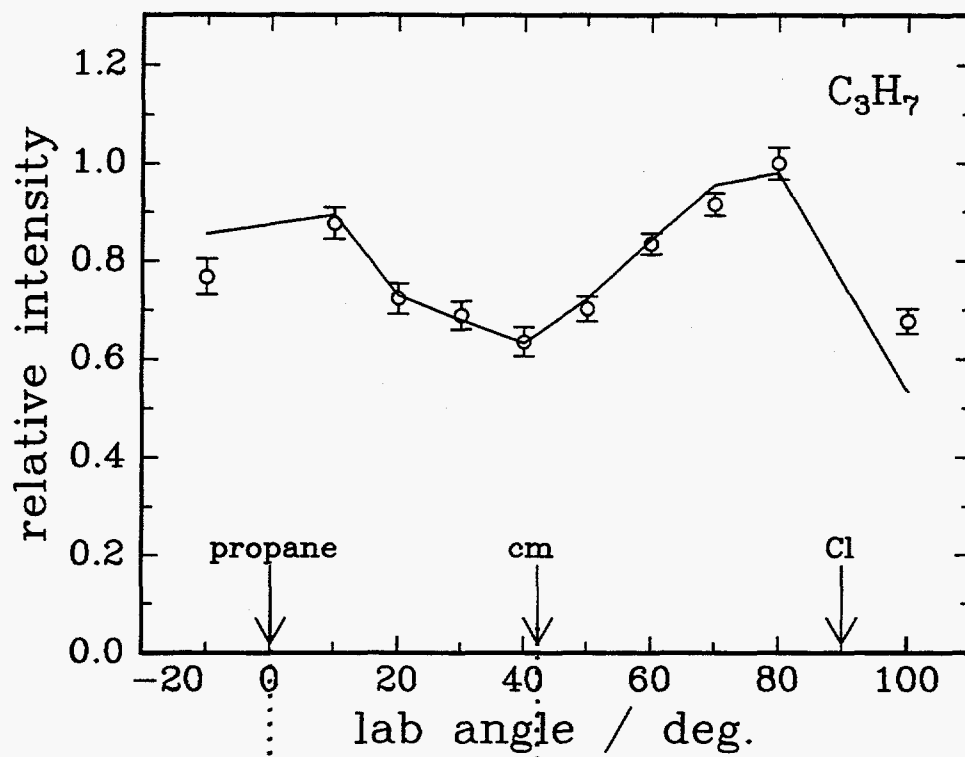
figure 3

8.0 kcal/mol collision energy

Number density / arbitrary units

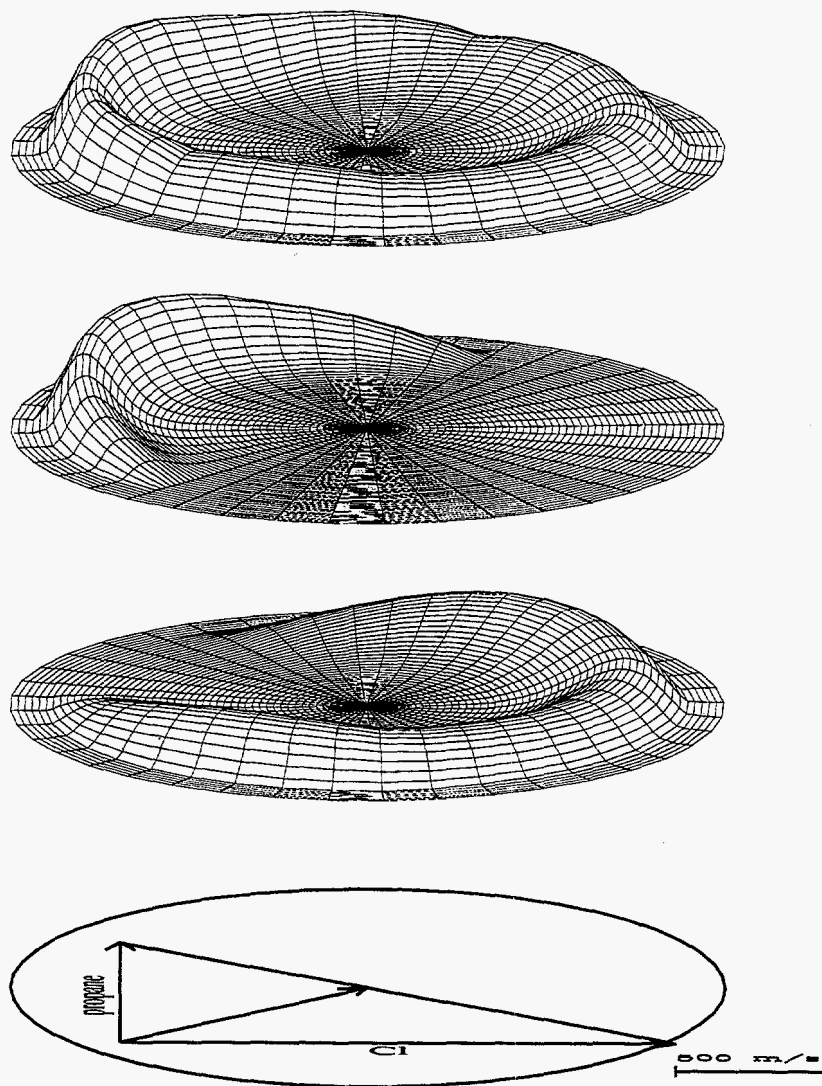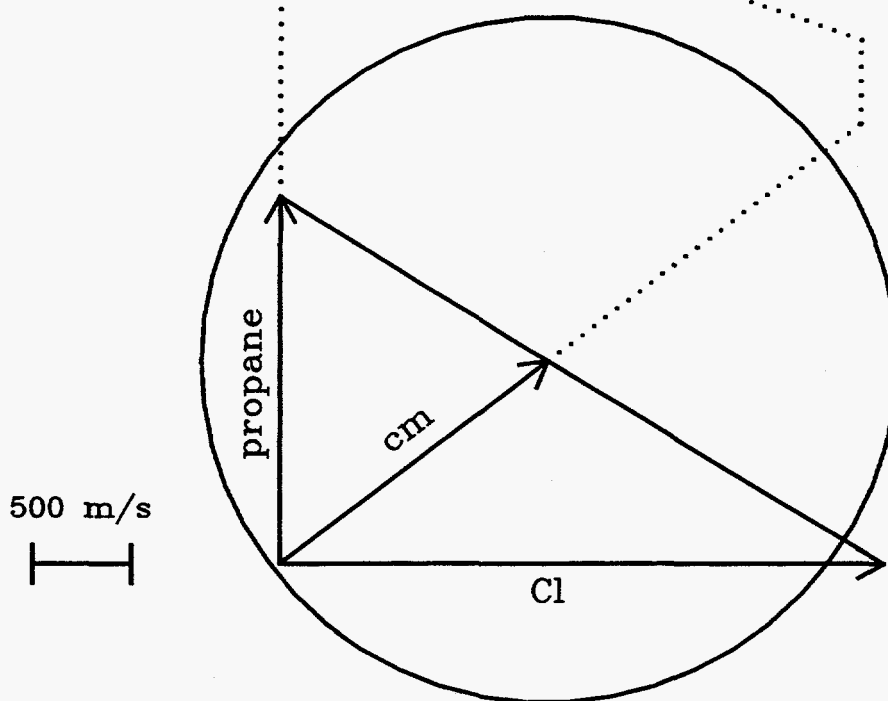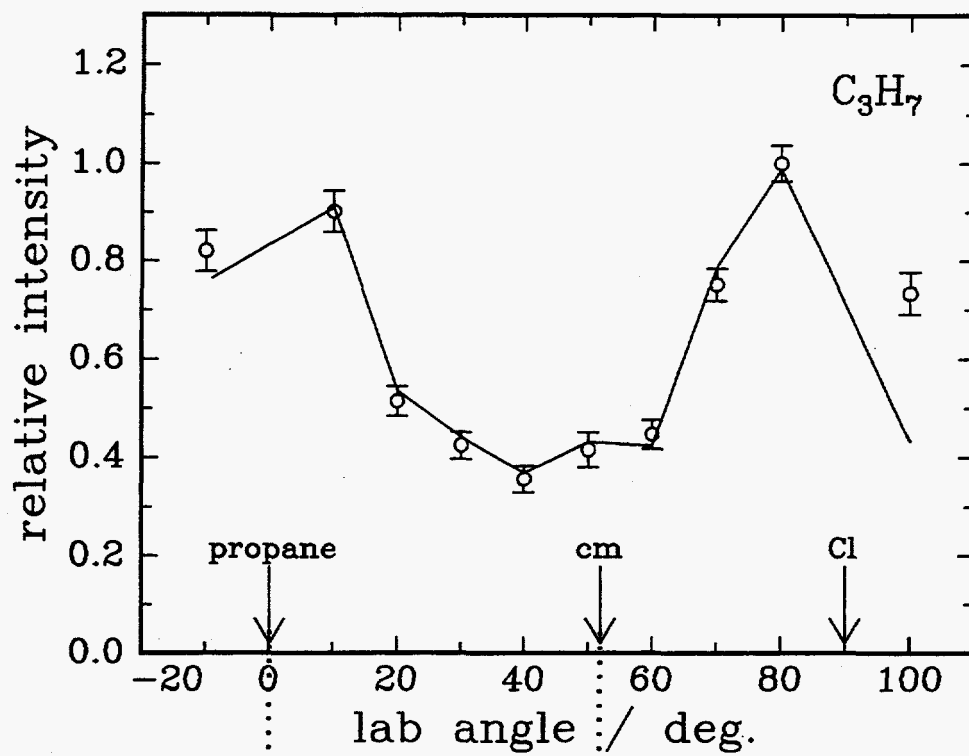C_3H_7 time of flight / μsec
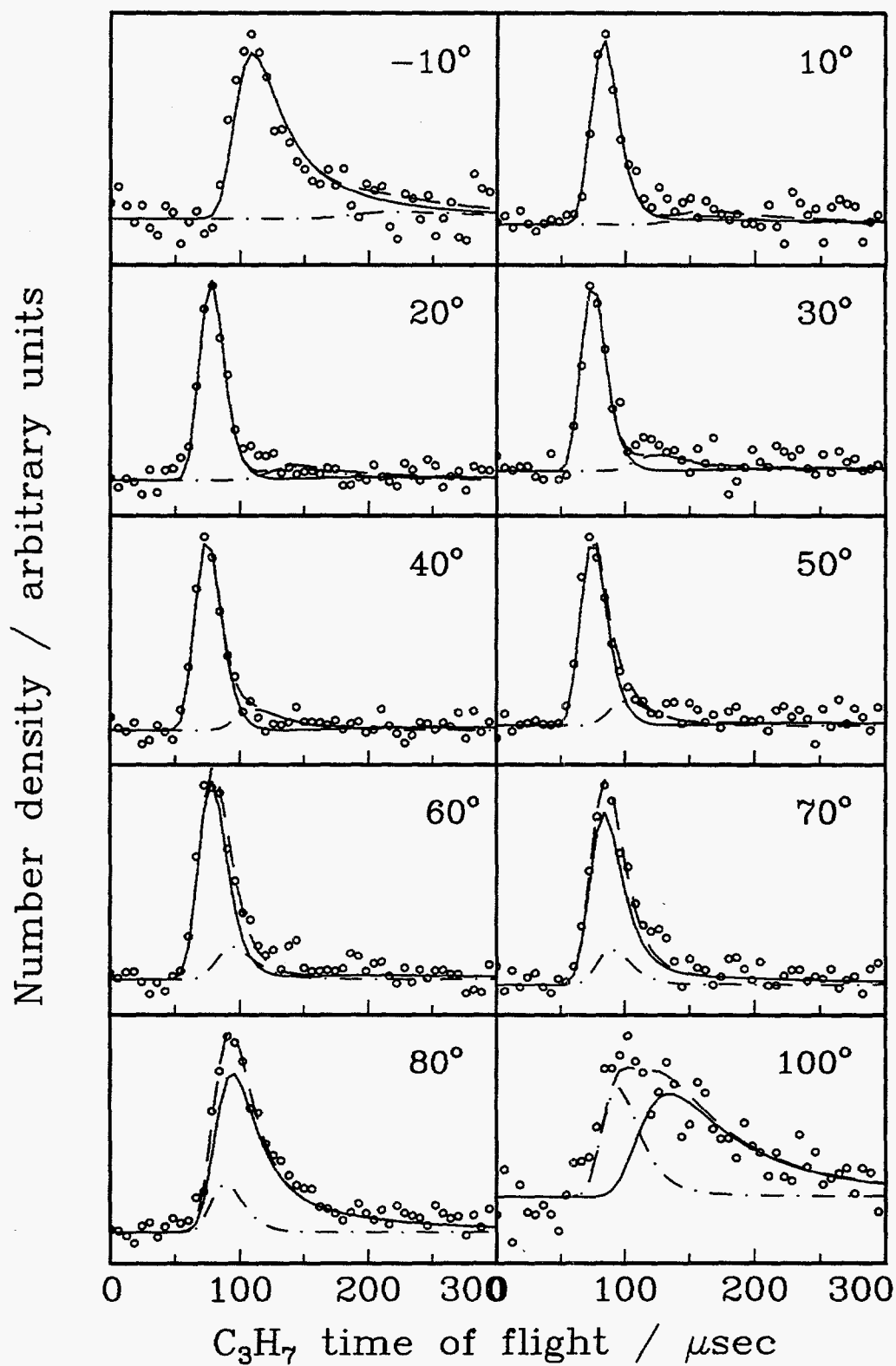
figure 4

8.0 kcal/mol collision energy
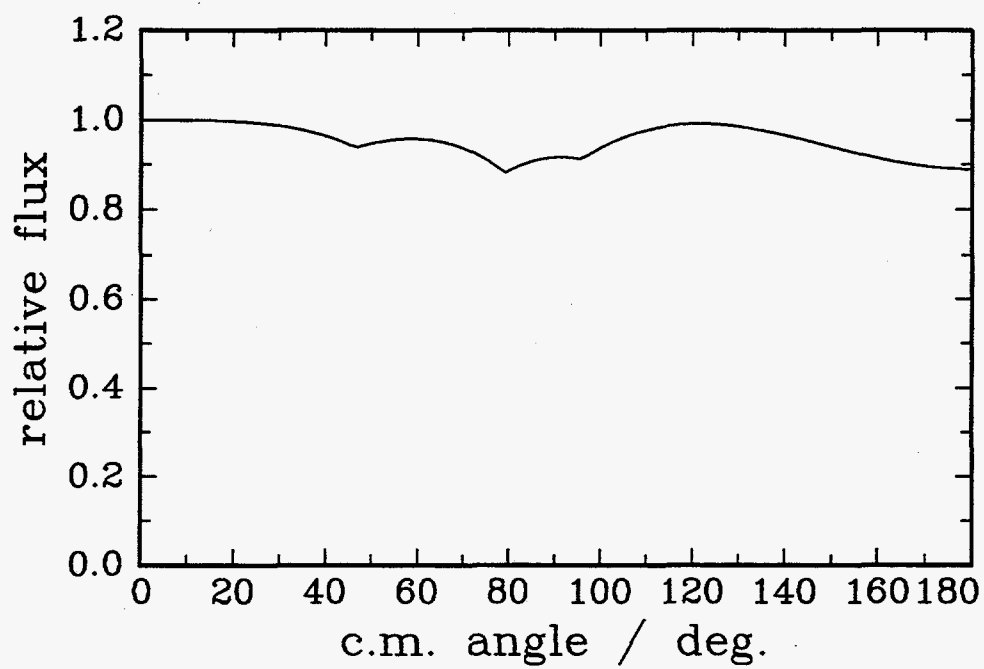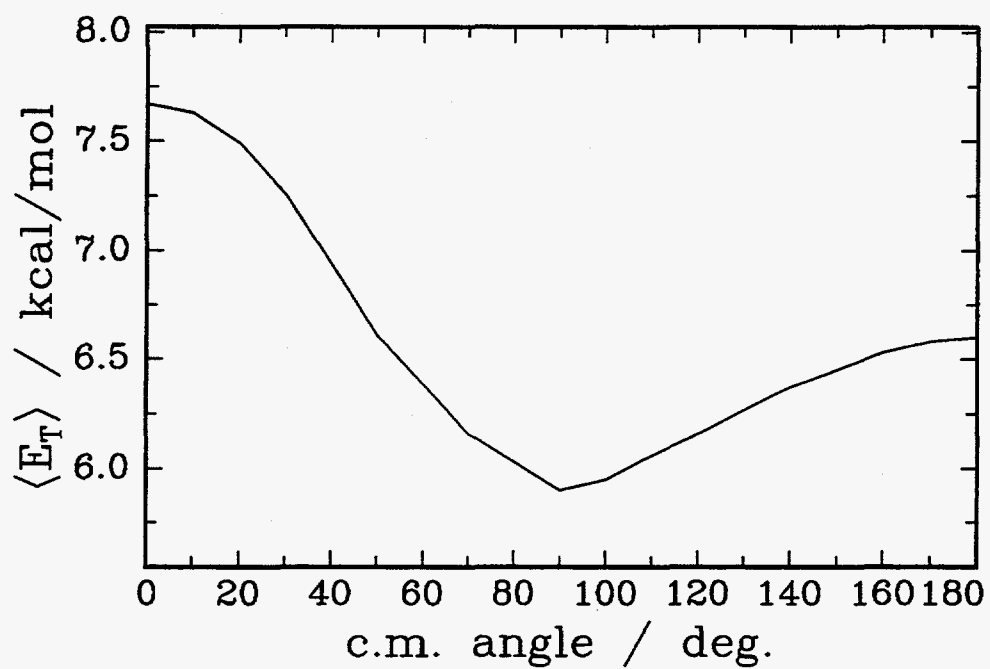
figure 5

8.0 kcal/mol collision energy
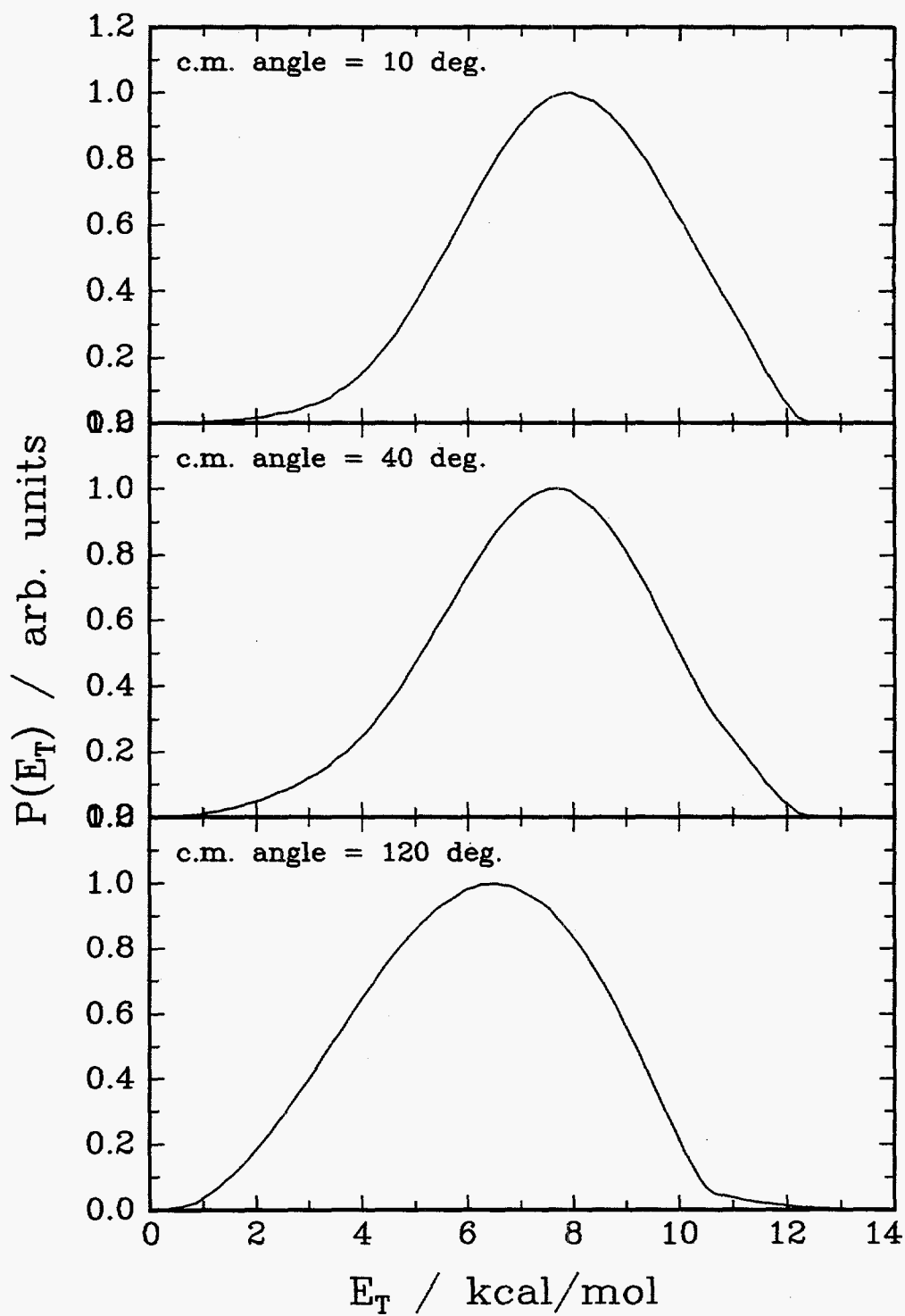
figure 6

8.0 kcal/mol collision energy
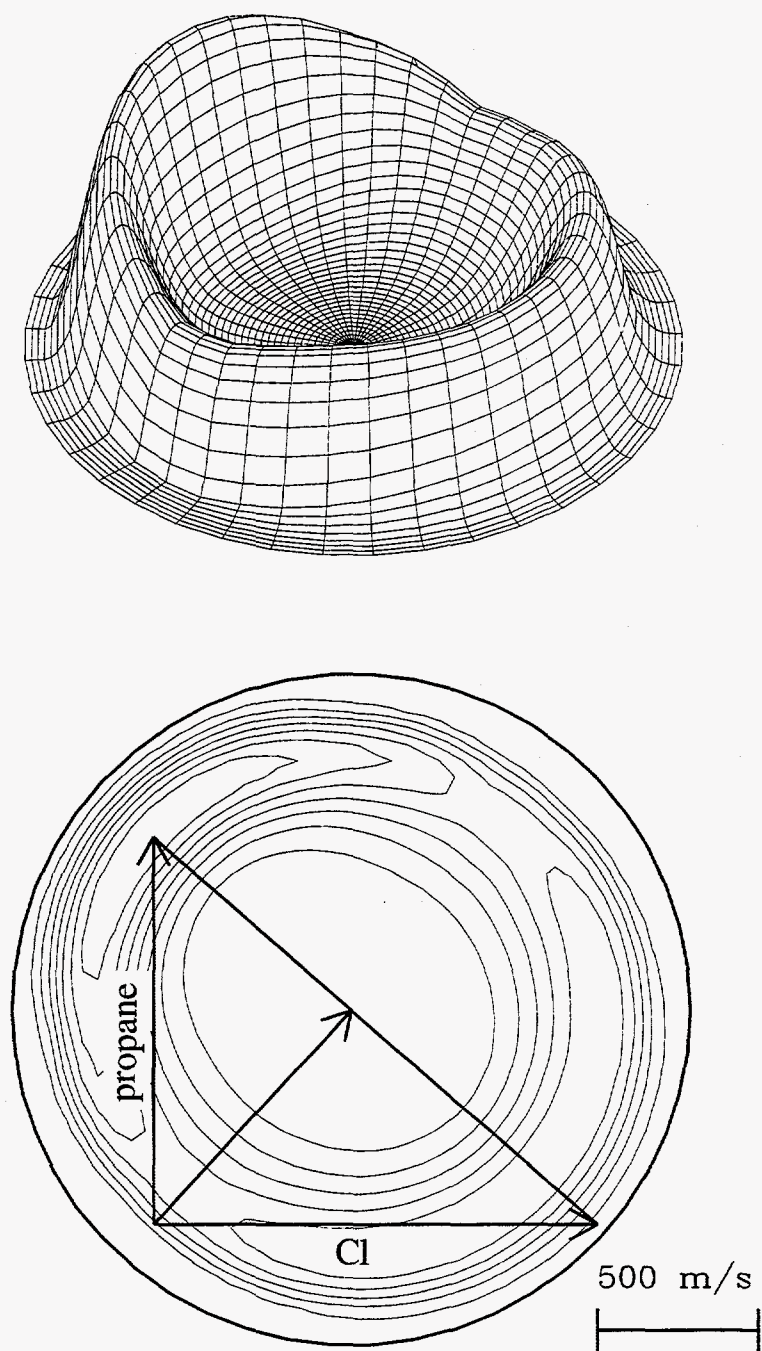
figure 7

8.0 kcal/mol collision energy
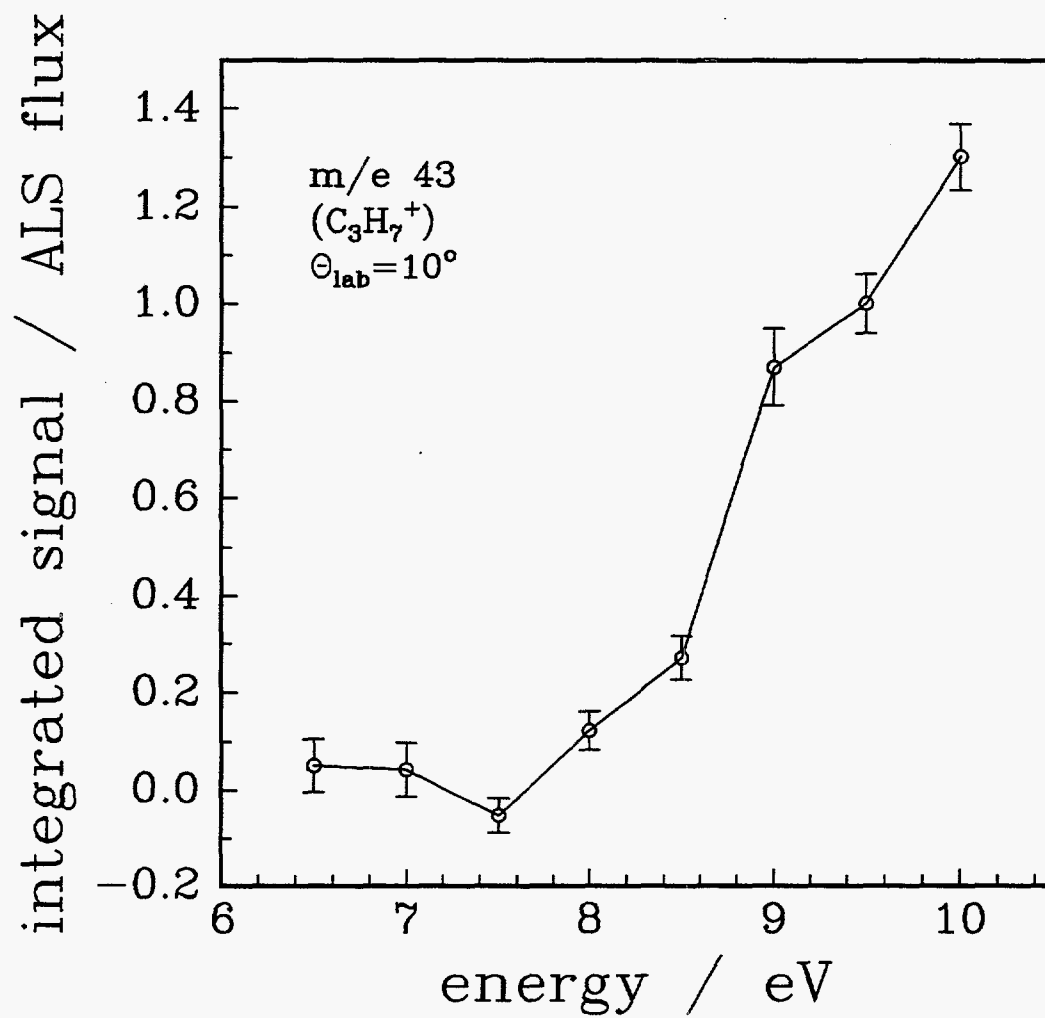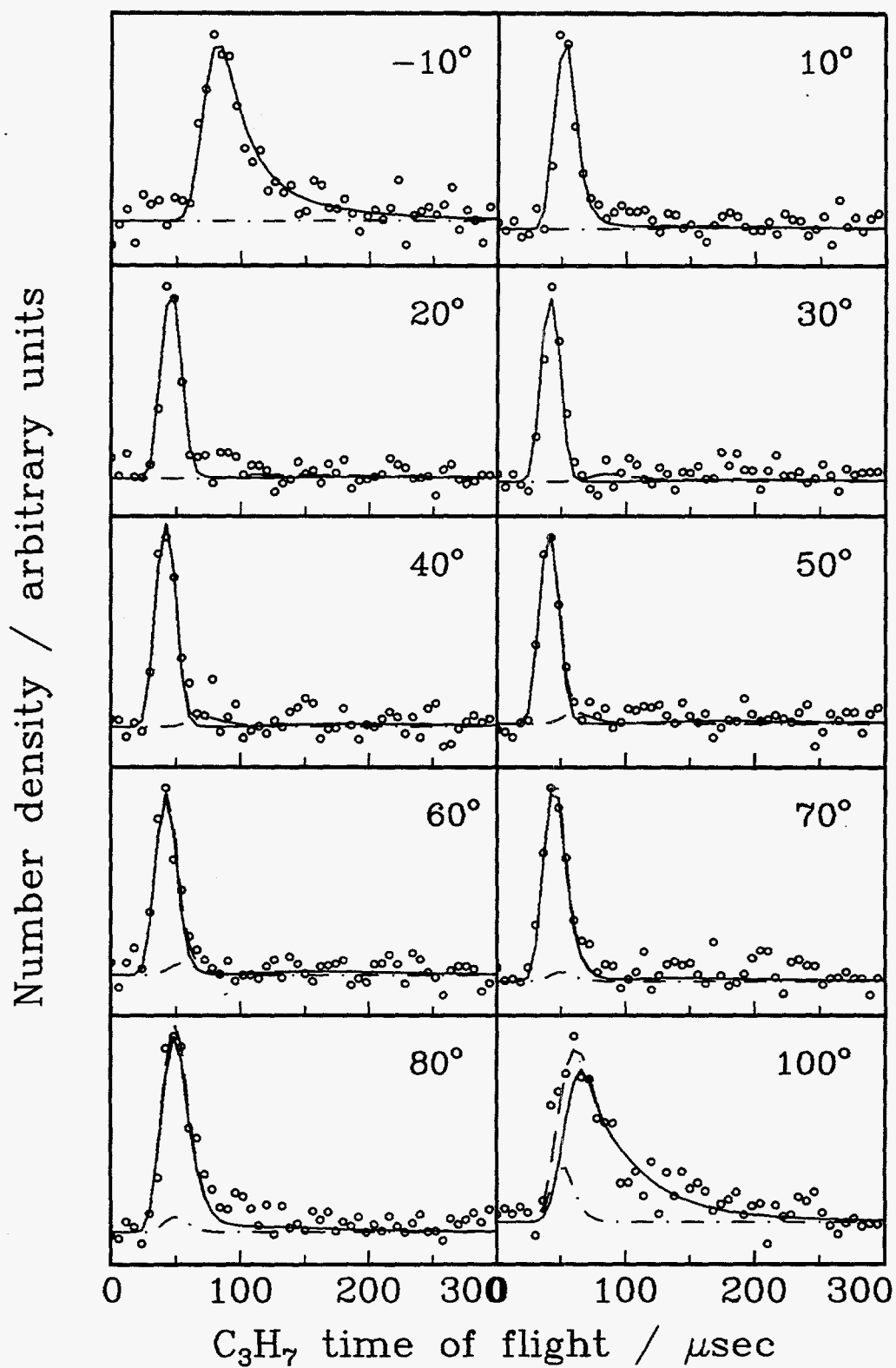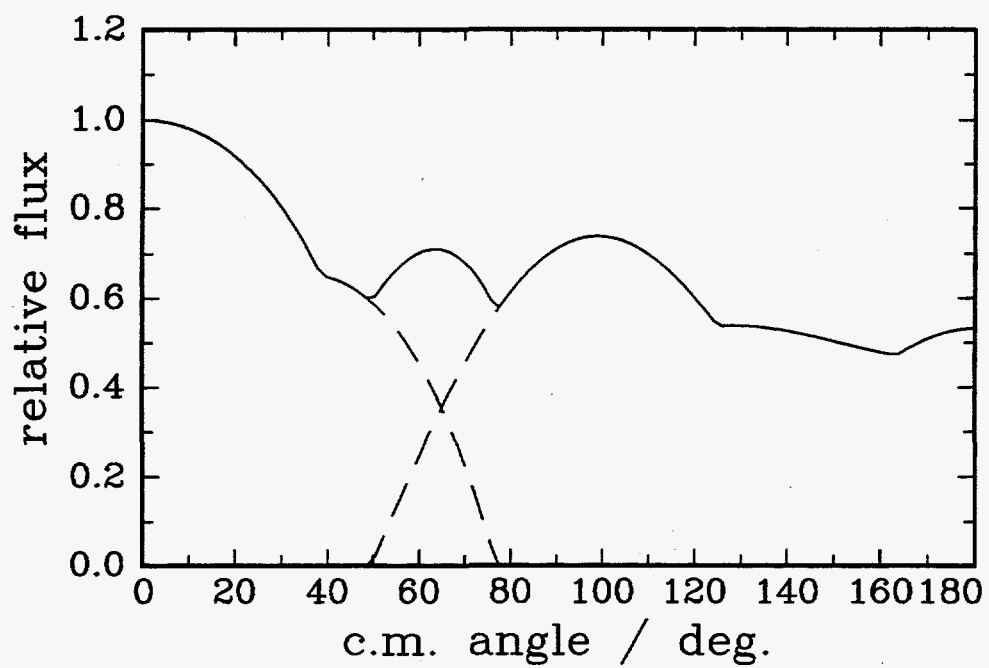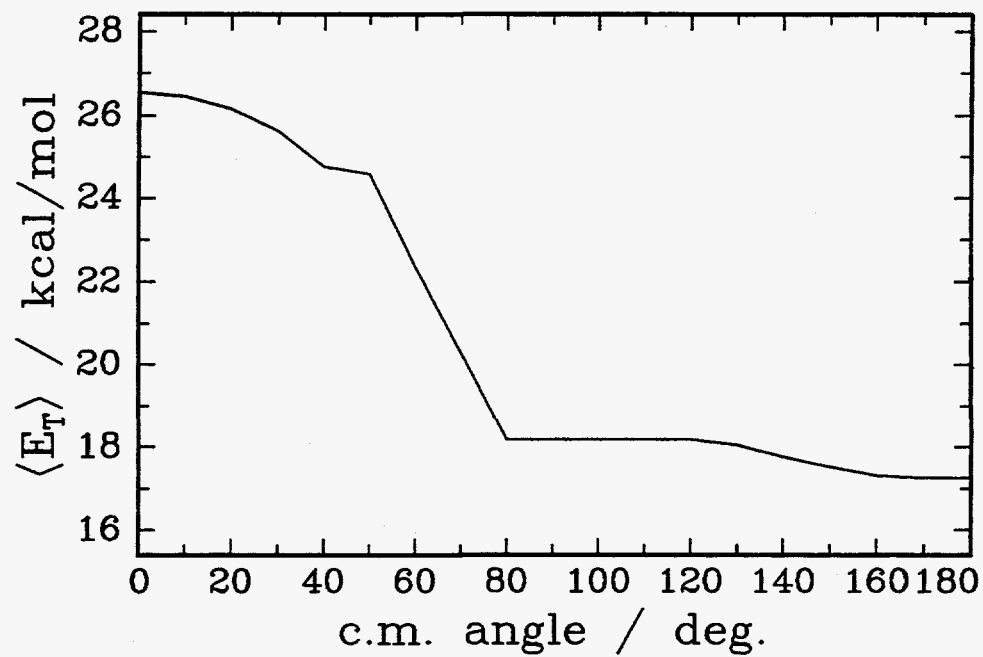

figure 8

11.5 kcal/mol collision energy
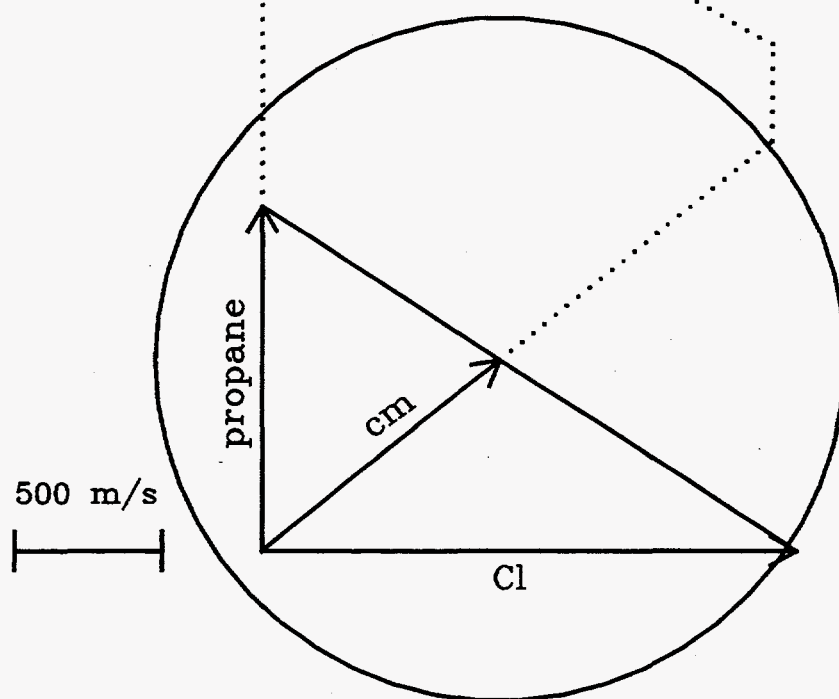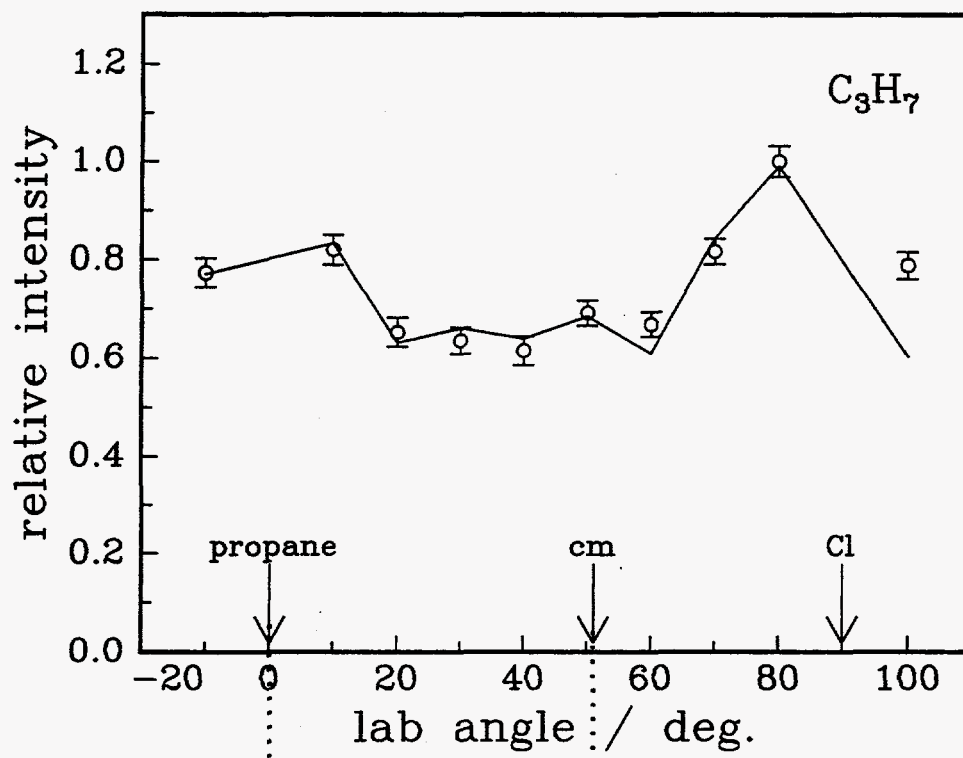
figure 9

11.5 kcal/mol collision energy

Plots of Number density / arbitrary units versus C_3H_7 time of flight / μsec, shown at angles $-10°$, $10°$, $20°$, $30°$, $40°$, $50°$, $60°$, $70°$, $80°$, and $100°$.
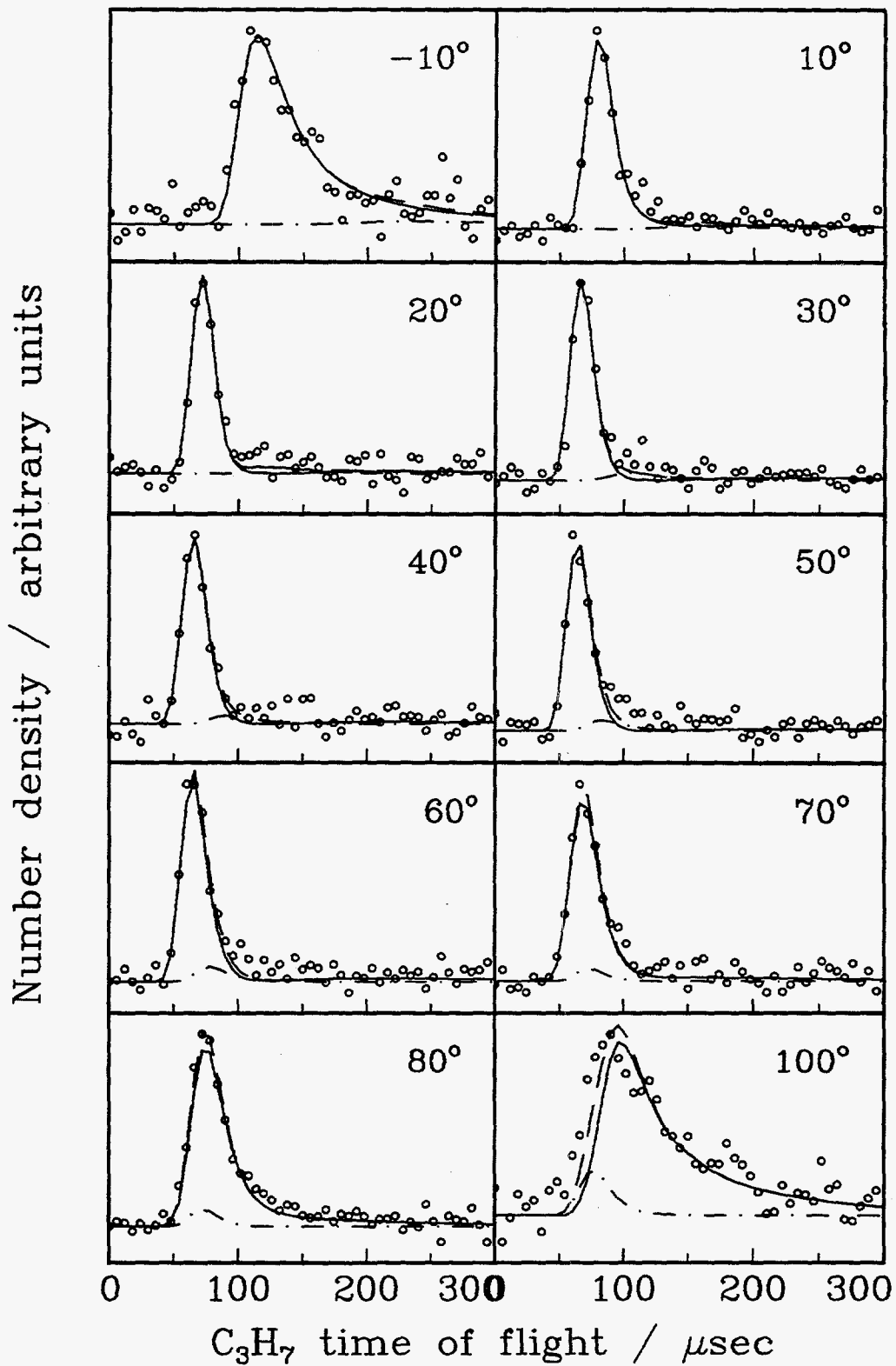
figure 10

11.5 kcal/mol collision energy
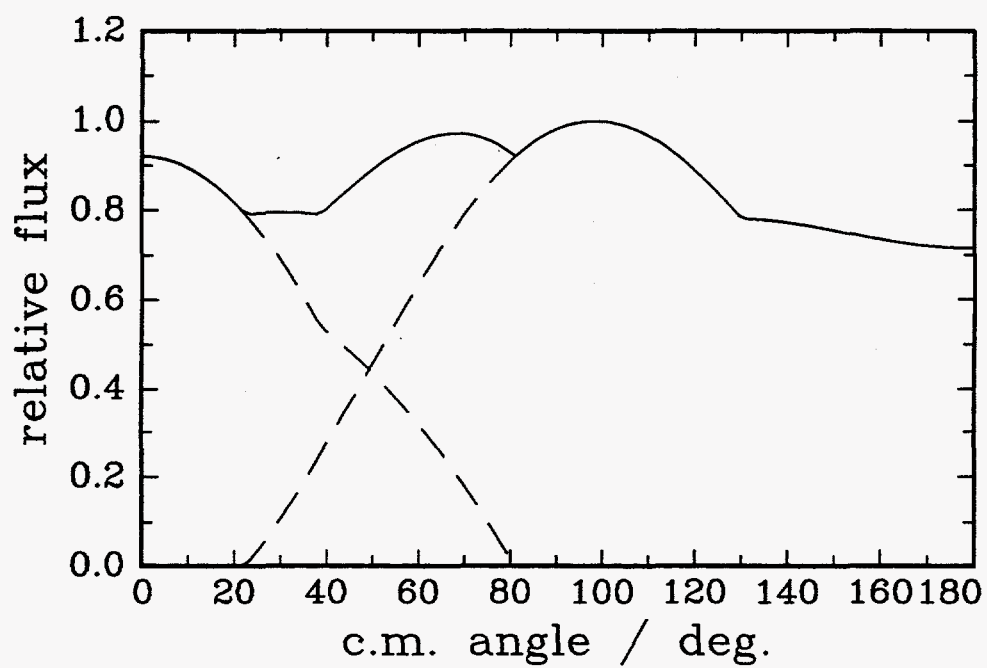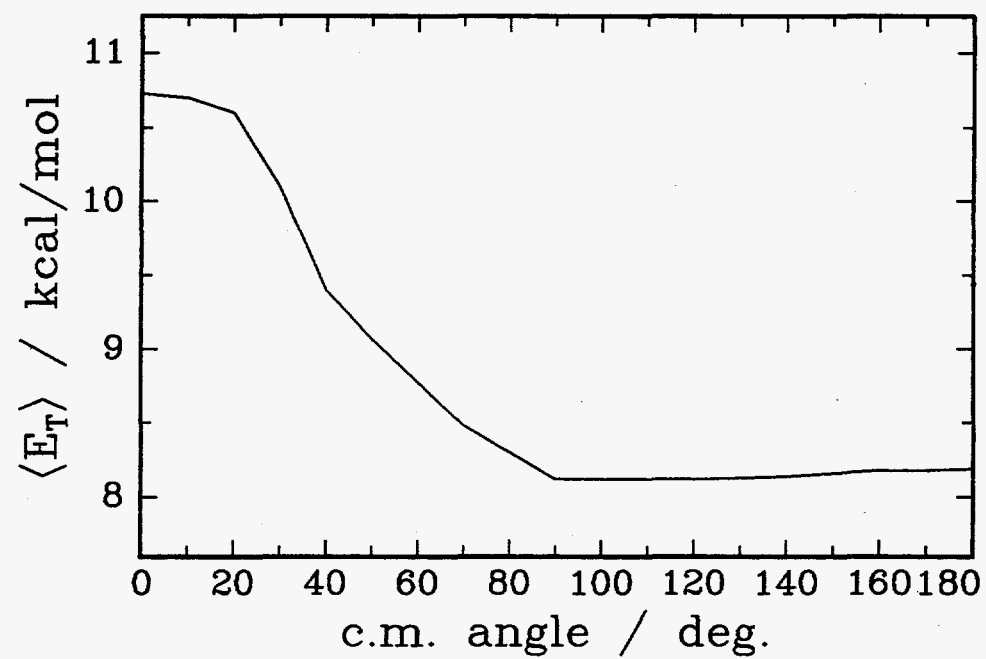
figure 11

11.5 kcal/mol collision energy
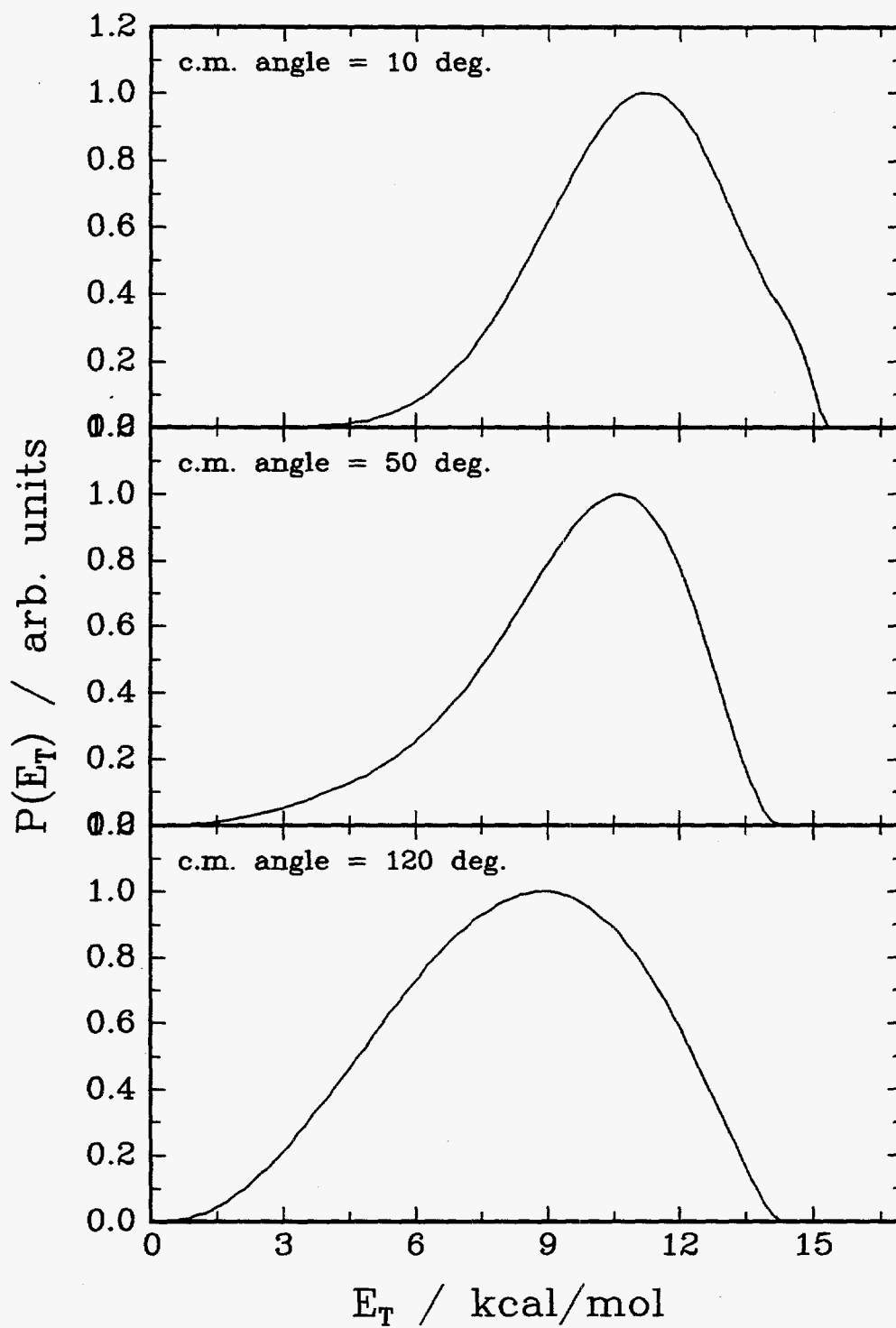
figure 12

11.5 kcal/mol collision energy
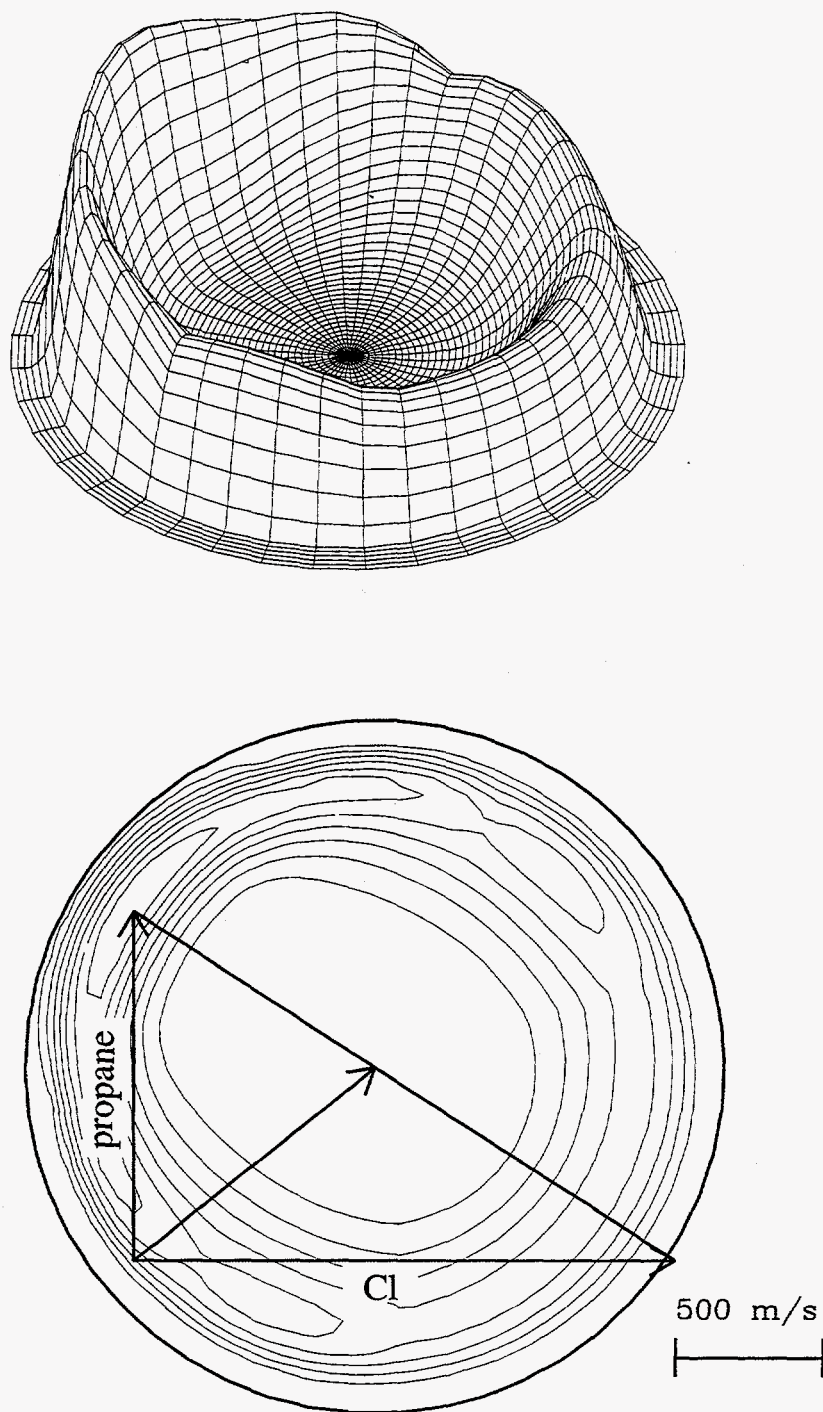
figure 13

11.5 kcal/mol collision energy

figure 14

31.6 kcal/mol collision energy
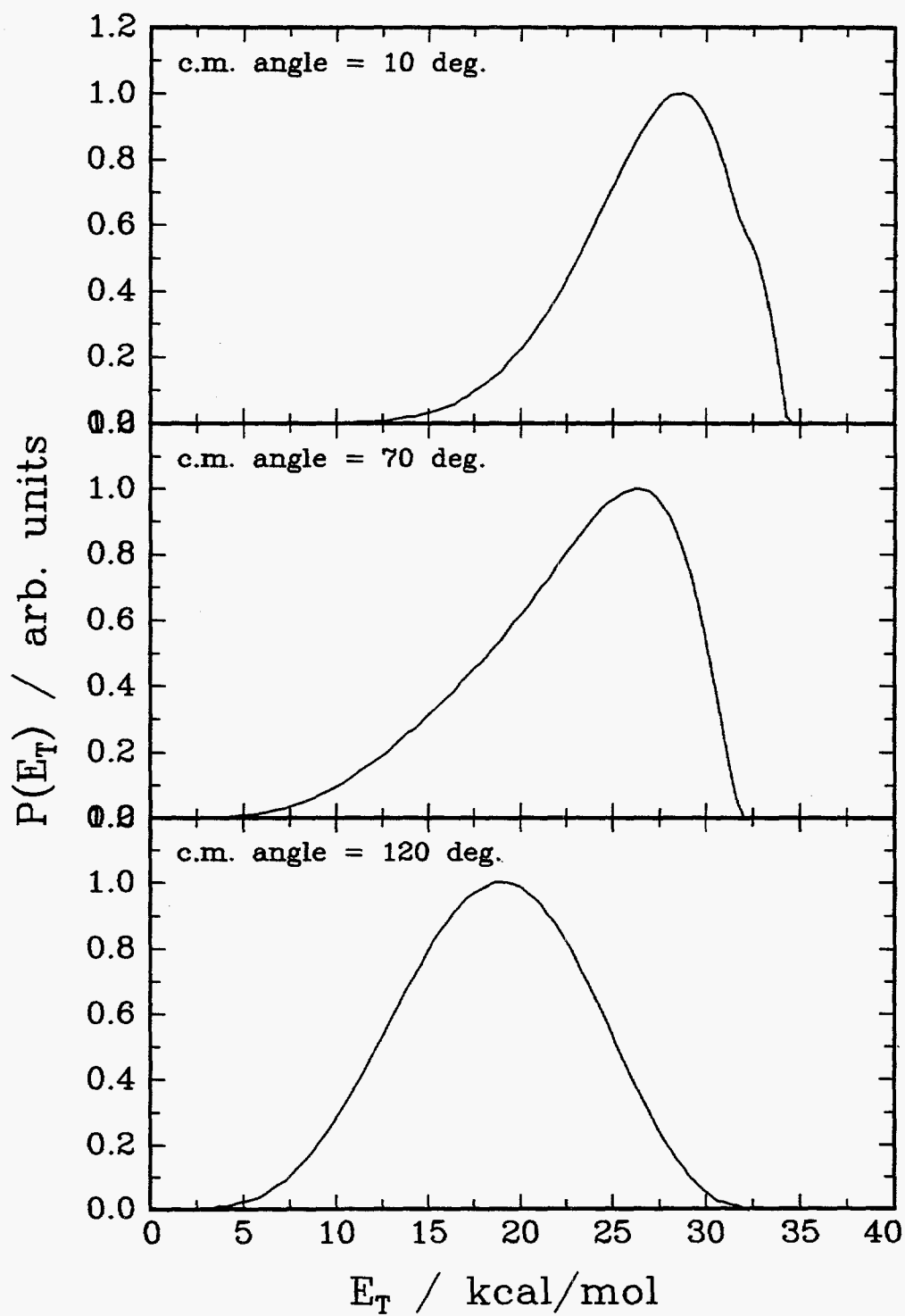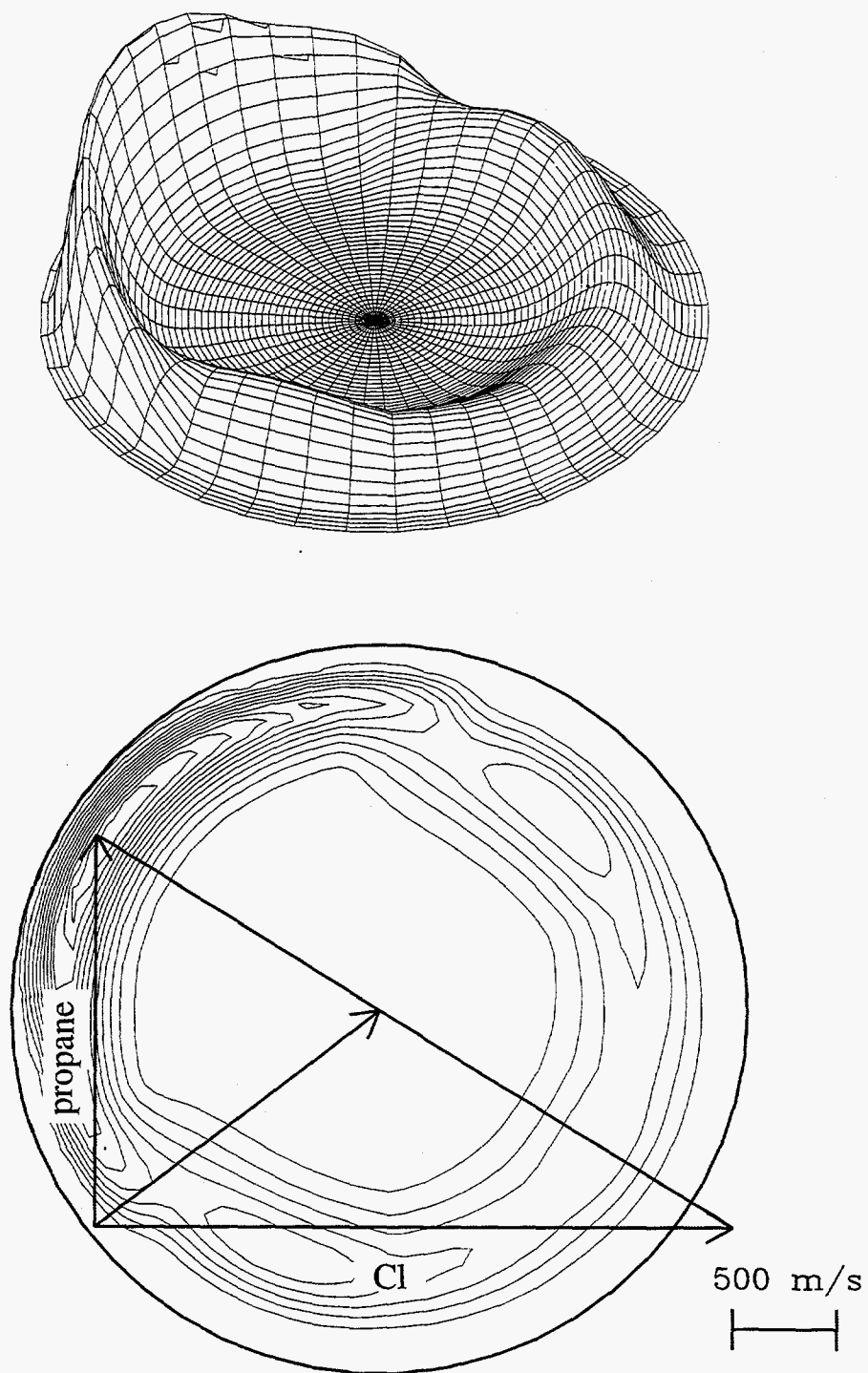

figure 15

31.6 kcal/mol collision energy

figure 16

31.6 kcal/mol collision energy

figure 17

31.6 kcal/mol collision energy

figure 18

31.6 kcal/mol collision energy

figure 19

31.6 kcal/mol collision energy

figure 20